Fantastic prints and where to find them

Citation for published version (APA):

Calore, A. R. (2023). *Fantastic prints and where to find them: processing routes for 3D scaffolds in Tissue Engineering*. [Doctoral Thesis, Maastricht University]. Maastricht University. https://doi.org/10.26481/dis.20231102ac

Document status and date:
Published: 01/01/2023

DOI:
10.26481/dis.20231102ac

Document Version:
Publisher's PDF, also known as Version of record

Please check the document version of this publication:

- A submitted manuscript is the version of the article upon submission and before peer-review. There can be important differences between the submitted version and the official published version of record. People interested in the research are advised to contact the author for the final version of the publication, or visit the DOI to the publisher's website.
- The final author version and the galley proof are versions of the publication after peer review.
- The final published version features the final layout of the paper including the volume, issue and page numbers.

Link to publication

General rights
Copyright and moral rights for the publications made accessible in the public portal are retained by the authors and/or other copyright owners and it is a condition of accessing publications that users recognise and abide by the legal requirements associated with these rights.

- Users may download and print one copy of any publication from the public portal for the purpose of private study or research.
- You may not further distribute the material or use it for any profit-making activity or commercial gain
- You may freely distribute the URL identifying the publication in the public portal.

If the publication is distributed under the terms of Article 25fa of the Dutch Copyright Act, indicated by the “Taverne” license above, please follow below link for the End User Agreement:

www.umlib.nl/taverne-license

Take down policy
If you believe that this document breaches copyright please contact us at:

repository@maastrichtuniversity.nl

providing details and we will investigate your claim.

Download date: 27 Apr. 2024

Fantastic Prints and where to find them

Processing routes for 3D scaffolds in Tissue Engineering

Andrea Roberto Calore

Fantastic prints and where to find them: Processing routes for 3D scaffolds in Tissue Engineering

Andrea Roberto Calore

Fantastic prints and where to find them: Processing routes for 3D scaffolds in Tissue Engineering

PhD Thesis, Maastricht University, Maastricht, The Netherlands

ISBN: 978-94-6469-572-4

Cover Art: Sidhant Sridhar

Printed by: ProefschriftMaken, De Bilt

Fantastic prints and where to find them: Processing routes for 3D scaffolds in Tissue Engineering

DISSERTATION

To obtain the degree of Doctor at Maastricht University,

on the authority of the Rector Magnificus, Prof. dr. Pamela Habibovič

in accordance with the decision of the Board of Deans,

to be defended in public on

Thursday 2nd November 2023, at 10:00 hours.

By

Andrea Roberto Calore

Born on the 17th December 1988, in Padova, Italy.

Supervisor:

Prof. dr. Lorenzo Moroni

Co-supervisors:

Dr. Jules Harings

Dr. Katrien Benrnaerts

Dr. Carlos Mota

Assessment committee:

Prof. dr. Kim Ragaert, CHAIR

Prof. dr. Patrick Anderson, Eindhoven University of Technology

Dr. Laurence Hawke, Catholic University of Louvain, Brussels, Belgium

Prof. dr. Martijn Poeze

Prof. dr. Roman Truckenmüller

The research described in this thesis was conducted at MERLN Institute for Technology Inspired Regenerative Medicine and at the Aachen-Maastricht Institute for Biobased Materials (AMIBM) in Maastricht University. The work in this thesis was financially supported by the Brightlands Materials Center (BMC).

TABLE OF CONTENTS

Chapter 1

MELT-EXTRUSION ADDITIVE MANUFACTURING FOR TISSUE ENGINEERING: APPLICATIONS AND LIMITATIONS

Andrea Roberto Calore[1,2], Carlos Mota[1], Katrien Bernaerts[2], Jules Harings[2], Lorenzo Moroni[1]

[1]MERLN Institute for Technology-Inspired Regenerative Medicine, Maastricht University, Maastricht, The Netherlands

[2]Aachen-Maastricht Institute for Biobased Materials (AMIBM), Maastricht University, Geleen, The Netherlands

Chapter accepted in 3D Printing and Additive Manufacturing

ABSTRACT

The application of Additive Manufacturing techniques has increased over the years in almost all production fields, thanks to the possibility of creating objects from scratch and with the desired shape, with no need for molds or complex machinery typical of subtractive manufacturing. This success has concerned the biomedical world as well, where melt-based methods represent the golden standard to produce scaffolds for hard-tissue engineering. Despite the large amount of studies present in literature on scaffold production, the fabrication process is still affected by drawbacks and limitations, which hinders the standardization and upscaling to industrial level. In this review, we briefly present the history of Additive Manufacturing and the reasons of its success, with particular reference to the Tissue Engineering and Regenerative Medicine world. We then proceed to highlight the current factors limiting the straightforwardness of the production process and affecting the quality and the performance of the manufactured scaffolds. Eventually, we suggest potential strategies to increase the level of control during manufacturing and to improve the biomimicry of the fabricated constructs, with the goal of obtaining a more optimal workflow.

1.1 INTRODUCTION

Lack of organ donors is a burden that has been affecting transplants all over the world for already two decades and it is still considered a major healthcare challenge [1]. If we take the example of Italy only, in 1985 113 people died because in need for organs that were not available. After the enforcement of the mandatory motorcycle helmet in mid-1986, the situation further worsened. In 1987, 1700 patients were awaiting for kidney transplants and 400 for heart transplants [2]. With the population increasing and the longer life expectation, the situation further worsened, with transplant lists counting, by the end of May 2022, 697 patients awaiting for new hearts and 7081 for kidneys [3]. Additionally, the expected awaiting times are 3.6 and 3.2 years, respectively. On one side, the lack of available organs has been the clear sign of progress and higher welfare standards, having institutions forced people to take more care of themselves. On the other hand, an endless list of patients has been bound to an uncomfortable life, such as those undergoing dialysis, more or less permanently. In addition to these, many patients were simply destined to die. To mitigate the critical shortage of donor organs, a completely new field has emerged, Tissue Engineering and Regenerative Medicine (TERM). The goal of this new discipline was, and still is, the application of the principles of engineering and life science to fabricate biological substitutes in vitro that are able to maintain, improve or restore the functions of a tissue or organ [4], [5].

Over the years, great progress has been made. A significant step forward was taken when the group of technologies commonly known as 3D printing was adopted in tissue engineering. Here it is important to highlight that, despite being used as a general term, “3D printing” refers to a specific technique, while the group of technologies in its entirety is referred to as “Additive Manufacturing (AM)” as established by the American Society for Testing and Materials (ASTM) in 2009 [6]. The name perfectly embodies the principle behind the new methods: “the process of joining materials to make objects from 3D model data, layer upon layer, as opposed to subtractive manufacturing methodologies, such as traditional machining”. AM devices have been around since 1986, when the first stereolithographic (SLA) device was produced [7]. This technology was followed by the development of several other techniques, which were categorized by the ASTM and ISO standardization organization as follows [8]: powder bed fusion (PBF, which includes selective laser sintering (SLS)), material extrusion (ME), VAT photopolymerization (VP, in which stereolithography (SLA) falls), material jetting (MJ), binder jetting (BJ), sheet lamination (SL) and directed energy deposition (DED) (Figure 1). Despite the huge plethora of methods developed over the years, all AM technologies share the common approach of layer-by-layer addition of material, which allows for the production of customized parts without the need for molds or subtractive machining. The main advantage of these technologies is therefore the possibility of manufacturing small quantities of customized products at relatively low costs, which shifted the application of 3D printing from the initial prototyping field to product production [9], [10]. This perfectly matches the patient-specific paradigm that has been advancing in medicine with the growth of tissue engineering [11]–[15].

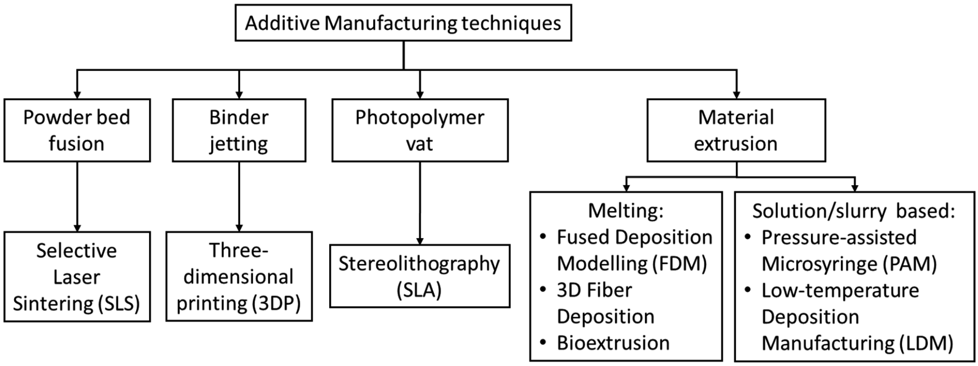

Figure 1. Overview of Additive Manufacturing techniques used in Tissue Engineering. Adapted from Calore et al. [16].

The goal of this review is to illustrate the potential of AM techniques for TE, their current limitations and suggested strategies to overcome them. We start by describing the so-called “conventional methods” for scaffold production and how AM took over, offering scientists a higher degree of control on the final constructs in a field where morphology is often synonym of biological performance. Particular attention will be given to the class of techniques based on polymer-melt deposition, largely widespread in the hard-tissue engineering field, because they allow the processing of mechanically-performing synthetic polymers. The focus will be then shifted to the challenges that tissue engineers still have to face when manufacturing scaffolds via melt-based AM, with particular reference to the unpredictability of the construct properties, lack of standardization, polymer thermal degradation and bioinertness, absence of topographical features, brittle mechanics uncontrolled crystallization. For each of these topics, a strategy with the potential to solve the issue will be suggested, with the goal of improving the control on the process and the quality of the final scaffold with limited steps.

1.2 ADDITIVE MANUFACTURING FOR TISSUE ENGINEERING

In the context of personalized regenerative medicine, engineered constructs are required to exhibit patient- and tissue-specific properties, such as geometry and porosity. While the former is needed to fill or treat a defect in its entirety ensuring morphological continuity with the surrounding healthy tissue, high macro porosity promotes nutrient and waste transport, tissue ingrowth and vascularization. Before the arrival of AM, tissue-engineering scaffolds were manufactured via the so-called “conventional methods”, which include gas foaming/particulate leaching [17], [18], freeze-drying [19], [20] or phase separation [21], [22]. All these techniques allow the manufacturing of constructs with sufficient amount of porosity, which is a requirement for cell infiltration, nutrients uptake, waste removal and thus proper tissue growth. Nevertheless, the overall morphology of the scaffold is dictated by the molds where scaffolds are fabricated or by post-manufacturing shaping operations. This represents a huge limit in view of the production of patient-specific implants. On top of this, the level of control on pore size and distribution is very limited and mainly left to the spontaneity of the process. As a result, the achieved porosity is often non-interconnected, resulting in inhomogeneous tissue development [15], [23]–[25]. This leads to scaffolds with uneven properties from batch to batch, making the process variable. In view of upscaling scaffold production and bring tissue engineering to the industrial market, more reliable and reproducible techniques are needed [26]–[28]. Additive manufacturing techniques offer tissue engineers those extra features that allowed to improve scaffold quality and process repeatability. AM allows the reproducible fabrication of 3D structures with tailorable geometrical complexity, interconnected and tunable porosity, with the possibility of including multiple materials [29], [30]. The control over the intra and inter-layer geometry (and therefore over the porosity) results into tailorable mechanical properties, which is particularly desirable for the manufacturing of scaffolds towards the regeneration of load-bearing tissues such as bone and cartilage [31]–[33]. Among the several available technologies, material-extrusion AM techniques (ME-AM, as categorized by ASTM and ISO organizations [8]) have gained tissue engineers' attention particularly. These are based on the melting and the subsequent extrusion of a material through a nozzle. While for industrial applications metals, ceramics and thermoplastic polymers can be used, in TERM polymers are preferred because of their mechanical properties, which place themselves in between the excessive stiffness of metals and the excessive brittleness of ceramics [34]. From the original Fused Deposition Modeling (FDM), also referred to as Fused Filament Fabrication (FFF) and commercially available since 1992 [35], other techniques based on the extrusion of thermoplastic polymers in a melt were developed to accommodate for the diverse states in which the raw material could be. Current technologies include: FDM, where a filament is pushed through a heated nozzle that melts the material and deposits it; 3D fiber deposition (3DF), in which the polymer in the form of powder, granules or pellets, is placed in heated syringe and the melt is extruded by application of pressure via a piston or compressed gas; bioextrusion, where polymer granules, pellets or powder are melted in a pressurized chamber and the melt is pushed to an auger screw, which eventually extrudes it [16]. A schematic representation of the three techniques is given in Figure 2, while a comparison between their features is offered in Table 1. However, melt-based technologies using thermoplastic materials suffer from limitations inherent to its polymeric constituents. The mechanical properties of additively manufactured polymeric constructs are particularly influenced by AM process parameters, specifically layer-by-layer deposition strategies. In melt-based techniques, interlayer bonds form by diffusion of polymer molecules between two consecutive layers. For this to happen, both layers have to be in a semi-molten state or in a state where anyways the mobility of single molecules is sufficiently high to diffuse from one layer to the other. Bonding is achieved when molecules diffuse sufficiently in depth into the other layer to form entanglements with the local polymer chains [36]. However, in contrast to metals or low molecular weight organic compounds, the diffusivity of polymer molecules is extremely low due to the adjacent chains imposing physical restrictions. If we model these restrictions as a tube, a single polymer molecule can only "reptate" or diffuse back- and forward along the chain/tube direction [37]. Then, it is evident that the time for a polymer to diffuse out of its tube scales strongly with their length and thus molar mass. Sufficiently high molar masses are needed for the polymer molecules to entangle, contributing to a physical network that is the origin of the praised mechanical properties of polymeric materials attained under mild conditions. Considering the relatively small difference between extrusion temperature and the temperature where mobility is hindered upon cooling (glass transition temperature), the useful time window for this process to happen is particularly narrow [38]. In addition, the section of the bottom layer involved in the bonding process is abundantly smaller than the corresponding of the top one. This happens because such a bottom layer, already in solid state, is passively reheated by the deposition on top of it of a new hot filament, but the process has limited spatial extent [39]. For this reason, the weaker bond interface between layers can result in strength along the build direction as low as 40-50% of that in other directions [40].

Furthermore, melt-based techniques suffer from lower resolution than other AM methods. In particular, printed parts by ME-AM can exhibit features of 100 - 150 µm in width while SLS and lithography-based techniques have the ability to reach resolutions down to 50 and 0.1 µm, respectively [41]. This difference arises from the relatively low control on the flow of polymeric materials with respect to the precision of a light (SLA) or laser (SLS) beam. To obtain comparable features, the flowrate should be in the order of nanoliters per second, which would require accurate molten flow delivery and precise temperature control systems currently unavailable on the market [42]. Nevertheless, melt-based AM has emerged as choice of reference to produce scaffolds for TE. The success of this class of techniques is mainly due to their versatility: the needed equipment is relatively simple and low-cost, and the palette of usable materials is wider [43]. Other techniques, in fact, require more advanced equipment such as a laser for SLS, a UV light source for SLA or actuator cartridges for 3DP. The material requirements are also very specific: photosensitive polymers are needed for stereolithography (SLA), while selective laser sintering (SLS) and three-dimensional printing (3DP) work with very fine and homogeneous polymer powders [31]. The only requirement for FDM materials is to be thermoplastic and the equipment is nothing but a heated nozzle with filament rollers, a piston or compressed gas depending on the technique.

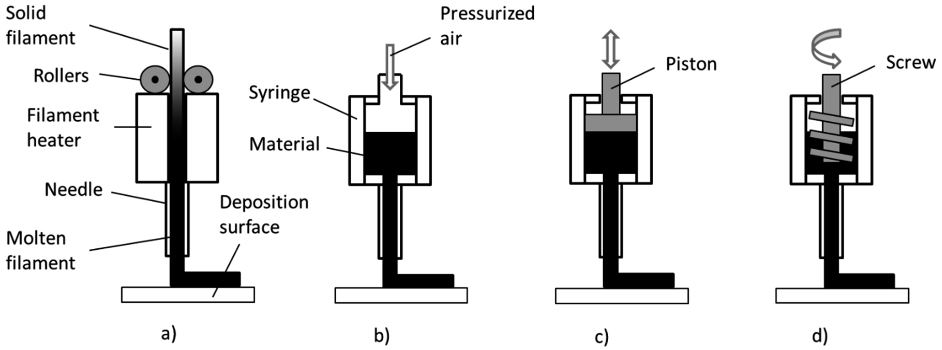

Figure 2. Schematic of material-extrusion techniques: (a) Fused Deposition Modelling, in which rollers push a filament though a heated channel where the material melts and is forced through the needle by the solid material.; (b) and (c) 3D Fiber Deposition, where in (b) pressurized air is used to induce flow through the needle whereas in (c) this is achieved by the action of a piston or a plunger; (d) bioextrusion, where flow is originated by the rotating action of a screw. Adapted from Calore et al. [16].

The first use of melt-based techniques in tissue engineering dates back to 2001, when Hutmacher et al. [44] showed that FDM allowed the fabrication of highly reproducible 3D scaffolds with a fully interconnected pore network. They manufactured scaffolds with several geometries and filament orientations, and evaluated their mechanical properties. *In vitro* tests showed fully populated scaffolds, which also supported differentiation and ECM production. Since then, FDM and the other melt-based techniques have been extensively used for hard-tissue engineering, bone in particular [14]. An extensive review of AM for bone applications is given by Wang et al. [45], while Agarwal et al. [46] reviewed scaffold manufacturing for cartilage engineering. However, the current application of ME-AM techniques is still facing some technical challenges that hinder large-scale production of TE constructs, and leaves the adoption of these technologies mainly to research level [13], [14]. In our opinion, these challenges can be ascribed to the lack of specific factors that renders the workflow still not very reproducible and automated. These are the lack of knowledge of the physics behind the process, the lack of flexibility in usable materials, the lack of biomimicry, and the lack of control over material and scaffold properties.

1.3 CHALLENGES IN MELT-EXTRUSION ADDITIVE MANUFACTURING FOR TISSUE ENGINEERING

1.3.1 Lack of knowledge in polymer physics

In AM, it is paramount to understand the process itself, as well as the physics behind it, in order to make it work, but also to improve the process further [47]. With the increasing adoption of these technologies, the knowledge of the fundamentals of the process has decreased and is certainly responsible for the traditional trial-and-error approach when exploring new paths in scaffold AM [48].

These could be manufacturing scaffolds with new materials or devices, or trying to speed up the production [49]–[54]. Before reaching a satisfactory product, these trial-and-error loops might be numerous, and the success of the trials relies on the user's experience [55]. Figure 3A and 3B show typical examples of this process, based on the adjustment of the most intuitive printing parameter, the printhead translational speed. In Figure 3A, it can be seen how different values of flow rate require the translational speed to be adjusted accordingly, in order to maintain the filament thickness comparable to the nozzle diameter. Without an *a priori* knowledge, matching the translational speed to the current flow rate requires several attempts, which leads to waste of material and time. This is further highlighted in Figure 3B, where a typical processing route is described. On the left, a scaffold manufactured with a too high translational speed, which led to extreme filament stretching resulting in poor contact between the layers and potentially unsatisfying mechanics. After full scaffold deposition and sectioning of the specimen, the manufacturing result can be analyzed and the parameters adjusted accordingly. However, due to the limited knowledge of the impact of even small variations, the translational speed might be reduced incorrectly, resulting in excessive material deposition and lateral pore occlusion (Figure 3B, right). The resulting waste of time and material highly hinders the process upscaling in favor of more established but less optimal techniques. Additionally, material waste represents a more critical issue in TE than in industrial applications. In fact, medical polymers are usually more expensive than technical ones, while research grades are often provided in very small amount and on longer timescales [14], [53]. This trial-and-error approach usually ends up in a working set of parameters, which somehow couples to the material properties in giving morphologically acceptable products. However, mechanical properties, not assessable by eye, are often non optimal and this set of parameters might have to be readjusted, resulting in an endless circle [56]. Considering that in scaffolds for TE the load bearing points are far less than in non-porous AM constructs, the knowledge of the temperature profile driving interlayer fusion is fundamental to optimize mechanical performances. As shown in Figure 3C, newly deposited layers cool down extremely rapidly, thus hindering fusion with the previous layer and molecular homogenization across the interface. Additionally, previously extruded material is reheated as well and this may alter its morphological as well as its mechanical properties. Currently, mechanical evaluation, whereas taking place, is carried out only down the manufacturing process, and this would be repeated for any potentially needed adjustment.

Further elements responsible for extended production times are the potential batch-to-batch variation in polymer properties and thermally sensitive grades [53]. The former may result in the necessity to refine the printing parameters, which may end in the above-mentioned endless circle whereas this was not done with a scientific methodology. Instead, the issue of processing thermally sensitive polymers arises from the fact that they retain their original molecular structure and flow properties for a limited amount of time once in molten state once not optimally stabilized, as described by Figure 3D. Like in terms of precious waste, biocompatibility limits the applicability of (physio)chemical stabilization concepts adopted in technical, non-medical material formulations as further elaborated on below. Once the degradation process starts, the resulting changes in molecular architecture like chain scission, branching or crosslinking will affect not only the material flow characteristics and the final morphology, but also the mechanical performances of the bulk material and of the scaffold [57]–[59]. For this reason, users must be aware of the processing window for these grades, with the goal of speeding up the process and reducing the residence time of the material inside the print head [60]. Alternatively, the processing parameters could be adjusted in real time to compensate for the change in flow behavior. Therefore, there seem to be the need for an in-process simulation model to pre-assess the impact of process parameters and to predict optimized process conditions, thus giving tissue engineers predictive capabilities. Without such *a priori* knowledge, typical screening and processing routes appear as the flowchart in Figure 4. We believe that by properly characterizing the materials of choice and considering the features of the device in use, it is possible to understand in advance how to process a specific polymer to obtain the desired scaffold morphology while optimizing the mechanical properties as well.

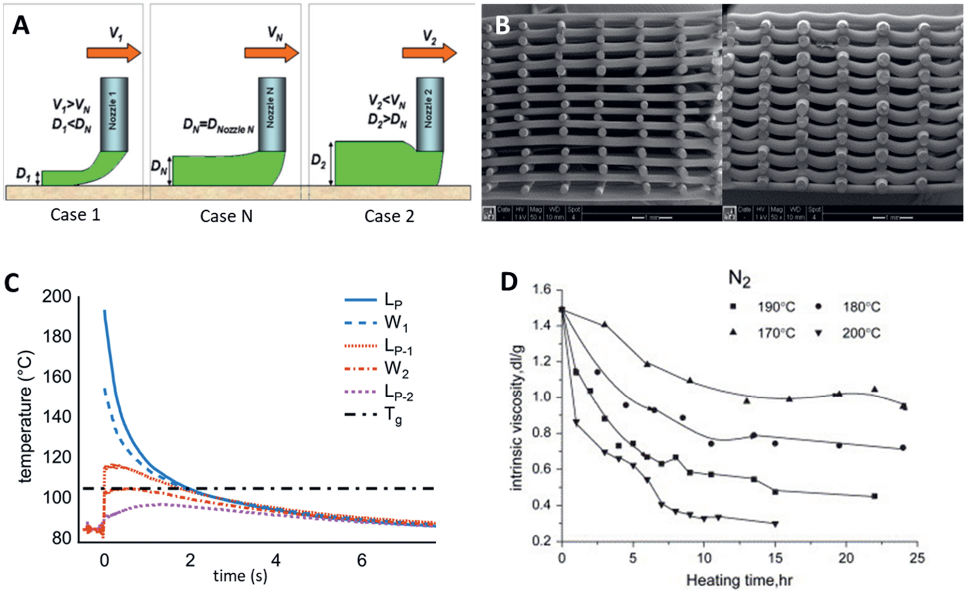

Figure 3. (A) The effect of different printhead translation speeds on filament diameter. Case 1: printhead speed (V_1) is greater than fluid velocity out of the nozzle (V_N) and therefore the fiber diameter (D_1) is lower than the nozzle diameter (D_N). Case N: the printhead speed matches the fluid velocity and fiber and nozzle diameter are identical. Case 2: printhead speed (V_2) is lower than fluid velocity out of the nozzle (V_N) and therefore the fiber diameter (D_1) is greater than the nozzle diameter (D_N). Adapted from Khalil et al. [61]. (B) The effect of different printhead translational speed on gap bridging. On the left, printhead speed is higher than fluid velocity out of the nozzle and the filament is stretched. This results in proper gap bridging but poor or, in some cases, non-existent contact with filaments from the bottom layer. On the right, the opposite relation between printhead speed and fluid velocity, leading to side pores occlusion. (C) Temperature profiles from layers formed during printing of ABS at 210 °C. Print layer (L_P) temperature, first sublayer (L_{P-1}) temperature, second sublayer (L_{P-2}) temperature, model estimate of weld temperature between print and first sublayer (W_1), model estimate of weld temperature between first and second sublayers (W_2) and glass transition temperature for ABS (T_g). Adapted from Seppala et al. [62]. (D) Reduction of Poly(D,L-lactic acid) (PDLLA) intrinsic viscosity over time when kept isothermally in a nitrogen atmosphere due to thermal degradation. Adapted from Liu et al. [58].

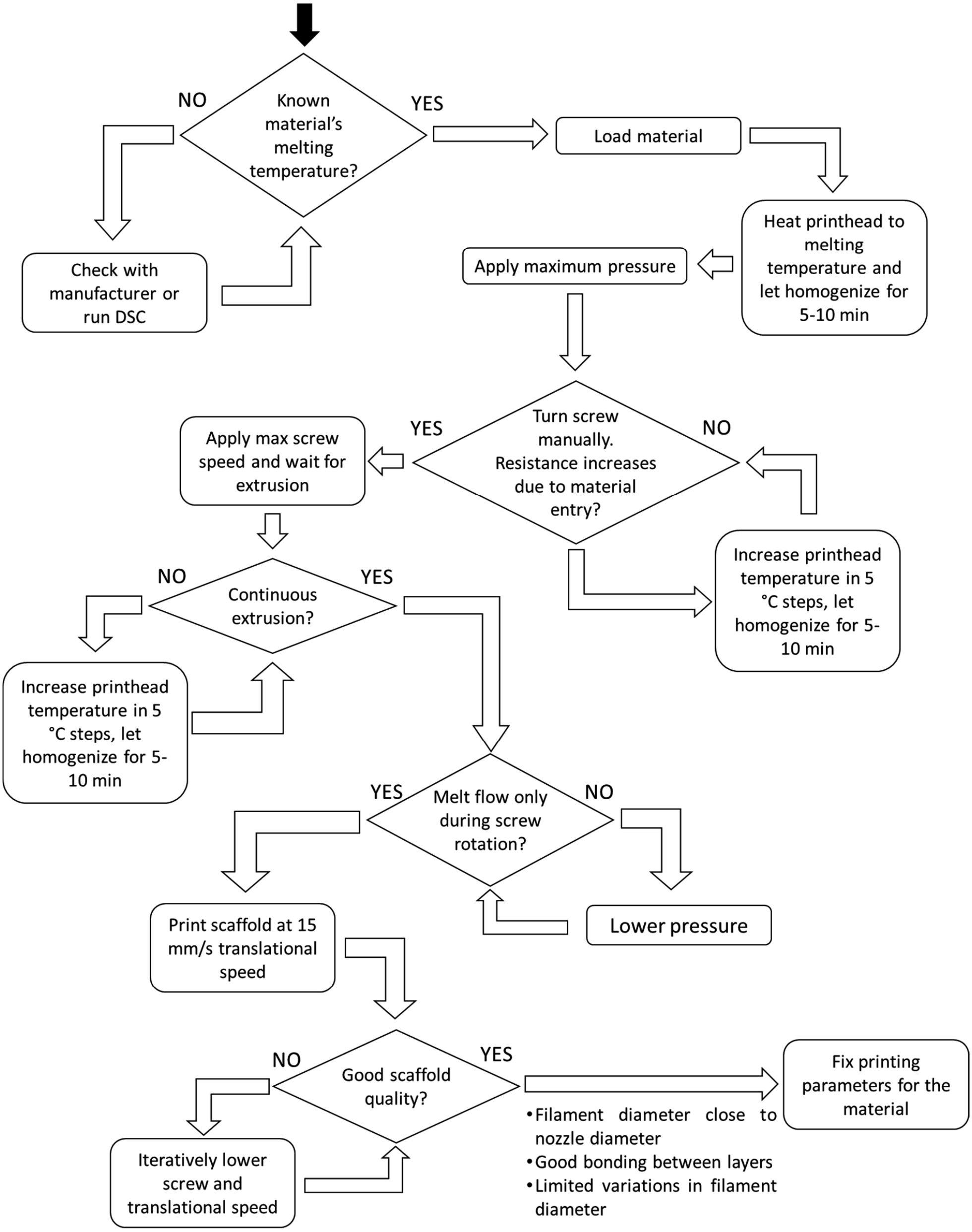

Figure 4. Flowchart of the empirical printing parameter tuning. The flowchart is to be followed for every new polymer grade to be tested or new printing device.

1.3.2 Lack of flexibility

The current inability to properly process thermally sensitive materials is the proof of the lack of flexibility of melt-based techniques [63]. For instance, poly(lactide) (PLA) is a widely used thermoplastic polymer for biomedical applications that, however, suffers due to limited stabilization routes from poor thermal stability limiting its processability by ME-AM (Figure 5A). Processing a thermally unstable material may result in changes in flow behavior, which affect both morphology (Figure 5B) and mechanical properties (Figure 5C). Despite the efforts invested in synthesizing and characterizing biodegradable polymers [64], the number of suitable materials is somewhat limited [15], [65]–[67]. As previously mentioned, the knowledge of the process fundamentals is key to overcome this limitation. Although a simple readjustment of the processing temperature would slow down the degradation kinetics [60], diffusion at the interface would be affected, negatively influencing the mechanical properties [39]. In industry, this issue is dealt with the use of stabilizers such as chain extenders, which can reconnect broken chains originated by the degradation process [68]. However, they are generally toxic or little information about their biocompatibility is available. For this reason, medical grade polymers are usually not stabilized by means of additives, which highly narrows the palette of usable materials. Tachibana et al. [69] tested myo-inositol (Figure 5D), a sugar present in the human body and

Table 1. Comparison of the main characteristics of the three different techniques, namely Fused Deposition Modelling (FDM), 3D Fiber Deposition (3DF) and Bioextrusion. Adapted from Calore et al. [16].

Characteristics	FDM	3DF	Bioextrusion
Control on flow rate	Good: can be quickly switched by changing roller speed, possible also during fabrication if the software permits it	Poor with just gas pressure; decent with plunger or piston pressure	Good: can be quickly switched by changing screw speed or rotation direction, possible also during fabrication if the software includes this functionality
Thermal degradation	Low: short exposure to high temperatures, just before extrusion. However, possible requirement of an extra thermal step to make filaments	High due to long exposures to high temperatures	High due to long exposures to high temperatures
Ease of use	Easy: molten material present only in a small region, removable along with the initial extrusion of the next material. Disassembling (whereas possible) and cleaning is recommended to avoid contaminations	Complicated: slightly fewer parts to disassemble for cleaning than in screw extrusion and one less parameter to control i.e. screw speed	Most complicated: assembly and disassembly, cleaning, need to regulate extra fabrication parameters
Addition of fillers	Not possible, unless source filament already includes fillers	Possible, but almost no mixing in molten state	Possible, with slight mixing in the screw
Material compatibility	Only materials that can be manufactured into appropriate size filament	Wide range of materials and forms including pellets and powders	Wide range of materials and forms including pellets and powders
Material wastage	Minimal due to absence of large dead volumes. Material directly passes from the rollers to the manufacturing substrate through a nozzle	Dead volumes lead to material waste, can be minimized by thoughtful design	Dead volumes lead to material waste, can be minimized by thoughtful design
Working temperature	Slightly lower temperatures, since the rollers can generate higher pressure on the filament and the melt	High, in order to melt material enough to flow under pressure	High, in order to melt material enough to flow under pressure
Minimum fiber diameter	Dependent on available needle or nozzle and material used (commonly around 150-200 μm)	Dependent on available needle or nozzle and material used (commonly around 150-200 μm)	Dependent on available needle or nozzle and material used (commonly around 150-200 μm)

involved in cell signal transduction [70], for stabilization effects on PLLA during processing. It was found that the addition of myo-inositol prevented the degradation of PLLA during thermal melting process and this was attributed to the cross-linking via esterification by the hydroxyl groups of the molecule. However, the use of chain extenders may be responsible for an unwanted and uncontrolled increase in molecular weight [68], or even branching depending on the molecule active groups [71]. Such changes might affect the material processability and alter its properties over the manufacturing process. Kang et al. [72] included magnesium hydroxide in a PLLA - PCL blend to neutralize the acidic moieties from thermal degradation of PLLA. They indeed observed that molecular weight reduction was alleviated by the addition of magnesium hydroxide via inactivation of those chain groups and degradation byproducts capable of backbiting reactions and hydrolysis. Despite appearing an appealing approach to include thermo-sensitive polymers in the palette of extrudable materials, further issues limiting the flexibility of ME-AM persist, which cannot be all tackled at the same time. In fact, it is important to note that processing involves polymer flow through nozzles of a few hundreds of µm in diameter, where very high shear stresses might develop (usually in the range 100 – 200 s^{-1} [48]). As devices employed in TE are usually of smaller scale than industrial equipment, the forces to process high molecular weight polymers are often not technically accessible. However, these grades are favorable in terms of mechanical properties [73], which means that scaffold production is often bound to less performant materials. In two recent studies, Camarero-Espinosa et al. [74], [75] fabricated scaffolds with poly(ester)urethane following an initial degradation step that allowed the extrusion through the printer nozzle (Figure 5E). Despite being a working alternative strategy, this approach slows down the manufacturing process, which is in contrast with the goal of upscaling AM for TE purposes. Additionally, it relies on the reproducibility of the degradation step, which is instead quite random. Residence times of different extent might result in different degradation degrees, different molecular structure and thus different final properties. It is important to note that substrate stiffness might influence cell fate via mechanotransduction [76]. Stiffer substrates (Elastic modulus E > 225 kPa) seem to trigger osteogenic differentiation [77], whereas softer substrates might promote chondrogenesis [78]. Such events appear to be influenced also by polymer molecular weight, as highlighted by Hendrikson et al. [79]. They reported that cells cultured on low (14 kDa) and high (65 kDa) Mw PCL both showed robust chondrogenic differentiation, but low Mw PCL induced stronger hypertrophic differentiation. However, it is important to note that the evaluated molecular weight range was rather narrow considering that thermoplastic polymers for biomedical use can reach molar masses beyond 100 kDa [74]. Furthermore, synthetic polymers are also more bioinert when compared to non-resorbable materials such as ceramics and titanium alloys, or natural polymers [45], [53], [80], [81]. Melt-based techniques do not generally allow the incorporation of bioactive molecules in the process, as they might degrade upon exposure to high temperatures [82]. This hinders the large-scale use of these technologies, as further steps are needed to make scaffolds fabricated by melt-deposition more bioactive [83]. Methods to post-treat the scaffold surface include plasma treatment [84] (Figure 5F), chemical etching [85] and chemical binding [86]. In the view of upscaling scaffold manufacturing and rendering the process more automated (increased productivity and quality control, and reduced cost [80]), embedding the bioactive compound in the scaffold deposition would be desirable. Lowering the processing temperature could favor the incorporation of bioactive molecules, in addition to tackling polymer degradation. However, this approach would narrow the palette of usable materials, as the maximum extrudable Mw would decrease. Alternatively, the inclusion of inorganic fillers has shown to help in protecting antibiotics from thermally degrading during ME-AM [87], which would dismiss the need for decreasing the processing temperature. Nevertheless, such strategy implies the use of one further compound and additional processing, and the risk of having thermal degradation of the polymer matrix would still persist. As it can be understood, being a thermoplast is not the only requirement for a polymer to be processable. More factors have to be taken into account before and during processing of a thermoplastic polymer to ensure compatibility with the equipment in use and stable properties over time for reproducible products.

All the aforementioned considerations suggest that temperature (as function of time) is the main factor to deal with to increase the flexibility of ME techniques. By reducing thermal stresses, unstable materials could retain their molecular structure and bioactive factors be included in the process. On the other hand, the energy input should be increased to compensate for higher viscosities. However, a class of small M_w compounds known as plasticizers are meant to increase the flowability of polymer melts by favoring the sliding of polymer molecules past each other. Should they exhibit bioactive effects, it seems that the embedding of plasticizers in the polymeric matrix could favor melt processing of thermoplastics and might increase the biological performance of scaffolds for TE. In a recent work of Calore et al. [88], vitamin D3 (VD3) was mixed with an amorphous PLA grade (PDLLA) to increase its flowability and thus reducing its processing temperature. In addition, human mesenchymal stromal cells (hMSCs) cultured on PDLLA+VD3 scaffolds showed a more sustained osteogenic differentiation when compared to positive controls cultured in osteogenic media. However, the authors underlined how their results were highly influenced by the specific processing conditions used. This arises from the fact that plasticizer concentration and release rate are controlled by the fabrication process and thus optimization is needed for every new manufacturing setup. It seems therefore that a more universal and controllable approach should be needed.

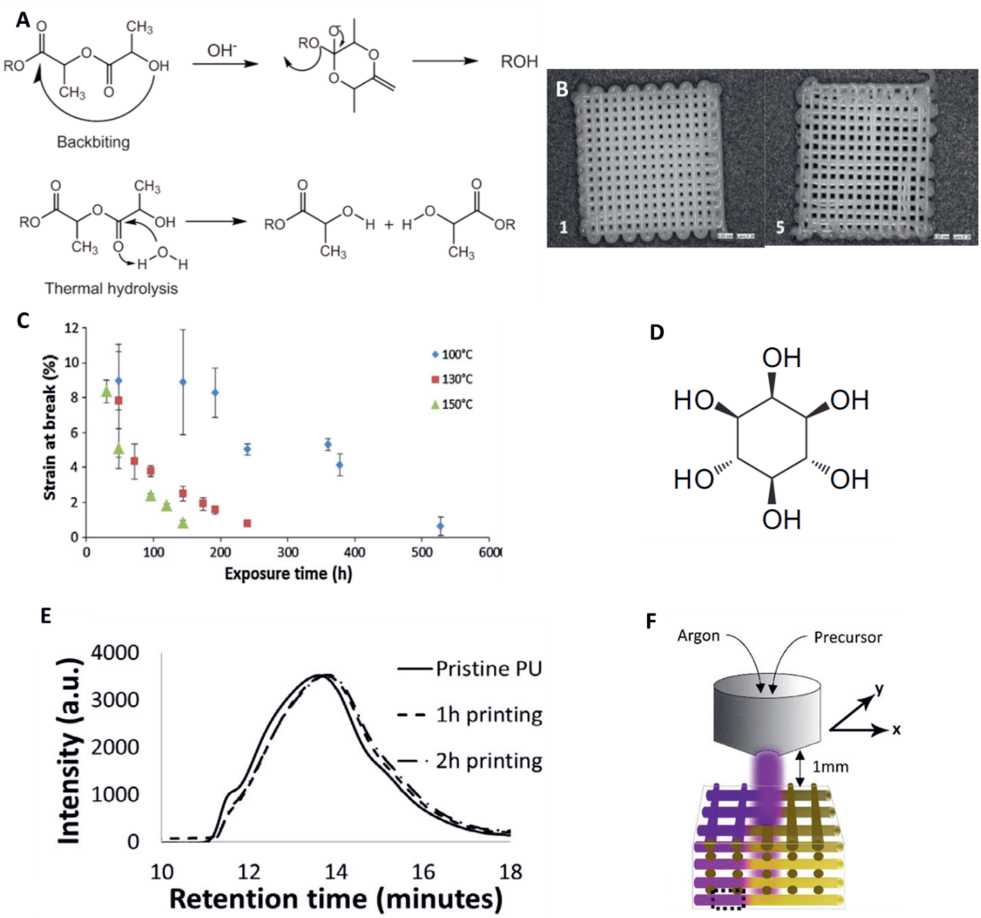

Figure 5. (A) Mechanisms of degradation of PLA. Adapted from Kang et al. [72]. (B) Effects of polymer thermal degradation on scaffold morphology: (1) first manufactured scaffold; (5) fifth consecutively manufactured scaffold. Adapted from Ragaert [89]. (C) Reduction in mechanical properties of PLA exposed for different times at different temperatures because of thermal degradation. Adapted from Rasselet et al. [59]. (D) Myo-inositol chemical structure. (E) Changes in molecular weight distribution of poly(ester)urethane (PU) before fabrication and after 1 and 2 h of processing. (F) Plasma treatment of additive manufactures scaffolds to increase surface bioactivity. Adapted from Cámara-Torres et al. [84].

1.3.3 Lack of biomimicry

What we defined as lack of biomimicry arises from the typical macroscale morphology of melt-extruded scaffolds. The x-y deposition pattern and the subsequent layer stacking allows the inherent formation of pores of several hundreds of μm^2. These pores, referred to as macropores [90], are responsible for supporting nutrients uptake, waste removal, tissue ingrowth and vascularization. With particular reference to the latter, it has been shown that pores with dimeters of 250 µm or above favored the *in vivo* growth of blood vessels more than smaller size pores [91]–[94]. Microscale porosity is instead inherent to the material and, whereas present on the surface of the fibers, can induce surface roughness. Rough surfaces were shown to influence both cell adhesion and proliferation in 2D [95]–[97] as well as in 3D [81], [98]–[101]. For instance, in Figure 6A and 6B, it can be seen how hMCSs adhered with a different level of spreading on 3D scaffolds exhibiting relatively smooth (A) and rougher surfaces (B) [98]. Kunzler et al. [97] created a roughness gradient (R_a (arithmetic average roughness) = 1 – 6 µm) on epoxy 2D substrates and evaluated the response of rat calvarial osteoblasts (RCO) and human gingival fibroblasts (HGF) in terms of cell attachment and proliferation. While osteoblasts attachment was not influenced by roughness values, fibroblasts showed slightly higher attachment on the rough part of the gradient (at R_a = 5.9 µm) with respect to smoother regions (R_a = 1.5 µm). After 7 days of culture, the two cell populations exhibited opposite behaviors, with the number of RCOs significantly increasing with increasing roughness. In particular, a R_a value of about 2 µm was identified as onset for the increase in cell number. For R_a > 3.9 µm, the amount of osteoblasts was two times higher compared to parts with R_a lower than 2 µm. Instead, the number of fibroblasts after 7 days of culture was found to gradually increase with decreasing roughness, below a R_a value of 2 µm. Zamani et al. [100] manufactured, by electrospinning, PLGA 3D scaffolds that exhibited either smooth (arithmetic average surface roughness S_a = 132 nm) or rough surfaces (S_a = 306 nm). Culture of A-172 nerve cells showed enhanced growth rate on rough scaffolds compared to smooth ones already after 4 days of culture. However, at the end of the culture period of 7 days, the increase in proliferation rate reached values up to 50 %. The group of Kim [101] 3D melt-plotted poly(ε-caprolactone) (PCL) scaffolds and treated them with oxygen plasma. The process resulted in surfaces with R_a values ranging from 23 nm to 1.9 µm. MG-63 cells cultured on scaffolds with roughness of 654 nm showed enhanced cell attachment and proliferation over 7 days of culture.

It is important to underline that cell attachment and consequent proliferation are prerequisites for proper tissue formation and regeneration [84]. However, extruded scaffold fibers are inherently smooth [45], a condition that might not faithfully represent the nanostructures of the extracellular matrix and affect tissue regeneration [45], [83], [102]. Whereas scaffolds are intended to regenerate bone tissue, rough surfaces were shown to promote osteogenesis [103]. However, current roughening methods are based on post-processing of the additive manufactured scaffolds, often by using toxic organic solvents (Figure 6C and D). Besides increasing the overall production time and being hardly upscalable, this type of post-processing poses safety risks and may cause deterioration in product quality [12], [26]. The lack in biomimicry manifests itself also at the level of mechanical performances. Trabecular bone tissue, for example, exhibits multi-scale porosity that results in different mechanical properties depending on the local density [45], as can be seen in Figure 6E. Pores can vary in size between 450 and 1310 µm [104], and this large distribution can provide increased toughness and prevent brittle failure. Scaffolds manufactured via melt-based techniques are characterized by the only presence of macroporosity, with pore sizes of at least 300 µm to allow neovascularization *in vivo* [93], [105], [106]. The lack of a wide pore size distribution results in the brittle collapse of the overall structure once the loads overcome the failure point. Several strategies have been successfully employed to introduce porosity at multiple length scales, such as salt leaching [107]–[109], supercritical CO_2 [110] and foaming [111], [112] (an example of microporosity induced by foaming can be seen in Figure 6F). However, current approaches limit the scope of the achieved microporosity to mechanical performance. In fact, the pores generated within the scaffold fibers are rarely interconnected or open to the outside. Whereas accessible, micropores may enhance waste removal and nutrients uptake, together with cell infiltration and tissue formation from within the scaffold fibers as well.

None of the cited approaches seems to solve the lack of biomimicry of ME-AM scaffolds on its own. Different strategies could be combined to overcome each other's limitations, but with the requisite of keeping the process straightforward. This can be achieved if researchers will exploit the conditions that allow the manufacturing to be carried out. For instance, a specific type of foaming agents known as Chemical Foaming Agents (CFA), decomposes creating a foam structure upon the application of heat, which is abundant in ME-AM. In addition, many chemical compounds are water soluble, which would make a potential leaching process possible during cell culture as well, avoiding the introduction of a further scaffold preparation step. It seems therefore that the right methods are already available, but that what is missing is the right strategy to combine them.

Recently, Calore et al. [113] introduced surface roughness and interconnected internal porosity in ME-AM scaffolds for bone tissue regeneration by coupling foaming and leaching in a straightforward manner. Briefly, they melt-blended PLA, sodium citrate (SOCIT) and PVA, melt-extruded the blend and incubated the scaffolds in water. Upon melt-processing, SOCIT decomposed forming pores inside the scaffold filaments. The subsequent PVA extraction in water induced surface roughness and allowed to connect the SOCIT pores with each other and to the outside. Such scaffolds showed a greater cell seeding efficiency and secretion of osteogenic-related proteins, with mechanical properties comparable to plain PLA ones. Nevertheless, the researchers pointed out that the final porosity distribution is highly sensitive to the manufacturing conditions, and that a deep understanding and a fine tuning of the process is needed to obtain the desired results. Therefore, it appears evident that further studies to optimize this promising strategy are needed towards the upscaling of scaffold production.

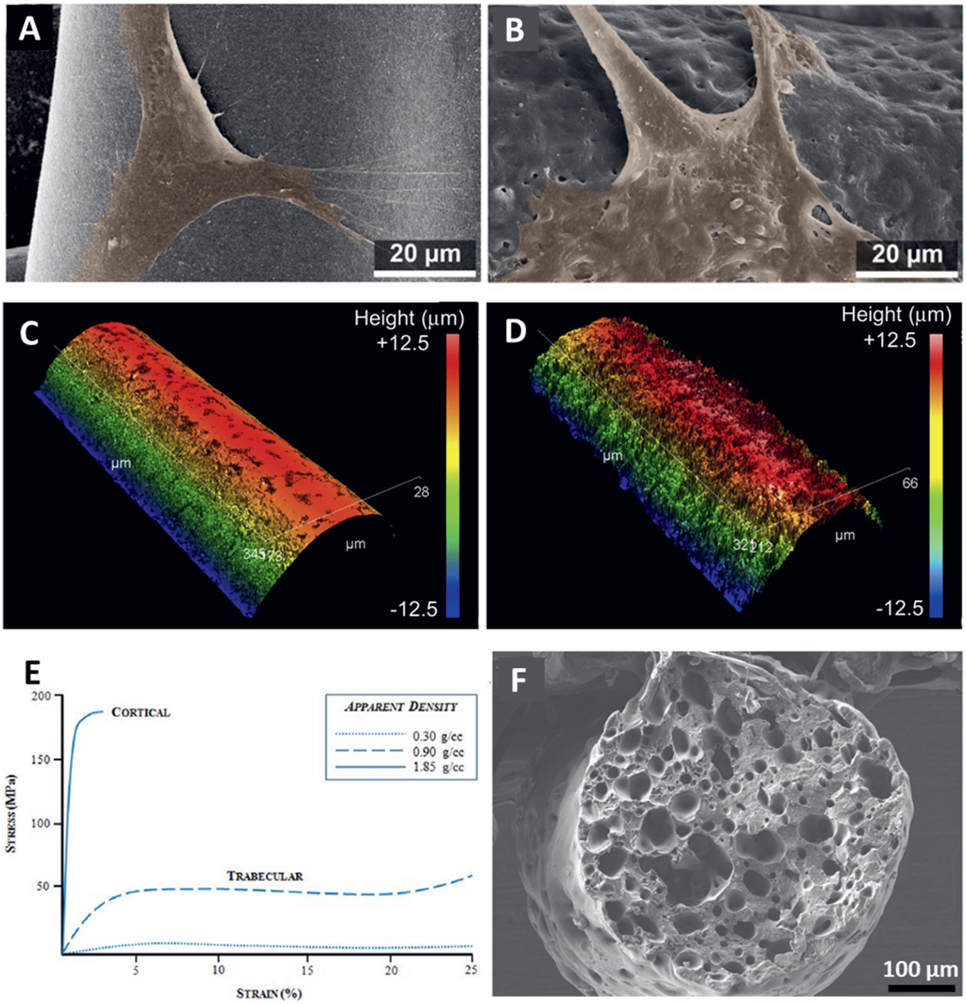

Figure 6. (A) and (B) Cell adhesion on AM scaffold fibers with low (A) and high (B) surface roughness. Adapted from Neves et al. [98]. (C) and (D) Surface morphology of AM scaffolds: (C) as manufactured and after chemical etching with chloroform (D). Adapted from Kumar et al. [103]. (E) Stress – Strain curves of cortical and trabecular bone. Adapted from Hart et al. [114].(F) Cross-section of an AM scaffold fiber with internal porosity introduced via extrusion foaming. Adapted from Choi et al. [111].

1.3.4 Lack of control

In the analysis of the lack of control, we refer to thermodynamic instability that is mostly expressed in semi-crystalline polymers in ME-AM, whose crystallization is often not taken under consideration when planning and evaluating scaffold performance. Semi-crystalline polymers are a widespread choice for TE purposes, because crystallization is able to enhance the mechanical performance of the final product, as can be seen in Figure 7A. The crystalline phase tends to increase the stiffness and the strength of the material thanks to the strong interactions between adjacent chain segments [115]. In addition to bulk performances, crystallinity has an influence on surface properties as well, which represent the interface between materials and cells. In particular, it has been shown that substrate stiffness can drive cell fate via cell shape [116]: stiffer surfaces induce cells to adopt a more spread morphology compared to soft materials. An overview can be seen in Figure 7B. In the specific case of hMSCs, their shape influences their phenotype [117], [118]. It was reported that stiff substrates ($E > 225$ kPa) induced a strong secretion of osteogenic markers [77], while a more chondrogenic response was seen on softer materials [78]. This is due to the fact that cell shape modulates the localization of the YAP/TAZ complex, transducers involved in the mechanotransduction process [76]. Stiffer surfaces induce a more spread cell morphology with a higher number of stress fibers and consequent greater cytoskeletal tensions. The YAP/TAZ complex migrates to the nucleus and enhances the expression of genes involved in osteogenesis [32]. On the other hand, softer substrates induce low cytoskeleton tension and a round shape, leading to cytoplasmatic localization and inactivation of the YAP/TAZ complex, which directs chondrogenic differentiation [119]. Furthermore, crystallinity influences surface roughness as well, via the size and density of the crystals formed in proximity and at the surface of the polymer [120]. In particular, Washburn et al. [96] evaluated the effect of variations in crystallinity on surface topography and reported the creation of features with root-mean-square (rms) roughness values ranging from 0.5 to 13 nm. The smoothest and the roughest surfaces achieved are shown in Figure 7C. Different levels of roughness have shown to induce different differentiation patterns [121]. This phenomenon is ascribed to differences in cytoskeletal organization associated with the microtopography of the substrate and the resulting cell morphology is known to impact gene expression as previously mentioned [98], [122], [123]. In particular, in the work of Chen et al. [123], hMSCs were cultured on electrospun scaffolds exhibiting different levels of surface roughness, with R_a going from 14.3 ± 2.5 nm to 71.0 ± 11.0 nm. The analysis of gene expression showed that the highest R_a value supported more induction of osteogenic genes while surfaces with the lowest roughness better promoted chondrogenic differentiation. Therefore, it seems clear that crystallinity is a parameter to be carefully considered when processing semicrystalline polymers, as it can influence surface properties known to impact cell behavior. Being surface stiffness and surface roughness strongly intertwined, particular attention should be given to the polymer thermal history, which is the driving factor for crystallization development during ME-AM [124]. Following the deposition, the material is often kept above its glass transition temperature (T_g) to promote interfacial diffusion and thus bonding, and crystallization, to achieve enhanced mechanical properties. Moreover, the inherent raster deposition pattern causes the nozzle to periodically return in the proximity of previously deposited material, whether within or on top of a specific layer. Consequently, the solidified polymer is reheated and its crystallinity might change. Srinivas et al. [125] showed that substantial spatial variations in crystallinity could be found along the build direction, resulting in inhomogeneous macroscopic mechanics over the object. Despite these potential inhomogeneities and their consequences on surface properties, there are several recent differentiation studies with semicrystalline polymers where the final construct was not characterized from a material-science perspective [74], [75], [79], [84], [126]–[128]. For instance, Di Luca et al. [32] manufactured scaffolds with a discrete gradient in surface stiffness by using three different materials, in the attempt to mimic the osteochondral region. The process was carried out in a non-heated environment and the crystallinity development was not taken into account. Despite managing to obtain a gradient in surface stiffness, potential differences in roughness were not assessed. It appears clear that a fine control over processing conditions is highly advantageous as they have a deep impact on the surface properties of the final scaffold, in particular whereas the construct is meant to promote or support differentiation. Knowledge of the material properties and the design of a proper deposition strategy seem paramount not only to obtain scaffolds with controlled properties, but also for the straightforward manufacturing of more complex structures such as gradient scaffolds. This topic was recently addressed by Calore et al. [124], who studied the effect of thermal treatments typical of ME-AM, on plasticized-PLLA surface stiffness and roughness separately. In particular, samples were kept at a constant temperature for different times or annealed for the same time at different temperatures, respectively. The first type of treatment resulted in samples with surface stiffness in a range typical of the osteochondral region (14-43 MPa). Samples that underwent the second type of treatment exhibited R_a values comparable among conditions but with a narrower roughness range for the highest annealing temperature (from 0.63±0.47 to 0.31±0.01 µm). In the second part of the study, hMSCs were cultured on these surfaces and any potential osteogenic commitment was evaluated. It was found that cells, under osteogenic culture conditions, were more susceptible to different surface topographies than stiffness values. The findings of this study suggest that a too-often-disregarded variable during manufacturing, such as thermal history, might eventually have an impact on cellular activity. Therefore, awareness and understanding of the whole manufacturing process are needed not only to avoid potentially undesired biological consequences but also to willingly steer cell behavior.

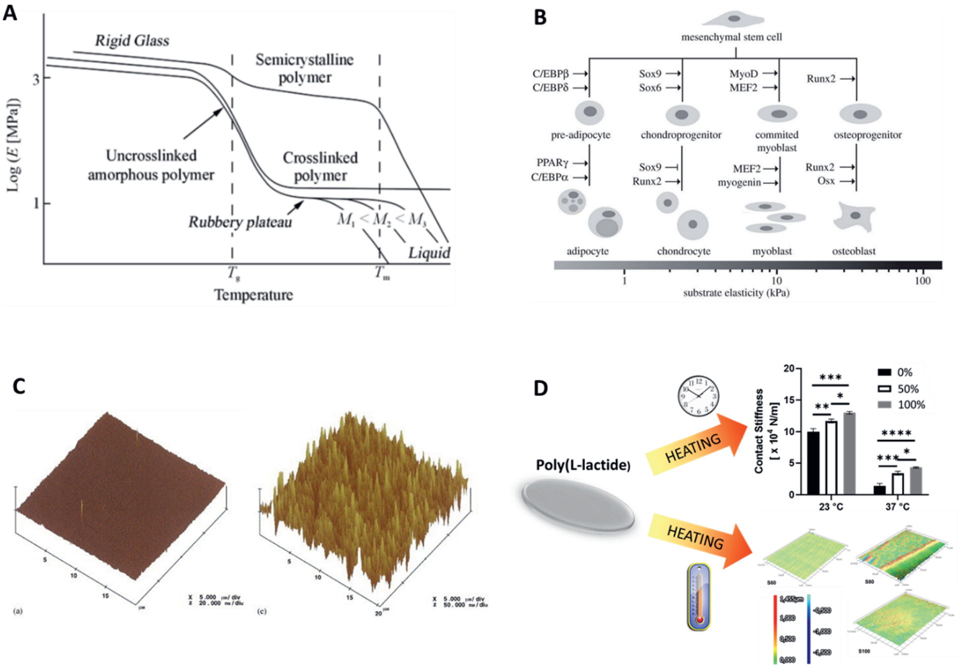

Figure 7. (A) Elastic modulus of thermoplastic polymers as a function of temperature, crystallinity and molecular weight (M) T_g and T_m are the glass transition and the melting temperatures, respectively. Adapted from Plummer [129]. (B) Mesenchymal stem cell lineage commitment depending on substrate surface stiffness. Adapted from MacQueen et al. [118]. (C) Surface roughness of poly(L-lactide) amorphous (left) and completely crystallized (right) films. Adapted from Washburn et al. [96]. (D) Effect of annealing time and temperature on, respectively, surface stiffness and surface roughness of poly(L-lactide) films. Adapted from Calore et al. [124].

1.4 CONCLUSIONS AND FUTURE PERSPECTIVES

ME-AM allows the production of complex scaffolds with the desired morphology and tunable mechanical performance for several TE applications, with interconnected and controllable porosity from thermoplastic polymers a wide palette of chemistries and properties. With respect to other AM techniques, ME-AM require relatively simple equipment that does not involve the use of potentially toxic compounds such as binders, curing agents or solvents, which favors the clinical application of the manufactured scaffolds. However, the use of thermoplastic polymers faces some challenges related to processing. Biocompatible grades or grades with no toxic additives are less common and more expensive than industrial polymers, because of the stricter production requirements. Alternatives and new formulations are continuously under development but quantities at research level are often scarce, thus limiting large scale testing of their compatibility with ME-AM technologies. In addition, melt-extrusion of thermoplastic polymers is a complex rheological process that requires a continuous feedback loop to obtain optimal results from both the morphological and mechanical perspective. In particular, mechanics are usually the random result of an optimization flow fully focused on acceptable morphological appearance. Furthermore, the high temperatures involved in the ME-AM process may induce thermal degradation and restrict the addition of bioactive compounds to overcome the inherent bioinertness of thermoplastic polymers. Thanks to the flexibility of the synthesis process, usually thermoplastic grades are available in a wide range of molecular weights, which gives researchers the possibility of decreasing the processing temperature to some extent by using lower M_W. This can reduce the impact of degradation and allow the inclusion of less thermally sensitive bioactive compounds. However, it is important to note that the use of lower M_W grades comes at the expenses of mechanical properties. A large amount of research has been carried out on enhancing the bioactivity of thermoplastic scaffolds manufactured via ME-AM, mainly via post-processing functionalization steps. Comparable efforts have been put on introducing surface roughness and micro-scale porosity. Chemical etching, salt leaching, gas foaming, supercritical CO_2 are some of the techniques employed to compensate for the inherently smooth surface of melt-extruded scaffolds and to create porosity within the scaffold fibers. Cell studies on scaffolds with enhanced topography reported improved cell attachment, higher proliferation and influence on cell fate commitment in function of the level of roughness. The introduction of microporosity resulted in constructs with less brittle behavior and tougher mechanical response. However, the strategies adopted so far involve additional processing steps, expensive equipment or toxic solvents, thus impeding the possibility of process upscaling and limiting clinical application. In addition, the micropores created are rarely interconnected or reaching to the fiber surface, causing them to be inaccessible to nutrients or cells. However, ME-AM techniques allow to have full control over the construct crystallinity by fine tuning the thermal history that the polymer experiences. Crystal formation is a phenomenon largely unaccounted for by tissue engineers but it has a great impact on two substrate properties known to influence cell activity, surface roughness and surface stiffness. The former has been shown to have a wide spectrum effect on cell behavior, going from initial attachment to the surface, to subsequent proliferation rate and potential differentiation. Studies reported that cell response to roughness is a function not only of the cell type, but also of roughness values. In the case of semi-crystalline thermoplastic polymers, surface topography is the result of the interplay between amorphous regions and crystal size and density on, and in proximity of, the surface. Nucleation, nucleation density, growth and crystal formation are events highly dependent on the temperatures and the times the material is exposed to those temperatures for. In a similar manner, surface stiffness can be controlled by the extent of crystallization, and many researchers have investigated how cell fate is affected by the stiffness of the substrate cell are cultured on. It was reported that cells spread differently on surfaces with different moduli and their shape modulates the localization of the YAP/TAZ complex, transducers involved in the mechanotransduction process. Only few studies evaluated the effect of processing thermal history on scaffold crystallinity or considered the potential effect of crystal formation on scaffold surface stiffness or roughness, properties with important impact on cell activity.

It seems therefore clear how scaffold manufacturing with ME techniques is a process that is often carried out not optimally, in terms of construct final performance or total amount of phases to achieve a ready-to-use scaffold. Additionally, constructs are often the result of spontaneous and uncontrolled physical phenomena as a thorough knowledge of the material-process interactions is not available. Although some steps forward have been made to overcome current limitations, the use of ME-AM is still far from being standardized and upscalable from their current status of lab techniques. It should be bore in mind that processing can greatly affect scaffold quality and performance, which in turn have an impact on cell activity. The overall goal of the field should be to optimize scaffolds manufacturing to optimize biological performance. To facilitate standardization, automation and reproducibility, an in-depth study of its fundamentals, its limitations and methods to overcome them is necessary.

Future studies should aim at developing an accurate knowledge of the process physics, so that to develop a model able to assist the researcher in manufacturing scaffolds in an optimal manner. A workflow for proper material characterization is to be established with the purpose of understanding whether materials are compatible with the device in use and how to process them for optimal morphology and mechanics. Focus should be also put on compensating for the thermal stresses imposed by the techniques themselves, with the double goal of preserving the properties of thermosensitive materials and overcome the inherent bioinertness of synthetic polymers. Plasticizers offer a valid solution to reduce polymer viscosity and therefore the energy requirements for processing. By lowering the operating temperature, the extent of thermal degradation can be reduced and bioactive compound can be included in the process as well. This would allow to widen the palette of usable materials and avoid further processing to functionalize the scaffold surface, especially whereas the bioactive functionality is carried out by the plasticizer itself. Keeping the amount of post-processing steps limited should be considered when implementing strategies to introduce surface roughness and internal porosity as well. Chemical compounds that exploit the heat intrinsic of the ME manufacturing seem a straightforward solution to introduce a microporous morphology. The addition of a leachable immiscible phase that can be extracted in a physiological environment could ensure interconnectivity while preserving the current workload. Furthermore, the knowledge of the flow profile during extrusion allows the tuning of the distribution of phases with relatively high M_W. The control on domain migration can be exploited to localize domains of the leachable phase also on the surface and consequently induce surface roughness as well, in one single process. We mentioned how control on the process is paramount when working semi-crystalline thermoplastic grades. This allows not only to avoid influence on cell behavior via unexpected scaffold properties but rather to tune those properties to induce the desired effect on cells. Future studies should aim at understanding the connection between processing conditions (thermal history in particular) and bulk material properties such surface stiffness and roughness with the goal of controlling the latter by adjusting the former. Such knowledge would offer tissue engineers the possibility of inducing the specific cell responses with no additional processing steps, but by just controlling bulk material properties.

Concluding, ME-AM techniques offer the flexibility to manufacture scaffolds with desired morphology and tunable mechanical properties but the knowledge to disclose their full potential is still limited. Current production strategies are either based on multiple processing steps or not fully in control of all the processing variables. The greatest limitations are represented by the difficulty to upscale the workflow and the potential random bulk properties of the constructs, which might result in unwanted cell response. However, approaches to improve the manufacturing process are currently under development. The main goals are to acquire further knowledge on the process and to overcome the inherent drawbacks of ME-AM in the most straightforward manner, thus offering tissue engineers simple solutions to optimize the production of scaffolds for tissue regeneration.

1.5 AIM OF THIS THESIS

The initial aim of this thesis is to generate a fundamental knowledge of the physical phenomena underlying the scaffold fabrication process by means of melt-extrusion additive manufacturing. This new level of understanding will then be applied to overcome the current limitations inherent in the AM process for tissue engineering, with the goal of fabricating optimized tissue scaffolds for bone tissue regeneration. In fact, although bone is able to self-repair, very often the injury or the volume loss due to tumor removal are too large or severe. The advent of tissue engineering represented a more suitable alternative to autografts, allografts or metallic prostheses in the treatment of large bone defects. The new discipline was born with the goal of creating in vitro the needed tissue replacement, with the patient's own cells. Once able to exert its function, the tissue substitute would be implanted in the patient's body. The possibility of creating tissue substitutes *in vitro* allows to go beyond the limitations of conventional approaches, such as lack of donors, immune response, own tissue harvesting or implantation of non-self devices. The adoption of AM techniques has further pushed forward the clinical application of TE approaches through an enhanced level of control over the morphology of tissue replacements. Additionally, by adjusting the fabrication pattern and therefore the network of macropores, the mechanical performances can be tuned as well. Synthetic thermoplastic polymers have found wide application as scaffold materials for bone TE thanks to their controllable properties via the synthesis process and adequate mechanics for bone replacement. Among the plethora of AM techniques, melt-extrusion based methods have emerged as the golden standard to process this class of polymers. The application of melt-based manufacturing maintains the general benefits of AM methodologies with respect to conventional methods with some key advantages over other additive manufacturing techniques. Specifically, the equipment needed is less complex, the choice of materials for processing is more flexible and there is no need for toxic compounds. These features allow to contain the manufacturing costs and ease the translation to clinical application. However, some drawbacks are present, which are related to the still limited knowledge of the process itself or inherent to the working principles behind it. The understanding developed initially in this thesis will be employed to design strategies for the processing of new materials for ME-AM and in the optimization of current protocols. Additionally, the thesis provides methodologies to improve and optimize scaffold manufacturing for enhanced biological performances. The proposed protocols will be tested by fabricating improved scaffolds whose biological performance will be evaluated on bone tissue formation.

In **Chapter 1,** we described how the need for organs and tissue replacements led to the birth of the tissue engineering field. Great progress has been made since the adoption of industrially-derived fabrication techniques known as Additive Manufacturing, which perfectly fit in the framework of personalized treatments at the core of TE. A subset of AM methods based on melt extrusion, ME-AM, has gained particular attention because allows the processing of thermoplastics synthetic polymers, a class of materials particularly indicated for scaffold fabrication for bone TE. Despite being able to manufacture scaffolds with highly customized macroscopic shape, morphology and mechanical properties, researchers are still bound to non-optimal production workflows, made of several processing steps or uncontrolled scaffold properties, which hinders upscaling and clinical translation. To further contribute to the field, this thesis aims at identifying the bottlenecks affecting the manufacturing of optimal scaffolds for bone tissue regeneration with the goal of proposing strategies to overcome the identified challenges. These approaches are addressed in the different chapters of the thesis.

In the context of TE, scaffolds are expected to have morphology and mechanical properties customized on the defect to be treated to optimize functionality recovery. Therefore, the first step in *in vitro* tissue regeneration is the production of a scaffold with properties matching the design expectations. However, in ME-AM for TE the final construct is often the result of a set of non-optimal, but rather simply working, fabrication parameters due to the lack of comprehension of the material's properties, device features and the combination thereof. **Chapter 2** addresses the current lack of knowledge in ME-AM. In this chapter, we establish an operative framework for optimal scaffolds manufacturing based on simple material characterization and knowledge of machine features. Specifically, we studied the effects of material properties and processing parameters on scaffold final morphology and mechanical performance that additionally sets a profound fundament for the successive chapters and challenges studied therein The interaction between the two factors was evaluated from a rheological and fluid-dynamical perspective, and we characterized how it influences polymer flow inside the printer and after deposition. Eventually, a numerical model predicting the final results is proposed.

In **Chapter 3** and **Chapter 4**, we propose strategies to overcome some of the identified challenges to fully optimize scaffold manufacturing for enhanced biological performance. In **Chapter 3**, we address the limited flexibility in ME-AM. In particular, we developed a method to solve the issues of the inherent lack of bioactivity of AM scaffolds made of synthetic polymers, of their potential thermal instability and of the impossibility of processing high M_W grades in one go. In fact, despite their flexibility in terms of chemical, physical, mechanical properties and processability, this class of materials do not exhibit the same biological performance of natural polymers such as collagen. Although literature can offer plenty of procedure to ensure scaffold bioactivity, approaches used nowadays involve post-processing steps that dilate the manufacturing process. In addition, tackling the issue of polymer thermal instability is currently based on embedding thermal stabilizers in the material, which are not always biocompatible and add a further phase in the workflow. Plasticizers have shown to reduce material viscosity and thus improve material processability both in terms of mechanical and thermal energy requirements. Vitamin D3 (VD3) was selected as plasticizer to reduce the viscosity of a biomedical and unstabilized poly(D,L-lactide) (PDLLA) grade, and thus reduce the energy requirements (mechanical (torque) and heat (temperature)) for extrusion, limiting ultimately polymer degradation. Being a compound naturally involved in bone homeostasis, we eventually evaluated the biological impact of VD3-loaded scaffolds on mesenchymal stromal cells (hMSCs) to verify the impact of the developed method on bone regeneration.

In **Chapter 4**, we tackle another limitation of scaffolds manufactured by ME, the lack of biomimicry. Bone is a rather complex tissue from the morphological point of view, with rough surfaces and pores of a size spanning hundredths of microns. Instead, ME-AM scaffolds present relatively smooth surfaces and bulky filaments, where porosity is present only in the voids originating from the deposition pattern. Current approaches to induce surface roughness necessitate of time-consuming post-processing steps and may include chemical etching with toxic solvents. To introduce a further level of porosity, instead, researchers have often employed additional machinery, such as supercritical CO_2 devices. Whereas more straightforward methods have been used, including leaching or foaming, results still did not show pores within the filaments connected to the outside, hindering their availability to nutrients diffusion or cell infiltration. Furthermore, the contribution of the achieved microporosity seemed indeed limited to the internal volume of the filaments, not inducing surface roughness. In this chapter, we present a blend system as manufacturing material to introduce both scaffold surface topography and intra-filament microporosity accessible from the outside, in the most straightforward manner possible. To reduce the amount of processing steps, sodium citrate (SOCIT) and poly(vinyl alcohol) (PVA) were chosen as additives to the main poly(L-lactide) (PLLA) matrix. The former decomposes upon the application of heat, which allowed us to obtain voids within the polymer filaments right during the extrusion process. PVA is a water-soluble material that immiscibly mixes with PLLA forming domains whose size and amount can be controlled via the processing parameters. By extruding the blend with a screw-based printer, we homogenously dispersed PVA in the PLLA matrix. By simple incubation in water, PVA could be leached, leaving pores that interconnected the void from SOCIT decomposition, opened them to the outside and induced surface roughness at the same time. To evaluate the enhanced morphological biomimicry, mechanical properties were assessed under compression and cell response in terms of attachment efficacy and osteogenic differentiation were investigated.

Chapter 5 is meant to close the circle around the current limitations in ME-AM by describing the effects of lack of control on polymer bulk properties with relevant biological influence. Currently, limited investigation and planning are carried out on the outcomes of the printing strategy when processing semi-crystalline polymers. This class of materials is particularly sensitive to the thermal stresses it is exposed to, which determines the extent and the morphology of the crystalline phase. As a result of different thermal histories, different crystal sizes and densities can be achieved, influencing surface properties such as roughness and stiffness. Many studies in literature showed that these two substrate properties can have strong impact on cell activity, ranging from attachment, through proliferation and to differentiation. However, in semi-crystalline polymers, surface roughness and surface stiffness are strongly intertwined via crystallinity and published research did not tackle the issue of tuning one while preserving the other. In this chapter, we designed a strategy to study the effect of crystallinity separately on surface stiffness and surface roughness on polymer films. The structure of the crystallinity phase was the result of thermal stresses and thermal histories typical of ME-AM, so that to resemble actual scaffold fabrication conditions. To highlight the importance of considering thermal history when processing semi-crystalline polymers, hMSCs were cultured on films undergone different thermal treatments and their response in terms of osteogenic commitment was evaluated.

In **Chapter 6**, a general discussion on the results reported in the previous chapters is presented, and contextualized to the current state of the art while providing future perspectives. The thesis is finalized with **Chapter 7**, which guides the reader through a reflection on the scientific and social impact of the research presented in the aforementioned chapters.

REFERENCES

[1] N. A. Kurniawan, "The ins and outs of engineering functional tissues and organs: evaluating the in-vitro and in-situ processes," *Curr Opin Organ Transplant*, vol. 24, no. 5, pp. 590–597, Oct. 2019, doi: 10.1097/MOT.0000000000000690.

[2] M. Mori, "Italy: Pluralism Takes Root," *Hastings Cent Rep*, vol. 17, no. 3, p. 34, 1987, doi: 10.2307/3562262.

[3] Ministero della Salute, "Lista d'attesa," 2022. https://trapianti.sanita.it/statistiche/liste_attesa_1.aspx (accessed Jun. 01, 2022).

[4] R. Langer and J. P. Vacanti, "Tissue engineering," *Science (1979)*, 1993, doi: 10.1126/science.8493529.

[5] A. Shafiee and A. Atala, "Tissue Engineering: Toward a New Era of Medicine," *Annu Rev Med*, vol. 68, no. 1, pp. 29–40, Jan. 2017, doi: 10.1146/annurev-med-102715-092331.

[6] ISO/ASTM, "Additive Manufacturing - General Principles Terminology (ASTM52900)," *Rapid Manufacturing Association*, pp. 10–12, 2013, doi: 10.1520/F2792-12A.2.

[7] C. Hull, "Apparatus for production of three dimensional objects by Stereolithography," 1986

[8] M. Salmi, "Additive manufacturing processes in medical applications," *Materials*, vol. 14, no. 1, pp. 1–16, 2021, doi: 10.3390/ma14010191.

[9] M. Attaran, "The rise of 3-D printing: The advantages of additive manufacturing over traditional manufacturing," *Bus Horiz*, vol. 60, no. 5, pp. 677–688, Sep. 2017, doi: 10.1016/j.bushor.2017.05.011.

[10] D. L. Bourell, D. W. Rosen, and M. C. Leu, "The roadmap for additive manufacturing and its impact," *3D Printing and Additive Manufacturing*, vol. 1, no. 1. Mary Ann Liebert Inc., pp. 6–9, Mar. 01, 2014. doi: 10.1089/3dp.2013.0002.

[11] M. Guvendiren, J. Molde, R. M. D. Soares, and J. Kohn, "Designing Biomaterials for 3D Printing," *ACS Biomater Sci Eng*, 2016, doi: 10.1021/acsbiomaterials.6b00121.

[12] A. Youssef, S. J. Hollister, and P. D. Dalton, "Additive manufacturing of polymer melts for implantable medical devices and scaffolds," *Biofabrication*, vol. 9, no. 1, p. 012002, Feb. 2017, doi: 10.1088/1758-5090/aa5766.

[13] D. Tang, R. S. Tare, L. Y. Yang, D. F. Williams, K. L. Ou, and R. O. C. Oreffo, "Biofabrication of bone tissue: Approaches, challenges and translation for bone regeneration," *Biomaterials*, vol. 83, pp. 363–382, 2016, doi: 10.1016/j.biomaterials.2016.01.024.

[14] C. Garot, G. Bettega, and C. Picart, "Additive Manufacturing of Material Scaffolds for Bone Regeneration: Toward Application in the Clinics," *Adv Funct Mater*, vol. 2006967, pp. 1–17, 2020, doi: 10.1002/adfm.202006967.

[15] P. Szymczyk-Ziółkowska, M. B. Łabowska, J. Detyna, I. Michalak, and P. Gruber, "A review of fabrication polymer scaffolds for biomedical applications using additive manufacturing techniques," *Biocybernetics and Biomedical Engineering*, vol. 40, no. 2. Elsevier Sp. z o.o., pp. 624–638, Apr. 01, 2020. doi: 10.1016/j.bbe.2020.01.015.

[16] A. R. Calore, R. Sinha, J. Harings, K. V Bernaerts, C. Mota, and L. Moroni, "Chapter 7 Thermoplastics for Tissue Engineering," in *Computer-Aided Tissue Engineering*, A. Rainer and L. Moroni, Eds., 2021, pp. 75–99.

[17] Y. S. Nam, J. J. Yoon, and T. G. Park, "A novel fabrication method of macroporous biodegradable polymer scaffolds using gas foaming salt as a porogen additive," *J Biomed Mater Res*, vol. 53, no. 1, pp. 1–7, Jan. 2000, doi: 10.1002/(SICI)1097-4636(2000)53:1<1::AID-JBM1>3.0.CO;2-R.

[18] S. S. Kim, M. Sun Park, O. Jeon, C. Yong Choi, and B. S. Kim, "Poly(lactide-co-glycolide)/hydroxyapatite composite scaffolds for bone tissue engineering," *Biomaterials*, vol. 27, no. 8, pp. 1399–1409, Mar. 2006, doi: 10.1016/j.biomaterials.2005.08.016.

[19] C. M. Murphy, M. G. Haugh, and F. J. O'Brien, "The effect of mean pore size on cell attachment, proliferation and migration in collagen-glycosaminoglycan scaffolds for bone tissue engineering," *Biomaterials*, vol. 31, no. 3, pp. 461–466, Jan. 2010, doi: 10.1016/j.biomaterials.2009.09.063.

[20] N. Sultana and M. Wang, "PHBV/PLLA-based composite scaffolds fabricated using an emulsion freezing/freeze-drying technique for bone tissue engineering: Surface modification and in vitro biological evaluation," *Biofabrication*, vol. 4, no. 1, p. 015003, Mar. 2012, doi: 10.1088/1758-5082/4/1/015003.

[21] G. Wei and P. X. Ma, "Structure and properties of nano-hydroxyapatite/polymer composite scaffolds for bone tissue engineering," *Biomaterials*, vol. 25, no. 19, pp. 4749–4757, Aug. 2004, doi: 10.1016/j.biomaterials.2003.12.005.

[22] R. Akbarzadeh and A.-M. Yousefi, "Effects of processing parameters in thermally induced phase separation technique on porous architecture of scaffolds for bone tissue engineering," *J Biomed Mater Res B Appl Biomater*, vol. 102, no. 6, pp. 1304–1315, Aug. 2014, doi: 10.1002/jbm.b.33101.

[23] K. F. F. Leong, C. M. M. Cheah, and C. K. K. Chua, "Solid freeform fabrication of three-dimensional scaffolds for engineering replacement tissues and organs," *Biomaterials*, vol. 24, no. 13, pp. 2363–2378, Jun. 2003, doi: 10.1016/S0142-9612(03)00030-9.

[24] Q. L. Loh and C. Choong, "Three-Dimensional Scaffolds for Tissue Engineering Applications: Role of Porosity and Pore Size," *Tissue Eng Part B Rev*, vol. 19, no. 6, pp. 485–502, Dec. 2013, doi: 10.1089/ten.teb.2012.0437.

[25] S. M. Peltola, F. P. W. Melchels, D. W. Grijpma, and M. Kellomäki, "A review of rapid prototyping techniques for tissue engineering purposes," *Ann Med*, vol. 40, no. 4, pp. 268–280, Jan. 2008, doi: 10.1080/07853890701881788.

[26] A. Youssef, S. J. Hollister, P. D. Dalton, R. Amin, S. Knowlton, and A. Hart, "Current and emerging applications of 3D printing in medicine," *Biofabrication*, vol. 9, no. 2, pp. 1–9, 2017, doi: 10.1088/1758-5090/aa7279.

[27] M. A. Woodruff and D. W. Hutmacher, “The return of a forgotten polymer—Polycaprolactone in the 21st century,” *Prog Polym Sci*, vol. 35, no. 10, pp. 1217–1256, Oct. 2010, doi: 10.1016/j.progpolymsci.2010.04.002.

[28] A. Di Luca *et al.*, “Tuning Cell Differentiation into a 3D Scaffold Presenting a Pore Shape Gradient for Osteochondral Regeneration,” *Adv Healthc Mater*, vol. 5, no. 14, pp. 1753–1763, Jul. 2016, doi: 10.1002/adhm.201600083.

[29] H.-W. Kang, S. J. Lee, I. K. Ko, C. Kengla, J. J. Yoo, and A. Atala, “A 3D bioprinting system to produce human-scale tissue constructs with structural integrity,” *Nat Biotechnol*, vol. 34, no. 3, pp. 312–319, Mar. 2016, doi: 10.1038/nbt.3413.

[30] S. Yang, K.-F. Leong, Z. Du, and C.-K. Chua, “The Design of Scaffolds for Use in Tissue Engineering. Part II. Rapid Prototyping Techniques,” *Tissue Eng*, vol. 8, no. 1, pp. 1–11, Feb. 2002, doi: 10.1089/107632702753503009.

[31] C. Mota, D. Puppi, F. Chiellini, and E. Chiellini, “Additive manufacturing techniques for the production of tissue engineering constructs,” *J Tissue Eng Regen Med*, vol. 9, no. 3, pp. 174–190, 2015, doi: 10.1002/term.1635.

[32] A. Di Luca *et al.*, “Surface energy and stiffness discrete gradients in additive manufactured scaffolds for osteochondral regeneration,” *Biofabrication*, vol. 8, no. 1, p. 015014, Feb. 2016, doi: 10.1088/1758-5090/8/1/015014.

[33] P. Song *et al.*, “Novel 3D porous biocomposite scaffolds fabricated by fused deposition modeling and gas foaming combined technology,” *Compos B Eng*, vol. 152, pp. 151–159, Nov. 2018, doi: 10.1016/j.compositesb.2018.06.029.

[34] M. Cámara Torres, “Tracing fast roads towards bone regeneration,” maastricht university, 2021. doi: 10.26481/dis.20210913mt.

[35] S. S. Crump, “United States Patent - US5121329A - Apparatus and method for creating three-dimensional objects,” Oct. 30, 1989

[36] C. McIlroy and P. D. Olmsted, “Deformation of an Amorphous Polymer during the Fused-Filament-Fabrication Method for Additive Manufacturing,” 2016, doi: 10.1122/1.4976839.

[37] P. G. de Gennes, “Reptation of a Polymer Chain in the Presence of Fixed Obstacles,” *J Chem Phys*, vol. 55, no. 2, pp. 572–579, Jul. 1971, doi: 10.1063/1.1675789.

[38] C. Bellehumeur, L. Li, Q. Sun, and P. Gu, “Modeling of bond formation between polymer filaments in the fused deposition modeling process,” *J Manuf Process*, vol. 6, no. 2, pp. 170–178, 2004.

[39] C. McIlroy and P. D. Olmsted, “Disentanglement effects on welding behaviour of polymer melts during the fused-filament-fabrication method for additive manufacturing,” *Polymer (Guildf)*, vol. 123, pp. 376–391, Aug. 2017, doi: 10.1016/j.polymer.2017.06.051.

[40] G. D. Goh, Y. L. Yap, H. K. J. Tan, S. L. Sing, G. L. Goh, and W. Y. Yeong, “Process–Structure–Properties in Polymer Additive Manufacturing via Material Extrusion: A Review,” *Critical Reviews in Solid State and Materials Sciences*, vol. 45, no. 2, pp. 113–133, Mar. 2020, doi: 10.1080/10408436.2018.1549977.

[41] S. C. Ligon, R. Liska, J. Stampfl, M. Gurr, and R. Mülhaupt, “Polymers for 3D Printing and Customized Additive Manufacturing,” *Chem Rev*, vol. 117, no. 15, pp. 10212–10290, Aug. 2017, doi: 10.1021/acs.chemrev.7b00074.

[42] M. Vaezi, H. Seitz, and S. Yang, “A review on 3D micro-additive manufacturing technologies,” *International Journal of Advanced Manufacturing Technology*, vol. 67, no. 5–8, pp. 1721–1754, 2013, doi: 10.1007/s00170-012-4605-2.

[43] S. Varun, “Timing of interfacial diffusion and (stereo)crystallization to tailor mechanical properties of additively manufactured poly(lactides),” maastricht university, 2020. doi: 10.26481/dis.20201013vs.

[44] D. W. Hutmacher, T. Schantz, I. Zein, K. W. Ng, S. H. Teoh, and K. C. Tan, “Mechanical properties and cell cultural response of polycaprolactone scaffolds designed and fabricated via fused deposition modeling,” *J Biomed Mater Res*, vol. 55, no. 2, pp. 203–216, May 2001, doi: 10.1002/1097-4636(200105)55:2<203::AID-JBM1007>3.0.CO;2-7.

[45] C. Wang *et al.*, “3D printing of bone tissue engineering scaffolds,” *Bioact Mater*, vol. 5, no. 1, pp. 82–91, Mar. 2020, doi: 10.1016/j.bioactmat.2020.01.004.

[46] T. Agarwal *et al.*, “Recent advances in bioprinting technologies for engineering different cartilage-based tissues,” *Materials Science and Engineering: C*, vol. 123, p. 112005, Apr. 2021, doi: 10.1016/j.msec.2021.112005.

[47] J. An, J. E. M. Teoh, R. Suntornnond, and C. K. Chua, “Design and 3D Printing of Scaffolds and Tissues,” *Engineering*, vol. 1, no. 2, pp. 261–268, Jun. 2015, doi: 10.15302/J-ENG-2015061.

[48] B. N. Turner, R. Strong, and S. A. Gold, “A review of melt extrusion additive manufacturing processes: I. Process design and modeling,” *Rapid Prototyp J*, vol. 20, no. 3, pp. 192–204, 2014, doi: 10.1108/RPJ-01-2013-0012.

[49] A. Bellini, “Fused deposition of ceramics: a comprehensive experimental, analytical and computational study of material behavior, fabrication process and equipment design,” 2002.

[50] C. Y. Lin, N. Kikuchi, and S. J. Hollister, “A novel method for biomaterial scaffold internal architecture design to match bone elastic properties with desired porosity,” *J Biomech*, vol. 37, no. 5, pp. 623–636, 2004, doi: 10.1016/j.jbiomech.2003.09.029.

[51] M. Hashemi, “Modeling of the Rotary-Screw-Driven Dispensing Process,” 2006.

[52] H. D. Ke, “INVESTIGATION INTO THE DISPENSING - BASED FABRICATION PROCESS FOR TISSUE SCAFFOLDS,” 2006.

[53] P. S. P. Poh *et al.*, “Polylactides in additive biomanufacturing,” *Adv Drug Deliv Rev*, vol. 107, pp. 228–246, 2016, doi: 10.1016/j.addr.2016.07.006.

[54] S. Kyle, Z. M. Jessop, A. Al-Sabah, and I. S. Whitaker, “‘Printability’’ of Candidate Biomaterials for Extrusion Based 3D Printing: State-of-the-Art,’” *Adv Healthc Mater*, vol. 6, no. 16, pp. 1–16, 2017, doi: 10.1002/adhm.201700264.

[55] A. E. Solomon and A. V Mathew, “3-D Comsol Analysis of Extruder Dies,” *Applied Sciences*, 2009.

[56] E. T. J. Klompen, "Mechanical properties of solid polymers: constitutive modelling of long and short term behaviour," 2005.

[57] P. S. Poh *et al.*, "Evaluation of polycaprolactone − poly-D,L-lactide copolymer as biomaterial for breast tissue engineering," *Polym Int*, vol. 66, no. 1, pp. 77–84, Jan. 2017, doi: 10.1002/pi.5181.

[58] X. Liu, Y. Zou, W. Li, G. Cao, and W. Chen, "Kinetics of thermo-oxidative and thermal degradation of poly(d,l-lactide) (PDLLA) at processing temperature," *Polym Degrad Stab*, vol. 91, no. 12, pp. 3259–3265, Dec. 2006, doi: 10.1016/j.polymdegradstab.2006.07.004.

[59] D. Rasselet, A. Ruellan, A. Guinault, G. Miquelard-Garnier, C. Sollogoub, and B. Fayolle, "Oxidative degradation of polylactide (PLA) and its effects on physical and mechanical properties," *Eur Polym J*, vol. 50, no. 1, pp. 109–116, Jan. 2014, doi: 10.1016/j.eurpolymj.2013.10.011.

[60] V. Taubner and R. Shishoo, "Influence of Processing Parameters on the Degradation of Poly(L-lactide) During Extrusion," 2001. doi: https://doi.org/10.1002/1097-4628(20010321)79:12<2128::AID-APP1020>3.0.CO;2-%23.

[61] S. Khalil, J. Nam, and W. Sun, "Multi-nozzle deposition for construction of 3D biopolymer tissue scaffolds," *Rapid Prototyp J*, vol. 11, no. 1, pp. 9–17, 2005, doi: 10.1108/13552540510573347.

[62] J. E. Seppala, S. Hoon Han, K. E. Hillgartner, C. S. Davis, and K. B. Migler, "Weld formation during material extrusion additive manufacturing," *Soft Matter*, vol. 13, no. 38, pp. 6761–6769, 2017, doi: 10.1039/C7SM00950J.

[63] K. Ragaert, L. Cardon, A. Dekeyser, and J. Degrieck, "Machine design and processing considerations for the 3D plotting of thermoplastic scaffolds," *Biofabrication*, vol. 2, no. 1, p. 14107, 2010, doi: 10.1088/1758-5082/2/1/014107.

[64] L. S. Nair and C. T. Laurencin, "Biodegradable polymers as biomaterials," *Progress in Polymer Science (Oxford)*, vol. 32, no. 8–9. Pergamon, pp. 762–798, Aug. 01, 2007. doi: 10.1016/j.progpolymsci.2007.05.017.

[65] P. Viswanathan *et al.*, "Mimicking the topography of the epidermal–dermal interface with elastomer substrates," *Integrative Biology*, vol. 8, no. 1, pp. 21–29, 2016, doi: 10.1039/C5IB00238A.

[66] O. A. Mohamed, S. H. Masood, and J. L. Bhowmik, "Optimization of fused deposition modeling process parameters: a review of current research and future prospects," *Adv Manuf*, vol. 3, no. 1, pp. 42–53, Mar. 2015, doi: 10.1007/s40436-014-0097-7.

[67] A. A. Zadpoor and J. Malda, "Additive Manufacturing of Biomaterials, Tissues, and Organs," *Ann Biomed Eng*, vol. 45, no. 1, pp. 1–11, Jan. 2017, doi: 10.1007/s10439-016-1719-y.

[68] G. Y. H. Choong and D. S. A. De Focatiis, "A method for the determination and correction of the effect of thermal degradation on the viscoelastic properties of degradable polymers," *Polym Degrad Stab*, vol. 130, pp. 182–188, 2016, doi: 10.1016/j.polymdegradstab.2016.06.018.

[69] Y. Tachibana, T. Maeda, O. Ito, Y. Maeda, and M. Kunioka, "Biobased myo-inositol as nucleator and stabilizer for poly(lactic acid)," *Polym Degrad Stab*, vol. 95, no. 8, pp. 1321–1329, 2010, doi: 10.1016/j.polymdegradstab.2010.02.007.

[70] L. K. Parthasarathy, R. S. Seelan, C. Tobias, M. F. Casanova, and R. N. Parthasarathy, "Mammalian inositol 3-phosphate synthase: Its role in the biosynthesis of brain inositol and its clinical use as a psychoactive agent," in *Subcellular Biochemistry*, Springer US, 2006, pp. 293–314. doi: 10.1007/0-387-27600-9_12.

[71] H. J. Lehermeier and J. R. Dorgan, "Melt rheology of poly(lactic acid): Consequences of blending chain architectures," *Polym Eng Sci*, vol. 41, no. 12, pp. 2172–2184, 2001, doi: Doi 10.1002/Pen.10912.

[72] E. Y. Kang, E. Lih, I. H. Kim, Y. K. Joung, and D. K. Han, "Effects of poly(L-lactide-ε-caprolactone) and magnesium hydroxide additives on physico-mechanical properties and degradation of poly(L-lactic acid)," *Biomater Res*, vol. 20, no. 1, p. 7, Dec. 2016, doi: 10.1186/s40824-016-0054-6.

[73] T. Osswald and N. Rudolph, *Polymer Rheology*. München: Carl Hanser Verlag GmbH & Co. KG, 2014. doi: 10.3139/9781569905234.

[74] S. Camarero-Espinosa, A. R. Calore, A. Wilbers, J. Harings, and L. Moroni, "Additive manufacturing of an elastic poly(ester)urethane for cartilage tissue engineering," *Acta Biomater*, vol. 102, pp. 192–204, Jan. 2020, doi: 10.1016/j.actbio.2019.11.041.

[75] S. Camarero-Espinosa, C. Tomasina, A. R. Calore, and L. Moroni, "Additive manufactured, highly resilient, elastic, and biodegradable poly(ester)urethane scaffolds with chondroinductive properties for cartilage tissue engineering," *Mater Today Bio*, vol. 6, p. 100051, Mar. 2020, doi: 10.1016/j.mtbio.2020.100051.

[76] S. Dupont *et al.*, "Role of YAP/TAZ in mechanotransduction," *Nature*, vol. 474, no. 7350, pp. 179–183, Jun. 2011, doi: 10.1038/nature10137.

[77] K. Chatterjee *et al.*, "The effect of 3D hydrogel scaffold modulus on osteoblast differentiation and mineralization revealed by combinatorial screening," *Biomaterials*, vol. 31, no. 19, pp. 5051–5062, Jul. 2010, doi: 10.1016/J.BIOMATERIALS.2010.03.024.

[78] J. S. Park *et al.*, "The effect of matrix stiffness on the differentiation of mesenchymal stem cells in response to TGF-β," *Biomaterials*, vol. 32, no. 16, pp. 3921–3930, Jun. 2011, doi: 10.1016/J.BIOMATERIALS.2011.02.019.

[79] W. J. Hendrikson, J. Rouwkema, C. A. Van Blitterswijk, and L. Moroni, "Influence of PCL molecular weight on mesenchymal stromal cell differentiation," *RSC Adv*, vol. 5, no. 67, pp. 54510–54516, 2015, doi: 10.1039/c5ra08048g.

[80] C. A. Van Blitterswijk and J. De Boer, *Tissue Engineering: Second Edition*. Elsevier, 2014. doi: 10.1016/C2013-0-00564-6.

[81] L. R. Jaidev and K. Chatterjee, “Surface functionalization of 3D printed polymer scaffolds to augment stem cell response,” *Mater Des*, vol. 161, pp. 44–54, Jan. 2019, doi: 10.1016/j.matdes.2018.11.018.

[82] H. Qu, “Additive manufacturing for bone tissue engineering scaffolds,” *Mater Today Commun*, vol. 24, p. 101024, Sep. 2020, doi: 10.1016/j.mtcomm.2020.101024.

[83] A. Wubneh, E. K. Tsekoura, C. Ayranci, and H. Uludağ, “Current state of fabrication technologies and materials for bone tissue engineering,” *Acta Biomater*, vol. 80, pp. 1–30, Oct. 2018, doi: 10.1016/j.actbio.2018.09.031.

[84] M. Cámara-Torres *et al.*, “Tuning Cell Behavior on 3D Scaffolds Fabricated by Atmospheric Plasma-Assisted Additive Manufacturing,” *ACS Appl Mater Interfaces*, vol. 13, no. 3, 2021, doi: 10.1021/acsami.0c19687.

[85] Y. Zhu, M. F. Leong, W. F. Ong, M. B. Chan-Park, and K. S. Chian, “Esophageal epithelium regeneration on fibronectin grafted poly(l-lactide-co-caprolactone) (PLLC) nanofiber scaffold,” *Biomaterials*, vol. 28, no. 5, pp. 861–868, Feb. 2007, doi: 10.1016/j.biomaterials.2006.09.051.

[86] G. Marchioli *et al.*, “Hybrid Polycaprolactone/Alginate Scaffolds Functionalized with VEGF to Promote de Novo Vessel Formation for the Transplantation of Islets of Langerhans,” *Adv Healthc Mater*, vol. 5, no. 13, pp. 1606–1616, 2016, doi: 10.1002/adhm.201600058.

[87] M. Cámara-Torres *et al.*, “3D additive manufactured composite scaffolds with antibiotic-loaded lamellar fillers for bone infection prevention and tissue regeneration,” *Bioact Mater*, vol. 6, no. 4, pp. 1073–1082, Apr. 2021, doi: 10.1016/j.bioactmat.2020.09.031.

[88] A. R. Calore *et al.*, “Cholecalciferol as Bioactive Plasticizer of High Molecular Weight Poly(D,L-Lactic Acid) Scaffolds for Bone Regeneration,” *Tissue Eng Part C Methods*, vol. 28, no. 7, pp. 335–350, Jul. 2022, doi: 10.1089/ten.tec.2022.0041.

[89] K. Ragaert, “Micro-extrusion of thermoplastics for 3D plotting of scaffolds for tissue engineering,” Ghent University, 2011.

[90] F. Shalchy, C. Lovell, and A. Bhaskar, “Hierarchical porosity in additively manufactured bioengineering scaffolds: Fabrication & characterisation,” *J Mech Behav Biomed Mater*, vol. 110, p. 103968, Oct. 2020, doi: 10.1016/j.jmbbm.2020.103968.

[91] D. Druecke *et al.*, “Neovascularization of poly(ether ester) block-copolymer scaffoldsin vivo: Long-term investigations using intravital fluorescent microscopy,” *J Biomed Mater Res*, vol. 68A, no. 1, pp. 10–18, Jan. 2004, doi: 10.1002/jbm.a.20016.

[92] E. L. Chaikof, H. Matthew, J. Kohn, A. G. Mikos, G. D. Prestwich, and C. M. Yip, “Biomaterials and scaffolds in reparative medicine,” *Ann N Y Acad Sci*, vol. 961, pp. 96–105, 2002, doi: 10.1111/j.1749-6632.2002.tb03057.x.

[93] V. Karageorgiou and D. Kaplan, “Porosity of 3D biomaterial scaffolds and osteogenesis,” *Biomaterials*, vol. 26, no. 27, pp. 5474–5491, Sep. 2005, doi: 10.1016/j.biomaterials.2005.02.002.

[94] S. Landers, A. Pfister, U. Hubner, H. John, R. Schmelzeisen, and R. Muhlaupt, “Fabrication of soft tissue engineering scaffolds by menas of rapid prototyping techniques,” *Journal of material science*, vol. 37: 3107–3, pp. 3107–3116, 2002.

[95] S. Neuss *et al.*, “Assessment of stem cell/biomaterial combinations for stem cell-based tissue engineering,” *Biomaterials*, vol. 29, pp. 302–313, 2008, doi: 10.1016/j.biomaterials.2007.09.022.

[96] N. R. Washburn, K. M. Yamada, C. G. Simon, S. B. Kennedy, and E. J. Amis, “High-throughput investigation of osteoblast response to polymer crystallinity: influence of nanometer-scale roughness on proliferation,” *Biomaterials*, vol. 25, no. 7–8, pp. 1215–1224, Mar. 2004, doi: 10.1016/j.biomaterials.2003.08.043.

[97] T. P. Kunzler, T. Drobek, M. Schuler, and N. D. Spencer, “Systematic study of osteoblast and fibroblast response to roughness by means of surface-morphology gradients,” *Biomaterials*, vol. 28, pp. 2175–2182, 2007, doi: 10.1016/j.biomaterials.2007.01.019.

[98] S. C. Neves, C. Mota, A. Longoni, C. C. Barrias, P. L. Granja, and L. Moroni, “Additive manufactured polymeric 3D scaffolds with tailored surface topography influence mesenchymal stromal cells activity,” *Biofabrication*, vol. 8, no. 2, p. 025012, May 2016, doi: 10.1088/1758-5090/8/2/025012.

[99] J. Y. Kim, J. J. Yoon, E. K. Park, D. S. Kim, S. Y. Kim, and D. W. Cho, “Cell adhesion and proliferation evaluation of SFF-based biodegradable scaffolds fabricated using a multi-head deposition system,” *Biofabrication*, vol. 1, no. 1, 2009, doi: Artn 015002 10.1088/1758-5082/1/1/015002.

[100] F. Zamani, M. Amani-Tehran, M. Latifi, and M. A. Shokrgozar, “The influence of surface nanoroughness of electrospun PLGA nanofibrous scaffold on nerve cell adhesion and proliferation,” *J Mater Sci Mater Med*, vol. 24, no. 6, pp. 1551–1560, 2013, doi: 10.1007/s10856-013-4905-6.

[101] H. Jeon, H. Lee, and G. Kim, “A surface-modified poly(ε-caprolactone) scaffold comprising variable nanosized surface-roughness using a plasma treatment,” *Tissue Eng Part C Methods*, vol. 20, no. 12, pp. 951–963, 2014, doi: 10.1089/ten.tec.2013.0701.

[102] A. Prasopthum, K. M. Shakesheff, and J. Yang, “Direct three-dimensional printing of polymeric scaffolds with nanofibrous topography,” *Biofabrication*, vol. 10, no. 2, p. 025002, Jan. 2018, doi: 10.1088/1758-5090/aaa15b.

[103] G. Kumar, M. S. Waters, T. M. Farooque, M. F. Young, and C. G. Simon, “Freeform fabricated scaffolds with roughened struts that enhance both stem cell proliferation and differentiation by controlling cell shape,” *Biomaterials*, vol. 33, no. 16, pp. 4022–4030, Jun. 2012, doi: 10.1016/j.biomaterials.2012.02.048.

[104] X. Song *et al.*, “Biomimetic 3D Printing of Hierarchical and Interconnected Porous Hydroxyapatite Structures with High Mechanical Strength for Bone Cell Culture,” *Adv Eng Mater*, vol. 21, no. 1, p. 1800678, Jan. 2019, doi: 10.1002/adem.201800678.

[105] A. A. Zadpoor, “Bone tissue regeneration: the role of scaffold geometry,” *Biomater Sci*, vol. 3, no. 2, pp. 231–245, 2015, doi: 10.1039/C4BM00291A.

[106] S. Van Bael *et al.*, “The effect of pore geometry on the in vitro biological behavior of human periosteum-derived cells seeded on selective laser-melted Ti6Al4V bone scaffolds,” *Acta Biomater*, vol. 8, no. 7, pp. 2824–2834, 2012, doi: 10.1016/j.actbio.2012.04.001.

[107] H. P. Dang *et al.*, “3D printed dual macro-, microscale porous network as a tissue engineering scaffold with drug delivering function,” *Biofabrication*, vol. 11, no. 3, p. 035014, Apr. 2019, doi: 10.1088/1758-5090/ab14ff.

[108] L. E. Visscher, H. P. Dang, M. A. Knackstedt, D. W. Hutmacher, and P. A. Tran, “3D printed Polycaprolactone scaffolds with dual macro-microporosity for applications in local delivery of antibiotics,” *Materials Science and Engineering: C*, vol. 87, pp. 78–89, Jun. 2018, doi: 10.1016/J.MSEC.2018.02.008.

[109] H. M. Yin *et al.*, “Engineering porous poly(lactic acid) scaffolds with high mechanical performance via a solid state extrusion/porogen leaching approach,” *Polymers (Basel)*, vol. 8, no. 6, 2016, doi: 10.3390/polym8060213.

[110] A. Salerno *et al.*, “Synthetic scaffolds with full pore interconnectivity for bone regeneration prepared by supercritical foaming using advanced biofunctional plasticizers,” *Biofabrication*, vol. 9, no. 3, p. 035002, Jun. 2017, doi: 10.1088/1758-5090/aa78c5.

[111] W. J. Choi *et al.*, “Rapid development of dual porous poly(lactic acid) foam using fused deposition modeling (FDM) 3D printing for medical scaffold application,” *Materials Science and Engineering C*, vol. 110, p. 110693, May 2020, doi: 10.1016/j.msec.2020.110693.

[112] C. J. Yoo, B. S. Shin, B. S. Kang, D. H. Yun, D. B. You, and S. M. Hong, “Manufacturing a Porous Structure According to the Process Parameters of Functional 3D Porous Polymer Printing Technology Based on a Chemical Blowing Agent,” *IOP Conf Ser Mater Sci Eng*, vol. 229, p. 012027, Sep. 2017, doi: 10.1088/1757-899X/229/1/012027.

[113] A. R. Calore *et al.*, “Manufacturing of scaffolds with interconnected internal open porosity and surface roughness,” *Acta Biomater*, vol. 156, pp. 158–176, Jan. 2023, doi: 10.1016/j.actbio.2022.07.017.

[114] N. H. Hart, S. Nimphius, T. Rantalainen, A. Ireland, A. Siafarikas, and R. U. Newton, “Mechanical basis of bone strength: Influence of bone material, bone structure and muscle action,” *Journal of Musculoskeletal Neuronal Interactions*, vol. 17, no. 3, pp. 114–139, 2017.

[115] M. Cocca, M. L. Di Lorenzo, M. Malinconico, and V. Frezza, “Influence of crystal polymorphism on mechanical and barrier properties of poly(l-lactic acid),” *Eur Polym J*, vol. 47, no. 5, pp. 1073–1080, May 2011, doi: 10.1016/j.eurpolymj.2011.02.009.

[116] T. Yeung *et al.*, “Effects of substrate stiffness on cell morphology, cytoskeletal structure, and adhesion,” *Cell Motil Cytoskeleton*, vol. 60, no. 1, pp. 24–34, Jan. 2005, doi: 10.1002/cm.20041.

[117] A. Zemel, F. Rehfeldt, A. E. X. Brown, D. E. Discher, and S. A. Safran, “Cell shape, spreading symmetry, and the polarization of stress-fibers in cells,” *Journal of Physics Condensed Matter*, vol. 22, no. 19, p. 194110, Apr. 2010, doi: 10.1088/0953-8984/22/19/194110.

[118] L. MacQueen, Y. Sun, and C. A. Simmons, “Mesenchymal stem cell mechanobiology and emerging experimental platforms,” *J R Soc Interface*, vol. 10, no. 84, p. 20130179, Jul. 2013, doi: 10.1098/rsif.2013.0179.

[119] W. Zhong, Y. Li, L. Li, W. Zhang, S. Wang, and X. Zheng, “YAP-mediated regulation of the chondrogenic phenotype in response to matrix elasticity,” *J Mol Histol*, vol. 44, no. 5, pp. 587–595, Oct. 2013, doi: 10.1007/s10735-013-9502-y.

[120] A. Larena and G. Pinto, “The effect of surface roughness and crystallinity on the light scattering of polyethylene tubular blown films,” *Polym Eng Sci*, vol. 33, no. 12, pp. 742–747, Jun. 1993, doi: 10.1002/pen.760331204.

[121] F. Guilak, D. M. Cohen, B. T. Estes, J. M. Gimble, W. Liedtke, and C. S. Chen, “Control of Stem Cell Fate by Physical Interactions with the Extracellular Matrix,” *Cell Stem Cell*, vol. 5, no. 1, pp. 17–26, Jul. 2009, doi: 10.1016/j.stem.2009.06.016.

[122] A. B. Faia-Torres *et al.*, “Osteogenic differentiation of human mesenchymal stem cells in the absence of osteogenic supplements: A surface-roughness gradient study,” *Acta Biomater*, vol. 28, pp. 64–75, 2015, doi: 10.1016/j.actbio.2015.09.028.

[123] H. Chen *et al.*, “Tailoring surface nanoroughness of electrospun scaffolds for skeletal tissue engineering,” *Acta Biomater*, vol. 59, pp. 82–93, Sep. 2017, doi: 10.1016/j.actbio.2017.07.003.

[124] A. R. Calore *et al.*, “Shaping and properties of thermoplastic scaffolds in tissue regeneration: The effect of thermal history on polymer crystallization, surface characteristics and cell fate,” *J Mater Res*, vol. 36, no. 19, pp. 3914–3935, 2021, doi: 10.1557/s43578-021-00403-2.

[125] V. Srinivas, C. S. J. van Hooy-Corstjens, and J. A. W. Harings, “Correlating molecular and crystallization dynamics to macroscopic fusion and thermodynamic stability in fused deposition modeling; a model study on polylactides,” *Polymer (Guildf)*, vol. 142, pp. 348–355, Apr. 2018, doi: 10.1016/j.polymer.2018.03.063.

[126] M. Cámara-Torres, R. Sinha, C. Mota, and L. Moroni, “Improving cell distribution on 3D additive manufactured scaffolds through engineered seeding media density and viscosity,” *Acta Biomater*, vol. 101, pp. 183–195, Jan. 2020, doi: 10.1016/J.ACTBIO.2019.11.020.

[127] A. Di Luca *et al.*, “Gradients in pore size enhance the osteogenic differentiation of human mesenchymal stromal cells in three-dimensional scaffolds,” *Sci Rep*, vol. 6, no. 1, p. 22898, Sep. 2016, doi: 10.1038/srep22898.

[128] P. F. Costa, A. M. Puga, L. Díaz-Gomez, A. Concheiro, D. H. Busch, and C. Alvarez-Lorenzo, “Additive manufacturing of scaffolds with dexamethasone controlled release for enhanced bone regeneration,” *Int J Pharm*, vol. 496, no. 2, pp. 541–550, 2015, doi: 10.1016/j.ijpharm.2015.10.055.

[129] C. J. G. Plummer, “Polymer Mechanical Properties,” in *Handbook of Polymer Reaction Engineering*, Weinheim, Germany: Wiley-VCH Verlag GmbH, 2008, pp. 721–756. doi: 10.1002/9783527619870.ch14.

Chapter 2

HOW WILL IT PRINT? A RHEOLOGY-BASED NUMERICAL MODEL TO PREDICT THE PROPERTIES OF MELT-EXTRUDED SCAFFOLDS FOR BONE TISSUE ENGINEERING

Andrea Roberto Calore[1,2], Laurence Hawke[3], Carlos Mota[1], Katrien Bernaerts[2], Jules Harings[2], Lorenzo Moroni[1]

[1] MERLN Institute for Technology-Inspired Regenerative Medicine, Maastricht University, Maastricht, The Netherlands

[2] Aachen-Maastricht Institute for Biobased Materials (AMIBM), Maastricht University, Geleen, The Netherlands

[3] Institute of Condensed Matter and Nanosciences (IMCN), Catholic University of Louvain, Louvain, Belgium

ABSTRACT

Despite the consolidated success of Additive Manufacturing in tissue engineering, the process of scaffold fabrication is still based on direct experience and on a trial-and-error approach when testing a new machine or evaluating the performance of a new material. This applies in particular when using research grades from small scale synthesis or when testing expensive medical grades commercially available. Focusing on extrusion-based techniques, we show that it is possible to evaluate in advance the compatibility between a specific machine and a specific material and to choose the best set of deposition parameters to obtain the desired results in terms of morphological accuracy and mechanical properties. This can be done by knowing *a priori* the rheological and thermal properties of the polymer and the machine features.

2.1 INTRODUCTION

Tissue Engineering and Regenerative Medicine (TERM) are interdisciplinary fields at the interface between biology, medicine, material science, and engineering, with the goal of overcoming the lack of tissue and organ donors and the inherent risks linked to transplant procedures [1]. The progressive improvements in medicine and general welfare are considered responsible for the shortage of available tissues and organs for transplantation. In addition, the transplantation procedure itself is not only a delicate surgical procedure, but also permeated by the risk of rejection [2].

Proper defect treatment requires the design and the production of substitutes with chemical, morphological and mechanical properties comparable to those of the tissue to be replaced. With this strategy, adequate integration of these substitutes can be achieved, mitigating performance mismatch with the surrounding healthy environment and thus avoiding failure. Such an approach is based on the synergy among the proper cell type, a supporting structure (scaffold) for tissue formation and growth and adequate stimuli (chemical, mechanical, topographical) mimicking physiological conditions. With this goal in mind, tissue engineers started taking inspiration from industry and exploiting manufacturing processes to obtain full control over scaffold architecture. This not only allows replicating the morphology of the defect and the structural organization of the specific tissue type, but also influences nutrients uptake, waste removal, mechanical properties and cell fate [3]. Therefore, Additive Manufacturing (AM) techniques are nowadays extensively used for scaffold-fabrication, taking over the so-called “conventional methods” such as gas foaming/particulate leaching, freeze-drying or phase separation [4]–[9].

Among the huge plethora of available AM processes, melt-extrusion additive manufacturing (ME-AM) has drawn particular attention for the production of scaffolds for hard-tissue engineering where stiff constructs able to withstand high loads are needed [10]. This is mainly due to the limited requirements needed for the material to be processed. In fact, the lack of potentially cytotoxic compounds such as binders, photo-initiators or organic solvents represent an essential feature for biomedical applications when compared to other AM techniques such as, respectively, 3D printing, stereolitography (SLA) and slurry-based extrusion [11]. Instead, ME-AM is based on the extrusion of polymers whose only prerequisite is to be thermoplastic, making the palette of suitable materials quite wide. In addition, the needed equipment is relatively simple and cheap, only having to melt the material of choice and extrude it. These reasons altogether have determined the success of ME-AM techniques for the production of scaffold for hard-tissue engineering [12].

ME-AM technologies can be divided into three classes depending on the type of driving force for melt extrusion: fused deposition modeling (FDM), 3D-fiber deposition (3DF) and bioextrusion [13]. FDM is based on a filament feedstock that, pushed by rollers, acts as a piston on the previously molten material. Instead, 3DF and bioextrusion work by pushing the melt via a piston or compressed air (3DF) or via an auger screw (bioextrusion). The use of the last two techniques has been preferred to FDM for TERM applications for two main reasons. First, the preparation of the filament feedstock requires high amounts of materials often not available at research level. Additionally, the shaping of the raw material into a feedstock filament is carried out with melt extruders and, therefore, via the application of high temperatures, which, coupled to the subsequent printing phase, could promote chain scission and molecular weight (M_w) decrease [12], [14].

However, despite the high level of morphological control that can be offered by ME-AM, manufacturing is still an empirically-optimized process to a certain extent, which hinders reproducibility and thus its adoption on large scale [15]–[17]. In fact, researchers usually go through trial-and-error loops before obtaining a combination of working parameters, which result in scaffolds that can be regarded as “satisfactory” in terms of correlation between theoretical and experimental structural features [18]. This is usually the case when adopting new materials, evaluating new devices or during production upscaling [19]–[24]. As the success of the trials relies on the user’s experience, these might be numerous and cause time and material waste. With reference to the latter, it is important to note that the used thermoplastic polymers are either expensive medical grades or materials synthetized in-house, thus usually available in low quantities. This aspect might further impede the process upscaling towards a standardized scaffold production line, favoring more validated but less flexible techniques. In addition, the current approach for scaffold-manufacturing optimization relies on sectioning the product and assessing only the morphology of the construct, while the investigation of the mechanical properties is usually neglected. Because of the presence of porosity, the load-bearing areas in TE scaffolds are far less than in non-biomedical ME-AM constructs, making the optimization of the final mechanical performance highly dependent on the porosity architecture and manufacturing more critical than for non-biomedical applications [25], [26].

From a deeper analysis, it appears evident that the main reason behind the trial-and-error approach is the search for the correct coupling between flow rate and printhead speed on one side, and between interlayer bonding and cross-section retention on the other [27]. Briefly, the former couple is responsible for the diameter of the deposited filament with potential effects on the later porosity too. Instead, interlayer bonding is favored by high extrusion temperatures but at the expenses of the cross-section, which might shift from circular to ellipsoidal in case of longer solidification times. However, it is important to underline how temperature has an impact on the flow rate as well. From these considerations, it can be easily understood how the scaffold manufacturing process can turn into an extensive fine-tuning operation, without an *a priori* knowledge to support in predicting the most suitable fabrication conditions [27]. The maximization of a bioextruder throughput is a typical scenario where the limited awareness of the process has a negative impact on the manufacturing process. A common practice is the increase of the screw revolutions per minute (rpm) to maximize the flow rate and speed up production. This may be the case also when working with thermally unstable polymer that should not be left in molten state for extended periods of time. However, excessively high rpm might generate high pressure at the nozzle inlet, and thus induce a backpressure flow, which is responsible for reducing the output being directed the other way around [28]. Therefore, it appears clear that a thorough understanding of the fundamentals of the process is paramount, and these encompass the material’s properties/fluid-dynamics, the printer features and the interplay thereof [29].

Mathematical modeling represents a useful tool to predict the outcome of physical processes. Lately, several models of the FDM technique have been developed, being FDM the most widespread ME-AM method for industrial or technical purposes [30]. We refer the reader to a comprehensive review on the topic written by Das et al. [31], but we underline how these models are mainly based on molecular dynamics of computational fluid-dynamics, thus requiring great simulation resources. The key processes of the extrusion procedure have been identified in the melt flow in the printhead, the filament spreading after deposition, the bonding of adjacent filaments and the part deformation due to thermal gradients. However, scaffold production via ME-AM for biomedical applications presents different manufacturing conditions and requirements, which often limits the applicability of the above-mentioned models. First, FDM is less widespread in the TERM field than 3DF and bioextrusion, which are based on slightly different processing principles. In addition, porosity is not considered a defect, but instead is a strict prerequisite [30]. Consequently, adjacent filaments are not in contact with each other and extruded filaments are not squeezed onto the previous layer during deposition. This is because most of the extrusion takes place over the gap between two filaments from the bottom layer, thus originating the intended porosity. Therefore, filaments do not exhibit a rectangular cross-section but rather a circular one, following the shape of the nozzle. Furthermore, the length scale of scaffolds is usually lower than industrial/consumer products. This makes the occurrence of warping rather limited and allows for the use of smaller (and cheaper) equipment. However, smaller equipment is often synonym of lower driving forces for the extrusion process, which might hinder processing of materials with high molar masses [32], [33]. This, therefore, poses the additional material processability question when coupled to the specific equipment.

In the TERM field, the definition of a printability window has been addressed mainly for hydrogel materials, as studied and reported in several papers on the topic [34]–[43]. However, hydrogels possess very different flow characteristics compared to thermoplastic polymers. An example is the relatively low viscosity in the pre-gel state during extrusion, which voids the extrudability issue. In addition, a rather important requirement during scaffold fabrication, bridging, has been modelled only partially. Bridging is the ability of the filament being extruded to cross a gap over unsupported space [44]. This can be parametrically described by its sagging degree, which is the maximum vertical displacement of the filament axis with respect to its ideal and straight horizontal position in case of a perfect bridge. In AM for TERM, this gap corresponds to a pore. Current hydrogel-printability models describe this phenomenon at a later stage, only after complete covering of the gap, according to the supported-beam or catenary theories [44], [45]. Instead, potential pore occlusion due to filament sagging may start occurring already before filament anchoring at the end of the gap, because of a non-optimal coupling between flow rate and printhead speed. In the case of thermoplastic polymers, solidification kinetics must be added to the interplay of multiple other factors. A proper understanding of the impact of these factors is often missing, as confirmed by the use of devices with no heated stage or chamber (e.g. EnvisionTEC V1.0 Bioplotter and SysEng BioScaffolder [46]. Besides affecting mechanics as previously described, suboptimal thermal management could result in pore occlusion thus limiting nutrients uptake and waste removal [47]–[49].

As mentioned, literature about modeling the printability of thermoplastic polymers for TERM purposes is scarce. To our knowledge, the only recent examples are the studies by Guo et al. [50] and Duty et al. [44]. In the former work, the correlation between material properties, printing parameters and printing outcome was first assessed experimentally with a parametric study. In particular, they printed poly(lactic-co-glycolic acid) (PLGA) with various lactic acid:glycolic acid (LA:GA) molecular weight ratios and end caps, and evaluated the printed scaffolds in terms of fiber morphology. From the results, they built a statistical model via regression to correlate the printing precision with printing conditions and material composition, with the goal of revealing the predominant factors for accurate manufacturing. Despite predicting the deposition is quite accurate, this strategy is based on a thorough screening of the possible combinations of experimental variables, resulting in great workload and material consumption. In addition, regression models are usually highly material- and printer-specific, limiting their applicability to other configurations. The work of Duty et al. [44] represents an example of a thorough study based on thermoplastic fluid-dynamics and rheology, which are the physical mechanisms ME-AM is based on [51]. The researchers developed a printability model of ME-AM for non-biomedical printing, taking therefore into account aspects such as the presence of reinforcing fibers and walls, warping and rectangular cross-sections. Nevertheless, they considered the bridging requirement as well, but maintaining the same modeling approach of the studies on hydrogels described earlier. Furthermore, polymer melt flow inside the printhead was described with a power-law relation, which does not account for lower shear-rate regions. In fact, considering the smaller-scale equipment for TERM and the consequent reduced flow rates, the polymer melt might be subjected to shear rates in the transition region between the power-law and the Newtonian behavior if not really in the Newtonian regime.

In our work, we have developed a mathematical model describing the scaffold manufacturing process via the bioextrusion technique. This specific class of ME-AM has a finer control on flow rate compared to 3DF, and can apply greater driving forces allowing to process polymers with higher molar masses [52]. The model is based on the coupling between machine specifications and rheological behavior of the polymer to be processed. While the former can be obtained from the device datasheet, the latter can be evaluated by simple and quick tests such as rheometry and Differential Scanning Calorimetry

(DSC). Given these initial data and the intended printing parameters, the numerical simulation can predict the flow rate and the consequent printhead speed, the deposited filament width and height, the amount of sagging and the strength of the welding points. Establishing the descriptive equations on the physics behind the process, the model is unlinked to a specific polymer grade or a specific bioextrusion printer, as it happens with printability models built on regression analysis.

2.2 EQUIPMENT AND MATERIAL PROPERTIES

A Bioscaffolder bioextrusion printer (SysENG, Germany) equipped with a G22 nozzle (DL Technologies) was used to model the melt flow behavior during extrusion. The geometrical features of interest for the model presented in this work are listed in Table 1.

Table 1. Geometrical features of used equipment.

Symbol	Parameter	Value
D_b	Barrel diameter	4.93 mm
ϕ_b	Screw pitch angle	12.5 °
t	Screw pitch	3.1 mm
w	Channel width	2.6 mm
h	Channel height	1.3 mm
L	Channel length	16.6 mm
R	Nozzle radius	0.2065 mm
L_n	Nozzle length	9.5 mm

The PDLLA amorphous grade 6302D (NatureWorks® Ingeo™) was used as sample material to obtain the physical properties requested by the model. The polymer chosen was amorphous to neglect the prominent shrinkage due to crystallization. Prior to any characterization, the polymer was dried in a vacuum oven at 35 °C for 24 h.

The material was characterized via Differential Scanning Calorimetry (DSC) to measure thermal properties such as glass transition temperature T_g, heat capacity C_p and thermal conductivity k. Briefly, 5 mg of sample were loaded and sealed in a hermetic aluminum pan, which then underwent a heating-cooling-heating cycle in a Q2000 DSC apparatus (TA Instruments) under nitrogen atmosphere. The first heating phase went from 25 to 200 °C at a rate of 10 °C/min, at the end of which the material was kept isothermally for 3 min. The polymer was then cooled down to 25 °C at 10 °C/min, kept isothermally for 3 min and reheated following the same procedure. Considering that the glass transition takes place over a range of temperature, the T_g is indicated as the onset of the transition itself.

Rheometry was employed to obtain flow characteristics such as the viscosity curve η as function of shear rate and temperature and the Rouse time of one entanglement segment τ_e^{ref}. The flow curve $\eta = \eta(\dot{\gamma}, T)$ was obtained by running a series of frequency sweeps (FS) (10 – 628 rad/s, 1 % strain) at different temperatures (220 – 60 °C) with TA DHR rheometer equipped with two parallel plates with gap of 0.5 mm. The shear-rate dependence of viscosity was extrapolated from FS data at the reference temperature of 200 °C by converting angular frequency data to shear rate according to the Cox-Merz transformation [12]. Then, the Cross model was fitted with $R^2 = 0.99$. This formulation allows to describe the transition from Newtonian behavior at low shear rates to the power-law region at higher rates, and well fits a variety of commercial polymers for melt processing [53]. In particular, the model has the following form for a given temperature:

$$\eta(\dot{\gamma}) = \frac{\eta_0}{1 + (\lambda|\dot{\gamma}|)^m} \tag{1}$$

With η_0 zero-shear rate viscosity, λ a material constant (consistency) with units of time and m another (dimensionless) material constant (rate index). The time-temperature-superposition (TTS) method [53] was applied to derive the polymer's zero-shear viscosity dependence over temperature according to:

$$\eta_0(T) = \eta_{0,ref}a_T \tag{2}$$

Where a_T is a shift-factor function defined by the William-Lendel-Ferry (WLF) model [54]:

$$a_T(T) = exp\left(\frac{-c_1(T - T_{ref})}{c_2 + T}\right) \tag{3}$$

With c_1 and c_2 fitting parameters. Eventually, τ_e^{ref} can be obtained as fitting parameter from the interpolation of rheological data (*G'/G"* vs angular frequency) with the predictions of the tube model [55]–[57].

Gel permeation chromatography (GPC) was performed to evaluate the weight average molecular weight M_w of the polymer. A Shimadzu LC-2030 Performance-I, with RID-20A RI detector and Shodex KF-850L column with chloroform (Carl Roth HPLC quality) as eluent, was used. For all the measurements, 50µL of a 2mg/mL polymer solution in the eluent were analyzed. The GPC column was calibrated with a polystyrene standard series up to 200.000 g/mol.

All the relevant material properties to implement the model obtained by DSC, rheological and GPC characterization, are listed in Table 3.

Table 2. Material properties obtained from DSC, rheological and GPC characterization.

Symbol	Property	Value
T_g	Glass transition temperature (onset)	60 °C
C_p	Heat capacity	870 J/(Kg °C)
k	Thermal conductivity	0.2 W(m °C)
η_0 (200 °C)	Zero-shear viscosity	936 Pa s
λ (200 °C)	Consistency	7.3E-3 s
m (200 °C)	Rate index	0.74
c_1		2.711
c_2		-21.931 °C
M_w	Weight-average molecular weight	211 Kg/mol

2.3 MORPHOLOGICAL DESCRIPTION

2.3.1 Flow analysis

In the printer considered in this study, the molten polymer travels first along the screw channel and then exits through a nozzle. The polymer melt is pushed by both the screw itself and nitrogen pressure applied to the molten polymer surface in the reservoir (system pressure p_{sys}) [58]. Due to the similarities with industrial polymer extrusion, modeling the bioextrusion process was carried out following the extensive literature already present, including the pioneering work of Carley et al. [59] for Newtonian fluids, while for power-law polymer melts we refer to the book of Rauwendaal [28] and the more recent analysis of Roland et al. [60]. However, the state in which the polymer is fed to the screw in most bioextrusion equipment represents a subtle but rather impactful difference with industrial extrusion. In fact, due to the lower available driving forces, the polymer is fed to the screw already in molten state, by the application of nitrogen pressure. For this reason, the models already present in literature are adequately modified and adapted to the bioextrusion technique used herein.

As previously mentioned, the polymer melt flows through the screw channel into the nozzle and eventually out of it, as can be seen in Figure 1A. For the law of conservation of mass [61], the flow rate at the nozzle outlet (Q_d) is equal to the flow rate through the screw channel (Q_s). However, the former is dependent on the pressure applied at the entrance of the nozzle, which is the result of the interplay between the pressure applied at the entrance of the screw channel and the pressure generated by the screw itself. For this reason, the flow analysis was divided according to the two main regions where it takes place: the screw channel and the nozzle. For ease of reading, we will omit subscripts referring to either the screw or the nozzle, in the formulas presented in the respective sections. Confusion will be avoided by keeping the flow analyses separate. We will limit the presence of subscripts to the overall flow rate through the nozzle tip, being this the only variable of interest for the other sections of the model.

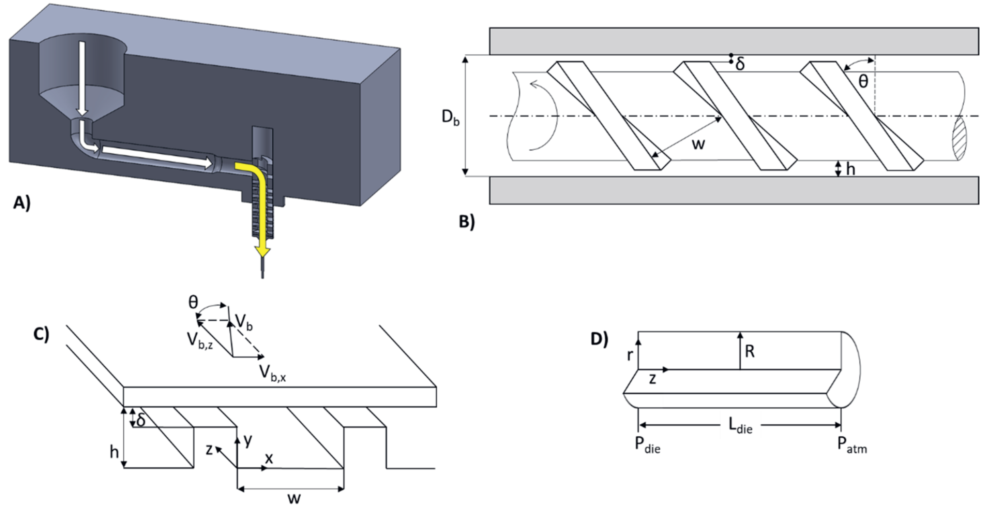

Figure 1. A) Cross-section of the Bioscaffolder printhead, where the path of the applied driving pressure and of the melt are highlighted by, respectively, white and yellow arrows. B) Geometry of the screw and the barrel. C) Unwound screw channel. D) Geometry of the nozzle.

2.3.1.1 Screw channel

2.3.1.1.1 Geometrical modeling

Following the derivation of Roland et al. [62] for a power-law fluid, the following considerations and assumption were preliminarily made:

1. The helical screw channel (Figure 1B) was considered unwound and as a flat rectangular channel (flat-plate assumption, Figure 1C). The surface of the barrel containing the screw was treated as an infinite flat plane. Such approach does not consider the curvature of the melt channel.
2. The screw was assumed to be stationary and the barrel to move with respect to the screw at a velocity v_b, calculated according to Equation 4, with barrel diameter D_b and screw speed N. v_b can be divided into a down-channel velocity $v_{b,z}$ (Equation (5)) and a cross-channel velocity $v_{b,x}$ (Equation (6)) component, with φ_b and t screw pitch angle and screw pitch, respectively.
3. The leakage flow in the gap between the screw flight and the barrel was ignored.
4. The polymer melt was incompressible.
5. The flow was isothermal, stationary and fully developed.
6. Gravitational and inertial forces were neglected.
7. There was no slip at the wall.

The velocity components describing the two-dimensional flat-plate model were:

$$v_b = D_b \pi N \ , \tag{4}$$

$$v_{b,z} = v_b \, cos(\phi_b) \ , \tag{5}$$

$$v_{b,x} = v_b \, sin(\phi_b) \ , \tag{6}$$

With:

$$\phi_b = arctan\left(\frac{t}{D_b \pi}\right) \ . \tag{7}$$

2.3.1.1.2 Governing equations

The volumetric flow rate (Q_s) can be calculated as the integral of the down-channel velocity profile $v_z(y)$ over the cross-sectional area:

$$Q_s = w \int_0^h v_z(y) dy \ . \tag{8}$$

Where *w* and *h* are, respectively, the screw channel width and height. Therefore, the velocity profile must first be obtained, by solving the momentum equation with appropriate boundary conditions (BC) [54]. Given the above-mentioned simplifications, the velocity vector becomes:

$$\boldsymbol{v} = \begin{pmatrix} v_x(y) \\ 0 \\ v_z(y) \end{pmatrix} \ , \tag{9}$$

Being v_x and v_z, respectively, the down- and the cross-channel velocities, both functions of the channel height coordinate. Therefore, the momentum equations for the down- and the cross-channel directions simplify to:

$$\frac{\partial p}{\partial x} = \frac{\partial \tau_{yx}}{\partial y} \ , \tag{10}$$

$$\frac{\partial p}{\partial z} = \frac{\partial \tau_{yz}}{\partial y} \ . \tag{11}$$

The solution of the momentum equations, for a given down-channel pressure gradient $\partial p/\partial z$, requires first the definition of boundary conditions appropriate to the case under examination. The no-slip condition (assumption 7) dictated that the down- and cross-channel velocities must be zero at the screw root (channel height zero). The velocities at the barrel must be equal to the respective components of the barrel speed. In addition, there was no net flow in the cross-channel direction, therefore the integral of the cross-channel velocity profile over the channel height must be zero.

$$v_x(y = 0) = 0 \ , \tag{12}$$

$$v_x(y = h) = v_{b,x} \ , \tag{13}$$

$$v_z(y = 0) = 0 \ , \tag{14}$$

$$v_z(y = h) = v_{b,z} \ , \tag{15}$$

$$Q_x = \int_0^h v_x(y) dy = 0 \ . \tag{16}$$

In addition, the two momentum partial-differential equations (Equations 10 and 11) were coupled via the shear-rate dependent viscosity η as follows:

$$\boldsymbol{\tau} = 2\eta\boldsymbol{D} \ , \tag{17}$$

Where **τ** is the stress tensor, ***D*** is the rate-of-deformation tensor given by:

$$\boldsymbol{D} = \frac{1}{2}(\boldsymbol{L} + \boldsymbol{L}^T) \ . \tag{18}$$

And ***L*** is the velocity gradient tensor:

$$\boldsymbol{L} = \nabla\boldsymbol{v} \ . \tag{19}$$

The viscosity function is specific for each polymer melt. Most melts exhibit viscosity going from a constant value at low shear rates (Newtonian plateau) to a decreasing trend with increasing shear-rates (shear-thinning), through a transition region. However, the melt flow behavior is usually modelled only for shear rates corresponding to either the Newtonian or in full shear-thinning region, because of the complexity of the mathematical treatment. We considered the full shear-rate range by using the Cross model described in Section 1.2, which we repropose for ease of reading:

$$\eta = \frac{\eta_0}{1 + (\lambda|\dot{\gamma}|)^m} \ , \tag{20}$$

The magnitude of the shear-rate is defined as:

$$|\dot{\gamma}| = \sqrt{2(\boldsymbol{D}:\boldsymbol{D})}. \tag{21}$$

For a channel with constant height and width, the non-zero velocity components v_x and v_z only depend on the direction y [63]. Therefore, the Cross model can be rewritten as

$$\eta = \frac{\eta_0}{1 + \lambda^m\left[\left(\frac{\partial v_x}{\partial y}\right)^2 + \left(\frac{\partial v_z}{\partial y}\right)^2\right]^{\frac{m}{2}}} \ . \tag{22}$$

Equation 22 can be expressed in terms of the shear-stress components τ_{yx} and τ_{yz}:

$$\tau_{yx} = \frac{\eta_0}{1 + \lambda^m\left[\left(\frac{\partial v_x}{\partial y}\right)^2 + \left(\frac{\partial v_z}{\partial y}\right)^2\right]^{\frac{m}{2}}}\frac{\partial v_x}{\partial y} \ , \tag{23}$$

$$\tau_{yz} = \frac{\eta_0}{1 + \lambda^m\left[\left(\frac{\partial v_x}{\partial y}\right)^2 + \left(\frac{\partial v_z}{\partial y}\right)^2\right]^{\frac{m}{2}}}\frac{\partial v_z}{\partial y} \ . \tag{24}$$

Equations 23 and 24 can be substituted into the momentum equations (Equations 10 and 11), giving the final version of the momentum equations:

$$\frac{\partial p}{\partial x} = \frac{\partial}{\partial y}\left(\eta(y)\frac{\partial v_x}{\partial y}\right) = \frac{\partial}{\partial y}\left\{\frac{\eta_0}{1 + \lambda^m\left[\left(\frac{\partial v_x}{\partial y}\right)^2 + \left(\frac{\partial v_z}{\partial y}\right)^2\right]^{\frac{m}{2}}}\frac{\partial v_x}{\partial y}\right\} \ , \tag{25}$$

$$\frac{\partial p}{\partial z}=\frac{\partial}{\partial y}\left(\eta(y)\frac{\partial v_z}{\partial y}\right)=\frac{\partial}{\partial y}\left\{\frac{\eta_0}{1+\lambda^m\left[\left(\frac{\partial v_x}{\partial y}\right)^2+\left(\frac{\partial v_z}{\partial y}\right)^2\right]^{\frac{m}{2}}}\frac{\partial v_z}{\partial y}\right\} \ . \tag{26}$$

By solving these momentum equations coupled to the boundary conditions (Equations 12 to 15) and the constraint of zero net cross-channel flow (Equation 16), the down- and cross-channel velocities can be obtained, as functions of the channel height (*y*) and the cross-channel pressure gradient *∂p/∂x*. Eventually, the flow rate through the screw channel can be evaluated from Equation 8.

2.3.1.1.3 Non-dimensionalization

The Cross viscosity model has a direct dependency on the shear-rate. Consequently, the momentum equations (Equations 25 and 26) are two non-linear coupled partial differential equations that require numerical methods to be solved. Before proceeding, the equations are transformed into dimensionless form, which can reduce the complexity of the problem and make it independent from the specific parameters of the phenomenon in object [64]. To this end, we first scale the variables, both independent (the channel height *y*) and dependent (the down- and cross-channel velocities v_z and v_x), with correspondent appropriate characteristic values to obtain their dimensionless counterparts (indicated by the symbol *):

$$v_x^*=\frac{v_x}{v_{b,z}} \ , \tag{27}$$

$$v_z^*=\frac{v_z}{v_{b,z}} \ , \tag{28}$$

$$y^*=\frac{y}{h} \ , \tag{29}$$

Where, $v_{b,z}$ is the down-channel velocity at the barrel surface and *h* is the channel height. Then, the viscosity function is non-dimensionalized by scaling it with an appropriate characteristic value and by applying the dimensionless variables:

$$\eta^*=\frac{\eta}{\eta_0}=\frac{1}{1+C^m\left[\left(\frac{\partial v_x^*}{\partial y^*}\right)^2+\left(\frac{\partial v_z^*}{\partial y^*}\right)^2\right]^{\frac{m}{2}}} \ , \tag{30}$$

$$C=\frac{\lambda v_{b,z}}{h} \ . \tag{31}$$

Where η_0 is the zero-shear rate viscosity of the Cross model.

The momentum equations were made dimensionless by applying the dimensionless variables and functions, giving:

$$6\Pi_{p,x}=\frac{\partial}{\partial y^*}\left(\eta^*\frac{\partial v_x^*}{\partial y^*}\right)=\frac{\partial}{\partial y^*}\left(\frac{1}{1+C^m\left[\left(\frac{\partial v_x^*}{\partial y^*}\right)^2+\left(\frac{\partial v_z^*}{\partial y^*}\right)^2\right]^{\frac{m}{2}}}\frac{\partial v_x^*}{\partial y^*}\right) \ , \tag{32}$$

$$6\Pi_{p,x} = \frac{\partial}{\partial y^*}\left(\eta^* \frac{\partial v_z^*}{\partial y^*}\right) = \frac{\partial}{\partial y^*}\left(\frac{1}{1 + C^m \left[\left(\frac{\partial v_x^*}{\partial y^*}\right)^2 + \left(\frac{\partial v_z^*}{\partial y^*}\right)^2\right]^{\frac{m}{2}}} \frac{\partial v_z^*}{\partial y^*}\right) \ , \tag{33}$$

With:

$$\Pi_{p,x} = \frac{h^2}{6\eta_0 v_{b,z}} \frac{\partial p}{\partial x} \ , \tag{34}$$

$$\Pi_{p,z} = \frac{h^2}{6\eta_0 v_{b,z}} \frac{\partial p}{\partial z} \ , \tag{35}$$

Being the dimensionless cross- and down-channel pressure gradients, respectively. The dimensional down-channel pressure gradient $\partial p/\partial z$ was defined as:

$$\frac{\partial p}{\partial z} = \frac{\Delta p}{L} = \frac{p_{die} - p_{sys}}{L} \tag{36}$$

The boundary conditions and the requirement of zero net cross-channel flow were made dimensionless in a similar manner:

$$v_x^*(y^* = 0) = 0 \ , \tag{37}$$

$$v_x^*(y^* = 1) = \frac{v_{b,x}}{v_{b,z}} = tan(\phi_b) = \frac{t}{D_b \pi} \ , \tag{38}$$

$$v_z^*(y^* = 0) = 0 \ , \tag{39}$$

$$v_z^*(y^* = 1) = 1 \ , \tag{40}$$

$$Q_x^* = \int_0^1 v_x^*(y^*) dy^* = 0 \ . \tag{41}$$

Solving the dimensionless equations of motion gives the down- and cross-channel velocity profiles, from which the dimensionless flow rate could be obtained as:

$$Q_s^* = 2\int_0^1 v_z^*(y^*) dy^* \ , \tag{42}$$

With:

$$Q_s^* = \frac{2Q_s}{whv_{b,z}} \ . \tag{43}$$

It can be seen that the equations are influenced by four independent dimensionless parameters:

- The dimensionless down-channel pressure gradient $\Pi_{p,z}$, which depends on the system pressure p_{sys} and on the nozzle geometry;
- The flow parameters C and m, obtainable via rheometry;
- The screw-pitch ratio t/D_b, which is a characteristic feature of the device in use.

2.3.1.2 Nozzle

The polymer melt pushed out of the screw channel flows subsequently into and through the nozzle. Flow through the nozzle takes place because the pressure at the nozzle inlet is higher than the pressure at the outlet [28]. The nozzle-inlet pressure was generated by both the system pressure and the action of the screw, as a result of the restriction to the flow represented by the nozzle itself [61].

To derive the velocity profile in the nozzle, the flow was assumed to be steady, fully developed and axis-symmetric. Considering the coordinate system in Figure 1D, we have $v_z = v_z(r)$, $v_r = v_\vartheta = 0$ and $p = p(z)$. It follows that the only non-zero components of the rate-of-deformation tensor and of the viscous stress were, respectively, the *zr*-component and τ_{zr}. The momentum equation along the *z* direction becomes [65]:

$$\frac{1}{r}\frac{\partial}{\partial r}(r\tau_{zr}) = \frac{\partial p}{\partial z} \tag{44}$$

Being $p = p(z)$ and $\tau_{zr} = \tau_{zr}(r)$, both sides of the equation must be constant. After integration, we obtained:

$$r\tau_{zr} = \frac{\partial p}{\partial z}\frac{r^2}{2} + c_1 \tag{45}$$

Considering the symmetry at $r = 0$, $\tau_{zr} = 0$ because the stress must be finite. Consequently, $c_1 = 0$. In addition, the pressure gradient $\partial p/\partial z$ must be a constant as *v* does not vary with *z*:

$$\frac{\partial p}{\partial z} = \frac{\Delta p}{L_n} = \frac{p_{atm} - p_n}{L_n} = -\frac{P_n}{L_n} \tag{46}$$

For a Cross fluid:

$$\tau_{zr} = -\frac{\eta_0|\dot{\gamma}|}{1 + (\lambda|\dot{\gamma}|)^m} \tag{47}$$

With:

$$|\dot{\gamma}| = \left[\left(\frac{\partial v_z}{\partial r}\right)^2\right]^{\frac{1}{2}} \tag{48}$$

Substituting this relationship in the momentum equation led to:

$$\lambda^m p_n r|\dot{\gamma}|^m - 2L\eta_0|\dot{\gamma}| + p_n r = 0 \tag{49}$$

Solved Equation 49 for the velocity profile $\partial v_z/\partial r$, the flow rate through the nozzle can be evaluated from:

$$Q_d = 2\pi\int_0^R v_z r dr \tag{50}$$

The evaluation of the flow rate through the nozzle was more straightforward than in the case of the screw channel, which renders the non-dimensionalization of the nozzle equations not needed. However, the flow rate in the nozzle must be compared with that in the screw channel. For this reason, the flow rate only was expressed in non-dimensional form, according to the following definition:

$$Q_d^* = \frac{2Q_d}{whv_{b,z}} \tag{51}$$

For comparison purposes, the same scale used to non-dimensionalize Q_s was applied.

2.3.1.3 Numerical solution

The momentum equations describing the flow in the screw channel and through the nozzle were coupled via the unknown pressure at the nozzle entrance. To solve either, this value must be obtained. As the flow rate in the screw channel and through the nozzle must be equal for the conservation of mass, the value of p_n was iteratively varied until the two calculated flow rates match. This value of p_n is usually referred to as operating point [66]. The iterative variation of p_n until the two flow rates match was carried out by using the Secant method [67], which uses a succession of roots of secant lines to better approximate the root of the equation to be solved. At every iteration, the corresponding value of p_n was used to evaluate the flow rate in the screw channel and through the nozzle, according to the sections below. The cycle stops when the difference between Q^*_s and Q^*_d, for the specific p_n, is lower than 10^{-10}. The numerical calculations were carried out in Matlab R2020b.

2.3.1.3.1 Screw

The velocity profile in the screw channel was calculated via the shooting method, which transforms a boundary value problem (BVP) into an initial value problem (IVP) [68]. Therefore, the momentum equations must be rearranged to obtain an explicit formulation with respect to the velocity gradients. To this end, the equations were first integrated over the dimensionless channel height, giving:

$$6\Pi_{p,z}y^* + C_1 = \eta^* \frac{\partial v_z}{\partial y^*} \tag{52}$$

$$6\Pi_{p,x}y^* + C_2 = \eta^* \frac{\partial v_x}{\partial y^*} \tag{53}$$

The two integrated equations were then squared and added:

$$\eta^{*2}\left[\left(\frac{\partial v_z}{\partial y^*}\right)^2 + \left(\frac{\partial v_x}{\partial y^*}\right)^2\right] = \left(6\Pi_{p,z}y^* + C_1\right)^2 + \left(6\Pi_{p,x}y^* + C_2\right)^2 \tag{54}$$

The term between square brackets was expressed as function of the dimensionless viscosity from the Cross-model formula:

$$\left[\left(\frac{\partial v_z}{\partial y^*}\right)^2 + \left(\frac{\partial v_x}{\partial y^*}\right)^2\right] = \frac{1}{C^2}\left(\frac{1}{\eta^*} - 1\right)^{\frac{2}{m}} \tag{55}$$

And substituted back into the equation to obtain:

$$(\eta^*)^m - (\eta^*)^{m-1} + C^m\left[\left(6\Pi_{p,z}y^* + C_1\right)^2 + \left(6\Pi_{p,x}y^* + C_2\right)^2\right]^{\frac{m}{2}} = 0 \tag{56}$$

The value solving Equation 56 was used in Equations 52 and 53. These were rearranged to obtain the explicit forms for the down- and cross-channel velocity gradients:

$$\frac{\partial v_z}{\partial y^*} = \frac{1}{\eta^*}\left(6\Pi_{p,z}y^* + C_1\right) \tag{57}$$

$$\frac{\partial v_x}{\partial y^*} = \frac{1}{\eta^*}\left(6\Pi_{p,x}y^* + C_2\right) \tag{58}$$

Given the Cross coefficient *C*, the Cross exponent *m* and the screw down-channel pressure gradient $\Pi_{p,z}$ (having P_n been provided by the current iteration of the secant method), the integration constants C_1

and C_2 and the dimensionless cross-channel pressure gradient $\Pi_{p,x}$ were the unknowns to be determined. Following the shooting method, an initial guess was provided, derived from the Newtonian case:

$$C_1 = 1 - 3\Pi_{p,z} \tag{59}$$

$$C_2 = -2\,tan(\phi_b) = -2\frac{t}{D_b\pi} \tag{60}$$

$$\Pi_{p,x} = tan(\phi_b) = \frac{t}{D_b\pi} \tag{61}$$

Using these initial guesses, the velocity gradients were to be numerically integrated over the dimensionless channel height via the Simpson method, to obtain the dimensionless velocity profiles:

$$v_z(y^*) = v_z(y^* = 0) + \int_0^1 \frac{\partial v_z}{\partial y^*} dy^* \tag{62}$$

$$v_x(y^*) = v_x(y^* = 0) + \int_0^1 \frac{\partial v_x}{\partial y^*} dy^* \tag{63}$$

This was done by first obtaining the dimensionless viscosity value solving Equation56, which was numerically solved using the Secant method [67].
If the boundary conditions 37 to 41 were not satisfied, the down- and cross-channel velocities at the barrel and the cross-channel flow would assume values that would differ from the required ones of amounts defined as residuals. A Newton-Raphson scheme [62] was used to iteratively vary the unknown values (C_1, C_2 and $\Pi_{p,x}$). The scheme suggests new guesses for the next iteration based on the minimization of the residuals. At every iteration, the current unknown values were used to recompute the velocity profiles. Subsequently, the dimensionless volume flow rate Π_V was evaluated with the Simpson rule. The procedure was stopped when the change in value of the unknowns between two consecutive iterations led to a change in dimensionless volume flow rate $\Delta\Pi_V$ lower than 10^{-8}.

2.3.1.3.2 Nozzle

For a given p_n, the velocity profile to evaluate the flow rate through the nozzle was calculated with Equation 49. The equation was solved for v_z with the Secant method [67], and then the flow rate was derived according to Equation 51.

2.3.2 Extrudability

Lab-scale equipment is often unable to provide the necessary driving forces to extrude high molecular weight (M_w) polymers. The need for processing such grades arises from their superior mechanical properties in the solid state [12]. Therefore, it was paramount to derive a model able to predict whether a specific thermoplastic polymer can be processed with the equipment in use or not.
Following the pioneering derivation of Mallouk and McKelvey [69], where dZ is the power to drag the melt through the screw channel, for a length dz, against the backpressure originated in the nozzle entrance. The screw geometry and the modeling assumptions used in section 1.3.1.1.1 remain valid. The power dZ was defined as:

$$dZ = v_b dF \tag{64}$$

Where dF is the force to maintain the channel in motion at a velocity v_b. dF can be expressed as its down-channel component dF_z:

$$dF = \frac{dF_z}{cos\phi_b} = \frac{\tau_{yz}(y = h)dA}{cos\phi_b} \tag{65}$$

Here, τ_{yz} is the shear stress in the direction of dF_z, which acts on the area dA. This can be rewritten as:

$$dA = wdz = \pi D_b sin\phi_b dz \tag{66}$$

In addition, the down-channel length dz can be expressed in terms of the axial screw length $d\lambda$:

$$dz = \frac{d\lambda}{sin\phi_b} \tag{67}$$

Considering these equivalencies, dZ can now be rewritten as:

$$dZ = \frac{\pi^2 D_b^2 N \tau_{yz}(y = h)}{cos\phi_b} d\lambda \tag{68}$$

The total power required over the entire screw length can be obtained by integrating Equation 69:

$$Z = \frac{\pi^2 D_b^2 N}{cos\phi_b} \int_0^L \tau_{yz}(y = h) d\lambda = \frac{\pi^2 D_b^2 N L \tau_{yz}(y = h)}{cos\phi_b} \tag{69}$$

With τ_{yz} as defined in Equation 24 for a Cross fluid, which we repropose here for convenience:

$$\tau_{yz} = \frac{\eta_0}{1 + \lambda^m \left[\left(\frac{\partial v_x}{\partial y}\right)^2 + \left(\frac{\partial v_z}{\partial y}\right)^2\right]^{\frac{m}{2}}} \frac{\partial v_z}{\partial y} \tag{70}$$

With the modeling approach of the stationary screw and rotating barrel, the torque required to turn the latter is determined by the shear rate at the barrel surface. Therefore, the shear stress τ_{yz} must be evaluated at the barrel, i.e. at $y = h$. The unknowns to be determined are the shear rate in the down- and cross-channel directions, $\partial v_z/\partial y$ and $\partial v_x/\partial y$ respectively, calculated at $y = h$. For a flow rate $Q_s = Q_d$ obtained according to section 1.3.1.3, the shear rate $\partial v_z/\partial y$ at the barrel surface can be evaluated via Equation 57 for $y^* = 1$ $(y = h)$. In particular, $\Pi_{p,z}$ was calculated using the value of p_n equating Q_s and Q_d and C_1 is given by the last executed Newton-Raphson iteration. The obtained value can then be re-dimensionalized as follows:

$$\frac{\partial v_z}{\partial y}(y = h) = \frac{v_{b,z}}{h} \frac{\partial v_z^*}{\partial y^*}(y^* = 1) \tag{71}$$

The same procedure can be followed to evaluate $\partial v_x/\partial y$ from Equation 58, with $\Pi_{p,x}$ given by the Newton-Raphson method together with C_2. The same scale as for $\partial v_z/\partial y$ can be used to obtain the dimensional version of $\partial v_x/\partial y$. Eventually, the shear stress at the barrel surface can be calculated and the power requirement obtained. By comparing the obtained value with the capabilities of the device in use, it can be predicted whether a certain polymeric grade can be processed or not.

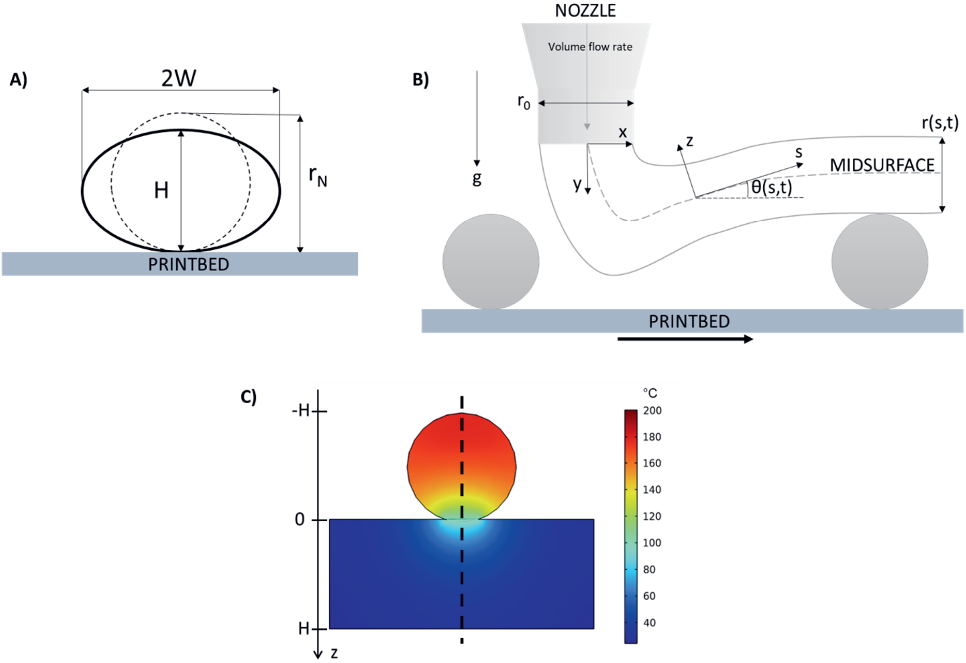

Figure 2. A) The process of filament spreading after deposition and during cooling. B) The geometrical configuration of a filament being deposited over a gap (bridging). C) Thermal distribution during the welding process.

2.3.3 Shape retention

Upon deposition, a filament spreads under the effect of an interplay between viscous forces and surface tension [70], while cooling and solidification take place. The ability of a deposited filament to preserve its cross-section, or to deform within a user-defined acceptable limit, can be considered as another prerequisite for manufacturing. Higher deformation not only might affect the quality of the final morphology, but also would increase the filament radius of curvature, reducing the perception of being in a 3D environment by the cells.

Crockett [71] derived a model to predict the radius of a filament deposited via slurry extrusion. Assuming a constant cross-sectional area (no shrinkage) and surface tension over the process, and deposition taking place on a smooth, hard and flat surface, Crockett derived the following formula:

$$\frac{dW}{dt} = \frac{A^2\gamma}{32\eta W^4} \tag{72}$$

Where W is half of the cross-sectional width, t is time, A is the cross-sectional area, γ the surface tension between the paste and the surrounding air and η is the paste viscosity. The model was derived under the assumption of negligible gravity, which is valid for length scales lower than the capillary limit Ca, defined as:

$$Ca = \left(\frac{\gamma}{\rho g}\right)^{\frac{1}{2}} \tag{73}$$

Where ρ is the material density and g the acceleration of gravity. The geometry of the filament deformation upon cooling is schematically represented in Figure 2A. In addition, constrained surface boundary conditions were adopted, according to which velocity was considered null at both the liquid-substrate and liquid-air interfaces. Therefore, the filament spreading was considered as a fluid flowing between two infinite parallel plates with a linear velocity profile. Such an approach was a mathematical workaround to describe more accurately the velocity gradients in the material compared to the other type of boundary condition, the free surface BC.

In the case of thermoplastic polymers, the flow responsible for spreading slows down as the material temperature decreases because of an increase in viscosity. For this reason, the above equation should be modified to take into account a temperature-dependent zero-shear viscosity $\eta_0 = \eta_0(T)$. In particular, the William-Lendel-Ferry (WLF) as employed, as described in Section 1.2. Again, the viscosity η_0 at a temperature T can be calculated according to:

$$\eta_0(T) = \eta_{0,ref}\, a_T \tag{74}$$

Where $\eta_{0,ref}$ is the zero-shear viscosity calculated at a reference temperature T_{ref}, and a_T is a shift-factor function defined as:

$$a_T(T) = exp\left(\frac{-c_1\left(T - T_{ref}\right)}{c_2 + T}\right) \tag{75}$$

With c_1 and c_2 fitting parameters. However, the calculation of the zero-shear viscosity at a certain temperature requires that temperature to be known. Therefore, Equations 74 and 75 must be coupled to a function of temperature over time. Li [72] developed a cooling model for filaments deposited via FDM, based on the lumped-capacity analysis. This method assumes that the temperature distribution over a cross-section is uniform, if the diameter of the extruded filament is sufficiently small. This assumption is considered reasonable for values of the Biot number lower than 0.1:

$$Bi = \frac{hV}{Ak} \tag{76}$$

Where *h* is the convection coefficient from the filament to the surrounding air, *V* and *A* are, respectively, the volume and the area of the sample filament element, and *k* is the thermal conductivity. Considering a freshly extruded filament with a circular cross-section and a length of 1 mm, the volume *V* and area *A* are, respectively, $0.134\ mm^3$ and $1.2975\ mm^2$. The convection coefficient h is estimated as $100\ W/m^2$ *°C* [72] while the thermal conductivity for the sample material of choice is measured as *0.2 W/m °C* (section 1.2). For these values, the Biot number is 0.05, making the lumped capacity assumption valid. Therefore, any potential temperature variation across the filament cross-section can be ignored and the cooling process can be modelled according to one-dimensional transient heat transfer analysis of Li. The governing equation is:

$$\frac{\partial T}{\partial t} = -\frac{hP}{\rho C_p A}(T - T_a) \tag{77}$$

With *P* the perimeter of the cross-section, C_p the heat capacity, *T* the temperature at a specific time *t*, and T_a the ambient temperature.

The numerical solution was coded in Matlab (ver. R2020b). First, it was verified whether the assumption of negligible gravity is applicable, by calculating the capillary limit *Ca*. A value of *2 mm* was obtained, well above the nozzle radius, which allows the model derived by Li to be adopted. Equations 72 and 77 were solved as a system of two coupled IVPs equations using the built-in Matlab (ver. R2020b) ode45 solver for non-stiff differential equations, which is based on an explicit Runge-Kutta formula [73]. The initial values were the nozzle radius $W(0) = r_N$ for Equation 72 and the nozzle temperature $T(t) = T_N$ for Equation 77. At every timestep, the temperature was evaluated and the correspondent shift factor calculated. Then, the viscosity at that temperature can be determined and the filament profile evolution can be obtained. It is important to note that, at every iteration, the filament perimeter P is recalculated as well, being it a function of the filament half-width W. The simulation stops at a user-defined condition based on the strain rate. For amorphous polymers, a single solidification point cannot be defined as flow takes place even at temperatures lower than the glass transition but at considerably lower rates. Therefore, the algorithm terminates the execution when a spreading strain rate as low as defined by the user is reached. At each timestep, this was defined as:

$$\dot{\epsilon} = \frac{2}{H}\frac{dW}{dt} \tag{78}$$

Where H is the final filament height, calculated as follows. At atmospheric pressure, the polymer can be considered incompressible and, therefore, the cross-sectional area is constant. Its value is equal to the nozzle cross-sectional area under the assumption of negligible nozzle swell. Consequently, the final filament height can be derived from:

$$H = \frac{2A}{\pi W} \tag{79}$$

It is important to note that the filament height corresponds to the actual layer height. Such information allows to set the proper printhead vertical displacement when proceeding to the deposition of the subsequent layer. If the distance between the nozzle and the previous layer (defined as “air gap”) is excessive, the freshly extruded material cools down before achieving intimate contact [74] with the latter, thus affecting the interlayer diffusion and weld quality as explained later.

2.3.4 Bridging

During scaffold (and, generally, intentionally-porous structures) manufacturing, filaments under deposition are often required to bridge the gap between two adjacent filaments belonging to the layer underneath. Whereas printhead translational speed and the viscosity of the extruded material (governed by cooling kinetics) are not adequately coupled, two opposite situations might potentially occur: fall of the material into the gap with resulting occlusion of the lateral pore or excessive stretching of the filament with consequences on interlayer welding and layer height. For this reason, a model able to predict the final bridge morphology could assist in properly adjusting the printing parameters for a given polymer grade so that to avoid sagging and guarantee proper lateral porosity.

Ribe [75] described the dynamics of a thin stream of viscous fluid falling from an orifice onto a surface. The fluid has constant viscosity η, buoyancy ρg, and surface tension coefficient γ, and is extruded downward at speed U_N from a nozzle of radius a_N towards a rigid plate at distance H. The filament’s radius is $a(s,t)$, where s is the arclength along the filament’s midsurface and t is time. The Cartesian coordinate of a point on the midsurface is indicated by the vector $\mathbf{r}(s,t)$ while $\mathbf{s}\equiv\partial\mathbf{r}/\partial s$ is a unit vector parallel to the midsurface. $\mathbf{z}$ is the unit vector normal to $\mathbf{s}$, $\vartheta(s,t)$ is the inclination of the midsurface from the horizontal, and $K(s,t)\equiv\partial\vartheta/\partial s$ is the midsurface curvature.

The equations governing the dynamics of the filament, involve the following variables, which describe the response of a fluid element to applied loads:

- $U(s,t)$ and $W(s,t)$ are, respectively, the tangential and normal component of the midsurface velocity
- The force $N(s,t)$ acting on a cross-section of the filament. This force can be divided into its shear and normal components $N_1(s,t)$ and $N_3(s,t)$, respectively.
- The vector $M(s,t)$ is the moment associated with twisting.
- The local rate of rotation $\omega(s,t)$ of the midsurface.

Assuming negligible inertia, the non-dimensional mechanical equations are:

$$U' = \frac{N_3}{3\eta\pi a^2} + KW + \frac{SH}{3\eta a a_N} \tag{80}$$

$$N_1' = -KN_3 + B\pi a^2 cos\theta - \frac{2\pi SaKH}{a_N} \tag{81}$$

$$N_3' = KN_1 + B\pi a^2 sin\theta - \frac{2\pi SHa'}{a_N} \tag{82}$$

$$M' = -\frac{1}{\epsilon^2}N_1 + \frac{1}{4}B\pi a^4 K sin\theta - \frac{S\pi a^2 K r'}{\epsilon} \tag{83}$$

$$W' = \omega - KU \tag{84}$$

$$\omega' = \frac{4M}{3\pi a^4 \eta} \tag{85}$$

Where the prime denotes *∂/∂s* and dependence on *s* and *t* is omitted for simplicity. *S*, *B* and *ε* are, respectively, the inverse capillary and the buoyancy numbers, and the slenderness parameter. These are defined as:

$$S = \frac{\gamma}{U_N \eta_0} \tag{86}$$

$$B = \frac{\rho g h^2}{\eta_0 U_N} \tag{87}$$

$$\epsilon = \frac{a_N}{h} \tag{88}$$

The dimensionless kinematic equations governing changes in the filament’s gemeotry are:

$$\frac{Ds}{Dt} = 1 + \int_0^s \Delta ds \tag{89}$$

$$\frac{Dx}{Dt} = Ucos\theta - Wsin\theta \tag{90}$$

$$\frac{Dy}{Dt} = Usin\theta + Wcos\theta \tag{91}$$

$$\frac{DA}{Dt} = -A\Delta \tag{92}$$

Where *D/Dt* is a convective derivative used in Lagrangian descriptions, which follows the motion of material points on the filament’s midsfurface [76]. The convective derivative is defined as:

$$\frac{D}{Dt} \equiv \left(U_N + \int_0^s \Delta ds \right) \frac{\partial}{\partial s} \tag{93}$$

Here, *Δ* is the rate of stretching that is calculated as:

$$\Delta = \frac{\partial U}{\partial s} - KW \tag{94}$$

And *A* is the cross-sectional area calculated as πr^2.

These equations had been made non-dimensional by using the following relations between dimensionless and dimensional variables:

$$U = \frac{\hat{U}}{U_N} \tag{95}$$

$$N_1 = \frac{H}{r_0^2 \eta_0 U_0} \widehat{N_1} \tag{96}$$

$$N_3 = \frac{H}{r_0^2 \eta_0 U_0} \widehat{N_3} \tag{97}$$

$$M = \frac{H^2}{r_0^4 \eta_0 U_N} \widehat{M} \tag{98}$$

$$W = \frac{\widehat{W}}{U_N} \tag{99}$$

$$\omega = \frac{H}{U_N} \widehat{\omega} \tag{100}$$

$$t = \frac{U_N}{H} \hat{t} \tag{101}$$

The problem studied by Ribe can be readapted to describe the deposition of a filament over a gap, following some adjustments. The process is visually described in Figure 2B. First, it is assumed that the nozzle is vertically located at a distance equal to its diameter from the previous layer, leading to $H = 2a_N$. In addition, the viscosity η of a specific fluid element is a function of time according to Equations 74 and 75 such that $\eta = \eta(s,t)$. Eventually, the right end of the filament is considered anchored to the layer underneath, which moves horizontally together with the base plate at a speed U_b.

The latter adjustment reflects on the boundary conditions of the system, which must be appropriately modified. At both ends, the filament is "clamped", meaning that its rotation rate and its velocity (in relation to that imposed at each end) must be zero. For the end where new material is continuously extruded, this translates into the following dimensional BCs:

$$\widehat{U}(0,t) = U_N, \widehat{W}(0,t) = 0, \widehat{\omega}(0,t) = 0 \tag{102}$$

Where U_N is the extrusion velocity, which can be obtained via Equation 49, and the hat indicates dimensional variables. At the end anchored on a filament from the previous layer, the dimensional BCs are:

$$\widehat{U}\big(L(t)\big) = U_b, \widehat{W}\big(L(t)\big) = 0, \widehat{\omega}\big(L(t)\big) = 0 \tag{103}$$

Where U_b is the speed of the printing bed, which here is assumed to be moving (instead of the printhead) for ease of modelling. Both sets of BCs are made dimensionless by scaling the velocities with U_N, leading to:

$$U(0,t) = 1, W(0,t) = 0, \omega(0,t) = 0 \tag{104}$$

$$U\big(L(t)\big) = \frac{U_b}{U_N}, W\big(L(t)\big) = 0, \omega\big(L(t)\big) = 0 \tag{105}$$

Additionally, the mechanics described by Ribe must be coupled with the polymer cooling kinetics after extrusion to include a temperature-dependent viscosity η. The model in Equation 77 still stands valid but, assuming a constantly circular cross-section, it can be rewritten as:

$$\frac{\partial T}{\partial t} = -\frac{2h}{\rho C_p a}(T - T_a) \tag{106}$$

Where the explicit dependence to the filament perimeter *P* and cross-sectional area *A* has been removed thanks to the aforementioned simplification. However, this equation must be non-dimensionalized as well, by scaling temperature, time and radius as follows:

$$T = \frac{\hat{T} - T_a}{T_N - T_a} \tag{107}$$

$$t = \frac{U_N}{H}\hat{t} \tag{108}$$

$$a = \frac{\hat{a}}{a_0} \tag{109}$$

By removing dimensions from Equation 106 by means of relations 107, 108, 109, the dimensionless equation for the temperature evolution of a fluid element can be obtained:

$$\frac{DT}{Dt} = -\beta\frac{T}{a} \tag{110}$$

With:

$$\beta = \frac{2hH}{\rho C_p a_0 U_N} \tag{111}$$

In summary, the bridging problem can be described via the mechanical Equations 80 - 85, the kinematic Equations 89 - 92 and 110, and the BCs 104 and 105.

The numerical solution is coded in Matlab (ver. R2020b), using a Lagrangian formulation that follows the motion of the fluid element in question. The simulation starts from a short horizontal proto-filament of length *π/2* [77], with the midsurface having the typical quarter-cycle form imposed by the deposition onto the moving platform. This is explicated by imposing the following geometrical conditions:

$$x = \frac{1}{2}\left(1 - cos\left(\frac{\pi}{2}\frac{s}{\alpha}\right)\right) \tag{112}$$

$$y = \frac{1}{2}\left(-sin\left(\frac{\pi}{2}\frac{s}{\alpha}\right)\right) \tag{113}$$

At these small times, $\vartheta = s - \pi/2$ and $K = 1$, and the filament radius and temperature are assumed to be equal to nozzle values. Therefore, the governing Equations 80 - 85 simplify to:

$$U' = \frac{N_3}{3\pi} + W \tag{114}$$

$$N_1' = -N_3 + B\pi\, cos\left(s - \frac{\pi}{2}\right) \tag{115}$$

$$N_3' = N_1 + B\pi\, sin\left(s - \frac{\pi}{2}\right) \tag{116}$$

$$M' = -\frac{N_1}{\epsilon^2} + \frac{1}{4} B\pi \sin\left(s - \frac{\pi}{2}\right) \tag{117}$$

$$W' = \omega - U \tag{118}$$

This small-times version of the mechanical equations was solved with the Matlab built-in solver for BVPs bvp4c. From this initial solution, the numerical time stepping was started and each cycle consisted of two parts. First, for a filament with a specified geometry, Equations 80 - 85 were solved as a sixth-order two-point BVP for the instantaneous flow within the filament, with the (second-order accurate) relaxation algorithm of Press et al. [67]. The geometry was then advanced in time by solving the kinematic Equations 89 - 92 and 110 with a second-order Runge-Kutta midpoint method. Eventually, a new material grid point was added at the nozzle and the time stepping could enter a new cycle. The simulation was stopped at the reach of a desired horizontal distance (simulating a gap to be bridged) between the right end of the filament and the nozzle. The conservation of mass was monitored and two independent calculations of the filament's total length were compared to evaluate the accuracy of the time-stepping algorithm [78].

2.4 MECHANICAL DESCRIPTION

As previously mentioned, higher deposition temperatures favor the bonding between subsequent layers (referred to as "weld"), but at the expenses of morphological accuracy. Being the latter the most immediate feedback about manufacturing quality, an interlayer-bonding model could assist in predicting how the deposition temperature of choice is going to affect the final mechanical properties. McIlroy and Olmsted [79] recently derived a system, based on molecular dynamics, to quantify the quality of the welding region between two layers. In particular, they focused on the thickness and the fracture toughness of the weld at the end of the deposition and cooling processes. Therefore, they based their model on the thermal history of the weld itself. Considering the relatively small length scales, the lumped capacity analysis cannot be applied, and a more detailed temperature profile must be obtained. This can be done via the one-dimensional heat equation through the weld cross-section:

$$\frac{dT}{dt} = \frac{k}{\rho C_p} \frac{\partial^2 T}{\partial z^2} \tag{119}$$

Where *z* indicates the coordinate along the axis across the two layers, falling in the interval *[-h, h]*, where *z = 0* is the interlayer contact point, *z = -h* is the base of the bottom layer and *z = h* is the top of the freshly-extruded filament. The coordinate system is described in Figure 2C. The equation can be solved coupling it to the boundary conditions at the fluid-air interfaces:

$$T(t, z = \pm h) = T_a \tag{120}$$

And the initial value for the temperature profile:

$$T(t = 0, z) = \begin{cases} T_N, z > 0 \\ T_a, z < 0 \end{cases} \tag{121}$$

The weld thickness originates from polymer chains diffusing from one filament to the other up to a certain interpenetration distance χ, which can be calculated from:

$$\frac{\chi}{R_g} = \left(36 \int_{t_w}^{t_g^W} \frac{1}{\tau_d\big(T(t)\big)} dt' \right)^{\frac{1}{4}} \tag{122}$$

Where R_g is the polymer radius of gyration (~ 10 nm), t_w is the time of deposition of the top filament and start of the welding process, t_g^W the time for the weld to reach the glass transition temperature T_g from deposition, τ_d the polymer reptation time, T is the temperature and $\dot{\gamma}$ is the shear rate. According to Wool [80], diffusion of the order of R_g is necessary to achieve bulk strength.

The reptation time τ_d is a function of temperature and follows the WLF model (Equation 75) according to:

$$\tau_d(T) = \tau_d^{ref} a_T \tag{123}$$

Where τ_d^{ref} is the reptation time at a reference temperature T_{ref}. The reference reptation time can be calculated via:

$$\tau_d^{ref} = 3\tau_e^{ref} Z_{eq}^3 \tag{124}$$

Being τ_e^{ref} the Rouse time of one entanglement segment and Z_{eq} the entanglement number of the melt at equilibrium. τ_e^{ref} was obtained according to Section 1.2. The entanglement number is instead defined as:

$$Z_{eq} = \frac{M_w}{M_e} \tag{125}$$

With M_w and M_e the molecular weight of the polymer and between entanglements, respectively. M_w is obtained experimentally from GPC measurements as described in section 1.2, while M_e is taken from literature (4.2 kg/mol) [81].

As mentioned, the quality of the weld can be described also by its fracture toughness G_c^w [82], [83], but in relation to the bulk fracture toughness G_c. G_c and G_c^w depend, respectively, on the bulk molecular weight between entanglements M_e and on the molecular weight between entanglements at the weld M_e^w according to:

$$G_c \sim \left(1 - \frac{M_e}{qM_w}\right)^2 \tag{126}$$

$$G_c^w \sim \left(1 - \frac{M_e^w}{qM_w}\right)^2 \tag{127}$$

With $q = 0.6$ [82] and M_e^w that can be calculated as:

$$M_e^w = \frac{M_e}{\nu_w} \tag{128}$$

Here, ν_w is the weld entanglement fraction defined as follows:

$$\nu_w = 1 - \left(1 - \nu_{dep}\right) exp\left(-\int_{t_w}^{t_g^w} \frac{1}{\tau_d\big(T(t)\big)} dt\right) \tag{129}$$

Where ν_{dep} is the entanglement fraction at the weld site after deposition, which depends on the shear rate during extrusion [84]. Considering the high shear rates due to the small-scale nozzles for scaffold fabrication, the melt was assumed to be nearly fully disentangled.

The temperature profile at the weld was obtained by solving Equation 119 in Matlab (ver. R2020b) with the pdepe solver for 1-D parabolic and elliptic partial derivative equations (PDEs) with one spatial variable and time. The solution was calculated by including the boundary conditions of Equation 120 and the initial condition expressed with Equation 121. The temperature dependence of the reptation time (Equation 123) could then be evaluated and used to estimate the interpenetration distance via Equation 122 and the weld entanglement fraction via Equation 129. The value of v_w was used to calculate the molecular weight between entanglements at the weld (Equation 128) to eventually obtain the weld fracture toughness via Equation 127. Whereas either of the ratio χ/R_g, v_w or the ratio G_c^w/G_c was below one, bulk strength of the weld could not be considered achieved and thermal management of the process should be redesigned.

2.5 SIMULATION RESULTS

2.5.1 Flow analysis

As it can be seen in Figure 3A-C, increasing the extrusion temperature expectedly increased the throughput at a given applied pressure, and this effect was even greater for the highest pressure value (0.861 bar). In addition, pressure did not influence the mass flow rate at the lowest extrusion temperature (180 °C) much (Figure 3C), while it increased its effect for increasing temperatures. These considerations appear particularly evident in Figure 3D,E, where the results are grouped by the applied pressure.

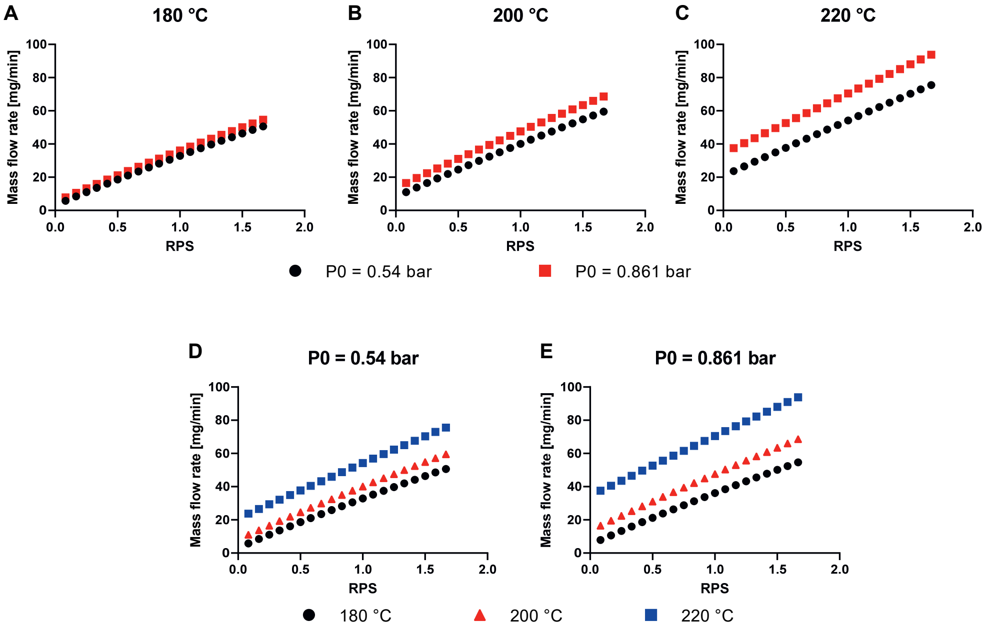

Figure 3. Mass flow rate as a function of screw speed. Top row: for each simulated extrusion temperature ((A) 180 °C, (B) 200 °C, (C) 220 °C), the results of two applied pressure values are compared. Bottom row: mass flow rate data from different extrusion temperatures are grouped by applied pressure ((D) 0.54 bar and (E) 0.861 bar).

2.5.2 Power

Interestingly, at a given temperature, the power requirement for extrusion did not depend on pressure, as shown in Figure 4A-C for each extrusion temperature. This can be appreciated even further in Figure 4D,E, where data are grouped by the applied pressure. In particular, it can be noted how the curves for a specific temperature matched over the different applied pressures. Instead, variations in temperature greatly affected the power need, with a drop of 102 % and 145 % due to the increase in the extrusion temperature from 180 °C to, respectively, 200 °C and 220 °C.

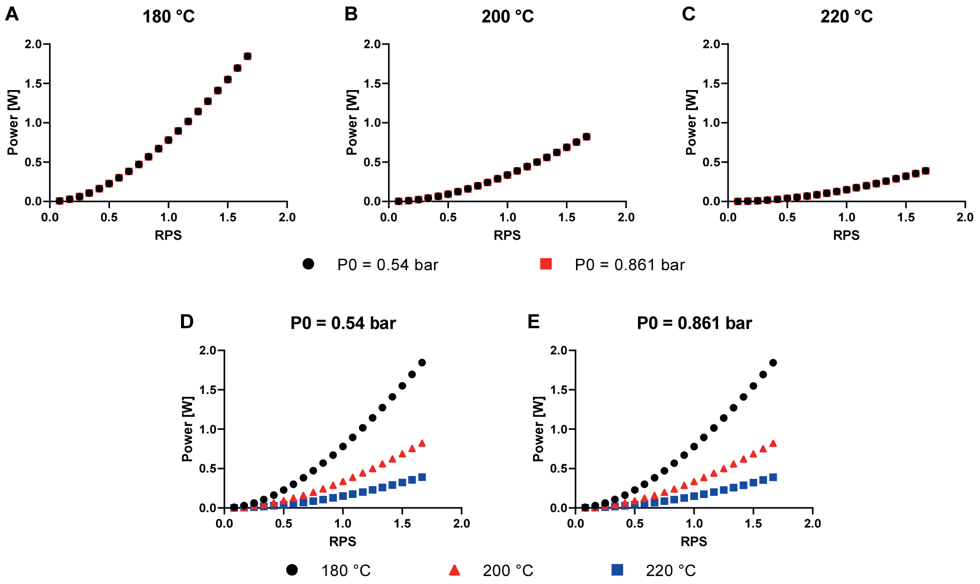

Figure 4. Power consumption as a function of screw speed. Top row: for each simulated extrusion temperature ((A) 180 °C, (B) 200 °C, (C) 220 °C), the results of two applied pressure values are compared. Bottom row: power consumption data from different extrusion temperatures are grouped by applied pressure ((D) 0.54 bar and (E) 0.861 bar).

2.5.3 Shape retention

As shown in Figure 5A,B, the spreading process mainly took place within 0.4 s, after which the trends for the filament width and diameter reached a plateau. Beyond this time, the shear rate values for filament spreading were below 0.005 s^{-1} for all the extrusion temperatures. Due to the difficulty of defining a single solidification point for amorphous polymers, Crocket [71] indicated this value as a reasonable choice, meaning that at later times the filament width would drop below 5 % strain over 10 s. In addition, the filament width upon cooling expectedly increased as a function of extrusion temperature, with a more marked rise between 200 and 220 °C than between 180 and 200 °C. As a direct consequence, the final actual layer height decreased following the same trend. The filament cross-section after the reach of the T_g can be seen in Figure 5C, for all the extrusion temperatures simulated. Here, the filament bulging can be appreciated, showing a more ellipsoidal shape for increasing extrusion temperatures.

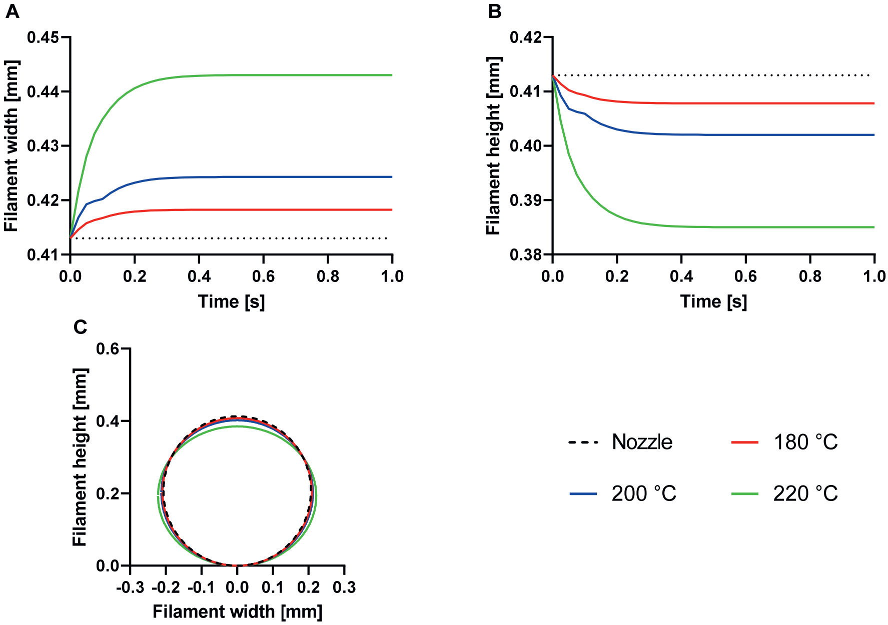

Figure 5. Filament cross-section evolution upon deposition. (A) Filament width and (B) filament height over time. (C) Filament cross-section at the reach of the glass transition temperature. The dotted lines represent the nozzle dimensions.

2.5.4 Bridging

In Figure 6A, the filament profile during extrusion at 180, 200 or 220 °C, with a stage velocity matching the extrusion, can be seen. The difference in filament shape was marginal, as further confirmed by the maximum vertical displacement (sagging) depicted in Figure 6B. Here, it can be noted how the sagging increased with extrusion temperature, yet of 8 µm at the most between 180 and 220 °C. In addition, the filament deflected downward sufficiently to hypothetically reach the printing platform, as shown by Figure 6A and quantified in Figure 6B. Interestingly, the temperature increase caused a decrease in diameter of the portion of the filament welded at the contact site with the previous layer (Figure 6C). The reduction between the two extremes extrusion temperatures was of around 8 µm, but with respect to the nozzle diameter was roughly 100 µm.

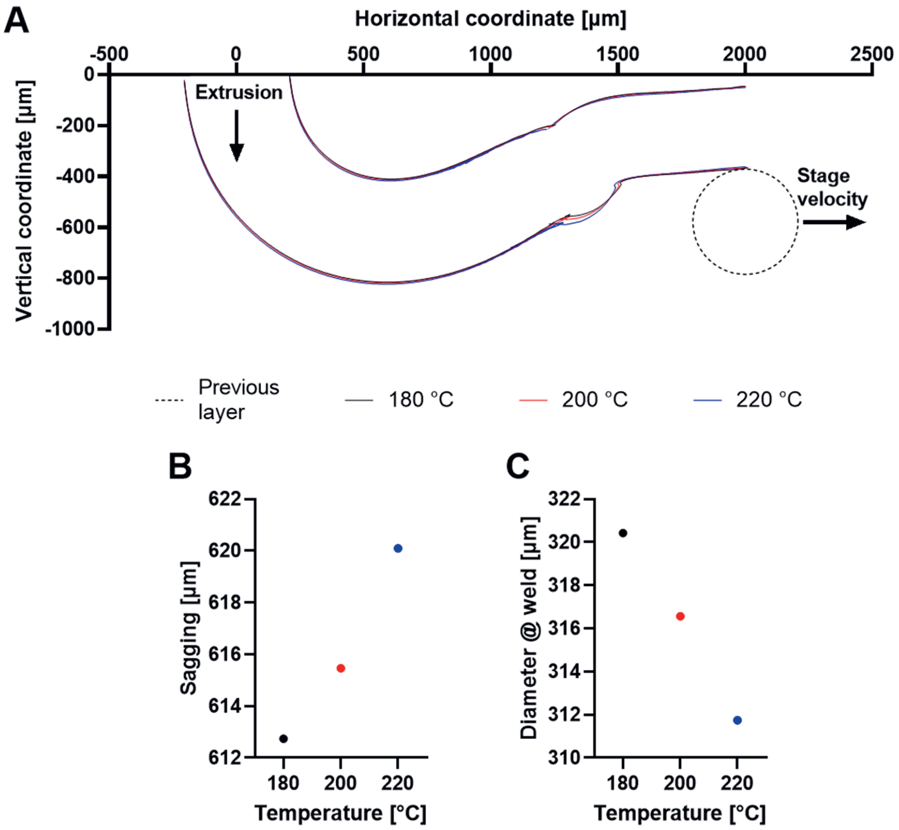

Figure 6. Dynamics of bridging a 2 mm-wide lateral pore with stage velocity equal to the extrusion one, at different temperatures. (A). (B) Maximum vertical displacement of the extruded filament's centerline at different temperatures, with respect to the horizontal. (C) Filament diameter at the weld with the previous layer at the end of the simulation.

2.5.5 Mechanics

Figure 7A shows that the welding process must take place within 0.34 and 0.41 s from deposition. In this time window, the molecules of the material extruded at 180 °C could not diffuse of a distance greater than their radius of gyration (Figure 7B), which is one of the criteria to reach bulk strength at the weld [79]. Instead, extrusion at the two other higher temperatures allowed for sufficiently long mobility to reach interpenetration distance values greater than R_g. Notably, as can be seen in Figure 7C, all the deposition temperatures simulated here were not high enough to allow for the entanglement fraction to recover to equilibrium values within the solidification time, being well below the threshold of 1 for bulk strength. This was further confirmed by the estimated values for the fracture toughness, all below bulk values as shown in Figure 7D.

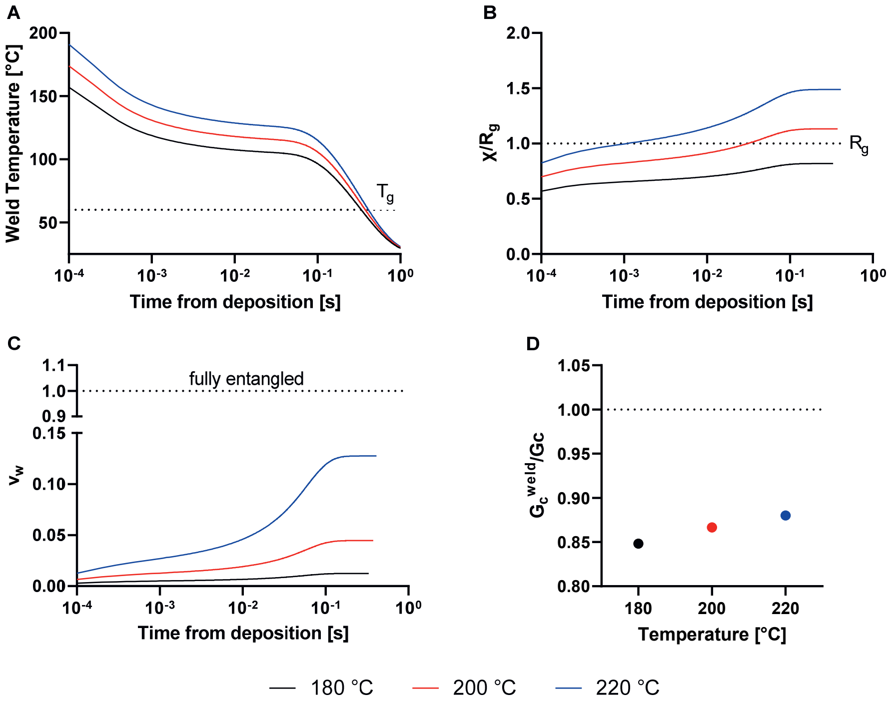

Figure 7. Dynamics of weld formation upon extrusion at different temperatures. (A) Temperature trend of the weld site after deposition. The dotted line represents the glass transition temperature T_g (60 °C). (B) Interpenetration distance over time after deposition. The dotted line is the limit for considering bulk strength achieved ($\chi/R_g = 1$). (C) Entanglement fraction over time after deposition. The limit for considering bulk strength achieved is indicated by the dotted line ($v = 1$). (D) Fracture toughness at the weld G_c^{weld} normalized by the equilibrium fracture toughness G_c, at the different extrusion temperatures. The dotted line at G_c^{weld}/G_c is the limit for the achievement of bulk strength.

2.6 DISCUSSION

The mathematical models here developed intended to describe what we identified as the main phases of the overall scaffold manufacturing process, from the actual scaffold deposition (flow rate and power requirement) to its final morphology (filament width, layer height and bridging of lateral pores) and mechanics. The description is based on the chosen manufacturing device, material and parameters, to provide the user with an estimation of the results of such combination. The goals were to gain fundamental know-how on polymer processing and to support researchers in the decision-making process for the manufacturing parameters, when processing new materials, testing new equipment or simply optimizing the results, by providing a time and computationally light assistant. As a proof-of-concept, the model was created for amorphous materials so that crystallization effects, hence heavy shrinkage upon cooling could be omitted. Nevertheless, particular focus was put on accurately modelling the polymer flow out of the printer, which is the driving factor in determining the final scaffold morphology. In TERM small-scale equipment, the shear-rate dependent behavior of thermoplastic polymers might indeed affect the throughput in a way that conventional Newtonian models cannot grasp. On the other hand, polymers are often processed at low screw RPS because of the limited driving forces available in such equipment [12]. This might shift the applied shear-rates towards the transition region, making the power-law flow model insufficient. An example is given by the specific model polymer of choice (6302D), which exhibits viscosity values right in the transition region at shear-rates typical of ME-AM [48]. For these reasons, we included the Cross-viscosity formulation (the first ones to our knowledge) to account for either of these situations, providing ME-AM users with a thorough model to estimate the throughput of their devices. As previously mentioned, the knowledge of the flow rate is needed to define the proper printhead translational speed but also to evaluate the feasibility of pore bridging. From our simulations, the throughput interestingly increases monotonically with both pressure and screw speed, unlike industrial extruders where the presence of a backpressure might cause a reduction in flow rate [28]. In such devices, a very large pressure drop might originate at very high RPS, causing material to flow backward and reducing the throughput. However, there is usually no pressure applied at the entrance of screw as the latter is applied sufficient torque to be able move the melt forward. In small scale equipment for TERM, pressure application is needed because of the limited specifications of the components. In addition, the amount of polymer melt moved along the screw channel is lower. These two facts together might determine the absence of a backdrop pressure and the consequent reduction in throughput. Further analysis of the results shows that temperature has a greater effect in increasing the mass flow rate compared to pressure, indicating that the viscosity of this material (rheological manifestation of its M_w) is too high for the pressure applicable by the system. However, potential thermal degradation must be taken into account, being the kinetics faster at higher temperatures. The polymer residence time inside the printhead could be calculated by summing the times to travel through the screw channel and the nozzle. These can be obtained by dividing their respective lengths by the melt velocity in each specific section. Data about the residence time could be coupled to rheological isothermal measurements to estimate any potential drop in molecular weight and define a safe processing window. Alternatively, extrusion could be carried out at lower temperatures, as long as the power requirements are within the range of the device. The same applies whereas the production speed is to be increased, being the power demands heavily dependent on the screw RPS. Instead, the influence of pressure is very limited, which is once again related to the relatively high viscosity of this specific grade. Being high M_w polymers favorable in terms of mechanical performances in the solid state, these analyses are of extreme importance when evaluating the adoption of new materials for scaffolds for load-bearing tissues.

Concerning the cross-sectional evolution, the small scale of scaffolds filaments leads to a relatively high cooling rate, which limits the deformation to a few tenth micrometers. As expected, the final filament width and height, respectively, increases and reduces as a function of extrusion temperature. This is because the filament takes longer to reach the glass transition temperature and molecular diffusion to slow down to scales lower than the phenomenon in object. However, the filaments small scale itself makes necessary the deposition of several layers to reach structures of biologically-relevant dimensions. For this reason, even a small discrepancy between imposed and actual layer height would accumulate over the scaffold height, leading to the production of constructs lower than planned. This is due to the fact that the actual layers would be thinner than those the slicing software employed to horizontally slice the CAD model. Another direct consequence of this is the increasing air gap (room between the nozzle and the previous layer) along the z-direction. This would cause the start of the cooling process to take place before the freshly extruded filament is deposited onto the previous layer, reducing the time window for diffusion at the welding point. Considering the already narrow margin for contact formation, such a situation not only is not advisable, but would also create a vertical gradient in mechanics that would result in the failure of the implant. Therefore, the importance of proper parameters selection emerges also in such an underrated effect of polymer melt deposition.

The above final consideration applies in particular to the bridging process. The results shown are relative to a stage speed (or printhead speed, depending on the machine type) equal to the extrusion one. This is the condition suggested by Khalil et al. [85] to obtain filaments with a diameter equal to the nozzle. The authors recommended such a procedure to favor faster planning of the manufacturing process together with more straightforward slicing, since no mismatches between actual and designed layer height would be present (avoiding the aforementioned potential consequences). However, we showed that bridging a 2 mm-wide pore would cause the filament to sag heavily. This not only would lead to occlusion of the pore but also to excessive stretching of the filament itself, resulting in an important decrease in diameter at the weld site. Knowing that cooling is rather fast, the decrease in diameter cannot happen in the later stages of bridging, when the material at the weld site is already below T_g and deformation takes place at rates well-above those of the phenomena in object. Instead, stretching must be caused already during the very first phases of extrusion and sagging, when the material is still well-above T_g. In that state, the polymer is still deformable by even limited stresses such as those originated by its own weight. Sagging can be counterbalanced by faster cooling, higher material viscosity or greater stretching by increasing the stage speed. However, each strategy has its own drawbacks: higher cooling rates might affect welding and mechanics; using more viscous materials require equipment able to process them; greater stretching would further reduce the filament diameter, with same consequences described for excessive filament spreading upon cooling. Independently on the chosen strategy, at least one more manufacturing parameter would have to be adjusted as well, entering in the aforementioned optimization loop. Therefore, the importance of the developed model can be easily understood, which allows to predict the effects of the chosen processing parameters in advance, without wasting material and economic resources.

Furthermore, the importance of proper temperature management emerged even more importantly when analyzing what happens at the weld between two layers. Scaffold manufacturing in a non-heated environment led to cooling kinetics that impact the weld properties in particular upon extrusion at 180 °C. While deposition at all simulated temperatures caused an entanglement recovery well below the threshold for bulk strength, polymer molecules do not diffuse sufficiently only for processing at 180 °C. Together with the rapid cooling freezing molecular motion, the relatively high M_w of the polymer in object further hinders diffusion. In fact, according to Equation 122, the interpenetration distance is a function of the reptation time and this scales with M_w as $\tau_d^0 \sim M_w^{3,4}$ [86], which reduces the diffusion depth upon cooling. Considering that according to McIlroy et al. [79] bulk strength is reached if both χ/R_g and ν_w are greater than one, improper thermal management might have detrimental effects on porous structures such as scaffolds for TERM where the load-bearing points are in a limited amount. Usually, printers not strictly for biomedical purposes, feature a heated stage to promote crystallization [87]. This has the additional effect of favoring fusion between the layers, by slowing down material cooling, thus widening the time window for molecular diffusion and entanglement recovery. However, the presence of a heated stage creates a vertical gradient in temperature that might result into a corresponding development of weld mechanics [87]. Therefore, it appears clear how the developed model could assist researchers in properly managing the thermal history applied on the polymer to improve scaffold mechanics, in particular when this is processed via research-scale devices with limited features.

The above considerations altogether suggest how different scaffold features are intertwined via thermal management, a processing parameter often not taken into consideration in ME-AM for TERM. As a result, when one processing condition is changed to optimize a specific aspect, other scaffold's properties might be affected as well, thus starting the aforementioned trial-and-error loops. In the biomedical research framework, materials are either medical grades costing up to 5000 €/kg [23] or synthetized in-house and thus available in small amounts and long times. Therefore, any optimization process based on guesses represents a waste not only in terms of time, but mainly of material and economic resources. For these reasons, in this study we developed a model to assist ME-AM users by predicting scaffold morphology and mechanics starting from the chosen set of manufacturing parameters. The formulated equations require limited input, specifically thermal and rheological data of the material to be processed, and the physical specifications of the printer melt channel. While the latter are ready-to-use datasheet information, the former can be easily obtained by quick DSC and rheometry measurements. The simulation results showed that the morphological and mechanical development upon manufacturing can be thoroughly described, fully grasping their interdependence. Nevertheless, a few simplifications were made, by ignoring shrinkage upon cooling and modelling only amorphous polymers with no crystallization effects. The rationale behind this choice was to first obtain a solid modelling and computational structure, to which further phenomena can be added in a second time. Therefore, future studies should aim at expanding the model to provide a more thorough description of the ME-AM process, by including the effect of crystallization for semi-crystalline grades and of shrinkage upon cooling also for amorphous polymers.

2.7 CONCLUSIONS

This study presents the derivation of mathematical models to describe the process of manufacturing scaffolds with thermoplastic synthetic polymers via melt-based extrusion. Furthermore, we reported how the formulated equations fully describe the interdependence between morphological features and mechanical performance via the thermal history to which the material is subjected. Overall, we suggest that the developed model could be used as support when evaluating the printability of candidate materials, testing new devices or optimizing the current manufacturing protocol, by giving full insight on the resulting scaffold morphology and mechanics.

ACKNOWLEDGMENTS

Some of the materials were kindly provided by Corbion Purac Biomaterials (The Netherlands). This work was financed by Brightlands Material Center and by the Dutch Province of Limburg.

REFERENCES

[1] C. A. Van Blitterswijk and J. De Boer, *Tissue Engineering*. Elsevier, 2015. doi: 10.1016/C2013-0-00564-6.

[2] N. A. Kurniawan, “The ins and outs of engineering functional tissues and organs: evaluating the in-vitro and in-situ processes,” *Curr Opin Organ Transplant*, vol. 24, no. 5, pp. 590–597, Oct. 2019, doi: 10.1097/MOT.0000000000000690.

[3] A. Di Luca *et al.*, “Gradients in pore size enhance the osteogenic differentiation of human mesenchymal stromal cells in three-dimensional scaffolds,” *Sci Rep*, vol. 6, no. 1, p. 22898, Sep. 2016, doi: 10.1038/srep22898.

[4] S. S. Kim, M. Sun Park, O. Jeon, C. Yong Choi, and B. S. Kim, “Poly(lactide-co-glycolide)/hydroxyapatite composite scaffolds for bone tissue engineering,” *Biomaterials*, vol. 27, no. 8, pp. 1399–1409, Mar. 2006, doi: 10.1016/j.biomaterials.2005.08.016.

[5] Y. S. Nam, J. J. Yoon, and T. G. Park, “A novel fabrication method of macroporous biodegradable polymer scaffolds using gas foaming salt as a porogen additive,” *J Biomed Mater Res*, vol. 53, no. 1, pp. 1–7, Jan. 2000, doi: 10.1002/(SICI)1097-4636(2000)53:1<1::AID-JBM1>3.0.CO;2-R.

[6] C. M. Murphy, M. G. Haugh, and F. J. O’Brien, “The effect of mean pore size on cell attachment, proliferation and migration in collagen-glycosaminoglycan scaffolds for bone tissue engineering,” *Biomaterials*, vol. 31, no. 3, pp. 461–466, Jan. 2010, doi: 10.1016/j.biomaterials.2009.09.063.

[7] N. Sultana and M. Wang, “PHBV/PLLA-based composite scaffolds fabricated using an emulsion freezing/freeze-drying technique for bone tissue engineering: Surface modification and in vitro biological evaluation,” *Biofabrication*, vol. 4, no. 1, p. 015003, Mar. 2012, doi: 10.1088/1758-5082/4/1/015003.

[8] R. Akbarzadeh and A.-M. Yousefi, “Effects of processing parameters in thermally induced phase separation technique on porous architecture of scaffolds for bone tissue engineering,” *J Biomed Mater Res B Appl Biomater*, vol. 102, no. 6, pp. 1304–1315, Aug. 2014, doi: 10.1002/jbm.b.33101.

[9] G. Wei and P. X. Ma, “Structure and properties of nano-hydroxyapatite/polymer composite scaffolds for bone tissue engineering,” *Biomaterials*, vol. 25, no. 19, pp. 4749–4757, Aug. 2004, doi: 10.1016/j.biomaterials.2003.12.005.

[10] M. Cámara-Torres *et al.*, “Tuning Cell Behavior on 3D Scaffolds Fabricated by Atmospheric Plasma-Assisted Additive Manufacturing,” *ACS Appl Mater Interfaces*, vol. 13, no. 3, 2021, doi: 10.1021/acsami.0c19687.

[11] C. Mota, D. Puppi, F. Chiellini, and E. Chiellini, “Additive manufacturing techniques for the production of tissue engineering constructs,” *J Tissue Eng Regen Med*, vol. 9, no. 3, pp. 174–190, 2015, doi: 10.1002/term.1635.

[12] A. R. Calore *et al.*, “Cholecalciferol as Bioactive Plasticizer of High Molecular Weight Poly(D,L-Lactic Acid) Scaffolds for Bone Regeneration,” *Tissue Eng Part C Methods*, vol. 28, no. 7, pp. 335–350, Jul. 2022, doi: 10.1089/ten.tec.2022.0041.

[13] L. Moroni *et al.*, “Biofabrication : A Guide to Technology and Terminology,” *Trends Biotechnol*, 2017, doi: 10.1016/j.tibtech.2017.10.015.

[14] M. Vaezi, G. Zhong, H. Kalami, and S. Yang, “Extrusion-based 3D printing technologies for 3D scaffold engineering,” in *Functional 3D Tissue Engineering Scaffolds: Materials, Technologies, and Applications*, Elsevier, 2018, pp. 235–254. doi: 10.1016/B978-0-08-100979-6.00010-0.

[15] A. Di Luca *et al.*, “Tuning Cell Differentiation into a 3D Scaffold Presenting a Pore Shape Gradient for Osteochondral Regeneration,” *Adv Healthc Mater*, vol. 5, no. 14, pp. 1753–1763, Jul. 2016, doi: 10.1002/adhm.201600083.

[16] M. A. Woodruff and D. W. Hutmacher, “The return of a forgotten polymer—Polycaprolactone in the 21st century,” *Prog Polym Sci*, vol. 35, no. 10, pp. 1217–1256, Oct. 2010, doi: 10.1016/j.progpolymsci.2010.04.002.

[17] A. Youssef, S. J. Hollister, P. D. Dalton, R. Amin, S. Knowlton, and A. Hart, “Current and emerging applications of 3D printing in medicine,” *Biofabrication*, vol. 9, no. 2, pp. 1–9, 2017, doi: 10.1088/1758-5090/aa7279.

[18] S. Jain, T. Fuoco, M. A. Yassin, K. Mustafa, and A. Finne-Wistrand, “Printability and Critical Insight into Polymer Properties during Direct-Extrusion Based 3D Printing of Medical Grade Polylactide and Copolyesters,” *Biomacromolecules*, vol. 21, no. 2, pp. 388–396, Feb. 2020, doi: 10.1021/acs.biomac.9b01112.

[19] A. Bellini, “Fused deposition of ceramics: a comprehensive experimental, analytical and computational study of material behavior, fabrication process and equipment design,” 2002.

[20] C. Y. Lin, N. Kikuchi, and S. J. Hollister, “A novel method for biomaterial scaffold internal architecture design to match bone elastic properties with desired porosity,” *J Biomech*, vol. 37, no. 5, pp. 623–636, 2004, doi: 10.1016/j.jbiomech.2003.09.029.

[21] M. Hashemi, “Modeling of the Rotary-Screw-Driven Dispensing Process,” 2006.

[22] H. D. Ke, “INVESTIGATION INTO THE DISPENSING - BASED FABRICATION PROCESS FOR TISSUE SCAFFOLDS,” 2006.

[23] P. S. P. Poh *et al.*, “Polylactides in additive biomanufacturing,” *Adv Drug Deliv Rev*, vol. 107, pp. 228–246, Dec. 2016, doi: 10.1016/j.addr.2016.07.006.

[24] S. Kyle, Z. M. Jessop, A. Al-Sabah, and I. S. Whitaker, “‘Printability’’ of Candidate Biomaterials for Extrusion Based 3D Printing: State-of-the-Art,’” *Adv Healthc Mater*, vol. 6, no. 16, pp. 1–16, 2017, doi: 10.1002/adhm.201700264.

[25] A. Di Luca *et al.*, “Surface energy and stiffness discrete gradients in additive manufactured scaffolds for osteochondral regeneration,” *Biofabrication*, vol. 8, no. 1, p. 015014, Feb. 2016, doi: 10.1088/1758-5090/8/1/015014.

[26] P. Song *et al.*, “Novel 3D porous biocomposite scaffolds fabricated by fused deposition modeling and gas foaming combined technology,” *Compos B Eng*, vol. 152, pp. 151–159, Nov. 2018, doi: 10.1016/j.compositesb.2018.06.029.

[27] B. N. Turner, R. Strong, and S. A. Gold, “A review of melt extrusion additive manufacturing processes: I. Process design and modeling,” *Rapid Prototyp J*, vol. 20, no. 3, pp. 192–204, 2014, doi: 10.1108/RPJ-01-2013-0012.

[28] C. Rauwendaal, *Polymer Extrusion*. München: Carl Hanser Verlag GmbH & Co. KG, 2014. doi: 10.3139/9781569905395.

[29] J. K. Placone and A. J. Engler, “Recent Advances in Extrusion-Based 3D Printing for Biomedical Applications,” *Adv Healthc Mater*, vol. 7, no. 8, Apr. 2018, doi: 10.1002/adhm.201701161.

[30] V. Srinivas, “Timing of interfacial diffusion and (stereo)crystallization to tailor mechanical properties of additively manufactured poly(lactides),” maastricht university, 2020. doi: 10.26481/dis.20201013vs.

[31] A. Das, C. McIlroy, and M. J. Bortner, “Advances in modeling transport phenomena in material-extrusion additive manufacturing: Coupling momentum, heat, and mass transfer,” *Progress in Additive Manufacturing*, vol. 6, no. 1, pp. 3–17, Feb. 2021, doi: 10.1007/s40964-020-00137-3.

[32] S. Camarero-Espinosa, C. Tomasina, A. R. Calore, and L. Moroni, “Additive manufactured, highly resilient, elastic, and biodegradable poly(ester)urethane scaffolds with chondroinductive properties for cartilage tissue engineering,” *Mater Today Bio*, vol. 6, p. 100051, Mar. 2020, doi: 10.1016/j.mtbio.2020.100051.

[33] S. Camarero-Espinosa, A. R. Calore, A. Wilbers, J. Harings, and L. Moroni, “Additive manufacturing of an elastic poly(ester)urethane for cartilage tissue engineering,” *Acta Biomater*, vol. 102, pp. 192–204, Jan. 2020, doi: 10.1016/j.actbio.2019.11.041.

[34] Z. Zhang *et al.*, “Evaluation of bioink printability for bioprinting applications,” *Appl Phys Rev*, vol. 5, no. 4, 2018, doi: 10.1063/1.5053979.

[35] J. Copus, S. J. Lee, and A. Atala, “Bioink Printability Methodologies for Cell-Based Extrusion Bioprinting,” in *3D Bioprinting and Nanotechnology in Tissue Engineering and Regenerative Medicine*, Elsevier, 2022, pp. 153–183. doi: 10.1016/B978-0-12-824552-1.00013-X.

[36] A. Schwab, R. Levato, M. D’Este, S. Piluso, D. Eglin, and J. Malda, “Printability and Shape Fidelity of Bioinks in 3D Bioprinting,” *Chem Rev*, vol. 120, no. 19, pp. 11028–11055, Oct. 2020, doi: 10.1021/acs.chemrev.0c00084.

[37] Y. He, F. Yang, H. Zhao, Q. Gao, B. Xia, and J. Fu, “Research on the printability of hydrogels in 3D bioprinting,” *Sci Rep*, vol. 6, p. 29977, Jul. 2016, doi: 10.1038/srep29977.

[38] J. H. Y. Chung *et al.*, “Bio-ink properties and printability for extrusion printing living cells,” *Biomater Sci*, vol. 1, p. 763, 2013, doi: 10.1039/c3bm00012e.

[39] H. Li, S. Liu, and L. Li, “Rheological study on 3D printability of alginate hydrogel and effect of graphene oxide,” pp. 10–12, 2016.

[40] L. Ouyang, R. Yao, Y. Zhao, and W. Sun, “Effect of bioink properties on printability and cell viability for 3D bioplotting of embryonic stem cells,” *Biofabrication*, vol. 8, no. 3, p. 035020, Sep. 2016, doi: 10.1088/1758-5090/8/3/035020.

[41] Y. Jin, W. Chai, and Y. Huang, “Printability study of hydrogel solution extrusion in nanoclay yield-stress bath during printing-then-gelation biofabrication,” *Materials Science and Engineering C*, vol. 80, pp. 313–325, Nov. 2017, doi: 10.1016/j.msec.2017.05.144.

[42] N. C. Paxton, W. Smolan, T. Böck, F. P. W. Melchels, J. Groll, and T. Juengst, “Proposal to Assess Printability of Bioinks for Extrusion-Based Bioprinting and Evaluation of Rheological Properties Governing Bioprintability,” *Biofabrication*, 2017, doi: 10.1088/1758-5090/aa8dd8.

[43] G. Montalbano, A. R. Calore, and C. Vitale-Brovarone, “Extrusion <scp>3D</scp> printing of a multiphase collagen-based material: An optimized strategy to obtain biomimetic scaffolds with high shape fidelity,” *J Appl Polym Sci*, Jan. 2023, doi: 10.1002/app.53593.

[44] C. Duty *et al.*, “What makes a material printable? A viscoelastic model for extrusion-based 3D printing of polymers,” *J Manuf Process*, vol. 35, pp. 526–537, Oct. 2018, doi: 10.1016/j.jmapro.2018.08.008.

[45] A. Ribeiro *et al.*, “Assessing bioink shape fidelity to aid material development in 3D bioprinting,” *Biofabrication*, vol. 10, no. 1, p. 014102, Nov. 2017, doi: 10.1088/1758-5090/aa90e2.

[46] A. R. Calore, R. Sinha, J. Harings, K. V Bernaerts, C. Mota, and L. Moroni, “Chapter 7 Thermoplastics for Tissue Engineering,” in *Computer-Aided Tissue Engineering*, A. Rainer and L. Moroni, Eds., 2021, pp. 75–99.

[47] H. M. Yin *et al.*, “Engineering porous poly(lactic acid) scaffolds with high mechanical performance via a solid state extrusion/porogen leaching approach,” *Polymers (Basel)*, vol. 8, no. 6, 2016, doi: 10.3390/polym8060213.

[48] A. R. Calore *et al.*, “Manufacturing of scaffolds with interconnected internal open porosity and surface roughness,” *Acta Biomater*, vol. 156, pp. 158–176, Jan. 2023, doi: 10.1016/j.actbio.2022.07.017.

[49] Q. L. Loh and C. Choong, “Three-Dimensional Scaffolds for Tissue Engineering Applications: Role of Porosity and Pore Size,” *Tissue Eng Part B Rev*, vol. 19, no. 6, pp. 485–502, Dec. 2013, doi: 10.1089/ten.teb.2012.0437.

[50] T. Guo *et al.*, “3D printing PLGA: a quantitative examination of the effects of polymer composition and printing parameters on print resolution,” *Biofabrication*, vol. 9, no. 2, p. 024101, Apr. 2017, doi: 10.1088/1758-5090/aa6370.

[51] T. J. Coogan and D. O. Kazmer, “In-line rheological monitoring of fused deposition modeling,” *J Rheol (N Y N Y)*, vol. 63, no. 1, pp. 141–155, Jan. 2019, doi: 10.1122/1.5054648.

[52] J. M. Justino Netto, H. T. Idogava, L. E. Frezzatto Santos, Z. de C. Silveira, P. Romio, and J. L. Alves, “Screw-assisted 3D printing with granulated materials: a systematic review,” *The International Journal of Advanced Manufacturing Technology*, vol. 115, no. 9–10, pp. 2711–2727, Aug. 2021, doi: 10.1007/s00170-021-07365-z.

[53] J. M. Dealy, D. J. Read, and R. G. Larson, *Structure and Rheology of Molten Polymers*. München: Carl Hanser Verlag GmbH & Co. KG, 2018. doi: 10.3139/9781569906125.

[54] C. Macosko, *Rheology: Principles, Measurements and Applications*. 1994.

[55] C. Das, N. J. Inkson, D. J. Read, M. A. Kelmanson, and T. C. B. McLeish, "Computational linear rheology of general branch-on-branch polymers," *J Rheol (N Y N Y)*, vol. 50, no. 2, pp. 207–234, Mar. 2006, doi: 10.1122/1.2167487.

[56] E. van Ruymbeke, R. Keunings, and C. Bailly, "Prediction of linear viscoelastic properties for polydisperse mixtures of entangled star and linear polymers: Modified tube-based model and comparison with experimental results," *J Nonnewton Fluid Mech*, vol. 128, no. 1, pp. 7–22, Jun. 2005, doi: 10.1016/j.jnnfm.2005.01.006.

[57] L. G. D. Hawke, D. Romano, and S. Rastogi, "Nonequilibrium Melt State of Ultra-High-Molecular-Weight Polyethylene: A Theoretical Approach on the Equilibrium Process," *Macromolecules*, vol. 52, no. 22, pp. 8849–8866, Nov. 2019, doi: 10.1021/acs.macromol.9b01152.

[58] K. Ragaert, "Micro-extrusion of thermoplastics for 3D plotting of scaffolds for tissue engineering," 2011. [Online]. Available: http://hdl.handle.net/1854/LU-1954144

[59] J. F. Carley, R. S. Mallouk, and J. M. McKelvey, "Simplified flow theory for screw extruders," *Ind Eng Chem*, vol. 45, no. 5, pp. 974–978, 1953, doi: 10.1021/ie50521a032.

[60] W. Roland and J. Miethlinger, "Heuristic analysis of viscous dissipation in single-screw extrusion," *Polym Eng Sci*, vol. 58, no. 11, pp. 2055–2070, Nov. 2018, doi: 10.1002/pen.24817.

[61] J.-M. Bouvier and O. H. Campanella, *Extrusion Processing Technology*. 2014. doi: 10.1002/9781118541685.

[62] W. Roland, M. Kommenda, C. Marschik, and J. Miethlinger, "Extended Regression Models for Predicting the Pumping Capability and Viscous Dissipation of Two-Dimensional Flows in Single-Screw Extrusion," *Polymers (Basel)*, vol. 11, no. 2, p. 334, Feb. 2019, doi: 10.3390/polym11020334.

[63] R. T. Steller, "Theoretical Model for Flow of Polymer Melts in the Screw Channel," vol. 30, no. 7, 1990.

[64] M. Conesa, J. F. Sánchez Pérez, I. Alhama, and F. Alhama, "On the nondimensionalization of coupled, nonlinear ordinary differential equations," *Nonlinear Dyn*, vol. 84, no. 1, pp. 91–105, Apr. 2016, doi: 10.1007/s11071-015-2233-8.

[65] T. Osswald and N. Rudolph, *Polymer Rheology*. München: Carl Hanser Verlag GmbH & Co. KG, 2014. doi: 10.3139/9781569905234.

[66] Z. Tadmor, *Principles of polymer processing*. 2006.

[67] W. H. Press, S. A. Teukolsky, W. T. Vetterling, and B. P. Flannery, *Numerical Recipes in FORTRAN 77*. Cambridge University Press, 1986.

[68] W. Roland and J. Miethlinger, "Analyzing the viscous dissipation of a two-dimensional flow of non-Newtonian fluids in single screw extruders," *Annual Technical Conference - ANTEC, Conference Proceedings*, vol. 2017-May, no. September, pp. 1005–1010, 2017.

[69] R. S. Mallouk and J. M. McKelvey, "Power Requirements of Melt Extruders," *Ind Eng Chem*, vol. 45, no. 5, pp. 987–989, May 1953, doi: 10.1021/ie50521a035.

[70] O. Pokluda, C. T. Bellehumeur, and J. Machopoulos, "Modification of Frenkel ' s Model for Sintering," *AIChE Journal*, vol. 43, no. 12, pp. 3253–3256, 1997, doi: 10.1002/aic.690431213.

[71] R. S. Crockett, "The liquid-to-solid transition in stereodeposition techniques," 1997.

[72] L. Li, "Analysis and fabrication of FDM prototypes with locally controlled properties." PRISM, 2002. doi: 10.11575/PRISM/10182.

[73] L. F. Shampine and M. W. Reichelt, "The MATLAB ODE Suite," *SIAM Journal on Scientific Computing*, vol. 18, no. 1, pp. 1–22, Jan. 1997, doi: 10.1137/S1064827594276424.

[74] F. Yang and R. Pitchumani, "Healing of thermoplastic polymers at an interface under nonisothermal conditions," *Macromolecules*, vol. 35, no. 8, pp. 3213–3224, 2002, doi: 10.1021/ma010858o.

[75] N. M. Ribe, M. Habibi, and D. Bonn, "Liquid Rope Coiling," *Annu. Rev. Fluid Mech*, vol. 44, pp. 249–266, 2012, doi: 10.1146/annurev-fluid-120710-101244.

[76] N. M. Ribe, "Periodic folding of viscous sheets," *Phys Rev E*, vol. 68, no. 3, p. 036305, Sep. 2003, doi: 10.1103/PhysRevE.68.036305.

[77] N. M. Ribe, "Bending and stretching of thin viscous sheets," *J. Fluid Mech*, vol. 433, pp. 135–160, 2001, doi: 10.1017/S0022112000003360.

[78] N. M. Ribe, "A general theory for the dynamics of thin viscous sheets," *J Fluid Mech*, vol. 457, pp. 255–283, Apr. 2002, doi: 10.1017/S0022112001007649.

[79] C. McIlroy and P. D. Olmsted, "Disentanglement effects on welding behaviour of polymer melts during the fused-filament-fabrication method for additive manufacturing," *Polymer (Guildf)*, vol. 123, pp. 376–391, Aug. 2017, doi: 10.1016/j.polymer.2017.06.051.

[80] R. P. Wool, *Polymer Interfaces: Structure and Strength*. New York: Hanser Publisher, 1995.

[81] M. Roy *et al.*, "On the nucleation of polylactide by melt-soluble oxalamide based organic compounds," *Polymer (Guildf)*, vol. 202, p. 122680, Aug. 2020, doi: 10.1016/j.polymer.2020.122680.

[82] Y. Sha, C. Y. Hui, A. Ruina, and E. J. Kramer, “Continuum and Discrete Modeling of Craze Failure at a Crack Tip in a Glassy Polymer,” *Macromolecules*, vol. 28, no. 7, pp. 2450–2459, May 2002, doi: 10.1021/ma00111a044.

[83] J. Rottler, S. Barsky, and M. O. Robbins, “Cracks and Crazes: On Calculating the Macroscopic Fracture Energy of Glassy Polymers from Molecular Simulations,” *Phys Rev Lett*, vol. 89, no. 14, p. 148304, Sep. 2002, doi: 10.1103/PhysRevLett.89.148304.

[84] C. McIlroy and P. D. Olmsted, “Deformation of an amorphous polymer during the fused-filament-fabrication method for additive manufacturing,” *J Rheol (N Y N Y)*, vol. 61, no. 2, pp. 379–397, Mar. 2017, doi: 10.1122/1.4976839.

[85] S. Khalil and W. Sun, “Biopolymer deposition for freeform fabrication of hydrogel tissue constructs,” *Materials Science and Engineering: C*, vol. 27, no. 3, pp. 469–478, 2007, doi: 10.1016/j.msec.2006.05.023.

[86] Masao. Doi, *The theory of polymer dynamics*. in The International series of monographs on physics ; 73. Oxford: Clarendon Press, 1986.

[87] A. R. Calore *et al.*, “Shaping and properties of thermoplastic scaffolds in tissue regeneration: The effect of thermal history on polymer crystallization, surface characteristics and cell fate,” *J Mater Res*, vol. 36, no. 19, pp. 3914–3935, 2021, doi: 10.1557/s43578-021-00403-2.

Chapter 3

CHOLECALCIFEROL AS BIOACTIVE PLASTICIZER FOR THE MANUFACTURING OF HIGH MOLECULAR WEIGHT POLY(D,L-LACTIC ACID) SCAFFOLDS FOR BONE REGENERATION

Andrea Roberto Calore[1,2], Darya Hadavi[3], Maarten Honing[3], Ane Albillos-Sanchez[1], Carlos Mota[1], Katrien Bernaerts[2], Jules Harings[2], Lorenzo Moroni[1]

[1] MERLN Institute for Technology-Inspired Regenerative Medicine, Maastricht University, Maastricht, The Netherlands

[2] Aachen-Maastricht Institute for Biobased Materials (AMIBM), Maastricht University, Geleen, The Netherlands

[3] Maastricht Multimodal Molecular Imaging Institute (M4I), Maastricht University, Maastricht, The Netherlands

Chapter published in Tissue Engineering Part C: Methods, 28(7), 335-350.

ABSTRACT

Synthetic thermoplastic polymers are a widespread choice as material candidates for scaffolds for tissue engineering (TE), thanks to their ease of processing and tunable properties with respect to biological polymers. These features made them largely employed in melt-extrusion based additive manufacturing (AM), with particular application in hard-tissue engineering. In this field, high molecular weight (M_w) polymers ensuring entanglement network strength are often favorable candidates as scaffold materials because of their enhanced mechanical properties compared to lower M_w grades. However, this is accompanied by high viscosities once processed in molten conditions, which requires driving forces not always accessible technically or compatible with often chemically non-stabilized biomedical grades. When possible, this is circumvented by increasing the operating temperature, which often results in polymer chain scission and consequent degradation of properties. Additionally, synthetic polymers are mostly considered bioinert compared to biological materials and additional processing steps are often required to make them favorable for tissue regeneration. In this study, we report the plasticization of a common thermoplastic polymer with cholecalciferol, the metabolically inactive form of vitamin D3. Plasticization of the polymer allowed us to reduce its melt viscosity, and therefore the energy requirements (mechanical (torque) and heat (temperature)) for extrusion, limiting ultimately polymer degradation. Additionally, we evaluated the effect of cholecalciferol, which is more easily available than its active counterpart, on the osteogenic differentiation of mesenchymal stromal cells (hMSCs). Results indicated that cholecalciferol supported osteogenic differentiation more than the osteogenic culture medium, suggesting that hMSCs possess the enzymatic toolbox for Vitamin D3 (VD3) metabolism.

3.1 INTRODUCTION

In recent years, tissue engineering and regenerative medicine (TERM) has made huge progresses in the production of high-fidelity tissue replacements. Much of this is due to the increasing use of well-established industrial techniques, such as additive manufacturing (AM). In fact, with respect to conventional TERM scaffold fabrication technologies, such as gas foaming/particulate leaching, freeze-drying or phase separation, AM gives full control over the morphology and high reproducibility of the manufactured scaffolds. Additionally, AM technologies are compatible with both natural and synthetic polymers. While the former provides cells with a familiar environment, the latter offer higher control and reproducibility of properties such as biodegradation and mechanical properties [1].

One specific subclass of AM methodologies, melt-extrusion based techniques, has emerged as one of the leading methods to fabricate scaffolds for hard tissues replacement from synthetic polymers. This success is mainly due to the versatility of these techniques. In fact, the only requirement for the material is to be a thermoplastic and the raw material can also be provided in any form, pellets or powder, making the range of usable polymers wider than other techniques. The only limitation is for fused deposition modelling (FDM), where the feedstock must be shaped in filaments. Other techniques, such as selective laser sintering (SLS) and three-dimensional printing (3DP), require the polymer to be in very fine powder as the resolution will depend on the granule size, while the material stereolitography (SLA) must be photocurable. In addition, the needed equipment for melt-extrusion based techniques is relatively simple as it mainly consists of a heated print head or nozzle to melt the material, and a vertically-moving table. SLA and SLS require expensive lasers and additional recoating devices, while 3DP works with an inkjet head and a powder delivery system [2].

For hard tissues, synthetic polymers are often the materials of reference for scaffold production. This is due to the fact that they can be designed and synthesized to cause minimal or mild foreign body reaction and can be easily modified and shaped with respect to the natural-based counterparts. Furthermore, many key properties for biological applications such as biodegradation rate, wettability and mechanical performances can be tailored by varying their chemical structure, architecture and molecular weight [3], [4]. An example is poly(lactide) (PLA), which has found application in orthopedic implants and scaffolds for bone regeneration thanks to its high elastic modulus (1.5 - 2.7 GPa) [5]. High molecular weight grades, i.e. well above the entanglement molecular weight, are favoured because of their higher mechanical properties in the solid state [6]. However, scaffold fibers have diameters in the order of a few hundreds of µm and this translates into making the polymer melt flow through very narrow channels. This results in high shear stresses, which requires driving forces like torque and temperature not always technically accessible by the equipment or imposable to chemically non-stabilized biomedical polymers, particularly of high molecular weight grades. This issue was highlighted by Camarero-Espinosa et al. [7], [8], where high molecular weight poly(ester)urethane had to go through a preliminary degradation step to become extrudable. Conventional ways to circumvent this issue are to reduce the material viscosity (and therefore the needed forces) with higher operating temperatures [9]. On the other hand, some widely used polymers such as PLA, are poorly thermally stable and elevated processing temperatures might promote chain scission and molecular weight decrease [10], [11]. Changes in the molecular structure would lead to unstable flow over processing and inhomogeneous products, which might further impact the final performances. In industry, this is often tackled by the addition of chemical stabilizers or chain extenders. The latter have the purpose of reconnecting broken chains caused by the degradation process [12]. Commonly used compounds are tris (nonylphenyl) phosphite (TNPP), polycarbodiimide (PCDI) and Joncryl [13]–[15]. To our knowledge, there are no studies about the biocompatibility of these molecules. Tachibana et al. [16] found that myo-inositol, a sugar present in the human body and involved in cell signal transduction [17], had a stabilization effect on PLLA during processing. This was attributed to the cross-linking with esterification by the hydroxyl groups of the molecule. However, cross-linking is highly undesirable during melt-processing as it would prevent flow of the material through the extruder/printer channels.

Plasticizers represent an alternative strategy to deal with polymer degradation during processing [18]. Plasticizers are additives that have been extensively used in industry to improve the mechanical properties of inherently rigid thermoplastic polymers. They are usually low molecular weight molecules, which tend to separate the polymer chains and allow easier relative motion between them, increasing the matrix flexibility, softness, extensibility and in particular their processability in terms of ease of flow [19]. Commonly used plasticizers are phthalate esters, aliphatic esters, epoxy esters and phosphate esters [20]. In tissue engineering, citrate esters, poly(ethylene glycol) (PEG), glucose monoesters, partial fatty acids, oligomeric lactic acid and glycerol found use as plasticizers for PLA, with the goal of increasing its elongation at break and impact resistance [21]. Plasticizers appear as a more straightforward choice to improve material processability compared to chain extenders. The latter may in fact lead to unwanted and uncontrolled increase in molecular weight [12], or even branching depending on the molecule active groups [13]. Such changes might negatively affect the capability of extruding the material.

Despite being potentially thermally unstable, synthetic polymers are also more bioinert when compared to non-resorbable materials such as ceramics and titanium alloys, or natural polymers [1]. Biological inertness may result in poor cell activity, which in turn could lead to poor tissue development. Researchers have been trying to promote cell responses by optimizing the scaffold material via post-treatment of the surface [22]. Techniques include plasma treatment [23], chemical etching [24] and chemical binding [25]. These treatments may involve some degradation of the polymer, may be non-permanent and may require several steps, limiting upscaling [26]. Another strategy that has been explored is loading bioactive agents in the polymer matrix. These will be partly available on the scaffold surface and partly released over time to induce the intended effect. Yoon et al. fabricated scaffolds with PLGA and dexamethasone that showed anti-inflammatory effects upon the controlled release of the steroid [27]. Bhutto et al. electrospun poly(l-lactide-co-caprolactone)/silk scaffolds with vitamin B5 and reported enhanced proliferation of Schwann cells cultured on scaffolds with the vitamin [28]. Damanik et al. blended PCL and retinoic acid, a metabolite of vitamin A1, and electrospun the mixture, which resulted in scaffolds able to enhance the synthesis of extracellular matrix proteins [29]. This type of approach has the advantages of requiring limited pre or post-manufacturing modifications, and of potentially controlling the release rate and cell response over time. However, it seems to be limited to techniques that can preserve the molecular structure, and thus the functionality, of the bioactive compound used. In fact, melt-based manufacturing would expose the additive to high temperatures, which might induce its thermal degradation and loss of bioactivity [30].

Vitamin D is the name of a group of vitamins that play a role in the calcium and phosphate metabolism of the bone homeostasis [31]. Vitamin D3 (VD3), or cholecalciferol, is synthetized in the skin upon UVB radiation and then hydroxylated twice, first in the liver and then in the kidney, to result into the metabolically active form calcitriol [32]. Calcitriol is known to contribute to the differentiation of osteoblasts but also to the commitment of mesenchymal stromal cells to the osteogenic lineage [33], [34]. However, synthetic calcitriol is industrially produced through a multistep and expensive reaction making it more expensive than the precursor cholecalciferol [35], [36]. Recently, it was suggested that some cell types including hMSCs, possess the enzymatic toolbox for VD3 metabolism and action, including the enzymes for cholecalciferol hydroxylation into calcitriol [37].

In the attempt to overcome the thermal instability of PLA and its inherent biological inertness, we explored the effect of vitamin D3 as a plasticizer. Our double goal was to reduce the processing temperature of a high-molecular weight amorphous PLA (PDLLA) while investigating VD3 potential osteogenic effect on mesenchymal stromal cells. Blends with different concentrations of VD3 were prepared by melt mixing and then characterized according to their intended use. Flow properties and thermal stability in a melt were evaluated by means of rheometry, the glass transition temperature (T_g) was measured by differential scanning calorimetry (DSC) to ensure high elastic modulus at body temperature and mechanical properties were tested with a tensile tester. Scaffolds where then manufactured via a melt extrusion-based technique and cell proliferation, metabolic activity and osteogenic differentiation were evaluated with mesenchymal stromal cells (hMSCs).

3.2 MATERIALS AND METHODS

3.2.1 Materials

The polymer PDLLA, with an inherent viscosity midpoint of 2.0 dl/g (PDL20), was kindly provided by Corbion Biomedical (the Netherlands). Vitamin D3 (VD3) was purchased from Abcam (ab143594, United Kingdom). Prior to any melt-based processing, the polymer was dried according to the manufacturer's protocol.

Dimethyl sulfoxide (DMSO) cell culture grade was purchased from VW and sodium hydroxide (NaOH, BioXtra, ≥98% (acidimetric), pellets) from Sigma Aldrich. ULC/MS-grade water (H2O), ULC/MS-grade methanol, LC/MS-grade isopropanol, LC/MS-grade dichloromethane (DCM) were obtained from Biosolve BV (Valkenswaard, The Netherlands). Ammonium acetate and cholesterol were purchased from Sigma-Aldrich.

3.2.2 Blending

The blend was prepared by mixing PDLLA with either 5 (PDLLA/5), 10 (PDLLA/10) or 15 (PDLLA/15) wt% VD3 in a twin-screw extruder (DSM Xplore twin-screw micro-extruder) pre-heated at 170 °C, for 2 min at 150 rpm. The extrudate was cut into pellets at need.

3.2.3 Rheological evaluation

The complex viscosity of blends over time was measured with an Anton Paar MCR rheometer with a parallel plate geometry (25 mm diameter and 0.5 mm gap). The samples were loaded at 150 °C and the time between the loading and the start of the test was kept constant between samples, at 60 s. The testing temperature was chosen to evaluate unbiased material properties as a compromise between actual processing conditions and negligible thermal degradation. The materials were subjected to a series of frequency sweeps for 120 min, from 100 to 10 rad/s at 1 % strain. The first frequency sweep per blend was used to compare the rheological behavior of the different blends. The complex viscosity vs. angular frequency data were first converted to dynamic viscosity vs. shear rate by means of the Cox-Merz transformation [38]. The data were then fitted with the Carreau-Yasuda model (1):

$$\eta = (\eta_0 - \eta_\infty)\left((1 + (k\dot{\gamma})^a)^{\frac{n-1}{a}}\right) + \eta_\infty \tag{1}$$

Where η is the complex viscosity, η_0 and η_∞ are respectively the zero-shear and infinite-shear viscosities, k the consistency (characteristic time), $\dot{\gamma}$ is the shear rate, n the power law index and a a parameter describing the transition between Newtonian plateau and power law region [39].

The blend viscosity over time was obtained by sequentially plotting the data points at 10 rad/s for all the sweeps. The viscosity drop over time was calculated according to the following formula (2):

$$\Delta\eta(t)[\%] = \frac{\eta(t) - \eta(0)}{\eta(0)} * 100 \tag{2}$$

Where η is the complex viscosity and t is the considered time point.

3.2.4 Thermal analysis

To ensure high elastic modulus of a thermoplastic polymer, it is important that the T_g is above body temperature. This applies in particular to amorphous grades such as the PDLLA used in this study. Such class of polymers do not have a crystalline phase that could compensate for the rubbery state of the amorphous regions up to a certain extent. For this reason, the T_g of the blends was determined as midpoint via Differential Scanning Calorimetry (DSC) with a TA instruments Q2000 DSC. Briefly, samples (+/- 5 mg) in sealed in hermetic aluminum pans were heated from -20 to 150 °C at a rate of 10 °C/min, cooled to -20 °C and reheated to 150 °C at the same rate. 3 minutes of isothermal conditions were applied at the temperature limits. Nitrogen was used as a purging gas.

3.2.5 Tensile testing

Dog-bone shaped specimens for tensile testing (ISO 527-2) with 2.0 mm gauge width and 10 mm gauge length were obtained by first compression-molding 300 mg of material at 180 °C for 60 s at 10 bar followed by 60 s at 240 bar. The specimens were then punched out of the film and tested at a strain rate of 100 µm/s at room temperature in a Linkam TST350 tensile stage. Elastic modulus E and yield stress σ_Y were derived from the engineering stress – strain diagrams. Data is presented as average of minimum 5 independent replicas with error bars indicating the standard deviation.

3.2.6 Additive manufacturing

Scaffolds were printed via a melt-extrusion based technique (Bioscaffolder, SysENG, Germany) equipped with a G22 nozzle (DL Technology, U.S.A.) and an in-house developed nozzle heater. After drying, the pellets from the blends or the granules of the plain PDLLA were loaded in the printhead cartridge, pre-heated at 190 °C. The nozzle was instead pre-heated at 215 °C in the case of PDLLA while at 205 °C for PDLLA/VD3. These temperatures were the result of an optimization process that led to morphologically accurate and mechanically stable scaffolds. The liquid material was then deposited by applying a pressure of 8.6 bar and following a 0-90° pattern between layers, at a translational speed of 600 mm/min. The blends with VD3 were extruded at a screw rotation of 100 rpm while, for the plain PDLLA the rotation speed was set to 125 rpm. The scaffold structure consisted of blocks of 5 x 5 x 3 mm^3, with a fiber diameter of 400 µm, fiber-to-fiber (center-to-center) distance of 1 mm and a layer thickness of 330 µm. The parameters describing the geometry of the screw and of the nozzle can be found in Table 1.

Table 1. Geometric parameters of the screw and nozzle used for scaffold AM. *D* is the screw outside diameter, *h* the thread depth (measured from root of screw to barrel surface), *t* the screw lead, *φ* the helix angle, *L* the axial length of flighted section of the screw, *r* and *l* the radius and the length of the nozzle, respectively.

***D* [mm]**	***h* [mm]**	***t* [mm]**	***φ* [rad]**	***L* [mm]**	***r* [mm]**	***l* [mm]**
4.93	1.28	3.1	0.1975	16.6	0.2063	9.5

3.2.7 Release kinetics study

3.2.7.1 Scaffold incubation

To evaluate whether any potential effect of the presence of VD3 was due to its diffusion into the medium or to its presence on the scaffold surface, the release kinetics of VD3 from PDLLA/VD3 scaffolds were evaluated. Plain PDLLA constructs were used as reference. and PDLLA/VD3 scaffolds were incubated after disinfection for 35 days in 1.5 ml of MilliQ water.

Being VD3 soluble in ethanol, scaffolds were first sterilized by treating them with oxygen plasma. Briefly, they were sealed in plasma sterilization pouches, which were then placed in the chamber of a plasma cleaner (Femto PCCE) and exposed for 4 min to oxygen plasma, at a pressure of 0.53 mbar and 100 W of power.

Scaffolds were then incubated for 35 days in conditions mimicking the cell culture environment or in medium to accelerate the degradation process. In the former case, 1.5 ml of MilliQ water were used, with or without the addition of 1% DMSO (cell culture grade, BioChemica) to increase the solubility of VD3. The accelerated degradation environment consisted of 125 mM NaOH in 1.5 ml of MilliQ water, with or without the addition of 1% DMSO as well. The incubation was carried out at 37 °C / 5% CO_2 in sterile conditions.
At each timepoint (1, 2, 3, 7, 10, 14, 17, 21, 24, 28, 31, 35 and 37 days), the supernatant was collected and the scaffolds were placed in 1.5 ml of fresh corresponding solution. The samples were then stored at -80 °C for liquid chromatography (LC) -mass spectrometry (MS) analysis. Samples were examined in triplicates.

3.2.7.2 Sample preparation

For LC-MS analysis the VD3 contained samples were extracted with 1.5ml of DCM, which included 817 uM of cholesterol as an internal standard. For this extraction step, the collected samples in a 2ml eppendorf were transferred to 5ml tube and the eppendorf filled with 1.5 ml of 817 uM of cholesterol dissolved in DCM. The eppendorf was vortex-mixed for 1 min to dissolve VD3 in DCM. The content of the eppendorf was then transferred to the same 5ml tube and followed by vortex-mixing for 1min and 10 min centrifuge at 4000 rcf. After removing the aqueous phase of the solution, the organic phase (including DCM, Cholesterol and VD3) kept at room temperature overtight to crystallise VD3 and Cholesterol. Samples were then concentrated and reconstituted with 1ml of LC mobile phase (15-85% mobile phase A and B). Samples were ultimately transferred to 2ml light sensitive LC vials for LC-MS analysis.

3.2.7.3 Liquid chromatography and Mass spectrometric conditions

Shimadzu LC-20AD was used for chromatic separation. Separation was achieved using Waters Corp ACQUITY UPLC CSH Fluoro-Phenyl Column, 130Å, 1.7 µm, 2.1 mm X 150 mm, 1/pk. The mobile phase A contained 5mM of ammonium acetate in water and the mobile phase B contained 5mM of ammonium acetate dissolved in methanol and isopropanol (80-20%). Chromatographic separations were performed at 40°C with the fixed flow rate of 0.18ml/min over 9min measurements. The method developed as such that the starting running buffer was 85% of mobile phase B for first 3 min, which then increase to 98% over 1min and kept at this rate until minute 5 before reducing back to 85% of buffer B over 1min. Mass spectrometer Synapt G2Si (Waters, Milford, MA, USA) with an electro spray ionization (ESI) source used as a detector. The MS analysis was performed in the positive ion mode after mass calibration by sodium formate under following ESI conditions: capillary voltage of 2.5 kV, desolvation gas flow of 600 L/h, source temperature of 100°C, cone voltage of 40 V and nebulizer gas pressure of 6.5 bar. The chromatographic data were extracted from Masslynx v4.1 (Waters) and pre-processed in Excel. The chromatograph of cholesterol was used as internal standard.

3.2.8 Cell seeding and culture

3.2.8.1 Cell expansion

hMSCs isolated from bone marrow were purchased from Lonza (Donor 19TL029340, male, age 24). MG-63 cells were obtained from ATCC. hMSCs and MG-63 were plated at 1000 cells/cm^2 in tissue culture flasks and cultured at 37 °C / 5% CO_2 in basic medium (BM), consisting of αMEM with Glutamax and no nucleosides (Gibco) supplemented with 10 vol% FBS (Sigma-Aldrich), until 80% confluence.

3.2.8.2 Cell seeding and culture

Scaffolds were sterilized as described in section 2.7.

MG-63 cells were used to preliminarily evaluate any potential toxic effect of the highest concentration of VD3, for the longest acceptable period with no medium refresh, 3 days. Trypsinized cells were centrifuged at 500 rcf for 5 min and then resuspended in BM at a density of 50000 cells/ml. 25000 cells/cm^2 were seeded in the wells of a 24-well plate and allowed to attach overnight. The next day (day 0), the medium was replaced with proliferation medium (PM, BM supplemented with penicillin (100 U/ml), streptomycin (100 µg/ml) (Fisher-Scientific) and 200 µM L-a Ascorbic acid 2-phosphate (Sigma-Aldrich)) and transwells (8 µm polycarbonate pore size, Corning) with 15wt%-loaded-VD3 scaffolds were placed on top of the wells. The culture was analyzed for metabolic activity and DNA content at day 1 and 3, with no medium refresh.

To investigate the osteogenic potential of VD3-loaded scaffolds, they were incubated overnight at 37 °C / 5% CO_2 in BM supplemented with penicillin (100 U/ml) and streptomycin (100 µg/ml) for protein attachment. The next day, scaffolds were placed on top of a sterile filter paper and allowed to dry. They were then placed in the wells of a non-tissue-culture treated plate. Passage 4 hMSCs were trypsinized and centrifuged for 5 min at 500 rcf. The cells were then resuspended at a density of 150000 cells per 37 µl in medium consisting of 10 wt% dextran (500 kDa, Pharmacosmos) in BM supplemented with penicillin (100 U/ml), streptomycin (100 µg/ml) (Fisher-Scientific) [40]. A 37 µl droplet of cell suspension was placed on top of each scaffold and these were incubated for 4 h at 37 °C / 5% CO_2 to allow cell attachment. Scaffolds were then transferred to new wells filled with 1.5 ml of PM. The medium was replaced after 24h and every two or three days from then on. After 7 days (day 0), scaffolds were cultured for another 35 days in PM or differentiation media (DM, PM supplemented with 10 nM dexamethasone (Sigma-Aldrich) and 10 mM β-glycerophosphate (Sigma-Aldrich)). The medium was replaced every two or three days. The culture was analyzed for metabolic activity, alkaline phosphatase (ALP), DNA content both at day 7 and 35, while for osteocalcin (OCN) and osteopontin (OPN) production and mineralization at day 35.

3.2.9 Biochemical assays

3.2.9.1 Metabolic activity

PrestoBlue assay (Thermo Fisher Scientific) was used to quantify cell metabolic activity. Briefly, cell culture medium in sample plates was replaced with medium containing 10 v/v% PrestoBlue reagent and the sample plates were incubated in the dark at 37 °C for 1 h. Fluorescence was measured at 590 nm with a plate reader (CLARIOstar®, BMG Labtech).

3.2.9.2 ALP assay

The scaffolds were washed 3x with PBS and freeze-thawed 3 times. Samples were then incubated for 1h at RT in a cell lysis buffer composed of 0.1 M KH_2PO_4, 0.1 M K_2HPO_4 and 0.1 vol% Triton X-100, at pH 7.8. 10 µl of cell lysate were collected and 40 µl of the chemiluminescent substrate for alkaline phosphatase CDP-star, ready-to-use (Roche) were added to. Luminescence (emission = 470 nm) was measured after 15 min incubation, using a spectrophotometer (CLARIOstar®, BMG Labtech). Remaining cell lysates were used for DNA quantification. Values were normalized to DNA content.

3.2.9.3 DNA assay

CyQUANT Cell Proliferation Assay Kit (Thermo Fisher Scientific) was used to perform DNA assay. Samples from ALP assay were first incubated overnight at 56 °C in 1 mg/ml Proteinase K (Sigma-Aldrich) in Tris/EDTA buffer and then freeze-thawed three more times. Subsequently, to degrade the cellular RNA, the lysate was incubated 1 h at RT in a buffer composed of 1:500 RNase A in the cell lysis buffer from the kit diluted 20x in dH_2O. The samples were then incubated for 15 min in the fluorescent dye provided by the kit (1:1) for 15 min and fluorescence was measured (emission/excitation = 520/480 nm) with a spectrophotometer. DNA concentrations were calculated from a DNA standard curve.

3.2.9.4 Elisa

The production of osteocalcin and osteopontin were quantified using ELISA kits (ab270202 and ab192143 respectively, Abcam) according to the manufacturer's instructions. Briefly, at the specified time points, the supernatant from the scaffolds was collected and the protein content was quantified using the ELISA kits. The same samples were used for both assays.

3.2.9.5 Alizarin red (ARS)

Calcium mineralization was quantitatively determined following a protocol from [41]. Scaffolds were washed 3x with PBS and fixed with 4 wt% paraformaldehyde for 30 min, followed by three washing steps in MilliQ water. Subsequently, scaffolds were cut in half and each section was stained with alizarin red S solution (60 mM, pH 4.1-4.3) for 20 min at RT. The samples were then washed with MilliQ water as long as the staining was leaching out and then incubated for 1h at RT with 30 vol% acetic acid while shaking. Following a 10 min incubation at 85 °C, scaffolds were removed and the solutions were centrifuged at 20000 rcf for 10 min. The pH was then adjusted to 4.1-4.3 with 5M ammonium hydroxide and eventually absorbance was measured at 405 nm using a spectrophotometer. The concentration of alizarin red was calculated from an alizarin red standard curve and the values were normalized to DNA content.

3.2.10 Immunofluorescence microscopy

Samples from the osteogenic study cultured in proliferation conditions were stained with DAPI and phalloidin and imaged via immunofluorescence microscopy. Briefly, samples were washed with PBS and fixed with 4 wt% paraformaldehyde for 30 min at RT, and then washed three times again with PBS. Cells were permeabilized with 0.1 vol% Triton-X for 30 min at RT, washed twice with PBS and eventually incubated in PBS for 5 min. The whole washing sequence was repeated twice. Samples were then incubated in phalloidin solution (Alexa Fluor 568, 1:75 dilution in PBS) for 1h at RT in the dark, under shaking. Samples were then washed three times with PBS and incubated in DAPI solution (1:300 dilution in PBS) for 15 min at RT while shaking, in the dark. Finally, samples were washed with PBS. Confocal laser scanning microscopy was performed with a Tandem confocal system (Leica TCS SP8 STED), equipped with a white light laser (WLL). Samples were excited with the dye specific wavelengths using the WLL or a photodiode 405 in the case of DAPI. Emission was detected with PMT detectors (DAPI) or HyD detectors (phalloidin).

3.2.11 Statistical analysis

GraphPad Prism (version 8.4.3) was used to run statistical analysis. For the transwell study, statistical significance was assessed with a one-way ANOVA test with Tukey's post-hoc test for comparison among the conditions in the same day. An unpaired t-test was used to compare the same condition between the two days. Statistically significant differences are marked with * ($p<0.05$), ** ($p<0.01$) or *** ($p<0.001$) when comparing the effect of different VD3 concentrations on cells at the same day and § ($p<0.05$), §§ ($p<0.01$) or §§§ ($p<0.001$) when the comparing the effect of different VD3 concentrations at different time points.

The same approach was adopted to statistically evaluate the results from the osteogenic study. A one-way ANOVA test with Tukey's post-hoc test was used for comparison among the conditions in the same culture medium. The same condition in the two different media was analyzed with an unpaired t-test. Statistically significant differences are marked with * ($p<0.05$), ** ($p<0.01$) or *** ($p<0.001$) when comparing the effect of different VD3 concentrations on cells at the same day and with § ($p<0.05$), §§ ($p<0.01$) or §§§ ($p<0.001$) when comparing the effect of different media on cells cultured on scaffolds with the same VD3 content.

3.3 RESULTS

3.3.1 Rheological evaluation

As expected, frequency sweeps showed a drop in viscosity with increasing VD3 concentration (Figure 1A). This result is confirmed by the fitting of the Carreau-Yasuda model to the flow curves, as shown in Table 2. The extrapolated data for the zero-shear viscosity η_0 showed in fact decreasing values with increasing VD3 concentration. In particular, there seemed to be a consistent drop when increasing the concentration from 5 to 10 wt% whereas the reduction appeared to be more limited when passing from 0 to 5 and from 10 to 15 wt%. The inverse of the parameter k gives the shear rate at which the polymer shifts from Newtonian to power-law behavior. In a log-log plot, this translates into the viscosity curve plateau at low shear rates turning into a straight line, with a transition sharpness given by a [42]. As it can be seen from Table 1, increasing VD3 concentration delayed the onset of the shear-thinning region on the shear rate scale. The transition to this flow region appeared to be more or less the same for all compositions with the exception of PDLLA/15, which exhibited a smoother behavior. The slope of the power-law region is given by n, which had the same values for all the compositions.

The trend over time of the complex viscosity of the blends, and viscosity drop percentage, can be seen respectively in Figure 1B and Figure 1C. Plain PDLLA showed an initial decrease in viscosity that reduced after 50 min, nearly reaching a plateau at around 10% with respect to the viscosity value at time zero. VD3-loaded samples all exhibited an increasing trend over time, although the initial drop as well as all other data points were higher for PDLLA/15. Notably, PDLLA/5 and PDLLA/10 exhibited the lowest decrease up to 100 min of test. For longer times, their viscosity drop was higher than plain PDLLA.

Table 2. Carreau-Yasuda parameters for PDLLA and VD3-loaded PDLLA at 150 °C.

Composition	η_0 [Pa s]	η_∞ [Pa s]	k [s]	n	a	R^2
PDLLA	67347.96	317.96	0.11	1E-4	0.55	1
PDLLA/5	60038.14	262.14	0.10	1E-4	0.52	1
PDLLA/10	33528.95	302.95	0.09	1E-4	0.57	1
PDLLA/15	28115.33	206.33	0.04	1E-4	0.41	0.99

3.3.2 Thermal analysis

The glass transition temperature (T_g) (Table 3, extrapolated from the DSC thermograms in Figure S1) showed a decrease as a function of VD3 concentration, proving successful mixing and plasticization of the polymer. None of the blends showed a T_g lower than body temperature, a characteristic that would limit their use in tissue engineering applications. Besides an initial consistent decrease in glass transition temperature with the addition of 5 wt% of VD3, the increase of plasticizer concentration did not lead to substantial further drops in T_g.

Table 3. Glass transition temperature midpoint, elastic modulus and yield stress of VD3 blends.

Composition	T_g midpoint[°C]
PDLLA	57.9
PDLLA/5	50.9
PDLLA/10	50.2
PDLLA/15	49.1

3.3.3 Tensile

In Figure 1D, the stress-strain characteristic curves from tensile testing of PDLLA and PDLLA/VD3 samples can be seen. It immediately appears how PDLLA/10 and PDLLA/15 exhibited an unexpected lower elongation at break with respect to plain PDLLA and PDLLA/5. Data extrapolation from the curves resulted into the elastic modulus E and yield stress σ_Y values shown respectively in Figure 1E and Figure 1F. Both elastic modulus and yield stress decreased with increasing VD3 concentration, as expected. In particular, the difference between conditions was more significant with increasing concentrations of VD3, with the drop in E and σ_Y being greater for the couple PDLLA/5-PDLLA/10 than for the couple PDLLA-PDLLA/5. Nevertheless, it can be noticed that samples PDLLA/10 and PDLLA/15 performed similarly, suggesting the existence of a saturation concentration of VD3.

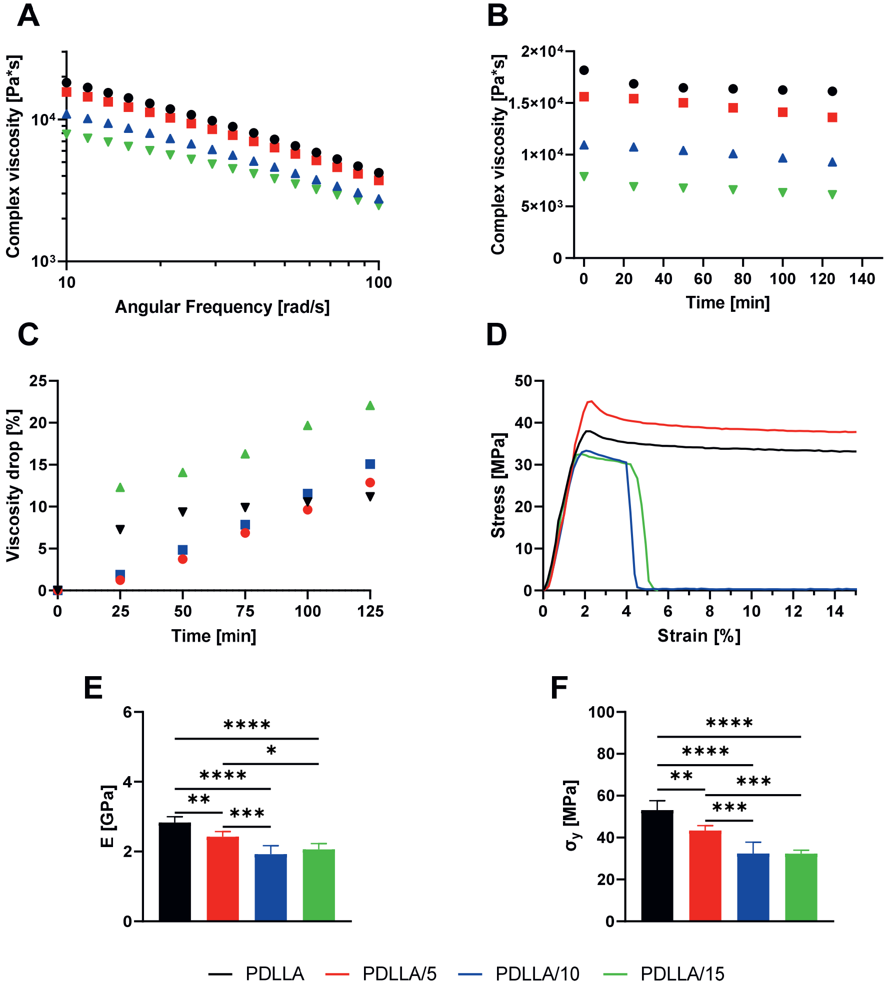

Figure 1. (A) Dependence of complex viscosity on angular frequency, at 150 °C. (B) Complex viscosity over time of plain PDLLA and PDLLA mixed with VD3 at various concentrations. Data generated at 10 rad/s at 150 °C. (C) Viscosity drop at the time points of figure (B) with respect to viscosity values at time 0. (D) Engineering Stress – strain curves recorded during tensile testing. (E) Elastic modulus and (F) yield stress extrapolated from the mechanical data of PDLLA and PDLLA/VD3 samples from Figure 1D.

3.3.4 Release kinetics

To study VD3 release from PDLLA, the 5, 10 and 15 wt% loaded-scaffolds were submerged in 4 different types of media consisting of distilled water, distilled water with 1% DMSO, distilled water with 125 mM NaOH, distilled water with 125 mM NaOH and 1% DMSO. The LC-MS analysis on the collected samples from the medium with pure distilled water and distilled water with 1% of DMSO showed no chromatographic peaks pertaining to VD3. This observation implies the absence of VD3 in the collected samples from day 1 until day 37. However, the collected samples from NaOH containing media (with and without DMSO) showed chromatographic peaks relating to oxidised form of VD3 at mass over charge ratio (m/z) of 383 Dalton. The average amounts of VD3 and their relative standard deviation per time interval are listed in Table 4, for samples incubated in NaOH, and Table 5, for samples incubated in NaOH+DMSO. Plotted VD3 release profiles showed an irregular release pattern of VD3 in the absence of DMSO (Figure 2A), especially at lowest concentrations of VD3. Instead, the release profile in the presence of DMSO exhibited a more sustained trend (Figure 2B). On the other hand, the collected samples from only NaOH containing medium (Table 4) exhibited higher total amount of VD3 than NaOH+DMSO medium (Table 5) for all concentrations of scaffold except for 10%wt-VD3 loaded one. In addition, a burst release was observed between day 3 and 7 in all scaffolds on both types of medium, except for 10%wt-VD3 loaded scaffold in NaOH medium.

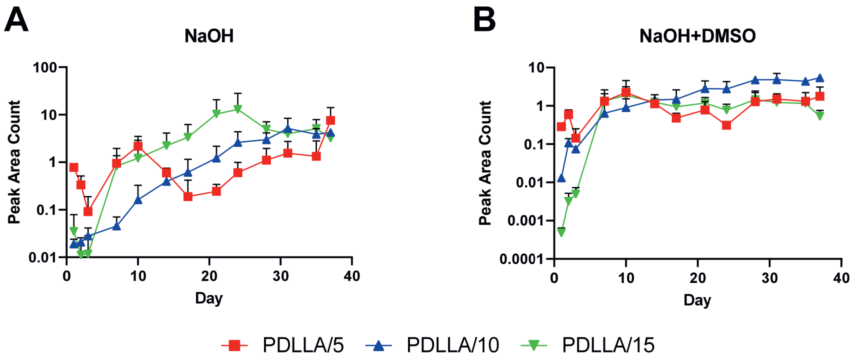

Figure 2. Release profile of VD3 from PDLLA/VD3 scaffolds incubated in (A) NaOH medium and (B) NaOH+DMSO medium. The release profile is expressed as peak area count per single time point.

Table 4. Release kinetics data from PDLLA/VD3 scaffolds incubated in NaOH. Data are expressed as average peak area counts with their relative standard deviation (in %) and total release amount.

Day	PDLLA/5		PDLLA/10		PDLLA/15	
	APAC	RSD [%]	APAC	RSD [%]	APAC	RSD [%]
1	0.78	9.6	0.02	26.0	0.04	126.1
2	0.34	53.4	0.02	17.9	0.01	129.9
3	0.09	106.2	0.03	47.8	0.01	144.3
7	0.95	44.5	0.05	53.8	0.83	135.9
10	2.17	62.1	0.16	101.3	1.21	138.3
14	0.60	24.5	0.40	65.5	2.24	84.6
17	0.19	122.4	0.61	87.6	3.35	86.8
21	0.24	40.1	1.23	77.3	10.32	102.1
24	0.60	65.2	2.61	67.9	12.92	118.2
28	1.11	76.4	2.98	39.1	4.97	43.6
31	1.55	77.5	5.16	62.5	3.98	23.6
35	1.33	110.8	3.87	32.2	5.10	55.3
37	7.63	86.3	4.26	13.7	3.23	11.9
Total	17.14		21.41		48.21	

Table 5. Release kinetics data from PDLLA/VD3 scaffolds incubated in NaOH+DMSO. Data are expressed as average peak area counts with their relative standard deviation (in %) and total release amount.

Day	PDLLA/5		PDLLA/10		PDLLA/15	
	APAC	RSD [%]	APAC	RSD [%]	APAC	RSD [%]
1	0.28	12.5	0.01	15.8	0.00	35.6
2	0.59	31.7	0.11	29.2	0.00	63.2
3	0.14	75.3	0.07	9.8	0.00	48.3
7	1.31	99.2	0.64	90.5	1.34	56.1
10	2.24	104.2	0.90	70.7	1.90	65.7
14	1.13	72.5	1.44	18.8	1.26	20.3
17	0.48	32.5	1.49	76.4	0.94	6.8
21	0.78	65.2	2.84	57.2	1.19	39.4
24	0.31	14.8	2.79	55.0	0.78	42.1
28	1.30	72.8	4.80	9.0	1.46	68.4
31	1.50	37.6	4.83	46.5	1.22	24.1
35	1.32	69.3	4.42	19.7	1.16	28.7
37	1.78	75.7	5.43	0.8	0.53	41.9
Total	12.64		29.76		11.79	

3.3.5 Cell studies

3.3.5.1 Biocompatibility

To evaluate any potential cytotoxic effect by the VD3 concentrations used, a biocompatibility study was run over 3 days. At day 1, all the samples showed comparable DNA amounts (Figure 3A). The same result was seen at day 3 as well. Over the three days of culture, only PDLLA/15 samples showed a statistically relevant increase in DNA between day 1 and day 3.

In terms of metabolic activity, all conditions resulted in comparable value, both at day 1 and day 3 (Figure 3B). Between day 1 and day 3, metabolic activity increased significantly only for cells cultured on PDLLA/5 scaffolds.

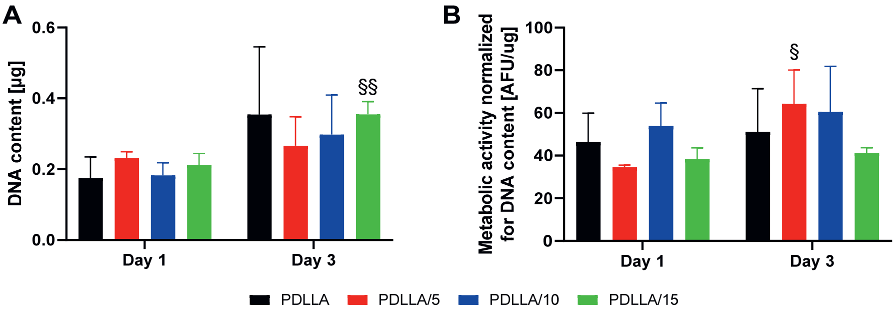

Figure 3. (A) DNA content and (B) metabolic activity from the biocompatibility study. Statistically significant differences are marked with * ($p<0.05$), ** ($p<0.01$) or *** ($p<0.001$) when comparing the effect of different VD3 concentrations on cells at the same day and § ($p<0.05$), §§ ($p<0.01$) or §§§ ($p<0.001$) when the comparing the effect of different VD3 concentrations at different time points.

3.3.5.2 Osteogenic

The different concentrations of VD3 in the additive-manufactured scaffolds were tested for osteogenic effects on hMSCs. Cells were cultured on plain PDLLA scaffolds and on constructs loaded with 5, 10 and 15 wt% VD3. The culture lasted up to 35 days, in proliferation or mineralization conditions, after 7 days of proliferation. At both time points, cells displayed comparable metabolic activities among scaffolds and media. At day 7 (Figure 4A), cells seemed to have proliferated homogeneously on all scaffolds in PM, except for those cultured on PDLLA/10. Cells cultured in mineralization conditions displayed instead lower proliferation, with particular reference to cultures on PDLLA/10 and 15 scaffolds. At the second time point (Figure 4C), the differences were less pronounced, with cells in basic conditions being in comparable amount to those cultured in MM. To be noted that PDLLA scaffolds showed higher DNA content than VD3-loaded scaffolds.

From Figure 4B and D, it can be seen that the addition of VD3 in the scaffolds did not have any impact on cell metabolic activity. In fact, cells cultured on VD3-loaded scaffolds showed a metabolic activity to those grown on plain PDLLA constructs at both time points, day 7 (Figure 4B) and day 35 (Figure 4D). Additionally, cells in each condition maintained a steady metabolic activity over the culture period, as shown by the comparable results.

In basic conditions, ALP, OPN and OCN generally showed upregulated values for scaffolds with 10 and 15 wt% VD3, at both time points (Figure 5A-F). At day 7, cells cultured on PDLLA/10 and 15 showed enhanced ALP production compared to those on other scaffold types, while at day 35 PDLLA/15 exhibited the highest secretion. OPN showed a substantially stable profile over time while OCN seemed to increase, with cells cultured on PDLLA/10 and on PDLLA/15 scaffolds exhibiting the highest production.

Markers secretion in mineralization conditions followed a similar trend (Figure 5A-F). ALP secretion (Figure 5A and B) resulted in an increase over time, with cells on PDLLA/5 and PDLLA/10 scaffolds showing higher activity than other conditions at day 35. OPN secretion (Figure 5C and D) did not significantly change although, at day 7, it exhibited the same profile as in PM, with PDLLA/10 scaffolds slightly standing out. Instead, a decrease in OCN (Figure 5E and F) production could be noticed over time. Once again, the profile at day 7 followed the one in basic conditions. Overall, there seemed to be limited differences between the two media conditions, except for OCN secretion at day 35. Here, cells cultured on VD3-loaded scaffolds showed enhanced production of OCN in basic conditions with respect to MM.

Alizarin Red staining and its quantification (Figure 5G) showed significantly higher calcium deposition for the compositions PDLLA/10 and 15 in basic conditions. In MM, instead, all three VD3 compositions exhibited higher amounts of calcium than the control PDLLA scaffold, although with substantial variation among the samples.

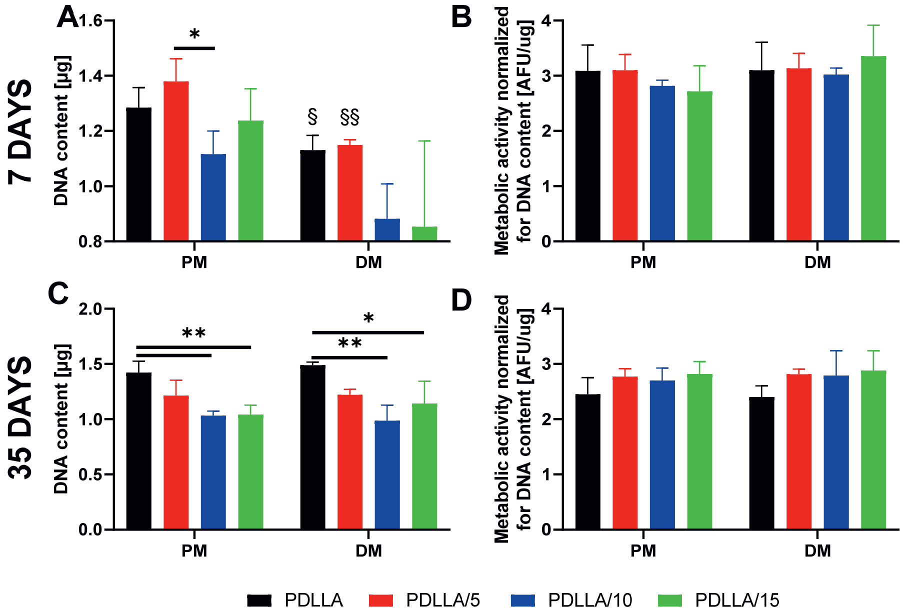

Figure 4. DNA content and metabolic activity from the osteogenic study, after 7 (A and B) and 35 (C and D) days. Statistically significant differences are marked with * ($p<0.05$), ** ($p<0.01$) or *** ($p<0.001$) when comparing the effect of different VD3 concentrations on cells at the same day and with § ($p<0.05$), §§ ($p<0.01$) or §§§ ($p<0.001$) when comparing the effect of different media on cells cultured on scaffolds with the same VD3 content.

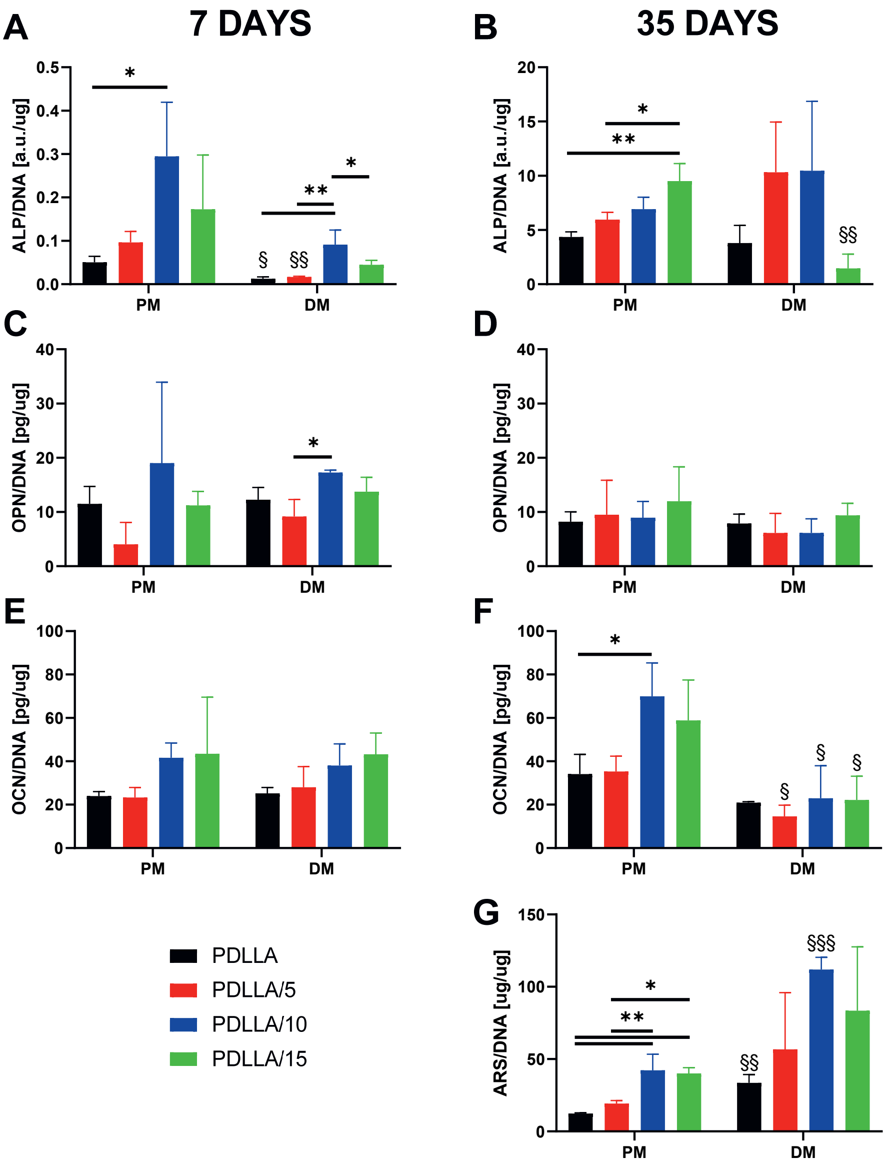

Figure 5. ALP (A and B), OPN (C and D) and OCN (E and F) secretion from the osteogenic study at day 7 (left column) and at day 35 (right column). Results from day 35 include the quantification of calcium deposition via Alizarin Red staining (G). Statistically significant differences are marked with * (p<0.05), ** (p<0.01) or *** (p<0.001) when comparing the effect of different VD3 concentrations on cells at the same day and with § (p<0.05), §§ (p<0.01) or §§§ (p<0.001) when comparing the effect of different media on cells cultured on scaffolds with the same VD3 content.

3.3.6 Immunofluorescence microscopy

VD3 is a relatively hydrophobic compound that might influence the protein adsorption pattern on scaffolds surface and, consequently, cell morphology. As it is known that stem cell morphology can influence cell differentiation, we investigated cell adhesion and spreading by confocal microscopy

(Figure 6 and Figure S2). Cells in MM conditions at 7 days, showed a relatively regular cell pattern on all scaffold types, with cells majorly aligned along the scaffold fiber (Figure S2). Cell cultured on PDLLA and PDLLA/5 exhibited a degree of transversal orientation. Immunofluorescence images at day 7 in PM showed similar cell morphology (data not shown).

We further investigated changes in cell morphology at day 35. Cells cultured for 35 days in PM appeared to have reached confluence and covered the scaffold filaments surface (Figure 6). No major differences in morphology could be seen, with most of the cells exhibiting an elongated shape along the fiber axis. Some cells cultured on PDLLA/10 scaffolds seemed to have aligned transversally with respect to the scaffold filament. Cells cultured for 35 days in MM exhibited a morphology similar to those grown in PM (data not shown).

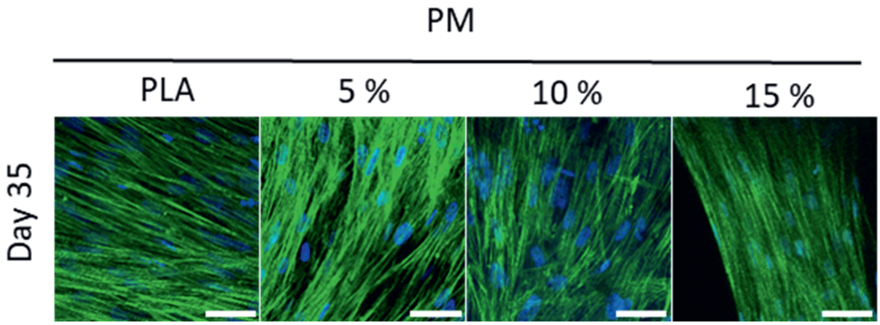

Figure 6. Immunofluorescence images of cells cultured for 35 days on all the scaffold types, in proliferating conditions, from the osteogenic study. In blue, cell nuclei stained with DAPI while in green actin filaments stained with phalloidin. The scale bar represents a distance of 50 µm.

3.4 DISCUSSION

PLA is a well-known polymer widely used in hard-tissue engineering because of its biocompatibility and excellent mechanical properties [1]. However, it exhibits unstable properties when processed in a liquid state at high temperatures, which hinders its use as scaffold material with melt-based AM techniques. Tachibana et al. [16] noticed that the blending with myo-inositol limited the drop in molecular weight during processing. They attributed this result to chain extension. Kang et al. [43] blended PLLA with PCL and magnesium hydroxide to improve, respectively, its brittle behavior and neutralize the acidic moieties from thermal degradation. They indeed observed that the addition of magnesium hydroxide alleviated the molecular weight reduction by inactivating the chain end groups and degradation byproducts capable of backbiting reactions and hydrolysis. Nevertheless, these approaches do not solve the issue of processing high molecular weight grades if not by increasing the operating temperature, which in turn would accelerate the degradation rate [44]. As highlighted by Camarero-Espinosa [7], [8], an initial degradation step is sometimes necessary to enable extrusion of high M_w thermoplastic polymer grades using the bioscaffolder technology. In their study, a poly(ester)urethane (PEU) had to be thermally degraded to enable its extrusion through the printer nozzle. In particular, the polymer M_w was reduced from 125771 kg/mol to 80295 kg/mol by keeping the material isothermally in the printer reservoir for 1 h. Such strategy is sometimes needed because the torque necessary to provide a certain flow rate in an extruder, or in a screw-driven printer such as the one used by Camarero-Espinosa and us, is directly proportional to the zero-shear viscosity of the polymer melt [45]. This is in turn proportional to M_w according to the formula $\eta_0 \sim M_w^{3.4}$ [39]. Therefore, polymer grades of higher molecular weight require higher torque applied to the screw at a constant temperature. In our study, we evaluated the performances of a plasticizer to reduce the viscosity (and therefore the mechanical and thermal energy requirement for extrusion) of a high molecular weight

PDLLA. To not limit the scope of the plasticizer to the manufacturing process, we chose a molecule with known physiological roles such as cholecalciferol, to investigate its additional bioactive potential on mesenchymal stromal cells.

The rheological results confirmed that the plasticization occurred effectively. This is evident from the decreasing trend of zero-shear viscosity with VD3 concentration: the higher the amount of plasticizer, the lower resistance to flow. It is also noteworthy the effect of plasticization on k, which is a material relaxation time: with higher amounts of VD3, the polymer macromolecules take shorter to relax after the cessation of a stress, causing them to be more mobile. In fact, when low molecular weight plasticizers dissolve properly in the polymer matrix, they diffuse between the macromolecules generating free volume and ease of movement, just as an increase in temperature would [6]. This will result in deformation occurring at lower stress and strain values [46], which implies lower energy to induce material flow during processing [47]. Interestingly, the concentration of plasticizer did not seem to have an effect on the slope in the shear-thinning region. This part of the flow curve describes orientation and stretching of the polymer chains along the direction of shear: at low shear rates (smaller than the reciprocal Rouse relaxation time) orientation dominates and is accompanied by disentanglement of the molecules while stretching becomes more and more significant at increasing shear rates [48], [49]. The identical values for n suggest that the plasticizer had no influence at the shear rates corresponding to the power-law region, where the polymer molecules were already sufficiently disentangled to render the plasticizer unnecessary. Instead, at those lower shear rates corresponding to the Newtonian plateau and the transition region, the chains were still in an entangled state, and the presence of the plasticizer played an effective role in determining a difference in the rheological curve for different concentrations.

The results from the time sweeps showed that the presence of VD3 did not have any appreciable stabilization effect. Whereas the drop in viscosity of PDLLA stabilized after an initial decrease, samples containing VD3 showed a reduction in viscosity increasing over time. This trend suggests that VD3 might be degrading for long residence times at such temperatures, as suggested by Pelc et al. and Jakobsen et al. [50], [51]. Thermal degradation results into compounds of lower M_w, which are responsible for the decrease in viscosity as explained previously. However, it is important to note that all blends were tested at the same temperature. Instead, the addition of VD3 allows the processing to be carried out at lower temperatures thanks to its plasticization effect, being the zero-shear viscosity (and therefore the torque requirement for extrusion) lower. Carley and Strub [52] derived the expression for the power required to drag a Newtonian polymer melt through the screw channel against the back pressure originated by the presence of the nozzle, which is (Eq. 3):

$$Z = \eta N^2 \left(\omega + \frac{\alpha\gamma}{\beta + k} \right) \tag{3}$$

Where η is the zero-shear rate viscosity of the polymer melt, N is the screw rotating speed in RPS and ω, α, γ, β and k are parameters containing only the dimensions of the screw and the nozzle and defined as follows:

$$\omega = \frac{\pi^3 D^3 L}{h} \tag{4}$$

$$\alpha = \frac{\pi D h t \cos^2\phi}{2} \tag{5}$$

$$\gamma = \frac{\pi^2 D^2 h \tan\phi}{2} \tag{6}$$

$$\beta = \frac{h^3 t \, sin\phi \, cos\phi}{12L} \tag{7}$$

$$k = \frac{\pi r^4}{8l} \tag{8}$$

Here, *D, h, t, φ, L, r* and *l* are as described in Table 1. By dividing the power *Z* (Eq. 3) by the screw rotation speed *N*, the torque *T* is obtained [45]:

$$T = \frac{Z}{N} \tag{9}$$

In the lab-scale printer used in this study, the torque provided by the stepper motor to the screw is abundantly lower than in the case of similar industrial printers and extruders, being the required throughput also reduced. For this reason, the processing temperatures have to be higher so that to favor the flow of the polymer melt through and screw channel and the nozzle. The low flow rate coupled to the high processing temperatures allow to make the assumption of Newtonian behavior of the polymer melt during deposition. Therefore, taking as η the zero-shear rate values of Table 2, Eq. 9 allows the calculation of the torque required to extruded the grades used in this study at given screw RPS. The extrusion of PDLLA/5 requires 10% less torque than that of PDLLA, the extrusion of PDLLA/10 is 50 and 44% less demanding than PDLLA and PDLLA/5 respectively, and depositing PDLLA/15 requires 42, 47 and 84% of the torque needed for PDLLA; PDLLA/5 and PDLLA/15 respectively. For this reason, the extrusion temperature of each grade could be lowered according to the torque requirement, thus slowing the degradation process, which is directly correlated to temperature itself [44].

Additionally, plasticization is also accompanied by a decrease in the T_g of the polymer [46], [53], [54]. For this reason, we verified whether this occurred to the extent of dropping below body temperature. Since PDLLA is amorphous, a T_g lower than 37 °C would result in rubbery and deformable implants. The results showed that the glass transition temperature did not excessively drop, allowing the safe use of this blend for tissue engineering purposes.

Polymer plasticizers have generally the objective of increasing flexibility and toughness of the matrix, while often contributing to a reduction in strength [21]. This is achieved by a separating the polymer chains and thus allowing easier relative motion [19]. The addition of VD3 to PDLLA, a noteworthy stiff and brittle material with low deformation at break [5], [55], effectively reduced its modulus, although to a limited extent. Nevertheless, we noticed that compositions with the highest plasticizer content unexpectedly exhibited lower elongation at break. Martin and Averous [21] suggested that such behavior could origin from lack of affinity between the materials, although the mechanical properties alone could not be considered absolute evidence of non-compatibility and consequent phase-separation. They suggested lack of affinity between the materials, although the mechanical properties alone could not be considered absolute evidence of non-compatibility. Rheological and DSC data seemed to confirm the miscibility of the two materials to molecular levels. However, these tests were conducted at temperatures that allow mobility in the system. We hypothesize that, upon cooling, some segregation might have taken place, whose extent might have been higher for higher VD3 concentrations. Additionally, an excessive amount of such a low M_w plasticizers might have reduced the entanglement network strength, with detrimental effects on the mechanical properties. These two phenomena could have been responsible for the unexpected mechanical data for PDLLA/10 and PDLLA/15, the blends with indeed the highest VD3 content.

The absence of VD3 in the collected samples from distilled water media (with and without DMSO) could be due to the poor solubility of VD3 as well as PDLLA in water. The insolubility property could result in the aggregation of both molecules on the surface of scaffold rather than diffusion into the medium. However, the addition of NaOH to the media could enhance the surface hydrophilicity of PDLLA by imposing alkaline hydrolysis and speed up polymer's degradation, as explained before [56]. The higher release amount of VD3 in NaOH medium in contrast to NaOH+DMSO containing medium could indicate the detrimental effect of DMSO on release profile. In the presence of DMSO, the miscibility of VD3 in PDLLA increases, which in turn reduced the diffusion rate of this plasticizer from polymer into the media. Similar finding has been reported for the release of doxorubicin from PLA polymer in the presence of DMSO [57]. In addition, the polar aprotic nature of DMSO that dissolves both polar and non-polar compounds could have enabled sustained release of VD3. However, VD3 is only sparingly soluble in DMSO [58], which could explain the lower total amount of this plasticizer in NaOH+DMSO than only NaOH containing medium. On the other hand, in the absence of DMSO, the release of VD3 was mainly dependent on polymer degradation, which was accelerated by NaOH. Furthermore, the irregular release pattern in NaOH medium could imply the inhomogeneous blend of VD3 in PDLLA. As explained by Utracki and Wilkie [55], low M_w compounds in a polymer matrix tend to migrate towards the region with the highest shear rate, thus lowering the energy state of the system. In the case of capillary flow such as the flow in the printer nozzle, the highest shear rate is located at the capillary walls. This should have led to an evenly distributed concentration of VD3 on the scaffolds surface, given a sufficiently long nozzle for full flow development. However, in the equipment used for this study, the fluid flowing through the nozzle arrives from a screw channel, where the flow profile is rather different [45], [59]. In particular, the shear rate is not axisymmetric but develops linearly from a null value at the barrel wall to its maximum at the screw root. We hypothesize that the L/D ratio of the nozzle in use was not sufficiently high for the flow to fully develop from the profile in the screw channel to that of a proper capillary. This could have result in an inhomogeneous distribution of VD3 over the filament cross-section. Additionally, even though by increasing the loading percentage of VD3 the overall release amount of this molecule raised in both media, this relation was not true for 10%wt-loaded scaffolds. This observation emphasizes on the importance of release behavior rather than the loading percentage of VD3 in PDLLA for drug delivery applications.

Vitamin D3 or cholecalciferol is known to be involved in bone metabolism [33], [34], [37] but to our knowledge there are not many examples of its use for TE purposes [60], [61]. In this study, relatively high concentrations were used, which could have had toxic effects on cells. For this purpose, a transwell study was conducted. Results showed comparable proliferation and metabolism for cells cultured on plain and VD3-loaded scaffolds, meaning that the plasticizer did not induced any cytotoxicity. On the contrary, PDLLA/15 scaffolds showed greater proliferation with respect to the other groups, which remains unexplained as several authors reported the anti-proliferative properties of VD3 [31], [33], [62], [63]. In addition, cells cultured on PDLLA/5 scaffolds exhibited an increase in metabolic activity over the culture. As highlighted by Calore et al. [64], the PrestoBlue^{TM} assay employed here is based on the reduction of resazurin to resorufin by mitochondrial activity, which is often increased during differentiation.

During the osteogenic study, cells showed to be similarly metabolically active on all scaffold types and in both media, indication that the high concentration of VD3 did not have any toxic effect on cultures longer than 3 days. The proliferation data showed lower cell amount for scaffolds with 10 and 15 wt% VD3, which we hypothesize being due to the probable higher concentration of the plasticizer on the fibers surface. VD3 is, in fact, relatively hydrophobic [65] and this characteristic might have affected the initial amount of attached cells. Comparing data from D7 with D35, it seems that cells cultured on VD3-loaded scaffolds did not proliferate. This appears to be in line with previous studies [34], [62], [66], where it was reported the anti-proliferative effect of vitamin D3.

The trend shown by the osteogenic markers in basic conditions suggests that cells cultured on PDLLA/10 and 15 scaffolds might be in the mature osteoblast phase, when mineralization is still in an early phase. This is suggested in particular by the significantly higher amount of deposited calcium and the peaks in OCN amounts, whose secretion is known to be VD3-responsive [67]. According to Aubin

[68], during osteogenic differentiation ALP increases until mineralization is well progressed, at the beginning of which OCN appears. PDLLA/10 and 15 conditions showed increasing ALP and OCN over the culture, in addition to greater calcium deposition compared to the other scaffolds. This could not be further supported by immunofluorescence images, where cells showed comparable morphology over all culture conditions and no specific lineage-related change could be noted. OPN is supposed to peak twice during proliferation and once more prior to the upregulation of OCN [68]. In this study, we did not see any condition inducing enhanced OPN secretion. We suggest that the chosen time points did not temporally match the OPN peaks. Nevertheless, we expect that the peaks relative to proliferation would have pertained only the PDLLA scaffolds while PDLLA/10 and 15 would have shown that peak supposed to appear right before OCN. It is important to note how cells cultured on PDLLA/5 exhibited the same behavior of those grown on PDLLA. This suggests that there might be a threshold concentration below which there seem to be no osteogenic effect on cells. Such a possibility arises from the potential inhomogeneous distribution of VD3 over the filament cross-section as previously explained, which would influence both the plasticizer availability per unit of time but also the release profile over the whole culture period.

In mineralization conditions, cells cultured on VD3-loaded scaffolds did not generally show significant differences in osteogenic markers secretion compared to cells grown on plain PDLLA. Despite the wide variations, ARS data suggest that VD3 enhanced mineralization. ALP values seems to support this finding for PDLLA/5 and 10 scaffolds, suggesting the presence in the mature osteoblast phase. It is important to note that Aubin [68] suggested that the secretion of bone lineage proteins is often heterogeneous in individual cells but mainly mineralization is the clearest expression of osteogenic differentiation. The low ALP values for PDLLA/15, coupled to the presence of deposited calcium, might be the sign of an even more advanced differentiation stage, for which it would be then plausible to observe a lower OCN secretion.

Comparing the cell behavior in the two different environments shows that the coupled presence of VD3 and dexamethasone might have a lower impact on osteogenesis than the sole VD3.

Overall, the results seem to suggest that the metabolically inactive cholecalciferol can promote osteogenic differentiation *in vitro* as well as its active metabolite calcitriol. This supports the finding that hMSCs have the enzymatic toolbox to metabolize vitamin D3 into the active form calcitriol [37]. Current *in vitro* osteogenic protocols include the use of dexamethasone, a steroid that is not present *in vivo* nor regulates the physiological differentiation of osteoblast precursors [69]. Costa et al. [70] pointed out that dexamethasone has toxic effects at concentrations above 1000 nM and that severe bone loss and osteoporosis were associated to prolonged treatments with dexamethasone. Our study suggests that cholecalciferol could be considered as a cheaper alternative to calcitriol but also as a less harmful substitute of dexamethasone for tissue engineering purposes. Nevertheless, our results derive from the specific processing conditions used. In fact, Wubneh et al. [71] suggested that drug concentration and spatial distribution are controlled by the fabrication process, and highly impact the drug effectiveness and release rate. As a blend morphology is a complex interplay between material properties and processing conditions [55], future studies should aim at evaluating the effect of different manufacturing parameters (namely, shear rate) on the distribution of VD3 within the scaffold fiber, and the resulting release kinetics and osteogenic potential.

3.5 CONCLUSIONS

This study presents the plasticization of a commonly used synthetic polymer to decrease its melt viscosity, and therefore the energy requirements for extrusion, with potential reduction of thermal degradation. In addition, the adoption of such strategy allows the processing of those high M_w grades that might require an initial degradation step for extrusion. The materials were blended in melt state to evaluate the feasibility of mixing directly in the printer, to obtain a single-step process. Rheological evaluation confirmed a reduction in viscosity whilst DSC measurements and tensile testing revealed a pronounced drop in glass transition and mechanical properties with the addition of VD3. However, the drop in performance reduces for higher concentrations of the plasticizer. This will not hinder performances in a biological environment. Furthermore, we report that the plasticizer of choice, the metabolically inactive cholecalciferol, seemed to support osteogenic differentiation and mineralization as much as mineralization culture conditions, confirming the presence in hMSCs of the enzymatic toolbox for VD3 metabolism.

ACKNOWLEDGMENTS

Some of the materials were kindly provided by Corbion Purac Biomaterials (The Netherlands). This work was financed by Brightlands Material Center and by the Dutch Province of Limburg.

REFERENCES

[1] C. A. Van Blitterswijk and J. De Boer, *Tissue Engineering: Second Edition*. Elsevier, 2014. doi: 10.1016/C2013-0-00564-6.

[2] C. Mota, D. Puppi, F. Chiellini, and E. Chiellini, “Additive manufacturing techniques for the production of tissue engineering constructs,” *J Tissue Eng Regen Med*, vol. 9, no. 3, pp. 174–190, 2015, doi: 10.1002/term.1635.

[3] J. C. Middleton and A. J. Tipton, “Synthetic biodegradable polymers as orthopedic devices,” *Biomaterials*, vol. 21, no. 23, pp. 2335–2346, 2000, doi: Doi 10.1016/S0142-9612(00)00101-0.

[4] D. W. Hutmacher, “Scaffold design and fabrication technologies for engineering tissues - State of the art and future perspectives,” *J Biomater Sci Polym Ed*, vol. 12, no. 1, pp. 107–124, 2001, doi: 10.1163/156856201744489.

[5] J. B. Hoying and S. K. Williams, *Essentials of 3D Biofabrication and Translation*. Winston-Salem, NC, USA: Elsevier, 2015. doi: 10.1016/C2013-0-18665-5.

[6] T. Osswald and N. Rudolph, *Polymer Rheology*. München: Carl Hanser Verlag GmbH & Co. KG, 2014. doi: 10.3139/9781569905234.

[7] S. Camarero-Espinosa, A. R. Calore, A. Wilbers, J. Harings, and L. Moroni, “Additive manufacturing of an elastic poly(ester)urethane for cartilage tissue engineering,” *Acta Biomater*, vol. 102, pp. 192–204, Jan. 2020, doi: 10.1016/j.actbio.2019.11.041.

[8] S. Camarero-Espinosa, C. Tomasina, A. R. Calore, and L. Moroni, “Additive manufactured, highly resilient, elastic, and biodegradable poly(ester)urethane scaffolds with chondroinductive properties for cartilage tissue engineering,” *Mater Today Bio*, vol. 6, p. 100051, Mar. 2020, doi: 10.1016/j.mtbio.2020.100051.

[9] A. R. Calore, R. Sinha, J. Harings, K. V Bernaerts, C. Mota, and L. Moroni, “Chapter 7 Thermoplastics for Tissue Engineering,” in *Computer-Aided Tissue Engineering*, A. Rainer and L. Moroni, Eds., 2021, pp. 75–99.

[10] K. Ragaert, A. Dekeyser, L. Cardon, and J. Degrieck, “Quantification of Thermal Material Degradation During the Processing of Biomedical Thermoplastics,” *J Appl Polym Sci*, vol. 120, no. 5, pp. 2872–2880, 2011, doi: 10.1002/app.33323.

[11] P. S. P. Poh *et al.*, “Polylactides in additive biomanufacturing,” *Adv Drug Deliv Rev*, vol. 107, pp. 228–246, 2016, doi: 10.1016/j.addr.2016.07.006.

[12] G. Y. H. Choong and D. S. A. De Focatiis, “A method for the determination and correction of the effect of thermal degradation on the viscoelastic properties of degradable polymers,” *Polym Degrad Stab*, vol. 130, pp. 182–188, 2016, doi: 10.1016/j.polymdegradstab.2016.06.018.

[13] H. J. Lehermeier and J. R. Dorgan, “Melt rheology of poly(lactic acid): Consequences of blending chain architectures,” *Polym Eng Sci*, vol. 41, no. 12, pp. 2172–2184, 2001, doi: Doi 10.1002/Pen.10912.

[14] M. Villalobos, A. Awojulu, T. Greeley, G. Turco, and G. Deeter, “Oligomeric chain extenders for economic reprocessing and recycling of condensation plastics,” *Energy*, vol. 31, no. 15, pp. 3227–3234, Dec. 2006, doi: 10.1016/j.energy.2006.03.026.

[15] L. X. Yang, X. S. Chen, and X. B. Jing, “Stabilization of poly(lactic acid) by polycarbodiimide,” *Polym Degrad Stab*, vol. 93, no. 10, pp. 1923–1929, 2008, doi: 10.1016/j.polymdegradstab.2008.06.016.

[16] Y. Tachibana, T. Maeda, O. Ito, Y. Maeda, and M. Kunioka, “Biobased myo-inositol as nucleator and stabilizer for poly(lactic acid),” *Polym Degrad Stab*, vol. 95, no. 8, pp. 1321–1329, 2010, doi: 10.1016/j.polymdegradstab.2010.02.007.

[17] L. K. Parthasarathy, R. S. Seelan, C. Tobias, M. F. Casanova, and R. N. Parthasarathy, “Mammalian inositol 3-phosphate synthase: Its role in the biosynthesis of brain inositol and its clinical use as a psychoactive agent,” in *Subcellular Biochemistry*, Springer US, 2006, pp. 293–314. doi: 10.1007/0-387-27600-9_12.

[18] T. D. Ngo, A. Kashani, G. Imbalzano, K. T. Q. Nguyen, and D. Hui, “Additive manufacturing (3D printing): A review of materials, methods, applications and challenges,” *Composites Part B: Engineering*, vol. 143. Elsevier Ltd, pp. 172–196, Jun. 15, 2018. doi: 10.1016/j.compositesb.2018.02.012.

[19] Norman E. Dowling, *Mehcanical Behavior of Materials*. Prentice hall, 2013.

[20] C. A. Harper, *Modern Plastics Handbook*. 2000.

[21] O. Martin and L. Avérous, “Poly(lactic acid): Plasticization and properties of biodegradable multiphase systems,” *Polymer (Guildf)*, vol. 42, no. 14, pp. 6209–6219, Apr. 2001, doi: 10.1016/S0032-3861(01)00086-6.

[22] Z. Ma, Z. Mao, and C. Gao, “Surface modification and property analysis of biomedical polymers used for tissue engineering,” *Colloids and Surfaces B: Biointerfaces*, vol. 60, no. 2. Elsevier, pp. 137–157, Nov. 15, 2007. doi: 10.1016/j.colsurfb.2007.06.019.

[23] M. Cámara-Torres *et al.*, “Tuning Cell Behavior on 3D Scaffolds Fabricated by Atmospheric Plasma-Assisted Additive Manufacturing,” *ACS Appl Mater Interfaces*, vol. 13, no. 3, 2021, doi: 10.1021/acsami.0c19687.

[24] Y. Zhu, M. F. Leong, W. F. Ong, M. B. Chan-Park, and K. S. Chian, “Esophageal epithelium regeneration on fibronectin grafted poly(l-lactide-co-caprolactone) (PLLC) nanofiber scaffold,” *Biomaterials*, vol. 28, no. 5, pp. 861–868, Feb. 2007, doi: 10.1016/j.biomaterials.2006.09.051.

[25] G. Marchioli *et al.*, “Hybrid Polycaprolactone/Alginate Scaffolds Functionalized with VEGF to Promote de Novo Vessel Formation for the Transplantation of Islets of Langerhans,” *Adv Healthc Mater*, vol. 5, no. 13, pp. 1606–1616, 2016, doi: 10.1002/adhm.201600058.

[26] E. S. Place, J. H. George, C. K. Williams, and M. M. Stevens, “Synthetic polymer scaffolds for tissue engineering,” *Chem Soc Rev*, vol. 38, no. 4, pp. 1139–1151, Mar. 2009, doi: 10.1039/b811392k.

[27] J. J. Yoon, J. H. Kim, and G. Park, “Dexamethasone-releasing biodegradable polymer scaffolds fabricated by a gas-foaming/salt-leaching method,” *Biomaterials*, vol. 24, pp. 2323–2329, 2003, doi: 10.1016/S0142-9612(03)00024-3.

[28] M. A. Bhutto, T. Wu, B. Sun, H. EI-Hamshary, S. S. Al-Deyab, and X. Mo, “Fabrication and characterization of vitamin B5 loaded poly (l-lactide-co-caprolactone)/silk fiber aligned electrospun nanofibers for schwann cell proliferation,” *Colloids Surf B Biointerfaces*, vol. 144, pp. 108–117, Aug. 2016, doi: 10.1016/J.COLSURFB.2016.04.013.

[29] F. F. R. Damanik, C. van Blitterswijk, J. Rotmans, and L. Moroni, “Enhancement of synthesis of extracellular matrix proteins on retinoic acid loaded electrospun scaffolds,” *J Mater Chem B*, vol. 6, no. 40, pp. 6468–6480, Oct. 2018, doi: 10.1039/C8TB01244J.

[30] W. Y. Yeong, C. K. Chua, K. F. Leong, and M. Chandrasekaran, “Rapid prototyping in tissue engineering: Challenges and potential,” *Trends in Biotechnology*, vol. 22, no. 12. Elsevier Current Trends, pp. 643–652, Dec. 01, 2004. doi: 10.1016/j.tibtech.2004.10.004.

[31] P. H. Anderson and G. J. Atkins, “The skeleton as an intracrine organ for vitamin D metabolism,” *Molecular Aspects of Medicine*, vol. 29, no. 6. Pergamon, pp. 397–406, Dec. 01, 2008. doi: 10.1016/j.mam.2008.05.003.

[32] Y.-C. Hou *et al.*, “The Role of Vitamin D in Modulating Mesenchymal Stem Cells and Endothelial Progenitor Cells for Vascular Calcification,” *Int J Mol Sci*, vol. 21, no. 7, p. 2466, Apr. 2020, doi: 10.3390/ijms21072466.

[33] S. Zhou, M. S. LeBoff, and J. Glowacki, “Vitamin D Metabolism and Action in Human Bone Marrow Stromal Cells,” *Endocrinology*, vol. 151, no. 1, pp. 14–22, Jan. 2010, doi: 10.1210/en.2009-0969.

[34] S. Geng, S. Zhou, Z. Bi, and J. Glowacki, “Vitamin D metabolism in human bone marrow stromal (mesenchymal stem) cells,” *Metabolism: Clinical and Experimental*, vol. 62, no. 6. W.B. Saunders, pp. 768–777, Jun. 01, 2013. doi: 10.1016/j.metabol.2013.01.003.

[35] D. J. Kang, H. S. Lee, J. T. Park, J. S. Bang, S. K. Hong, and T. Y. Kim, “Optimization of culture conditions for the bioconversion of vitamin D3 to 1α,25-dihydroxyvitamin D3 using Pseudonocardia autotrophica ID9302,” *Biotechnology and Bioprocess Engineering*, vol. 11, no. 5, pp. 408–413, Oct. 2006, doi: 10.1007/BF02932307.

[36] D. Feldman, J. W. Pike, and J. S. Adams, *Vitamin D*. Elsevier, 2011. doi: 10.1016/C2009-1-63406-7.

[37] F. Meng *et al.*, “Fibroblast growth factor 23 counters vitamin D metabolism and action in human mesenchymal stem cells,” *J Steroid Biochem Mol Biol*, vol. 199, p. 105587, May 2020, doi: 10.1016/j.jsbmb.2020.105587.

[38] R. Sinha *et al.*, “Additive manufactured scaffolds for bone tissue engineering : physical characterization of thermoplastic composites with functional fillers,” 2021, doi: https://doi.org/10.1101/2021.03.23.436548.

[39] C. Macosko, *Rheology: Principles, Measurements and Applications*. 1994.

[40] M. Cámara-Torres, R. Sinha, C. Mota, and L. Moroni, “Improving cell distribution on 3D additive manufactured scaffolds through engineered seeding media density and viscosity,” *Acta Biomater*, vol. 101, pp. 183–195, Jan. 2020, doi: 10.1016/J.ACTBIO.2019.11.020.

[41] C. A. Gregory, W. G. Gunn, A. Peister, and D. J. Prockop, “An Alizarin red-based assay of mineralization by adherent cells in culture: Comparison with cetylpyridinium chloride extraction,” *Anal Biochem*, vol. 329, no. 1, pp. 77–84, Jun. 2004, doi: 10.1016/j.ab.2004.02.002.

[42] F. A. Morrison, *Understanding Rheology*, vol. 12, no. 5. 2001.

[43] E. Y. Kang, E. Lih, I. H. Kim, Y. K. Joung, and D. K. Han, “Effects of poly(L-lactide-ε-caprolactone) and magnesium hydroxide additives on physico-mechanical properties and degradation of poly(L-lactic acid),” *Biomater Res*, vol. 20, no. 1, p. 7, Dec. 2016, doi: 10.1186/s40824-016-0054-6.

[44] V. Speranza, A. De Meo, and R. Pantani, “Thermal and hydrolytic degradation kinetics of PLA in the molten state,” *Polym Degrad Stab*, vol. 100, pp. 37–41, Feb. 2014, doi: 10.1016/j.polymdegradstab.2013.12.031.

[45] C. Rauwendaal, *Polymer Extrusion*. München: Carl Hanser Verlag GmbH & Co. KG, 2014. doi: 10.3139/9781569905395.

[46] M. A. Meyers and K. K. Chawla, *Mechanical Behavior of Materials*, vol. 2. Cambridge: Cambridge University Press, 2008. doi: 10.1017/CBO9780511810947.

[47] R. S. Mallouk and J. M. McKelvey, “Power Requirements of Melt Extruders,” *Ind Eng Chem*, vol. 45, no. 5, pp. 987–989, May 1953, doi: 10.1021/ie50521a035.

[48] S. Coppola, N. Grizzuti, and P. L. Maffettone, “Microrheological modeling of flow-induced crystallization,” *Macromolecules*, vol. 34, no. 14, pp. 5030–5036, 2001, doi: 10.1021/ma010275e.

[49] C. McIlroy and P. D. Olmsted, “Deformation of an Amorphous Polymer during the Fused-Filament-Fabrication Method for Additive Manufacturing,” 2016, doi: 10.1122/1.4976839.

[50] B. Pelc and D. H. Marshall, “Thermal transformation of cholecalciferol between 100-170°C,” *Steroids*, vol. 31, no. 1, pp. 23–29, 1978, doi: 10.1016/0039-128X(78)90017-X.

[51] J. Jakobsen and P. Knuthsen, “Stability of vitamin D in foodstuffs during cooking,” *Food Chem*, vol. 148, pp. 170–175, Apr. 2014, doi: 10.1016/j.foodchem.2013.10.043.

[52] J. F. Carley and R. A. Strub, “Application of Theory to Design of Screw Extruders,” *Ind Eng Chem*, vol. 45, no. 5, pp. 978–982, 1953, doi: 10.1021/ie50521a033.

[53] D. W. Van Krevelen and K. Te Nijenhuis, *Properties of polymers*. Elsevier, 2009.

[54] I. M. Ward and J. Sweeney, *An Introduction to the Mechanical Properties of Solid Polymers*, vol. 17. 2004. doi: 10.1002/1521-3773(20010316)40:6<9823::AID-ANIE9823>3.3.CO;2-C.

[55] L. A. Utracki and C. A. Wilkie, *Polymer Blends Handbook*. Dordrecht: Springer Netherlands, 2014. doi: 10.1007/978-94-007-6064-6.

[56] C. Y. Tham, Z. A. A. Hamid, Z. A. Ahmad, and H. Ismail, “Surface Engineered Poly(lactic acid) (PLA) Microspheres by Chemical Treatment for Drug Delivery System,” *Key Eng Mater*, vol. 594–595, pp. 214–218, Dec. 2013, doi: 10.4028/www.scientific.net/KEM.594-595.214.

[57] S. Park, Y. Yuan, K. Choi, S.-O. Choi, and J. Kim, “Doxorubicin Release Controlled by Induced Phase Separation and Use of a Co-Solvent,” *Materials*, vol. 11, no. 5, p. 681, Apr. 2018, doi: 10.3390/ma11050681.

[58] F. Almarri *et al.*, “Solubility and thermodynamic function of vitamin D3 in different mono solvents,” *J Mol Liq*, vol. 229, pp. 477–481, Mar. 2017, doi: 10.1016/j.molliq.2016.12.105.

[59] J. Vlachopoulos and D. Strutt, “The role of rheology in polymer extrusion,” in *New Technology for Extrusion Conference. Milan, Italy. Nov*, 2003, pp. 20–21.

[60] N. Ignjatović, V. Uskoković, Z. Ajduković, and D. Uskoković, “Multifunctional hydroxyapatite and poly(d,l-lactide-co-glycolide) nanoparticles for the local delivery of cholecalciferol,” *Materials Science and Engineering C*, vol. 33, no. 2, pp. 943–950, Mar. 2013, doi: 10.1016/j.msec.2012.11.026.

[61] F. Fayyazbakhsh, M. Solati-Hashjin, A. Keshtkar, M. A. Shokrgozar, M. M. Dehghan, and B. Larijani, “Release behavior and signaling effect of vitamin D3 in layered double hydroxides-hydroxyapatite/gelatin bone tissue engineering scaffold: An in vitro evaluation,” *Colloids Surf B Biointerfaces*, vol. 158, pp. 697–708, Oct. 2017, doi: 10.1016/J.COLSURFB.2017.07.004.

[62] O. Fromigué, P. J. Marie, and A. Lomri, “Differential effects of transforming growth factor β2, dexamethasone and 1,25-Dihydroxyvitamin D on human bone marrow stromal cells,” *Cytokine*, vol. 9, no. 8, pp. 613–623, 1997, doi: 10.1006/cyto.1997.0209.

[63] P. Lips, “Vitamin D physiology,” *Prog Biophys Mol Biol*, vol. 92, no. 1, pp. 4–8, Sep. 2006, doi: 10.1016/j.pbiomolbio.2006.02.016.

[64] A. R. Calore *et al.*, “Shaping and properties of thermoplastic scaffolds in tissue regeneration: The effect of thermal history on polymer crystallization, surface characteristics and cell fate,” *J Mater Res*, vol. 36, no. 19, pp. 3914–3935, 2021, doi: 10.1557/s43578-021-00403-2.

[65] S. Deb, A. A. Reeves, and S. Lafortune, “Simulation of Physicochemical and Pharmacokinetic Properties of Vitamin D3 and Its Natural Derivatives,” *Pharmaceuticals*, vol. 13, no. 8, p. 160, Jul. 2020, doi: 10.3390/ph13080160.

[66] S. Geng, S. Zhou, and J. Glowacki, “Effects of 25-hydroxyvitamin D3 on proliferation and osteoblast differentiation of human marrow stromal cells require CYP27B1/1α-hydroxylase,” *Journal of Bone and Mineral Research*, vol. 26, no. 5, pp. 1145–1153, May 2011, doi: 10.1002/jbmr.298.

[67] J. B. Lian and G. S. Stein, “Concepts of Osteoblast Growth and Differentiation: Basis for Modulation of Bone Cell Development and Tissue Formation,” *Critical Reviews in Oral Biology & Medicine*, vol. 3, no. 3, pp. 269–305, Apr. 1992, doi: 10.1177/10454411920030030501.

[68] J. E. Aubin, “Regulation of Osteoblast Formation and Function,” *Rev Endocr Metab Disord*, vol. 2, no. 1, pp. 81–94, 2001, doi: 10.1023/A:1010011209064.

[69] F. E. Freeman, H. Y. Stevens, P. Owens, R. E. Guldberg, and L. M. McNamara, “Osteogenic Differentiation of Mesenchymal Stem Cells by Mimicking the Cellular Niche of the Endochondral Template,” *Tissue Eng Part A*, vol. 22, no. 19–20, pp. 1176–1190, Oct. 2016, doi: 10.1089/ten.tea.2015.0339.

[70] P. F. Costa, A. M. Puga, L. Díaz-Gomez, A. Concheiro, D. H. Busch, and C. Alvarez-Lorenzo, “Additive manufacturing of scaffolds with dexamethasone controlled release for enhanced bone regeneration,” *Int J Pharm*, vol. 496, no. 2, pp. 541–550, 2015, doi: 10.1016/j.ijpharm.2015.10.055.

[71] A. Wubneh, E. K. Tsekoura, C. Ayranci, and H. Uludağ, “Current state of fabrication technologies and materials for bone tissue engineering,” *Acta Biomater*, vol. 80, pp. 1–30, Oct. 2018, doi: 10.1016/j.actbio.2018.09.031.

SUPPLEMENTARY INFORMATION

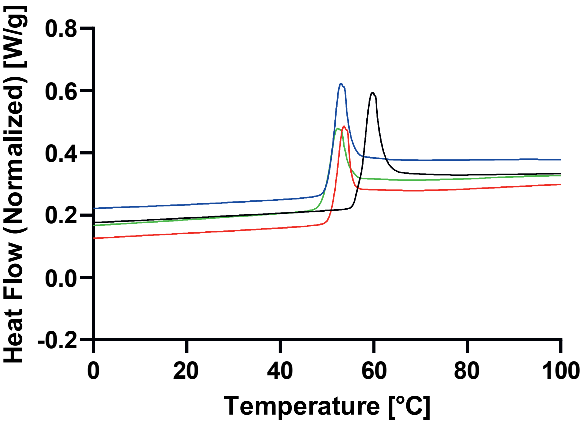

Figure S1. Representative DSC thermograms of plain PDLLA and PDLLA/VD3 blends. The peak is typical of latent stresses in the material originated by the quenching of the extrudate.

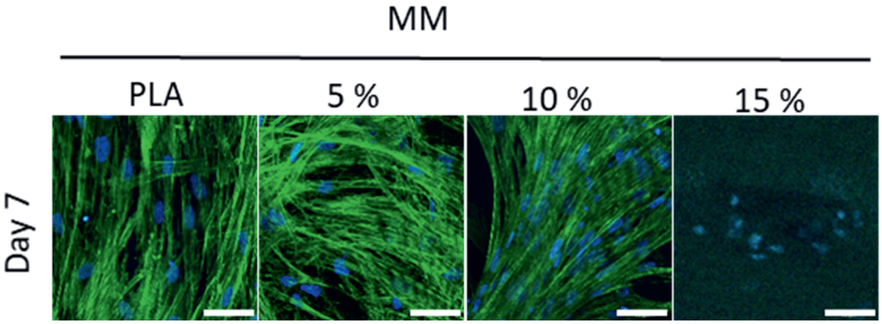

Figure S2. Immunofluorescence images of cells cultured on all scaffold types from the osteogenic study, ad day 7 from mineralization conditions. In blue, cell nuclei stained with DAPI while in green actin filaments stained with phalloidin. The scale bar represents a distance of 50 µm.

Chapter 4

MANUFACTURING OF SCAFFOLDS WITH INTERCONNECTED INTERNAL OPEN POROSITY AND SURFACE ROUGHNESS

Andrea Roberto Calore[1, 2], Varun Srinivas[2], Linda Groenendijk[2], Andrada Serafim[3], Izabela Cristina Stancu[3,4], Arnold Wilbers[5], Nils Leoné[2], Ane Albillos Sanchez[1], Dietmar Auhl[2,6], Carlos Mota[1], Katrien Bernaerts[2], Jules A.W. Harings[2], Lorenzo Moroni[1]*

[1] MERLN Institute for Technology-Inspired Regenerative Medicine, Complex Tissue Regeneration department, Maastricht University, Maastricht, the Netherlands

[2] Aachen-Maastricht Institute for Biobased Materials (AMIBM), Maastricht University, Geleen, the Netherlands

[3] Advanced Polymer Materials Group, University Politehnica of Bucharest, Romania

[5] DSM Materials Science Center, Geleen, the Netherlands

[6] Polymerwerkstoffe und -technologien, Technische Universität Berlin

Chapter published in Acta Biomaterialia, 156, 158-176.

ABSTRACT

Manufacturing of three-dimensional scaffolds with multiple levels of porosity are an advantage in tissue regeneration approaches to influence cell behavior. Three-dimensional scaffolds with surface roughness and intra-filament open porosity were successfully fabricated by additive manufacturing combined with chemical foaming and porogen leaching without the need of toxic solvents. The decomposition of sodium citrate, a chemical blowing agent generated pores within the scaffold filaments, which were interconnected and opened to the external environment by leaching of a water-soluble sacrificial phase, as confirmed by micro-CT and buoyancy measurements. The additional porosity did not result in lower elastic modulus, but in higher strain at maximum load, *i.e.* scaffold ductility. Human mesenchymal stromal cells cultured for 24 h adhered in greater numbers on these scaffolds when compared to plain additive-manufactured ones, irrespectively of the scaffold pre-treatment method. Additionally, they showed a more spread and random morphology, which is known to influence cell fate. Cells cultured for a longer period exhibited enhanced metabolic activity while secreting higher osteogenic markers after 7 days in culture.

4.1 INTRODUCTION

Tissue engineering is gaining every day more interest as a strategy to regenerate tissues with the patient's own cells without waiting for a human donor or dealing with rejection. Key to this framework are scaffolds. Scaffolds are temporary macroscopically shaped structures that support cell growth and provide the right environmental stimuli to drive tissue regeneration with a designated geometry.

Additive manufacturing (AM) has emerged as a very versatile group of techniques for scaffold production, where objects are produced in a layer-by-layer manner [1], [2]. Depending on the specific technique, a single layer is created by depositing, joining and solidifying materials according to the desired patterns. This allows the production of scaffolds with the desired morphology and a highly interconnected porous structure, with the goal of matching the architecture of the tissue to be regenerated. In parallel, it provides adequate internal space for cell and tissue growth and matching macroscopic mechanical properties. Among AM technologies, extrusion-based techniques are based on extruding the targeted material through a nozzle by applying pressure and depositing it along the desired pattern by moving the extrusion head or the underneath stage. The material can be either in molten state (heating is therefore needed in addition to pressure) or a slurry (for which pressure suffices but a liquid suspension bath is often needed additionally). This set of techniques has emerged as one of the most appealing within the AM domain. This is mainly due to the relatively simple equipment needed and the limited requirements for the materials to be processed.

Poly(lactide) (PLA) is a thermoplastic polyester that has been extensively used with melt-extrusion based methods for scaffold manufacturing. The main reasons for its success are the biodegradability via hydrolysis and the tunable properties as a function of enantiomeric purity [3]. Its relatively high glass transition temperature (T_g) of around 55-60 °C makes it a glassy material at body temperature when compared to more ductile polymers like Poly(caprolactone) (PCL) [4]. This translates into stiff scaffolds able to withstand high loads with very limited deformation. For this reason, PLA has been successfully employed for hard-tissue engineering [5], [6]. However, highly stiff scaffolds typically undergo brittle failure, leaving the surrounding tissue unsupported. Furthermore, excessive stiffness of the implant could also lead to a reduction in loads on the healthy tissue (stress shielding), resulting in its weakening over time [7].

Thanks to the full control over the layers' geometry, AM allows the tuning of the scaffold mechanical properties without selecting different materials. By simply varying the layer pattern, the overall porosity can be tailored and therefore the final mechanical properties [8], [9]. While coarser morphologies allow for lower compression performances [10], the available surface area for cell attachment and proliferation would decrease as well, reducing the regeneration efficiency. Taking inspiration from nature, tissue engineers have turned their attention to hierarchical cellular structures to increase both scaffold ductility and available surface area. This would allow properly mimicking of tissues with complex architectures and mechanics such as the trabeculated region of cancellous bone, to restore small- to mid-size defects. With particular reference to the mechanical properties of trabecular bone, ductility is in fact favorable with respect to toughness when manufacturing scaffolds with thermoplastic polymers. The reason is that a ductile scaffold can plastically deform under load instead of failing at (potentially) very large stresses but in a brittle manner, as it might happen with very stiff yet tough materials. In addition, intrafiber open porosity may further assist in a gradual disposal of degradation products from the regenerated tissue, such as those acidic compounds originating from PLA molecules breakdown. Accumulation of acidic degradation products like lactic acid were reported to form and accumulate in the bulk volume of PLA objects and may cause upon sudden burst release adverse effect on the direct physiological environment [11]. By coupling extrusion-based techniques and conventional techniques such as phase separation [12], particulate leaching [13], freeze-drying [14], emulsion/foam templating [15], lower-scale porosity (microporosity) could be generated both within the fibers and on the surface in addition to the porosity coming from the deposition pattern (macroporosity).

Endothermic chemical blowing or foaming agents (CBA or CFA, respectively) are compounds that decompose to form gases under processing conditions. They have been successfully coupled to AM of metals [16] and bioactive glasses [17] to introduce lower-scale porosity. The main advantage of CFAs is that they do not require specific equipment or any modification of the existing one: the agent can be simply added with the polymer in the machine [18]. This makes CFAs attractive for melt-extrusion-based techniques and thermoplastic polymers, as shown by Yoo et al. [19]. The researchers used an extruder to blend polypropylene (PP) and azodicarbonamide (ADC) as main thermoplastic matrix and CFA, respectively. The obtained filament was then fed to a Fused Deposition Modelling (FDM) printer to print structures with pores originating from the decomposition of ADC. They reported several length scales of porosity but they did not investigate the possible interconnectivity and accessibility to the pores from outside the printed parts. CFA have been employed also in the context of additive manufacturing for tissue engineering. An example is given by the work of Choi et al. [20]. In this study, ADC was once again chosen as CFA, while the main matrix consisted of PLA. A filament was produced by blending the components in an extruder, and then printed with a FDM machine. The biological performances of manufactured scaffolds were tested and cells cultured on foamed constructs showed higher proliferation rate than those grown on neat PLA scaffolds. Nevertheless, the interconnectivity between pores and their accessibility from the outside was again not evaluated. However, the foaming agent needs to be chosen with care from a chemical point of view, as it shall not decompose during compounding, but thermally triggered upon AM. The foaming process starts with the formation of high-density nuclei upon reaching the decomposition temperature. Following the nucleation, cell growth starts and coalescence might occur. To avoid the collapse of the extrudate and facilitate processing, it is advisable to control and contain the growth to prevent excessive coalescence [21], [22]. Reducing the polymer melt temperature, and therefore increasing its viscosity, allows for limited coalescence [18]. As a result, the formation of open pores on the surface and interconnectivity throughout the fiber will be hindered, making this further porosity not available for cell infiltration.

Surface roughness is also a key property to consider when designing scaffolds for tissue regeneration, as it was shown to have an effect on both cell adhesion and proliferation in 2D [23]–[25] as well as in 3D [26], [27]. Mesenchymal stromal cells (hMSCs) differentiation was also influenced by roughness in 2D [28] and in 3D [26], [29], [30]. However, as demonstrated in the 3D studies, further steps following the scaffold manufacturing were needed to introduce roughness. In extrusion-based techniques, in fact, a polymer melt flows through a nozzle with a diameter in the order of hundreds of micrometers. The high shear rates are partially responsible for extrudates with very smooth surfaces, making additional processing necessary [26], [31]–[33]. More specifically, the balance between molecules relaxation rate and surface tension during cooling determines whether the polymer will continue flowing thus filling any potential inhomogeneity originated during extrusion, or asperities and void will remain [34].

In an attempt to manufacture scaffolds with both surface roughness and internal microporosity in a single step, we combined chemical foaming with porogen leaching. A side beneficial effect of this approach is that the interconnected porosity entails enhanced transport of nutrients and degradation products. Sodium citrate, a chemical foaming agent, was employed to introduce microporosity within the deposited fibers. Many examples from literature show that salts were the preferential choice for their straightforward solubility and leaching [13], [35], [36]. Nevertheless, remnants of salts in an implanted scaffold could be problematic [37]. To avoid this issue, poly(vinyl alcohol) (PVA) was chosen as sacrificial phase to create micropore interconnectivity and surface roughness. Additionally, blends of immiscible polymers allow the formation of domains, whose size can be controlled via molecular and processing parameters [38], [39]. PVA, which is water-soluble and biocompatible [40]–[42], was pre-blended with poly (l-lactide) (PLLA) and sodium citrate. After AM and foaming of the CFA, the sacrificial phase was leached out and scaffolds with surface roughness and interconnected micro-porosity could be obtained. This was confirmed by SEM, micro-CT and Archimedes method [43]. The resulting mechanical properties were evaluated and the effects of this further level of porosity on cell attachment and osteogenesis was investigated.

4.2 MATERIALS AND METHODS

4.2.1 Materials

Sodium citrate monobasic (SOCIT) was purchased from Sigma Aldrich. PLLA, with an inherent viscosity midpoint of 1.8 dl/g (PL18), was kindly provided by Corbion Purac Biomaterials (the Netherlands) and used as the matrix phase. PVA (M_w 30,000-70,000 g/mol, 87-90% hydrolyzed) was purchased from Sigma Aldrich and used as the dispersed phase. These two molar masses were chosen among the possibilities because the viscosity of PVA under shear (preliminarily measured as described in section 2.6) was lower than 4 times the viscosity of PLLA, which is the upper bound for the breakup of dispersed phase droplets in shear flow and proper mixing [44]. Prior to any melt-based processing, the polymers were dried at 35 °C in a vacuum oven for 24 h.

4.2.2 Thermogravimetric Analysis (TGA)

The decomposition temperature of sodium citrate was assessed by TGA using a TA Instruments Q500. The experiment was performed under a nitrogen atmosphere with a heating rate of 10 °C/min from 25 °C to 700 °C.

4.2.3 Blend screening and choice

The morphology of three PLLA:PVA blends was preliminarily assessed before the introduction of SOCIT in the composition. The formulations were (PLLA:PVA, wt%) 50:50, 70:30 and 80:20. The blends were prepared according to the blending protocol in section 2.4. The materials were then used for additive manufacturing and the scaffolds leached as described in section 2.5. The cross-section of filaments from the scaffolds were imaged via scanning electron microscopy (SEM) following the protocol of section 2.8.1.

Based on visual analysis from SEM images, the PLLA:PVA blend in the composition of 80:20 was chosen for further studies. To this purpose, the ratio was slightly changed to 80:19 and SOCIT was introduced in the concentration of 1 wt%.

4.2.4 Blending

Blends were prepared by mixing the components in a twin-screw extruder (DSM Xplore twin-screw micro-extruder) preheated at 180 °C, for 1 min at 100 rpm. The extrudate was manually cut into pellets of approximately 2 mm in length as needed.

4.2.5 Additive manufacturing and leaching

Scaffolds were fabricated via a bioextrusion technique (Bioscaffolder, SysENG, Germany). A custom-made aluminum heater with dedicated PID temperature controller was employed to control separately print head and needle temperatures. The print head was pre-heated to 210 °C at the needle (G21, DL Technologies) and to 200 °C at the reservoir for the blend, while to 205 °C in both zones for plain PLLA. The pellets of the blend or the granules of the plain PLLA were then loaded and the molten material was deposited by applying a pressure of 8.6 bars, following a 0-90° pattern. The blend was printed with a screw rotation of 50 rpm and a translational speed of 700 mm/min, while for PLLA only the screw rotation was 125 rpm and the translational speed 1000 mm/min. For both materials, the fiber diameter, the fiber-to-fiber (center-to-center) distance and the layer thickness were 400 µm, 1 mm and 330 µm, respectively. To facilitate quenching and preserve the extrusion-induced morphology [45], the printer platform was kept at room temperature (RT). Cubical scaffolds of 5 x 5 mm^2 in horizontal section and 3 mm in height were cut out from a 20 x 20 x 4 mm^3 manufactured block using a razor blade and used for further experiments.

For contact angle measurements, scaffolds consisting of only two layers were created, with either PLLA or blend. The deposition parameters were as described above, except for fiber spacing, which was reduced to the fiber diameter to remove intralayer porosity.

Prior to any characterization or study, each scaffold was immersed in 50 ml of distilled water (dH$_2$O) and incubated on a shaker at 50 rpm for 24 h at room temperature. Subsequently, scaffolds were dried in a vacuum oven at 35 °C overnight. Scaffolds manufactured from PLLA:PVA:SOCIT are referred to as "Blend" from now on.

4.2.6 Rheological properties

The rheological behavior of raw PLLA and PVA was evaluated at the manufacturing temperature, 210 °C. The complex viscosity as function of angular frequency (10 – 628 rad/s) was recorded with a TA DHR rheometer with a parallel plates configuration (25 mm diameter and gap in the range 0.5 – 0.7 mm), at 1 % strain. The samples were loaded at the test temperature and the time between the loading and the start of the test was kept constant between samples. The data were converted to dynamic viscosity vs. shear rate via the Cox – Merz transformation [1] available in the rheometer software and then fitted with the Cross model (eq. 1):

$$\eta = \frac{\eta_0}{1 + (k\dot{\gamma}\ )^n} \tag{1}$$

Where η is the complex viscosity, η_0 is the zero-shear viscosity, k the consistency (characteristic time), $\dot{\gamma}$ is the shear rate, n the power law index + 1 [38].

4.2.7 Contact angle measurement

Static contact angle measurements with dH$_2$O were performed by the sessile drop technique using an optical contact angle device DSA25 (KRÜSS GmbH) equipped with an electronic syringe unit (OCA15, Dataphysics, Germany). Two-layer scaffolds were tested along both the longitudinal and the transversal direction with respect to the fibers' orientation. The drop analysis and contact angle measurements were run with the machine software DSA4, by applying the Young-Laplace method.

4.2.8 Morphological analysis

4.2.8.1 Scanning electron microscopy

SEM was employed to analyze the structure and morphology of the additive manufactured scaffolds. Samples were gold-sputtered with a Cressington Sputter Coater 108 auto for 100 s at 30 mA and then imaged using a Philips XL-30 ESEM at 10 kV on secondary electrons mode.

4.2.8.2 Image analysis and theoretical considerations

SEM images of the surface pores were analyzed via ImageJ 1.53c (http://imagej.nih.gov/ij). The images were converted to binary and the surface pores were evaluated via the "Analyze Particles" function available in the software. The measured pore areas were analyzed and compared to the theory of morphological development of polymer blends during processing, within the framework of break-up and coalescence processes [39]. The behavior of a droplet in a matrix in a flow field can be described by the reduced capillary number κ^* (eq. 2) [46]:

$$\kappa^* = \frac{\kappa}{\kappa_{critical}} \tag{2}$$

Where κ is the capillary number (eq. 3) and $\kappa_{critical}$ is the critical capillary number (eq. 4):

$$\kappa = \frac{\eta_{matrix} \cdot \dot{\gamma} \cdot d}{\nu_{12}} \tag{3}$$

$$log(\kappa_{critical}) = c_1 + c_2 \cdot log(\lambda) + c_3 \cdot log(\lambda^2) + \frac{c_4}{log(\lambda) + c_5} \tag{4}$$

Here, η_{matrix} represents the viscosity of the matrix phase, $\dot{\gamma}$ is the applied shear rate, d represents the droplet diameter, ν_{12} is the interfacial tension, and λ is the viscosity ratio, defined as (eq. 4):

$$\lambda = \frac{\eta_{droplet}}{\eta_{matrix}} \tag{5}$$

where $\eta_{droplet}$ is the viscosity of the dispersed phase. The constants $c_1 - c_2$ are specific for the type of flow. As the deposition process used in this study in shear flow dominated [47], the constants assume the values $c_1 = -0.506, c_2 = -0.0994, c_3 = 0.124, c_4 = -0.115$ and $c_5 = -0.611$. The capillary number expresses the balance between hydrodynamic and surface forces that act on a droplet of a specific diameter d.

Depending on the value of κ^*, four regimes can be identified. When $\kappa^* < 1$ (regime 1), there is no deformation of droplets taking place. In regime 2 ($0.1 > \kappa^* > 1$), droplets are deformed but do not break-up. Regime 3 corresponds to $1 > \kappa^* > 4$, and deformation of droplets up to their splitting into primary droplets occurs. For values of κ^* greater than 4, droplets deform into stable filaments. In the latter regime, when the stress causing the droplet deformation decreases, the reduced capillary number falls below 4, and the fibers breakup under the effect of surface tension (a phenomenon called Rayleigh instability) [46]. The time for the complete breakup can be calculated via eq. 6:

$$t_b = \frac{\kappa}{\dot{\gamma}} t_b^* \tag{6}$$

Where t_b^* is given by eq.7 [44]:

$$t_b^* \cong 84\lambda^{0.355}\kappa^{*-0.559} \tag{7}$$

To understand whether the obtained morphology was stable or could be further affected by processing, the critical capillary number and the minimum achievable droplet diameter were calculated following the workflow described in [48], ignoring buoyancy. The reduced capillary number was calculated by first evaluating the capillary number via eq. 2. The value used for the interfacial tension was 10 mN m^{-1} [48] while the shear rate was derived as apparent shear rate (being the extrudate a polymer blend) according to eq. 8 [49]:

$$\dot{\gamma} = \frac{4Q}{\pi R^3} \tag{8}$$

where the volume flow rate Q was calculated from the deposition parameters and R is the needle radius. The viscosity of the matrix was obtained from the rheological measurements and extrapolated at the shear rate calculated with eq. 7. Finally, droplets were assumed to be spherical, and the average droplet area measured with ImageJ was used to evaluate the droplet diameter d. The critical capillary number was calculated with eq. 3, where the droplet viscosity was derived as for the matrix viscosity. Keeping in mind the previous considerations about the four existing regimes, no further breakup can occur and the droplet exhibits the minimum achievable radius as soon as the capillary number equals the critical capillary number. Therefore, by equating equations 2 and 3, the minimum achievable droplet diameter is given by eq. 8:

$$d_{min} = \frac{\kappa_{critical} \cdot \nu_{12}}{\eta_{matrix} \cdot \dot{\gamma}} \tag{9}$$

The droplets were considered circular and their area calculated accordingly.

The calculation of the reduced capillary number resulted in a value of 47, placing the droplet behavior in regime 4, where they are expected to deform into stable filaments. This was expected to promote the interconnection between the pores originated from SOCIT decomposition. To further favor the process, the deposition was carried out at room temperature. The rapid quenching of the extrudate was expected to prevent any morphological modification due to material relaxation right after material extrusion.

It is important to note that the process so far described applies to individual droplets. However, real systems are composed of multiple droplets. This means that collisions between droplets can take place and, whereas the conditions for coalescence are met, bigger droplets might form. For this reason, the experimental particle size is often larger than the value predicted by the theory above [48]. Additionally, droplets can evolve into more complex structures as the concentration of the dispersed phase increases. The morphology of the minor component may change from dispersed droplets to cylinders, fibers, sheets at higher concentrations. At a certain concentration named "Phase inversion volume fraction", matrix and dispersed phase can no longer be distinguished and the morphology assumes a co-continuous structure [50].

4.2.8.3 Porosity measurement by buoyancy

A Mettler Toledo XSR105DU with the Mettler Toledo Density kit XPR/XSR-Ana and Sinker 10 cm^3 was used to measure scaffold density and calculate microporosity according to the Archimedes method. In the order, scaffolds were weighed in dry conditions (M_{dry}), prewetted in ethanol to facilitate water penetration in the pores and air expulsion, and eventually weighed immersed in dH_2O (M_{sub}) [43]. After quick removal of excess water by blotting, samples were weighed again in air (M_{wet}). All the measurements were taken at room temperature.

The following equation was used to calculate the open pore (OP) percentage:

$$OP = \frac{OPV}{EV}[\%] \tag{10}$$

Where open pore volume (OPV) and exterior volume (EV) are given by:

$$OPV = \frac{M_{wet} - M_{dry}}{\varrho_{dH2O}}[cm^3] \tag{11}$$

$$EV = \frac{M_{wet} - M_{sub}}{\rho_{dH2O}}[cm^3] \tag{12}$$

The equation to calculate the closed pore (CP) percentage was:

$$CP = \frac{IV - TSV}{EV}[\%] \tag{13}$$

Where impervious volume (IV) and theoretical solid volume (TSV) are given by:

$$IV = \frac{M_{dry} - M_{sub}}{\rho_{dH2O}}[cm^3] \tag{14}$$

$$TSV = \frac{M_{dry}}{\rho_{sample}}[cm^3] \tag{15}$$

ρ_{dH2O} and ρ_{sample} are the densities of deionized water and of the polymer, respectively. For microporous scaffolds, being PLLA the main component and having leached out part of the PVA, a density of 1.290 g/cm^3 [51] was used.

4.2.8.4 *Micro computed tomography (μCT)*

The samples were scanned as described by Camarero-Espinosa [10]. Briefly, a Bruker Skyscan 1272 11Mp scanner was used to record μCT scans of the leached scaffolds and potentially confirm the porosity values from the buoyancy test. The machine had a cone beam geometry, a 4032 × 2688 detector and was air damped to reduce vibration disturbances. Thermal drift of the cathode spot, alignment, ring artefacts and beam hardening were corrected using the software suite supplied by the manufacturer. The isotropic voxel size was 3^3 μm^3. The 3D datasets were reconstructed using FDK implemented in NRecon 1.7.1.0 (Bruker microCT) [52] and analyzed for open and closed microporosity quantification with the software AVIZO 2019.4 (Materials Science). For porosity measurements, images were binarized, noise and small spots were removed, a mask was created by selective closing and erosion and applied to the original thresholded image, and eventually voids within the masked area where identified and quantified. The available surface area was measured following the same protocol.

4.2.9 Compression test

Micro-CT imaging was performed using a SkyScan 1272 high-resolution X-Ray microtomograph (Bruker MicroCT, Belgium) equipped with a mechanical testing stage of 440 N. The projections were recorded at a camera binning of 1x1 with a voltage of 50 kV and an emission current of 175 μA. All samples were scanned at a pixel size of 4 μm with 3 average frames at every 0.3˚angle step and an exposure time of 475 ms. No filter was applied. The projections were reconstructed using the NRecon software (version 1.7.1.6) and the obtained cross-sections were further utilized to obtain 3D images of the scanned samples using CTVox software (version 3.3.or1403). In addition to an initial scan performed in the absence of any load, the samples were also scanned at two pre-established compression points, *i.e.* 75 and 150 N, respectively. The compression speed was set at 1.5 μm/s and 15 minutes were allowed for the samples to stabilize under load before scanning. Data are presented as macroscopic stress (not normalized by porosity) vs. strain.

4.2.10 Cell studies

4.2.10.1 *Cell expansion*

Human mesenchymal stromal cells (hMSCs) isolated from bone marrow were purchased from Lonza (Donor 19TL029340, male, age 24). Cells were plated at 1000 cells/cm^2 in tissue culture flasks and cultured at 37 °C / 5% CO_2 in basic medium (BM), consisting of αMEM with Glutamax and no nucleosides (Gibco) supplemented with 10 vol% FBS (Sigma-Aldrich), until 80% confluency.

4.2.10.2 *Cell seeding and culture*

Scaffolds were disinfected by incubation in 70% ethanol for 20 min and then washed 3x with PBS. Scaffolds for the attachment study were incubated overnight at 37 °C in either BM supplemented with penicillin (100 U/ml) and streptomycin (100 µg/ml) (Fisher-Scientific) or a solution of 1 mg/ml collagen type 1 from rat tail (Corning) in 0.02 N acetic acid. Before seeding, they were dried on top of a sterile filter paper and then placed in non-treated tissue-culture well plates. Cells at passage 4 were trypsinized, centrifuged for 5 min at 500 RCF and resuspended in seeding medium (SM, BM supplemented with penicillin (100 U/ml) and streptomycin (100 µg/ml) (Fisher-Scientific)) at a density of 200000 cells per 38 µl. A 38 µl droplet was pipetted on top of each scaffold and these were incubated for 1.5 h at 37 °C / 5% CO_2. The scaffolds were then gently flipped and cells allowed to attach for further 2.5 h at 37 °C / 5% CO_2. After a total 4 h of attachment, scaffolds were moved to non-treated tissue-culture wells filled with proliferation medium (PM, BM supplemented with 200 µM L-ascorbic acid 2-phosphate (Sigma-Aldrich)). The culture was observed after 24 h.

Scaffolds for the osteogenic study were incubated overnight in SM, dried and placed in well plates as previously described. Passage 4 hMSCs were trypsinized and centrifuged for 5 min at 500 RCF. The cells were then resuspended at a density of 200000 cells per 37 µl in medium consisting of 10 wt% dextran (500 kDa, Pharmacosmos) in BM supplemented with penicillin (100 U/ml), streptomycin (100 µg/ml) (Fisher-Scientific) [53]. A 37 µl droplet of cell suspension was placed on top of each scaffold and these were incubated for 4 h at 37 °C / 5% CO_2 to allow cell attachment. Scaffolds were then transferred to new wells filled with 1.5 ml of PM. The medium was replaced after 24h and every two or three days from then on. After 7 days (day 0), scaffolds were cultured for another 35 days in PM or mineralization media (MM, PM supplemented with 10 nM dexamethasone (Sigma-Aldrich) and 10 mM β-glycerophosphate (Sigma-Aldrich)). The medium was replaced every two or three days. The culture was analyzed for metabolic activity, ALP, DNA content both at day 7 and 35, while for osteocalcin and osteopontin production and mineralization at day 35.

4.2.10.3 SEM

Scaffolds from the attachment study were imaged with a Jeol JSM-IT200 to evaluate any potential cell infiltration into the internal pores. Sample were prepared as follows: at the end of the culture, scaffolds were washed twice with PBS, sectioned with a razor blade and fixed in 4% paraformaldehyde. Subsequently, they were dehydrated using a graded ethanol series (30, 50, 70, 80, 90, 96, 3 × 100%). Samples were soaked for 30 min in each solution and, at the end of the sequence, the ethanol was evaporated in a critical point dryer (Leica EM CPD300) to preserve the surface details of the cultured cells. Eventually, scaffolds were sputter-coated and imaged as described in Section 2.8.1, at a magnification of 1500x.

4.2.10.4 Biochemical assays

4.2.10.4.1 Metabolic activity

PrestoBlue assay (Thermo Fisher Scientific) was used to quantify cell metabolic activity. Briefly, cell culture medium in sample plates was replaced with medium containing 10 v/v% PrestoBlue reagent and the sample plates were incubated in the dark at 37 °C for 1 h. Fluorescence was measured at 590 nm with a plate reader (CLARIOstar®, BMG Labtech).

4.2.10.4.2 ALP assay

The scaffolds were washed 3x with PBS and freeze-thawed three times. Samples were then incubated for 1h at RT in a cell lysis buffer composed of 0.1 M KH_2PO_4, 0.1 M K_2HPO_4 and 0.1 vol% Triton X-100, at pH 7.8. 10 µl of cell lysate were collected and 40 µl of the chemiluminescent substrate for alkaline phosphatase CDP-star, ready-to-use (Roche) were added too. Luminescence (emission = 470 nm) was measured after 15 min incubation, using a spectrophotometer (CLARIOstar®, BMG Labtech). Remaining cell lysates were used for DNA quantification. Values were normalized to DNA content.

4.2.10.4.3 DNA assay

CyQUANT Cell Proliferation Assay Kit (Thermo Fisher Scientific) was used to perform DNA assay. Samples from ALP assay were first incubated overnight at 56 °C in 1 mg/ml Proteinase K (Sigma-Aldrich) in Tris/EDTA buffer and then freeze-thawed three more times. Subsequently, to degrade the cellular RNA, the lysate was incubated for 1 h at RT in a buffer composed of 1:500 RNase A in the cell lysis buffer from the kit diluted 20x in dH_2O. The samples were then incubated for 15 min in the fluorescent dye provided by the kit (1:1) for 15 min and fluorescence was measured (emission/excitation = 520/480 nm) with a spectrophotometer. DNA concentrations were calculated from a DNA standard curve.

4.2.10.4.4 Elisa assays

The production of osteocalcin and osteopontin were quantified using ELISA kits (ab270202 and ab192143 respectively, Abcam) according to the manufacturer's instructions. Briefly, at the specified time points, the supernatant from the scaffolds was collected and the protein content was quantified using the ELISA kits. The same samples were used for both assays.

4.2.10.4.5 Alizarin red

Calcium mineralization was quantitatively determined following a protocol described in [54]. Scaffolds were washed 3x with PBS and fixed with 4 wt% paraformaldehyde for 30 min, followed by three washing steps in distilled water. Subsequently, scaffolds were cut in half and each section was stained with alizarin red S solution (60 mM, pH 4.1-4.3) for 20 min at RT. The samples were then washed with distilled water as long as the staining was leaching out and then incubated for 1h at RT with 30 vol% acetic acid while shaking. Following a 10 min incubation at 85 °C, scaffolds were removed and the solutions were centrifuged at 20000 RCF for 10 min. The pH was then adjusted to 4.1-4.3 with 5M ammonium hydroxide and absorbance was measured at 405 nm using a spectrophotometer. The concentration of alizarin red was calculated from an alizarin red standard curve and the values were normalized to DNA content.

4.2.10.4.6 Immunofluorescence microscopy

Samples from the attachment study were washed with PBS and fixed with 4 wt% paraformaldehyde for 30 min at RT, followed by three washing steps again with PBS. Cells were permeabilized with 0.1 vol% Triton-X for 30 min at RT, washed twice with PBS and incubated in PBS for 5 min. This washing sequence was repeated twice. Samples were then incubated in phalloidin solution (Alexa Fluor 568, 1:75 dilution in PBS) for 1h at RT in the dark, while shaking. After 3 washings with PBS, samples were incubated in DAPI solution (1:300 dilution in PBS) for 15 min at RT while shaking, in the dark. Finally, samples were washed with PBS. Confocal laser scanning microscopy was performed with a Tandem confocal system (Leica TCS SP8 STED), equipped with a white light laser (WLL). Samples were excited with the dye specific wavelengths using the WLL or a photodiode 405 in the case of DAPI. Emission was detected with PMT detectors (DAPI) or HyD detectors (phalloidin).

4.2.11 Statistical analysis

GraphPad Prism (version 8.4.3) was used to perform statistical analysis. An unpaired t-test was used to compare between scaffold morphologies in the Archimedes test, in the contact angle measurement and in the cell studies. The same test was additionally used to compare between coatings and media for the same scaffold type in the attachment and the osteogenic study, respectively. A p value lower than 0.05 was considered significant. (*), (**) and (***) indicate, respectively, $p<0.05$, $p<0.01$ and $p<0.001$ when comparing scaffold types while (§), (§§) and (§§§) indicate $p<0.05$, $p<0.01$ and $p<0.001$, respectively when evaluating the effect of medium type in the osteogenic study.

4.3 RESULTS

4.3.1 Blend screening and choice

One of the goals of this study was to obtain small uni-axially deformed pores inside the scaffold fibers, as larger scale porosity (in the form of cylindrical or co-continuous phase) coupled to the pores from SOCIT might have affected macroscopic mechanics. Additionally, we aimed for the creation of a cell-scale rough morphology on the scaffolds surface via the same methodology. For this purpose, we explored the effect of varying PVA concentration in a PLLA:PVA blend. Considering the influence of the dispersed phase concentration on blend morphology (as explained in section 2.8.2), PLLA:PVA blends in the compositions 50:50, 70:30, 80:20 wt% were preliminarily used to manufacture scaffolds. PVA from the scaffolds was then leached out and the cross-sections of the filaments making the scaffolds were imaged with SEM. Visual analysis of the images (Figure S1 in Supplementary information) showed the presence of an interconnected pore network in samples from 50:50 blend, suggesting the creation of a co-continuous phase during manufacturing. Samples from this specific blend showed an extremely brittle behavior, which highly limited their handling. By reducing the fraction of PVA, the pores no longer appeared connected to each other, and their sized reduced with decreasing concentration of PVA. This is in line with the final remarks in section 2.8.2, where we explained how the overall blend morphology is highly dependent on the concentration of the dispersed phase. In the 50:50 blend, the ratio between the two components coincides with the phase inversion volume fraction, where the formation of a co-continuous structure is expected. Instead, a 20 wt% reduction in PVA concentration was sufficient to shift from a co-continuous morphology to dispersed droplets. Additionally, images from the 80:20 blend showed pores more of cell-scale than the 70:30 blend, which we considered favorable in terms of surface roughness. Lower concentrations of PVA were not tested to avoid a further reduction in pore size that might have hindered the interconnection between the pores originated from SOCIT decomposition.

Considering the poor mechanical properties of the 50:50 blend and the goal of introducing cell-scale roughness on scaffolds surface, the 80:20 blend was chosen for further studies.

4.3.2 Thermogravimetric Analysis (TGA)

To determine proper processing conditions for the foaming to happen, thermogravimetric analysis was used to evaluate the temperature at which sodium citrate decomposes. From Figure 1A, it can be seen that decomposition takes place with a very sharp drop in weight, with the onset at around 201 °C, in line with typical processing temperatures for PLLA [55]. For this, it was decided to keep the melt reservoir of the print head at 200 °C to ensure easy melt flow without premature decomposition. The needle area was instead kept at 210 °C to promote complete foaming.

4.3.3 Rheological properties

The rheological properties were evaluated to understand whether the experimentally obtained blend morphology was in line with theoretical predictions, and whether this morphology was a stable state or it could be further influenced by processing. PVA exhibited a higher viscosity than PLLA over the measured shear rate range (Figure 1B), but also the extrapolated zero-shear viscosity was 6 times higher (Table 1). In particular, the viscosity of PVA was nearly the double of that of PLLA at the calculated apparent shear rate of manufacturing. Additionally, PVA showed a slightly more marked shear-thinning behavior, as confirmed by the fitted parameter n.

Table 1. Cross parameters for PLLA and PVA at 210 °C.

Material	η_0 [Pa s]	k [s]	n	R^2
PLLA	1022	3.31E-3	0.55	0.99
PVA	6083	0.08	0.53	0.99

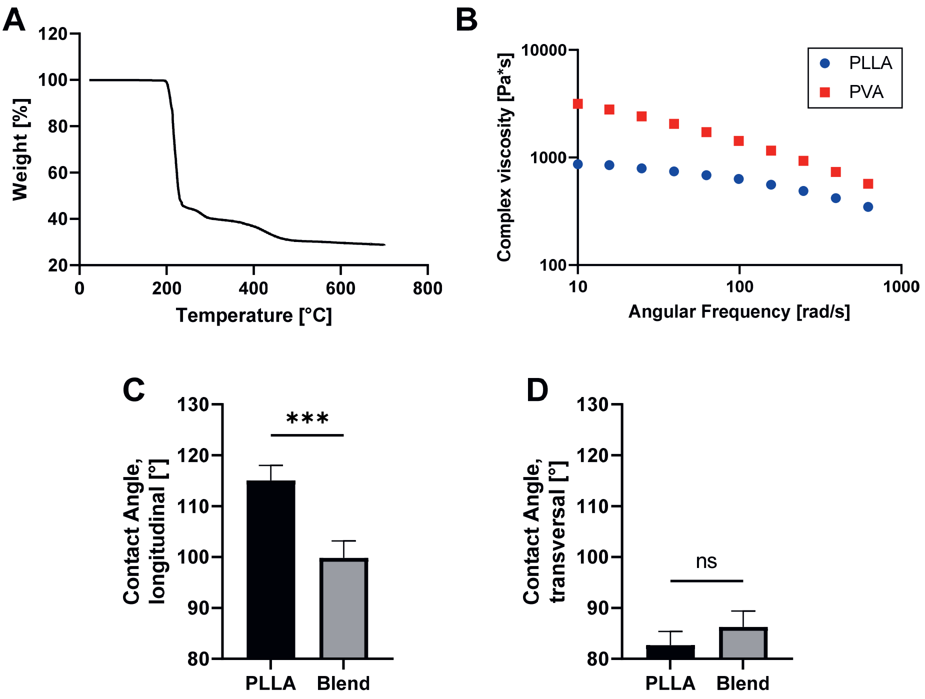

Figure 1. (A) TGA plot of sodium citrate. (B) Frequency sweep for native materials at 210 °C. (C) and (D) Contact angle measurements along the longitudinal and transversal direction, respectively. Statistically significant differences are marked with * ($p<0.05$), ** ($p<0.01$) or *** ($p<0.001$).

4.3.4 Contact angle measurement

Results from contact angle measurement (Figure 1C, D) showed a rather hydrophobic behavior in both measurement orientations and for both materials. Nevertheless, scaffolds printed with the blend exhibited a significantly lower contact angle along the longitudinal direction of test, 99.8 ° ± 3.3 ° compared to 115.1 ° ± 2.9 ° for PLLA.

4.3.5 Morphological analysis

4.3.5.1 SEM

SEM images of microporous scaffolds obtained by foaming and PVA leaching (Figure 2A-D) show both features that this strategy was expected to generate: surface roughness and intrafiber porosity. Voids from sodium citrate decomposition covered good part of the fiber cross-section, although in some cases they seemed to be localized around the center of the fiber (Figure 2A). Interestingly, some large pores, which are attributed to the CBA, were present on the fiber surface as well. Figure 2B shows pores of smaller scale, probably originating from the leaching of PVA. In fact, having PVA in relatively lower concentration than PLLA, it was expected to form the dispersed phase [56]. These covered most of the surface, greatly increasing the roughness of the fiber. The pores were also interconnected by voids on the fiber surface generating an open interconnected network by connecting the internal pores to the fiber to the outside environment (Figure 2C and D). Conversely, PLLA scaffolds showed a bulky cross-section and smooth fiber surface (Figure 2E and F).

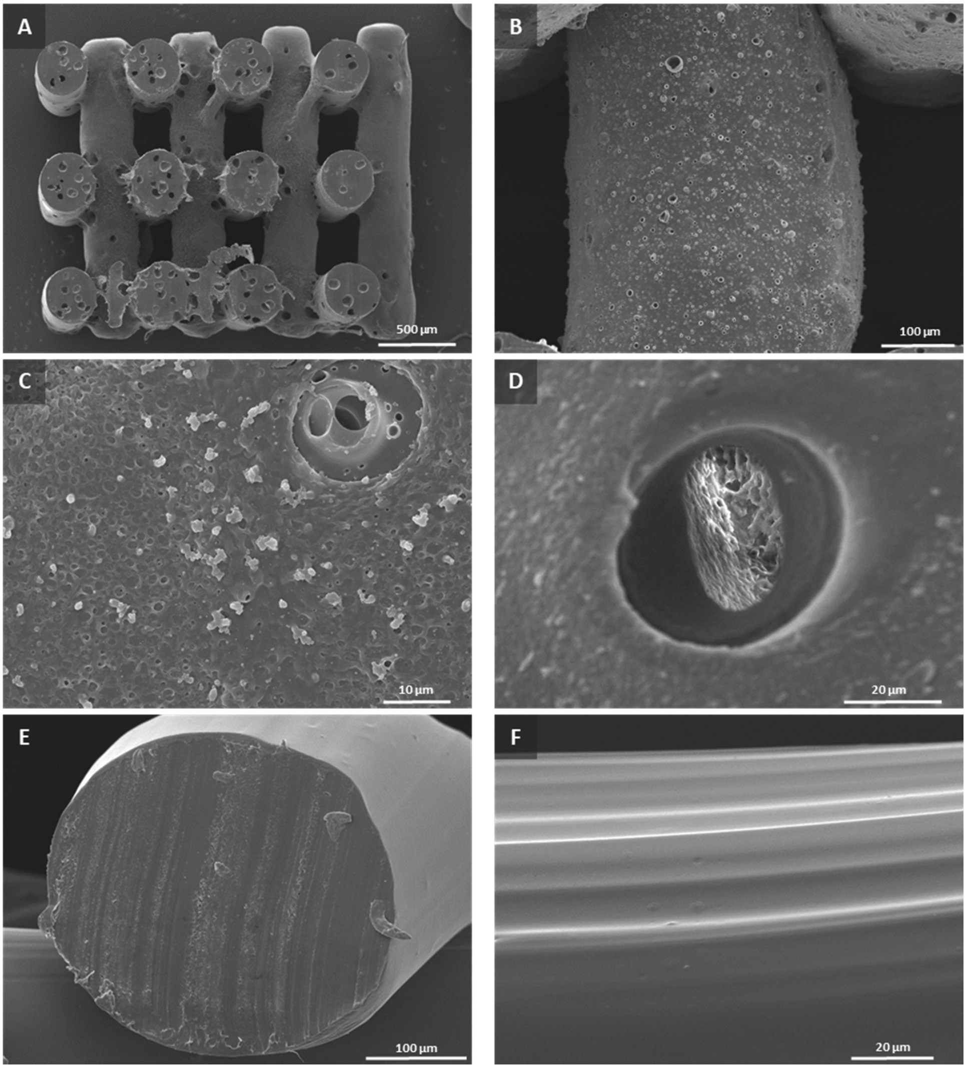

Figure 2. SEM micrographs of microporous (A, B, C and D) and PLLA (E and F) scaffolds. (A) and (B) show details of scaffold cross-section and fiber surface, respectively. Intrafiber and surface porosity can be clearly seen. In (C) and (D), two surface pores connecting to the core of the fiber are visible. (E) and (F) show the bulky cross-section and smooth surface of fibers from PLLA scaffolds. In particular, in the last image it is possible to see some parallel stripes along the fiber surface, probably coming from irregularities at needle surfaces.

4.3.5.2 Image analysis and theoretical considerations

SEM images showed roughly spherical voids, suggesting that the filaments were not stabilized but upon quenching broke up instead. To confirm this, the time to full breakup was calculated according to eqs. 5 and 6, and a value of 1.49 s was obtained. This was compared to the time for the filament to cool down to the glass transition temperature of the PLLA matrix (60 °C) surrounding the droplets, below which the motion of polymer molecules is highly restricted. The cooling time of the filament was evaluated to be 1.61 s (calculation in Supporting Information, according to Li [57]), resulting in a window wide enough for fibrils breakup.

The measured and the theoretical PVA droplet sizes are shown in Table 2. The actual droplet area was one order of magnitude larger than the estimated one. Additionally, a wide size distribution could be seen spanning four orders of magnitude. $Area_{th}$ represents the predicted droplet area as calculated from d_{min} of equation 3; $Area_{min}$ and $Area_{max}$ are respectively the smallest and the biggest area obtained from image analysis; $Area_{avg}$ provides mean and standard deviation from all the pores identified by ImageJ.

Table 2. Morphological parameters of the blends after leaching.

$Area_{th}$ [µm^2]	$Area_{min}$ [µm^2]	$Area_{max}$ [µm^2]	$Area_{avg}$ [µm^2]
1.11x10^{-2}	2.5x10^{-1}	1885.7	6.4 ± 33.5

4.3.5.3 *Porosity measurement by buoyancy*

Buoyancy tests showed significantly higher porosity percentages for scaffolds manufactured with the blend after leaching, for both open and closed porosity (Table 2). Microporous scaffolds showed higher variability in the process.

Table 3. Microporosity (open and closed, measured by buoyancy test) and available surface (measured via microCT) for PLLA and microporous scaffolds. Statistically significant differences are marked with * ($p<0.05$), ** ($p<0.01$) or *** ($p<0.001$).

Composition	Open porosity [%]	Closed porosity [%]	Available surface [x 10^6 µm^3]
PLLA	3.7 ± 3.4	5.7 ± 0.6	219.7 ± 24.2
Blend	11.2 ± 2.6 **	12.7 ± 6.1 *	425.9 ± 13.9****

4.3.5.4 *Micro-CT*

As expected, PLLA scaffold did not show any surface roughness or major internal porosity, as can be seen from Movie S1 in Supporting Information. A limited amount of small pores can be spotted, which we ascribe to the presence of air bubbles in the melt. Instead, micro-CT imaging of blend scaffolds shows a large presence of pores, both on the surface of the fibers and internally (Figure 3A). From the longitudinal section of the fibers (Figure 3B), it was possible to see that a sort of tunnel develops through the fibers. This is further confirmed by frames from a video navigation through a reconstructed fiber (Figure 3C) and from the video navigation itself (Supporting Movie S2). Starting from an open pore at one cross-section, the network of pores spreads along the fiber, allowing the visualization of the internal structure without passing through material walls (Movie S2, Supporting Information).

The microporosity calculation gave an open porosity value of 9.9 ± 0.7 % while the closed porosity was calculated to be 1.4 ± 0.9%. The open porosity seemed unexpectedly low, even with reference to the PVA weight fraction only and not considering the foaming too. The result from the calculation of the micropore volume was $(2.2 \pm 27.2)*10^3$ µm^3, spanning from a minimum value of 4.5 µm^3 to a maximum value of $2.6*10^6$ µm^3. Additionally, blend scaffolds showed a significantly higher surface area than PLLA scaffolds (Table 3) as measured from the microCT reconstructions. Both the high standard deviation in the pore volume data and the values for the surface area are in line with the SEM images and the microCT models. These showed not only rougher filament surfaces and internal pores but also a large distribution in pore volume.

4.3.6 Compression test

Figure 4A depicts the scaffolds in the testing chamber, before and after compression. Micro-CT scans after testing showed that the internal micropores in blend scaffolds did not collapse at the testing force used. Micropores deformed under the applied load (Figure 4B), without initiating failure (top images). Furthermore, the bottom images indicate that breaking originated in a different location once scaffolds began to fail.

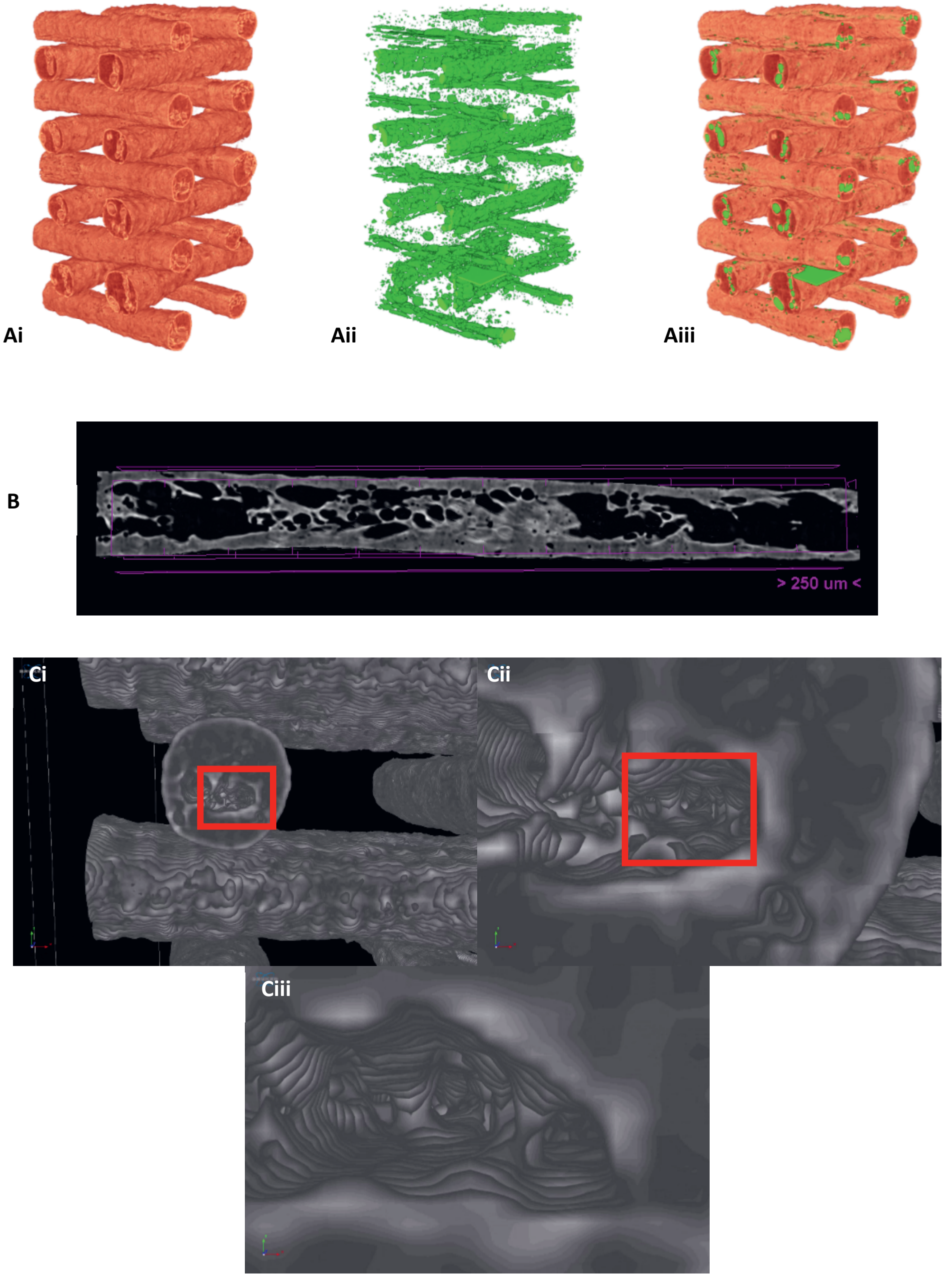

Figure 3. Micro-CT reconstructions of microporous scaffolds. (A) Volume reconstruction of a foamed scaffold: (i) solid volume, (ii) pores on the surface and inside the fibers, (iii) overlay of the first two images. It can be seen that pores are present within the fibers but also all over the surface. (B) Longitudinal section of a fiber: in grey scale, the solid PLLA volume, in black the pores inside the fiber. Quite some internal porosity is visible, which successfully develops along the fiber itself. (C) Video navigation inside a fiber internal pore: (i), (ii) and (iii) are subsequent frames from the video volume rendering.

The stress-strain curves (Figure 4C) revealed an initial elastic region followed by another linear area but with a lower slope, which we ascribe to the progressive collapse of the macropores. In the case of blend scaffolds, the start of the second linear region was anticipated, yielding at around 2.5 %. This behavior could be attributed to the deformation of the micropores, although the load is not sufficient to induce the collapse of the scaffold. A similar phenomenon could be observed along the second linear region, where the fluctuations in the curve originate from the collapse of the internal micropores. It is important to point out that both curves exhibit a drop in stress, corresponding to the pause in compression at 3 MPa for imaging purposes, during which a distribution of effort occurred. At the maximum applied load, neither scaffold types reached the densification step caused by the collapse of the macropores, usually characterized by an exponential trend [58]. The two scaffold compositions did not result in statistically significantly different Young's modulus values ($p < 0.15$), which were 1.1 ± 0.4 and 0.5 ± 0.2 MPa for plain PLLA and microporous scaffolds respectively (Figure 4D). Additionally, scaffolds manufactured with the blend exhibited higher strain at maximum load, 37.5 % higher than PLLA constructs.

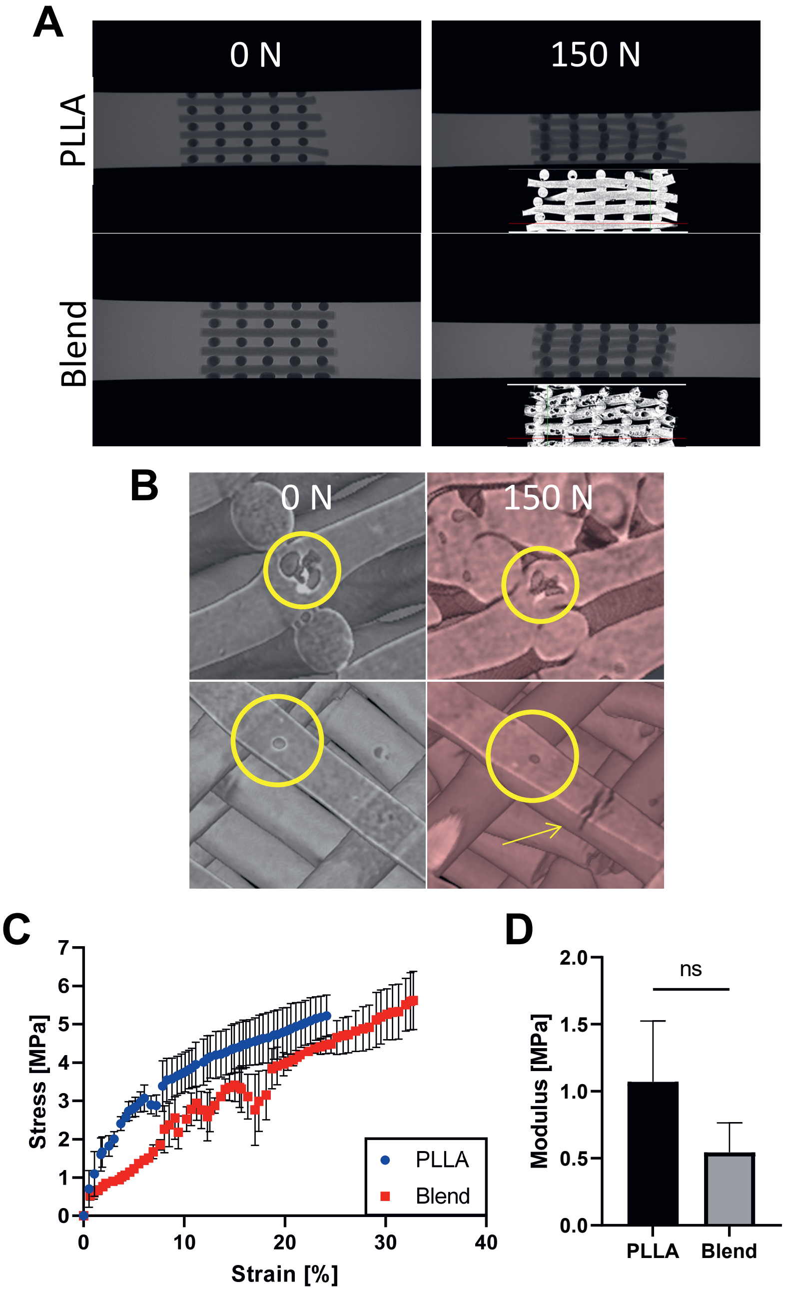

Figure 4. Results from compression tests. (A) Pictures of PLLA and leached-blend scaffolds before (0 N) and after (150 N) compression, including micro-CT scan at 150 N. (B) Details of pores in leached-blend scaffolds before (grey) and after (red) compression. The arrow highlights a crack appeared during testing. (C) Stress - strain curves from compression tests and (D) compressive modulus for PLLA and leached-blend scaffolds.

Scaffolds at the intermediate compression force of 75 N can be seen in Figure S3 in Supporting Information. Additionally, 3D reconstructions of PLLA and PLLA:PVA:SOCIT scaffolds before compression and after compression at 75 and 150 N are shown, respectively, in Supporting Movie S3 and S4.

4.3.7 Cell studies

4.3.7.1 Cell attachment

Microporous scaffolds exhibited greater cell attachment at 24 h than plain PLLA scaffolds, both when pre-incubated overnight in medium or coated with collagen (Figure 5A). Figure 5B shows the SEM micrograph of a scaffold cross-section, from the collagen-coated group. In particular, an internal pore can be seen, whose walls are populated with cells. In Figure 5C, a detail of particularly populated fibers is presented, depicting the organization of the cells in an aligned manner on PLLA fibers (left), while on a blend fiber the orientation seemed more random, with cells exhibiting a slightly more spread morphology (right).

4.3.8 Osteogenic study

Cells cultured on foamed scaffolds were significantly less than those seeded on plain PLLA constructs after 7 days, in both culture environments (Figure 6A). Nevertheless, they expressed much higher metabolic activity per cell. After 35 days of culture (Figure 6B), cell numbers were comparable between the conditions, indicating greater proliferation for cells on microporous scaffolds. Metabolic activity was comparable as well.

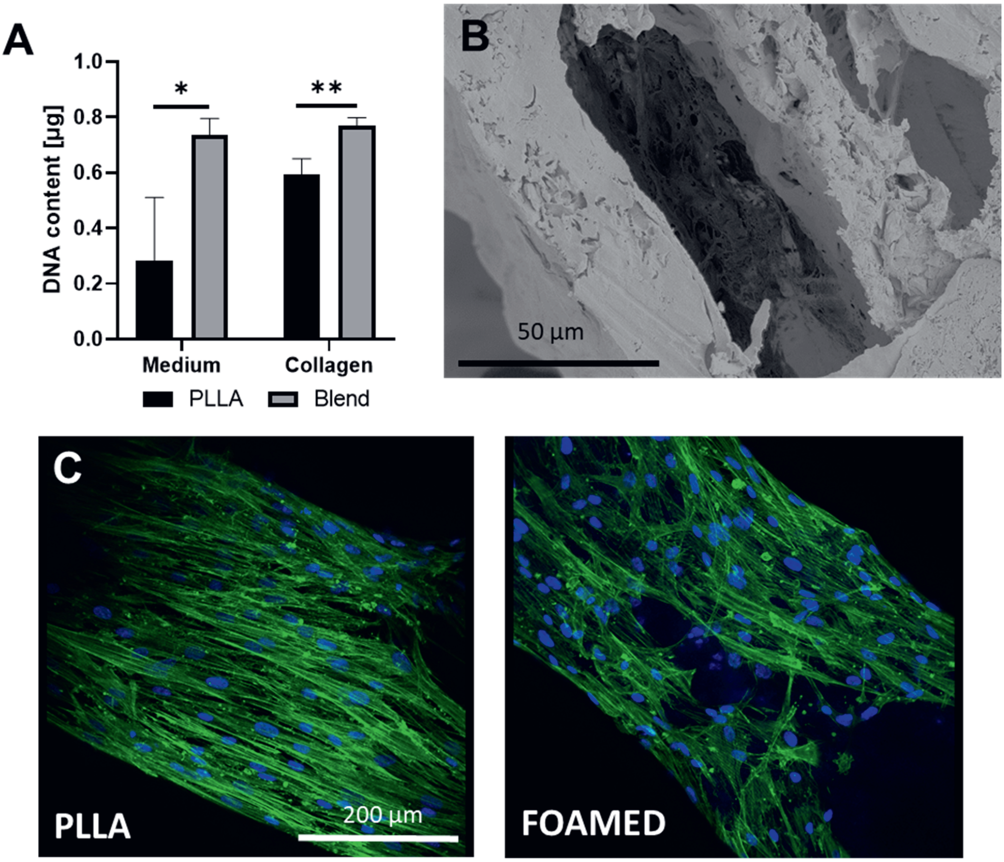

Figure 5. Results from the attachment study. (A) DNA content on PLLA and microporous scaffold after 24 h from seeding. (B) Confocal images of cell morphology after 24 h from seeding (left: PLLA scaffold; right: foamed scaffold). Cells on microporous scaffolds seem more spread and randomly distributed. Statistically significant differences are marked with * ($p<0.05$), ** ($p<0.01$) or *** ($p<0.001$).

At day 7, all osteogenic markers were higher for cells on foamed scaffolds, in both culture environments, although ALP secretion did not show significant differences (Figure 7A). Interestingly, ALP values for cells on microporous scaffolds were comparable between the two different culture media, unlike PLLA scaffolds. At day 35, the expression values were all comparable between the two different scaffold types, with the exception for osteocalcin (OCN). In mineralization conditions, cells cultured on microporous scaffolds secreted more OCN per cell with respect to plain PLLA scaffolds (Figure 7B).

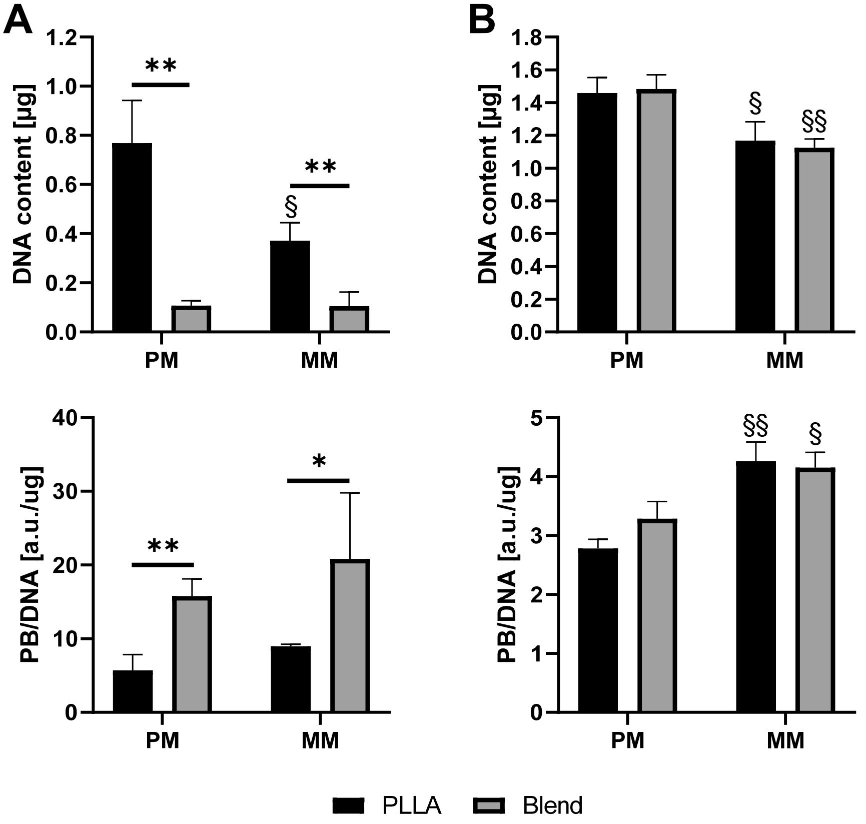

Figure 6. Proliferation and metabolic activity of the human mesenchymal stromal cells (hMSCs) at day 7 (A) and day 35 (B), in either proliferation or differentiation conditions (after 7 days in proliferation medium), on PLLA and microporous scaffolds. Statistically significant differences are marked with * (p<0.05), ** (p<0.01) or *** (p<0.001) when comparing the effect of different scaffold types on cells cultured in the same cell medium and § (p<0.05), §§ (p<0.01) or §§§ (p<0.001) when comparing the effect of different media on cells cultured on the same scaffold type.

4.4 DISCUSSION

The main aim of this study was the development of a straightforward process based on AM, chemical foaming and porogen leaching to produce scaffolds with intrafiber open porosity and surface roughness. These goals have been previously targeted in AM by means of scaffold etching [59], porogen leaching [35], or a combination of porogen leaching and supercritical foaming [60]. A recent example of the combination between porogen leaching and AM is the work of Dang et al. [35]. The researchers dissolved PCL in chloroform and mixed it with the porogen (grounded disodium hydrogen phosphate and sodium chloride salts, sieved to less than 38 µm). Following solvent evaporation, the mixture was fed to a FDM machine to manufacture scaffolds. The constructs were eventually incubated in NaOH to leach out the porogen, resulting in scaffolds with micropores inside the fibers. As recent is the study of Visser et al. [61], who developed a new AM method referred to as direct bubble writing. The new technique relies on the generation of liquid shell-gas core droplets by means of a core-shell nozzle. By polymerizing the outer shell during the printing process, the manufactures polymer foams are able to retain their overall shape. Additionally, the group showed the possibility to control the transition between open- and closed-cell foams via the specific gas used. Nevertheless, all these studies included either week-long leaching steps, toxic organic solvents or additional equipment and processing steps. For this work, we elaborated a strategy based on steps that could be potentially reduced only to the deposition phase. The manufacturing chosen process was based on single-screw melt extrusion, which provides good enough mixing when compared to twin-screw mixers [62]. In addition, the heat-based process allowed an *in situ* foaming process. Due to PVA water solubility and biocompatibility, the leaching process can take place *in vitro* or *in vivo* within 24 hours.

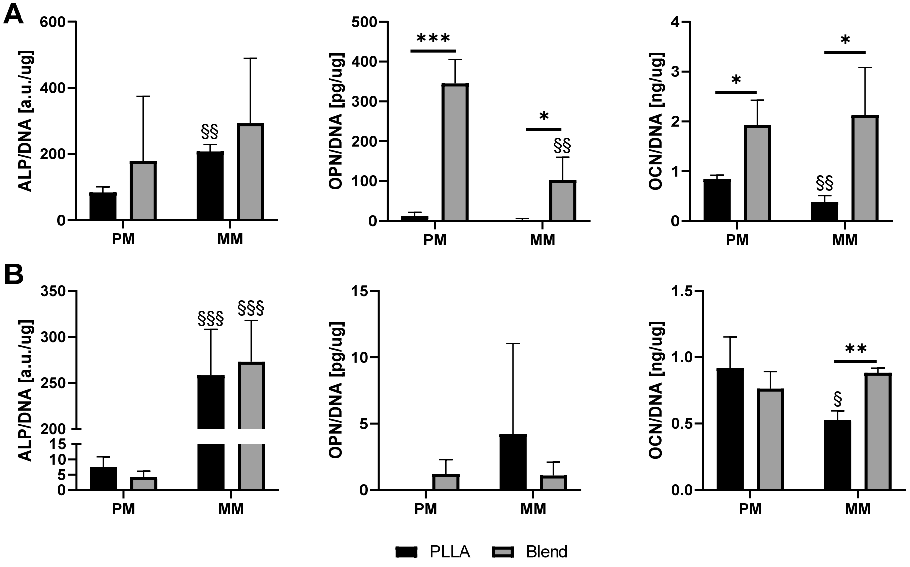

Figure 7. Expression of osteogenic markers from the human mesenchymal stromal cells (hMSCs) at day 7 (A) and day 35 (B), in either proliferation (PM) or differentiation (MM) conditions (after 7 days in proliferation medium), on PLLA and microporous scaffolds. Statistically significant differences are marked with * ($p<0.05$), ** ($p<0.01$) or *** ($p<0.001$) when comparing the effect of different scaffold types on cells cultured in the same cell medium and § ($p<0.05$), §§ ($p<0.01$) or §§§ ($p<0.001$) when comparing the effect of different media on cells cultured on the same scaffold type.

Chemical foaming agents have been used in industry to produce plastic parts with lower weights, higher impact strength and enhanced thermal insulation properties. Established CBAs are azodicarbonamide (ADC) and sodium bicarbonate [63]. ADC produces toxic chemical compounds, while sodium bicarbonate has a decomposition temperature considerably lower than the required processing temperature for PLLA. Sodium citrate is a non-toxic compound that has already been used as a leachable porogen in TE [64], [65]. It is known to decompose into carbon dioxide and water but, to our knowledge, it has not been used as foaming agent. To establish the foaming protocol during the printing process, a TGA heating ramp was run and the onset of the decomposition was calculated. The compound decomposes slightly above 200 °C, which is in a good range for PLLA processing. In fact, to allow foaming during extrusion the CBA must decompose at temperatures above the melting point of the polymer matrix. On the other hand, too high decomposition temperatures are not advisable as thermosensitive materials like polyesters might undergo thermal degradation, resulting in an unstable and unreliable process. As a result, the temperature of the melt reservoir of the print head was set at 200 °C while the nozzle area was set at 210 °C. This allowed the polymer melting at a sufficiently low viscosity without premature foaming.

We exploited the foaming properties of sodium citrate to generate porosity inside the fibers. The channels (pores) resulted following foaming were expected to interconnect but also to open to the surface via the use of a water-leachable dispersed phase. PVA was chosen for this aim, with the further effect of generating surface roughness. When immiscible with the matrix phase, the polymer in lower concentration (defined as "dispersed") phase separates and tends to form domains. With increasing concentration of the dispersed polymer, the domain morphology smoothly shifts from spherical drops to cylinders, fibers, and sheets. Eventually, these large features will coalesce, and a continuous phase will be created, coexisting with the matrix. This happens in the middle range of the concentration scale [18]. Whereas models to describe the shift between the different domain types seem not to exist, a simple empirical relationship predicting the phase inversion composition was derived, relating the dispersed phase volume fraction to the viscosity ratio [66]:

$$\phi_{2,PI} = \frac{1}{1+\lambda} \tag{16}$$

By increasing the dispersed polymer concentration even further, the dispersed component will ultimately become the matrix, resulting in phase inversion [18]. The morphology and size of the domains can be controlled up to a certain extent by fine tuning the processing parameters, and the dimensions can span over hundreds of micrometers.

We preliminarily evaluated the effect of different PVA weight fractions on the morphology of voids originated by leaching. The highest concentration, 50 wt%, resulted in an interconnected network of internal pores, in line with eq. 16, which gave $\phi_{2,PI} = 0.34$ or $34\%$for our system. Although morphologically desirable, this interconnected pore network highly influenced the mechanical properties of the scaffolds, which had such a brittle behavior to limit even their handling. Decreasing the PVA fraction resulted in voids of spherical shape, suggesting that the concentration was sufficiently low to have had the blend to phase-separate in the shape of droplets. Once again, this was further supported by eq. 16. The choice between the 70:30 and the 80:20 blend was dictated by a two-fold requirement in terms of voids dimension. We targeted pores big enough to potentially allow cell passage but also sufficiently small to induce roughness on the scaffold surface. The 70:30 blend resulted in voids of a scale greater than cells while the 80:20 composition gave slightly smaller pores. Lower concentrations of PVA where not tested as the 80:20 responded to the demands of this study. For this reason, the ratio of this blend was changed to 80:19 to accommodate for the introduction of 1 wt% SOCIT, which was further tested and analyzed.

From SEM images of scaffolds printed with 80:19:1 PLLA:PVA:SOCIT blend, two scales of pore sizes could be identified. We attribute the bigger ones, mainly located inside the fibers, to the foaming of sodium citrate. In fact, Gendron [18] states that the foam cellular structure and the blend morphology belong to two different scales: the pores from the foaming are usually in the range of 100 to 200 µm, while the blend morphology can go as down as 1 to 2 µm. This is further confirmed by SEM analysis (Figure S2, supporting information) of cross-sections of scaffolds printed with no PVA. Pores with diameters in order of tenth of µm could be seen, with smooth and full walls not interconnected with each other. These pores are clearly of a greater size scale compared to those populating the blend scaffolds surface. Therefore, smaller scale pores are, in our opinion, the result of the leaching of the PVA domains formed during mixing in the printer. The specific printer used, in fact, is equipped with an auger screw that provides some shear mixing like single screw extruders. Unlike physical foaming agents, CBAs decompose and foam at the reach of a critical temperature. This allows to tune the system to have the decomposition take place at the desired location down the flow path. To have more control over the overall morphology, the foaming was induced right at the needle to limit the diffusion of the largest pores towards the fiber surface. Dispersed particles are subjected to migration and geometric exclusion effects in non-uniform shear fields, such as flow through a capillary (Poiseuille flow). The former phenomenon is due to the requirement of lowering the energy of the system, which causes the particles to migrate to low shear stress regions, the center of the capillary. Additionally, the presence of the capillary wall is responsible for a lower than average concentration of particles near the wall and a retardation of their motion [50], [67]. Considering that SOCIT is in solid form prior to decomposition, this explanation seems to be applicable to this study as well. SEM images confirmed the achievement of the predicted morphology. Additionally, as bubble nucleation, growth and possible migration develop in a few seconds [18], the printing process took place at room temperature to have rapid quenching of the fiber and freeze the morphology right after deposition. This prevented the migration of the SOCIT pores to the surface.

To interconnect these main pores and to access them from the surface, we took inspiration from the well-established TE technique of salt leaching, but decided to employ a thermoplastic polymer. This choice originated from the achievable domain size, which is difficult to control when small molecules such as salts are used. As pores too small may hinder cell infiltration as well as nutrients transport, the use of macromolecules represents a valid alternative. Keeping in mind the previous considerations about domain formation in polymer blends, we decided to employ a thermoplastic polymer as sacrificial leachable phase. PVA is a water soluble polymer that has already been used for TE purposes [42]. Being it immiscible with PLLA, it phase-separates once in a melt and forms domains. As the final morphology of the system is dependent not only on the processing conditions but also on the material parameters, we measured the viscosity of PLLA and PVA at the processing temperature, at different angular frequencies. Results showed that PVA, the less concentrated phase, was more viscous than PLLA, the matrix component. In capillary flow, the shear rate is non-homogeneous as its maximum at the wall and null at the capillary center [68]. In polymer blends, this gradient of shear rate is at the origin of a selective species migration in the capillary because of different friction coefficients [67], [69], which results in the tendency of the less viscous component to migrate to the wall [70]. This shear-induced segregation allows to minimize the energy dissipated in the flow [71]. Nevertheless, SEM images clearly showed the presence of surface pores originated by the leaching of PVA domains. We attribute this result to the interplay between different factors. Marín-Santibáñez et al. [72] studied the formation of stratified morphologies in polypropylene/high-density polyethylene immiscible blends and stated that capillaries with length/diameter (L/D) greater than 20 allow for reaching a fully developed flow and a stable morphology. The L/D of the needle used in our study was 23, which should have resulted in a fully developed flow and a stable morphology. However, Chen et al. [73] described the forces acting on particles during capillary flow, highlighting how the difference in viscosity between the two phases plays a critical role in radial migration. We therefore hypothesize that here the difference in viscosity was insufficient to induce substantial or fully developed radial migration of the dispersed phase within the length (and therefore the extrusion time) of our needle. Such incomplete migration of PVA droplets towards the center of the needle might be at the origin of the fluctuations in the open and closed porosity values. Being PVA domains responsible for connecting the internal pores to the outside following leaching their greater or lower availability at the filament surface influences whether closed internal pores are transformed into open ones or not. Longer needles might allow longer residence times and therefore the development of a stable morphology, with greater migration of the PVA droplets to the center. As this is not desirable in our application, we infer that needle with lower L/D might induce greater surface roughness by limiting the time for radial migration of the PVA domains.

The value of the reduced capillary number for the used processing parameters suggests that the PVA droplets were stretched into fibrils during blend deposition. Preservation of this morphology may have favored the creation of the interconnected internal network of pores, but simultaneously may negatively alter the negative properties. In fact, the leaching of such PVA fibrils would have created longer voids, increasing the chance of interconnecting CFA pores too far apart for spherical droplets. According to calculations, the process of complete fibril breakup was faster than filament quenching, resulting in the formation of smaller spherical droplets, which was confirmed by SEM images. These results suggest that it may be possible to influence droplet (and therefore void) morphology by tuning the processing parameters and the cooling rate, although the final result is a complicated interplay between the several factors, which requires careful evaluation. For instance, the time to complete breakup could be extended by reducing the shear rate, which in turn would give a lower capillary number resulting in a decrease of κ^* and a potential shift to a different droplet behavior regime. The same result could be obtained by increasing the fraction of the dispersed phase. However, as explained in section 2.8.2, this would translate into a higher amount of material removed during leaching, with potential reduction in mechanical properties. Therefore, in future studies it might be more straightforward to increase the cooling rate of the deposited strands [45], for example by using a cooled plate or an assisted cooling device [74]. On the other hand, rapid quenching would affect diffusion at the interface, leading to weaker intralayer bonds. Furthermore, droplet stretching is accompanied by a reduction in radius and it remains unclear whether this could be detrimental for cell infiltration or flow of nutrients/degradation products.

As for droplet dimensions, the minimum size of the PVA domains predicted by theory was considerably smaller than the actual value. This is often the case for blends of viscoelastic materials, where the material elasticity hinders the droplet breakup leading to a larger equilibrium droplet diameter [75]–[77]. One additional factor is represented by the presence of the foaming agent. In fact, Elkovitch and Tomasko [78] reported that the dissolution of carbon dioxide in a blend of 75 wt% poly(styrene) and 25 wt% poly(methyl methacrylate) reduced the size of the dispersed phase from 1.5 to 0.48 µm. Additionally, the theoretical framework to predict blend morphology considers only single droplets, whereas real systems consist of large amount of droplets that can collide and coalesce. Nevertheless, the prediction allows to understand whether an even finer dispersion could be achieved, in this case to potentially increase the surface roughness. On the other hand, the additional potential benefit of open pores, which is cell infiltration, might be hindered in this case. Concluding, it is observed that the voids on the surface open to the inside of the fiber, allowing for the connection between the outer environment and the fiber internal porosity. The micro-CT scans show channels through the deposited fibers, confirming not only the decomposition of the CBA, but also the interconnection between the foam cells.

Data from the buoyancy tests and micro-CT analysis quantitatively confirm that further open porosity was successfully achieved. The two characterization techniques gave roughly the same values, indicating the existence of a second length-scale of porosity in the samples. Nevertheless, considering the PVA weight fraction used, the value for open porosity seemed relatively low, indicating that not all the material was leached out. This might be due to the formation of isolated PVA domains, presumably not sufficiently accessible by water to be leached out. Being indeed PVA water soluble, incomplete leaching should not represent an issue in microporosity formation over time. In fact, with the progression of the main matrix degradation, these isolated domains will become available to water infiltration and dissolve, offering cells further surface to populate. Besides, the effect of relative viscosity on blend morphology offers the possibility to tailor the micropores size and distribution in terms of PVA leaching.

Both techniques showed that closed porosity was present as well, although they gave quite different values. It is important to underline that both methodologies have some limitations, which could account for this discrepancy. In the case of micro-CT scans processing, the segmentation step is user dependent [79], [80]. A wrong threshold setting could transform a closed pore into an open one, especially when thin pore walls are present. Therefore, in the following counting, the pore would increase the overall open pore volume and decrease the amount of closed ones. For the buoyancy technique, challenges for a proper measurement are represented by air bubbles that might adhere to the scaffold surface or insufficient wetting of the pores because of the strong surface tension at such small scales. Both factors would increase the buoyancy of the scaffold reducing M_{sub} [79]. Nonetheless, closed porosity values should arise from the presence of foam bubbles inside the fibers but not connected to the outer environment. These pores, although not being immediately available during cell seeding, attachment and proliferation, will become accessible along the main PLLA matrix degradation process. As in the case of unleached PVA domains, this should provide further volume for the growing tissue to infiltrate and fill with extracellular matrix. Furthermore, these foamed pores are expected to still contribute to the overall mechanical performance of the scaffolds.

Micro-CT porosity analysis showed quite high standard deviation (up to 20 and 50% for open and closed porosity, respectively). It is important to note that the final microporosity morphology is highly sensitive to flow conditions. In this study, we have used two dispersed phases, which have different flow properties but that can also interfere with each other (and were expected to). Additionally, with length scales smaller than industrial compounders, small disturbances alter the overall flow steady state. All these elements suggest that flow instabilities likely arise, affecting the phase behavior and variations in the final morphologies. This is further supported by the wide distribution in pore volume, which we attribute to the presence of regions with different shear rate profile and, subsequently, breakup forces of different entity acting on the droplets. Noteworthy, the pores showed volumes going from few μm^3, clearly not accessible to cells, to volumes in the order of 10^6 μm^3. These bigger pores are potentially able to allow flow of nutrients and waste removal, to host multiple cells, and support tissue regeneration from within the scaffold filaments. This scenario, coupled to the increased available surface, would accelerate the growth of a self-supporting tissue, without having to rely on the free space left by scaffold degradation.

According to Wenzel et al. [81], hydrophobicity is directly proportional to roughness. This was further confirmed by other researchers [82], [83]. Here, an opposite trend was observed. Scaffolds made of PLLA showed higher longitudinal contact angle with respect to the rougher scaffolds printed with the blend. It could be suggested that some PVA was still present on the scaffold surface. However, PVA is highly soluble in water and the adopted duration of the employed leaching protocol was the result of preliminary dissolution tests (data not reported) and abundantly exceeded the time needed for the material to dissolve. Whereas PVA had not been leached out, we hypothesize that it was not right at the surface (otherwise it would have been removed) but underneath. What we hypothesize instead is that the rougher fibers may have initially absorbed some water through the pores on their surface. This sort of pre-wetting during the first seconds of the test could have resulted in increased hydrophilicity, giving lower contact angle values than the PLLA scaffolds. This is in line with the findings of Park et al. [84], who manufactured PCL/PEG scaffolds with porous fibers after washing of the PEG domains. Tamada et al. [85] found a parabolic trend of attached cells with contact angle, exhibiting a peak between 60 and 80°. Whether the reason for lower contact angle is actual higher hydrophilicity of the blend scaffolds or water absorption, this phenomenon is expected to facilitate wetting and consequent protein adsorption, which is paramount for cell adhesion.

This difference in contact angle values appeared only for longitudinal measurements. Transversal measurements imply that the droplet baseline develops along a fiber. As shown by SEM and micro-CT images, some internal porosity was present, which was also accessible from the outside. Nevertheless, the extent of this along the fibers might have been limited. If indeed water absorption occurred, we suggest that the amount of absorbed water was smaller than in longitudinal measurements. This because it relies on the absorbing ability of a single fiber, unlike in longitudinal measurements. This hypothesis explains the comparable contact angle values between PLLA and microporous scaffolds, where the only difference is the presence of surface pores.

PLLA is a semi-crystalline polymer with elastic modulus between 1.5 and 2.7 GPa [86] that has been often used for bone tissue engineering. Nevertheless, its stiffness combined with high yield stress makes it also a brittle material, susceptible to brittle failure upon the application of excessive loads. With additively manufactured scaffolds, this behavior can be mitigated by increasing the macroporosity, up to a certain extent [87]. The introduction of microporosity is expected to further improve this aspect as hierarchical porous structures are known to exhibit higher compressive strength than their bulky counterparts [15]. The microporous scaffolds developed in this study showed elastic modulus comparable to those in PLLA, meaning that in the linear elastic regime both scaffold types can withstand the same amount of load without plastically deform. In this regime, the developed micropores are not collapsing yet, but still able to elastically deform by bending of the cell edges [58]. The more prominent stress plateau and the higher strain at maximum load suggest that the foamed scaffolds are able to deform to a greater extent thanks to the presence of the additional pores. This could have been further favored by the amorphous state of the PLLA phase (as shown in Figure S4) as low or no crystallinity increases material ductility [2]. It is important to note that this amorphous state can be preserved under in-vitro test conditions thanks to the relatively high glass transition temperature of PLLA of about 57 °C, which makes this thermoplast a proper choice for our blend system. In addition, we hypothesize that the micropores progressively collapse allowing the construct to bear increasing loads without failing at once. Such mechanism follows nature's design rules in generating ductility/compliance in intrinsically stiff materials [88].

Cell attachment is a prerequisite for cell proliferation, possible differentiation and successful tissue regeneration. Because of this, much research has been done on optimizing this critical step, as shown by Leferink et al. [89] and Cámara-Torres et al. [53]. For this reason, we investigated whether the microporous scaffolds support greater cell attachment than plain PLLA scaffolds, thanks to the rougher surface topography. According to our initial expectations, microporous scaffolds did show significantly higher seeding efficiency in both scaffold pre-treatment conditions. This could be due to the higher wettability (and therefore surface energy) shown by these scaffolds, which could have enhanced protein adsorption and consequent cell attachment [90]. Another possible reason lies in the increased surface area available, allowing a greater number of cells to attach. In a study by Leferink et al. [89], it was shown that increasing the initial cell numbers did not lead to a higher cell seeding efficiency, which was explained with the potential lack of scaffold surface area. Wang et al. [91] suggested instead that surface roughness could supply better anchoring for filopodia. Additionally, SEM imaging suggested that internal pores were sufficiently large and accessible that cells could diffuse into them and adhere upon scaffold seeding. In the perspective of tissue regeneration, this phenomenon represents a considerable advantage, allowing tissue formation and growth not only on the fiber surface but also from within the scaffold fibers. The slower resorption kinetics of some thermoplastic polymers with respect to tissue formation [92] would allow cell proliferation and ECM secretion only in the space made available by the degradation of the scaffold and following the speed of the process. By increasing the surface area available to cells, the formed tissue at each time point could be in larger amount, potentially resulting in superior mechanical and biological performances. The morphology adopted by cells on the different scaffolds is of particular interest as well, being hMSCs differentiation highly influenced by cell shape [26], [28], [93], [94]. PLLA scaffolds showed a relatively smooth surface, as shown by SEM images As stated by Di Luca et al. [95], cells exhibiting a more spread morphology tend to show an enhanced expression of osteogenic related markers. We therefore investigated whether the induced rough topography promotes osteogenic differentiation. After 7 days of culture, microporous scaffolds showed higher secretion of osteogenic markers than PLLA ones. Both in basic and mineralization environment, ALP production was higher for cells cultured on foamed scaffolds. This is in line with studies where osteoblasts were shown to secrete higher ALP amounts on titanium surfaces with increased roughness [96], [97]. Moreover, Gasquez et al. [98] reported higher ALP levels for hMSCs cultured in mineralization conditions on a rougher surface when compared to a smooth one. Data from both OPN and OCN secretion further supported the onset of the differentiation process. However, it is important to note that osteopontin is expressed also during the proliferation phase and OCN should be a late marker of osteogenic differentiation, appearing with the onset of the mineralization process [99].

Despite the overall secreted amount was low, data from day 35 showed significant signs of osteogenesis from cells cultured on the foamed scaffolds when compared to plain PLLA scaffolds in MM. Our hypothesis is that the roughness introduced by the formation of pores on the surface of the fibers could have effectively influenced cell fate as early as after one week from culture, due to the localized created microporosity. The mechanism by which surface topography seems to influence cell fate is through cytoskeletal reorganization following adhesion [100], [101].

However, considering the results from the seeding efficiency study, we were surprised to note the significantly lower cell amount on foamed scaffolds at day 7. Our explanation is that sodium citrate might have not fully decomposed. The incubation in distilled water for the leaching step might have not washed away the undecomposed CBA powder, which might have been right underneath the scaffold surface. During the first 7 days in cell culture medium, the degradation of the PLLA molecules on the surface could have released the compound, causing an increase in pH [102]. The low cell number at day 7 could have affected the low secretion of OCN and OPN that we observed, resulting in a globally low osteogenic potential. In fact, the amount of doublings is known to reduce the differentiation potential [103]. Osteogenesis induction has been reported to be also dependent upon confluence [104]–[106]. It is plausible that cells were not yet confluent at day 35, having microporous scaffolds more surface area to populate [107]. We could not exclude the possibility that enhanced differentiation could have happened at later culturing time.

Nevertheless, cells cultured on microporous scaffolds showed higher metabolic activity per cell at day 7 compared to the smooth PLLA scaffolds. Gaharwar et al. [108] explained that cells adhere on micro-sized rough structures by anchoring and stretching their filopodia, which would lead to an increase in their metabolic activity. This seems to be also in line with the fluorescent images from the cell seeding efficiency study, where stretched and spread cells could be seen on foamed scaffolds. However, our metabolic data refer to day 7. Considering this, we hypothesize that the higher metabolic activity from microporous scaffolds could either derive from newly formed cells adhering to the rough surface or be a sign of enhanced proliferation activity. The effect of rougher scaffold surfaces was indeed shown to have positive effect on cell proliferation by several studies [59], [91], [109].

The preliminary assessment of the effectiveness of the developed strategy indicates that full removal of reagents is a relevant step, although not essential, that should be further optimized in the future. The overall morphology obtained in this study can be tuned in forthcoming studies by changing the deposition parameters or the material properties [18], [39] to better investigate its effect on mechanical properties and cell activity. Our study supports that the well-established use of foaming agents to introduce internal porosity can be further optimized by the addition of a leachable agent. In fact, the voids originated by the leaching of PVA allowed to interconnect the internal pores with each other and to the outside, thus inducing surface porosity/ roughness. An alternative strategy could be based on the generation of co-continuous phases, without the use of a foaming agent. Despite seeming more straightforward, scaffold fibers would lose up to 50% of their bulk volume, as one phase would have to be leached out, with potential negative effects on the mechanical properties. The approach described in this study was shown to positively influence the initial success of a scaffold, which is a critical step in subsequent tissue formation. Nevertheless, it is important to note that the induced increase in surface area might increase the scaffold degradation rate resulting in faster loss of mechanical integrity over time. In this respect, future studies should aim at evaluating the effect of dynamic culture conditions on the scaffold microenvironment and morphology evolution over time.

4.5 CONCLUSIONS

This study presents the use of AM combined with chemical foaming and porogen leaching for the fabrication of scaffolds with interconnected internal open porosity and enhanced surface roughness.

Furthermore, we report that this methodology was developed specifically to potentially allow microporous scaffold fabrication in a single step without recurring to any kind of post-processing or toxic solvents. The PLLA:PVA:SOCIT scaffolds presented a network of pores developing within the fibers, which was also connected to the outside by means of pores on the surface. Compression tests did not show any reduction in elastic modulus, but rather compliance in intrinsically stiff materials, as can be often seen in nature. A 24 h long study performed using hMSCs demonstrated that cells were able to adhere in greater numbers on these scaffolds, independently on the surface pretreatment. In a longer culture study, the microporous scaffolds supported lower cell amount at day 7. Nevertheless, hMSCs showed significantly higher metabolic activity per cell and enhanced OPN and OCN secretion at day 7 and OCN secretion at day 35, suggesting that the developed strategy might be suitable for *in vivo* applications.

ACKNOWLEDGMENTS

Some of the materials were kindly provided by Corbion Purac Biomaterials (The Netherlands). This work was financed by Brightlands Material Center and by the Dutch Province of Limburg. The micro-CT imaging of the compressed samples was possible due to European Regional Development Fund through Competitiveness Operational Program 2014-2020, Priority axis 1, ID P_36_611, MySMIS code 107066, INOVABIOMED.

REFERENCES

[1] R. Sinha *et al.*, “Additive manufactured scaffolds for bone tissue engineering : physical characterization of thermoplastic composites with functional fillers,” 2021, doi: https://doi.org/10.1101/2021.03.23.436548.

[2] A. R. Calore *et al.*, “Shaping and properties of thermoplastic scaffolds in tissue regeneration: The effect of thermal history on polymer crystallization, surface characteristics and cell fate,” *J Mater Res*, vol. 36, no. 19, pp. 3914–3935, 2021, doi: 10.1557/s43578-021-00403-2.

[3] P. S. P. Poh *et al.*, “Polylactides in additive biomanufacturing,” *Adv Drug Deliv Rev*, vol. 107, pp. 228–246, 2016, doi: 10.1016/j.addr.2016.07.006.

[4] S. H. Park *et al.*, “Scaffolds for bone tissue engineering fabricated from two different materials by the rapid prototyping technique: PCL versus PLGA,” *J Mater Sci Mater Med*, vol. 23, no. 11, pp. 2671–2678, Nov. 2012, doi: 10.1007/s10856-012-4738-8.

[5] D. W. Hutmacher, “Scaffolds in tissue engineering bone and cartilage,” *Biomaterials*, vol. 21, no. 24, pp. 2529–2543, 2000, [Online]. Available: http://www.ncbi.nlm.nih.gov/pubmed/11071603

[6] S. Camarero-Espinosa, C. Tomasina, A. R. Calore, and L. Moroni, “Additive manufactured, highly resilient, elastic, and biodegradable poly(ester)urethane scaffolds with chondroinductive properties for cartilage tissue engineering,” *Mater Today Bio*, vol. 6, p. 100051, Mar. 2020, doi: 10.1016/j.mtbio.2020.100051.

[7] A. R. Calore, R. Sinha, J. Harings, K. V Bernaerts, C. Mota, and L. Moroni, “Chapter 7 Thermoplastics for Tissue Engineering,” in *Computer-Aided Tissue Engineering*, A. Rainer and L. Moroni, Eds., 2021, pp. 75–99.

[8] L. Moroni, J. R. de Wijn, and C. A. van Blitterswijk, “3D fiber-deposited scaffolds for tissue engineering: Influence of pores geometry and architecture on dynamic mechanical properties,” *Biomaterials*, vol. 27, no. 7, pp. 974–985, Mar. 2006, doi: 10.1016/j.biomaterials.2005.07.023.

[9] K. C. Ang, K. F. Leong, C. K. Chua, and M. Chandrasekaran, “Investigation of the mechanical properties and porosity relationships in fused deposition modelling-fabricated porous structures,” *Rapid Prototyp J*, vol. 12, no. 2, pp. 100–105, 2006, doi: 10.1108/13552540610652447.

[10] S. Camarero-Espinosa, A. R. Calore, A. Wilbers, J. Harings, and L. Moroni, “Additive manufacturing of an elastic poly(ester)urethane for cartilage tissue engineering,” *Acta Biomater*, vol. 102, pp. 192–204, Jan. 2020, doi: 10.1016/j.actbio.2019.11.041.

[11] M. S. Taylor, A. U. Daniels, K. P. Andriano, and J. Heller, “Six bioabsorbable polymers:In vitro acute toxicity of accumulated degradation products,” *Journal of Applied Biomaterials*, vol. 5, no. 2, pp. 151–157, 1994, doi: 10.1002/jab.770050208.

[12] A. Di Luca, J. R. Wijn, C. A. Blitterswijk, S. Camarero-Espinosa, and L. Moroni, “Tailorable Surface Morphology of 3D Scaffolds by Combining Additive Manufacturing with Thermally Induced Phase Separation,” *Macromol Rapid Commun*, vol. 38, no. 16, p. 1700186, Aug. 2017, doi: 10.1002/marc.201700186.

[13] L. E. Visscher, H. P. Dang, M. A. Knackstedt, D. W. Hutmacher, and P. A. Tran, “3D printed Polycaprolactone scaffolds with dual macro-microporosity for applications in local delivery of antibiotics,” *Materials Science and Engineering: C*, vol. 87, pp. 78–89, Jun. 2018, doi: 10.1016/J.MSEC.2018.02.008.

[14] Y.-W. Moon, I.-J. Choi, Y.-H. Koh, and H.-E. Kim, “Porous alumina ceramic scaffolds with biomimetic macro/micro-porous structure using three-dimensional (3-D) ceramic/camphene-based extrusion,” *Ceram Int*, vol. 41, no. 9, pp. 12371–12377, Nov. 2015, doi: 10.1016/j.ceramint.2015.06.069.

[15] C. Minas, D. Carnelli, E. Tervoort, and A. R. Studart, “3D Printing of Emulsions and Foams into Hierarchical Porous Ceramics,” *Advanced Materials*, vol. 28, no. 45, pp. 9993–9999, Dec. 2016, doi: 10.1002/adma.201603390.

[16] D. S. Shim, J. Y. Seo, H. S. Yoon, K. Y. Lee, and W. J. Oh, “Additive manufacturing of porous metals using laser melting of Ti6Al4V powder with a foaming agent,” *Mater Res Express*, vol. 5, no. 8, p. 86518, Aug. 2018, doi: 10.1088/2053-1591/aad117.

[17] E. Fiume, D. Tulyaganov, G. Ubertalli, E. Verné, and F. Baino, “Dolomite-Foamed Bioactive Silicate Scaffolds for Bone Tissue Repair,” *Materials*, vol. 13, no. 3, p. 628, Jan. 2020, doi: 10.3390/ma13030628.

[18] R. Gendron, *Thermoplastic Foam Processing*. CRC Press, 2004. doi: 10.1201/9780203502167.

[19] C. J. Yoo, B. S. Shin, B. S. Kang, D. H. Yun, D. B. You, and S. M. Hong, “Manufacturing a Porous Structure According to the Process Parameters of Functional 3D Porous Polymer Printing Technology Based on a Chemical Blowing Agent,” *IOP Conf Ser Mater Sci Eng*, vol. 229, p. 012027, Sep. 2017, doi: 10.1088/1757-899X/229/1/012027.

[20] W. J. Choi *et al.*, “Rapid development of dual porous poly(lactic acid) foam using fused deposition modeling (FDM) 3D printing for medical scaffold application,” *Materials Science and Engineering C*, vol. 110, p. 110693, May 2020, doi: 10.1016/j.msec.2020.110693.

[21] A. Larsen and C. Neldin, “Physical extruder foaming of poly(lactic acid)processing and foam properties,” *Polym Eng Sci*, vol. 53, no. 5, pp. 941–949, 2013, doi: 10.1002/pen.23341.

[22] L. M. Matuana, O. Faruk, and C. A. Diaz, “Cell morphology of extrusion foamed poly(lactic acid) using endothermic chemical foaming agent,” *Bioresour Technol*, vol. 100, no. 23, pp. 5947–5954, 2009, doi: 10.1016/j.biortech.2009.06.063.

[23] S. Neuss *et al.*, “Assessment of stem cell/biomaterial combinations for stem cell-based tissue engineering,” *Biomaterials*, vol. 29, pp. 302–313, 2008, doi: 10.1016/j.biomaterials.2007.09.022.

[24] N. R. Washburn, K. M. Yamada, C. G. Simon, S. B. Kennedy, and E. J. Amis, “High-throughput investigation of osteoblast response to polymer crystallinity: influence of nanometer-scale roughness on proliferation,” *Biomaterials*, vol. 25, no. 7–8, pp. 1215–1224, Mar. 2004, doi: 10.1016/j.biomaterials.2003.08.043.

[25] T. P. Kunzler, T. Drobek, M. Schuler, and N. D. Spencer, “Systematic study of osteoblast and fibroblast response to roughness by means of surface-morphology gradients,” *Biomaterials*, vol. 28, pp. 2175–2182, 2007, doi: 10.1016/j.biomaterials.2007.01.019.

[26] S. C. Neves, C. Mota, A. Longoni, C. C. Barrias, P. L. Granja, and L. Moroni, “Additive manufactured polymeric 3D scaffolds with tailored surface topography influence mesenchymal stromal cells activity,” *Biofabrication*, vol. 8, no. 2, p. 025012, May 2016, doi: 10.1088/1758-5090/8/2/025012.

[27] J. Y. Kim, J. J. Yoon, E. K. Park, D. S. Kim, S. Y. Kim, and D. W. Cho, “Cell adhesion and proliferation evaluation of SFF-based biodegradable scaffolds fabricated using a multi-head deposition system,” *Biofabrication*, vol. 1, no. 1, 2009, doi: Artn 015002 10.1088/1758-5082/1/1/015002.

[28] A. B. Faia-Torres *et al.*, “Osteogenic differentiation of human mesenchymal stem cells in the absence of osteogenic supplements: A surface-roughness gradient study,” *Acta Biomater*, vol. 28, pp. 64–75, 2015, doi: 10.1016/j.actbio.2015.09.028.

[29] A. Nandakumar *et al.*, “Surface modification of electrospun fibre meshes by oxygen plasma for bone regeneration,” *Biofabrication*, vol. 5, no. 1, 2013, doi: 10.1088/1758-5082/5/1/015006.

[30] H. Chen *et al.*, “Tailoring surface nanoroughness of electrospun scaffolds for skeletal tissue engineering,” *Acta Biomater*, vol. 59, pp. 82–93, Sep. 2017, doi: 10.1016/j.actbio.2017.07.003.

[31] C. Wang *et al.*, “3D printing of bone tissue engineering scaffolds,” *Bioact Mater*, vol. 5, no. 1, pp. 82–91, Mar. 2020, doi: 10.1016/j.bioactmat.2020.01.004.

[32] W. Y. Yeong, C. K. Chua, K. F. Leong, and M. Chandrasekaran, “Rapid prototyping in tissue engineering: Challenges and potential,” *Trends in Biotechnology*, vol. 22, no. 12. Elsevier Current Trends, pp. 643–652, Dec. 01, 2004. doi: 10.1016/j.tibtech.2004.10.004.

[33] A. Prasopthum, K. M. Shakesheff, and J. Yang, “Direct three-dimensional printing of polymeric scaffolds with nanofibrous topography,” *Biofabrication*, vol. 10, no. 2, p. 025002, Jan. 2018, doi: 10.1088/1758-5090/aaa15b.

[34] C. Rauwendaal, *Polymer Extrusion*. München: Carl Hanser Verlag GmbH & Co. KG, 2014. doi: 10.3139/9781569905395.

[35] H. P. Dang *et al.*, “3D printed dual macro-, microscale porous network as a tissue engineering scaffold with drug delivering function,” *Biofabrication*, vol. 11, no. 3, p. 035014, Apr. 2019, doi: 10.1088/1758-5090/ab14ff.

[36] H. M. Yin *et al.*, “Engineering porous poly(lactic acid) scaffolds with high mechanical performance via a solid state extrusion/porogen leaching approach,” *Polymers (Basel)*, vol. 8, no. 6, 2016, doi: 10.3390/polym8060213.

[37] F. Shalchy, C. Lovell, and A. Bhaskar, “Hierarchical porosity in additively manufactured bioengineering scaffolds: Fabrication & characterisation,” *J Mech Behav Biomed Mater*, vol. 110, p. 103968, Oct. 2020, doi: 10.1016/j.jmbbm.2020.103968.

[38] D. W. Van Krevelen and K. Te Nijenhuis, *Properties of polymers*. Elsevier, 2009.

[39] L. A. Utracki and C. A. Wilkie, *Polymer Blends Handbook*. Dordrecht: Springer Netherlands, 2014. doi: 10.1007/978-94-007-6064-6.

[40] M. I. Baker, S. P. Walsh, Z. Schwartz, and B. D. Boyan, “A review of polyvinyl alcohol and its uses in cartilage and orthopedic applications,” *Journal of Biomedical Materials Research - Part B Applied Biomaterials*, vol. 100 B, no. 5. pp. 1451–1457, Jul. 2012. doi: 10.1002/jbm.b.32694.

[41] Y. Kaneo, S. Hashihama, A. Kakinoki, T. Tanaka, T. Nakano, and Y. Ikeda, “Pharmacokinetics and biodisposition of poly(vinyl alcohol) in rats and mice.,” *Drug Metab Pharmacokinet*, vol. 20, no. 6, pp. 435–442, Jan. 2005, doi: 10.2133/dmpk.20.435.

[42] E. Chiellini, A. Corti, S. D’Antone, and R. Solaro, “Biodegradation of poly (vinyl alcohol) based materials,” *Progress in Polymer Science (Oxford)*, vol. 28, no. 6. Pergamon, pp. 963–1014, Jun. 01, 2003. doi: 10.1016/S0079-6700(02)00149-1.

[43] S. T. Ho and D. W. Hutmacher, “A comparison of micro CT with other techniques used in the characterization of scaffolds,” *Biomaterials*, vol. 27, no. 8. Elsevier, pp. 1362–1376, Mar. 01, 2006. doi: 10.1016/j.biomaterials.2005.08.035.

[44] H. P. Grace, “Dispersion phenomena in high viscosity immiscible fluid systems and application of static mixers as dispersion devices in such systems,” *Chem Eng Commun*, vol. 14, no. 3–6, pp. 225–277, Mar. 1982, doi: 10.1080/00986448208911047.

[45] Z. H. Shi and L. A. Utracki, “Development of polymer blend morphology during compounding in a twin-screw extruder. Part II: Theoretical derivations,” *Polym Eng Sci*, vol. 32, no. 24, pp. 1834–1845, 1992, doi: 10.1002/pen.760322406.

[46] M. A. Huneault, Z. H. Shi, and L. A. Utracki, “Development of polymer blend morphology during compounding in a twin-screw extruder. Part IV: A new computational model with coalescence,” *Polym Eng Sci*, vol. 35, no. 1, pp. 115–127, Jan. 1995, doi: 10.1002/pen.760350114.

[47] C. McIlroy and P. D. Olmsted, “Deformation of an Amorphous Polymer during the Fused-Filament-Fabrication Method for Additive Manufacturing,” 2016, doi: 10.1122/1.4976839.

[48] G. W. De Kort, S. Rastogi, and C. H. R. M. Wilsens, “Controlling processing, morphology, and mechanical performance in blends of polylactide and thermotropic polyesters,” *Macromolecules*, vol. 52, no. 15, pp. 6005–6017, 2019, doi: 10.1021/acs.macromol.9b01083.

[49] J. Vlachopoulos and D. Strutt, “The role of rheology in polymer extrusion,” in *New Technology for Extrusion Conference. Milan, Italy. Nov*, 2003, pp. 20–21.

[50] M. R. Kamal, L. A. Utracki, and A. Mirzadeh, “Rheology of polymer alloys and blends,” in *Polymer Blends Handbook*, 2014, pp. 725–873. doi: 10.1007/978-94-007-6064-6_9.

[51] Y. Wang, “New biomaterials derived from poly(lactic acids) : novel approaches to combine biodegradation, x-ray contrast and controlled local drug release,” Maastricht University, 2015. doi: 10.15347/wjm/2014.010.

[52] L. A. Feldkamp, L. C. Davis, and J. W. Kress, “Practical cone-beam algorithm,” *Journal of the Optical Society of America A*, vol. 1, no. 6, p. 612, Jun. 1984, doi: 10.1364/josaa.1.000612.

[53] M. Cámara-Torres, R. Sinha, C. Mota, and L. Moroni, “Improving cell distribution on 3D additive manufactured scaffolds through engineered seeding media density and viscosity,” *Acta Biomater*, vol. 101, pp. 183–195, Jan. 2020, doi: 10.1016/J.ACTBIO.2019.11.020.

[54] C. A. Gregory, W. G. Gunn, A. Peister, and D. J. Prockop, “An Alizarin red-based assay of mineralization by adherent cells in culture: Comparison with cetylpyridinium chloride extraction,” *Anal Biochem*, vol. 329, no. 1, pp. 77–84, Jun. 2004, doi: 10.1016/j.ab.2004.02.002.

[55] D. Garlotta, “A literature review of poly(lactic acid),” *J Polym Environ*, 2001, doi: 10.1023/A:1020200822435.

[56] J. K. Lee and C. D. Han, “Evolution of polymer blend morphology during compounding in an internal mixer,” *Polymer (Guildf)*, vol. 40, no. 23, pp. 6277–6296, Nov. 1999, doi: 10.1016/S0032-3861(99)00022-1.

[57] L. Li, “Analysis and fabrication of FDM prototypes with locally controlled properties.” PRISM, 2002. doi: 10.11575/PRISM/10182.

[58] L. J. Gibson, “Biomechanics of cellular solids,” *J Biomech*, vol. 38, no. 3, pp. 377–399, Mar. 2005, doi: 10.1016/j.jbiomech.2004.09.027.

[59] G. Kumar, M. S. Waters, T. M. Farooque, M. F. Young, and C. G. Simon, “Freeform fabricated scaffolds with roughened struts that enhance both stem cell proliferation and differentiation by controlling cell shape,” *Biomaterials*, vol. 33, no. 16, pp. 4022–4030, Jun. 2012, doi: 10.1016/j.biomaterials.2012.02.048.

[60] P. Song *et al.*, “Novel 3D porous biocomposite scaffolds fabricated by fused deposition modeling and gas foaming combined technology,” *Compos B Eng*, vol. 152, pp. 151–159, Nov. 2018, doi: 10.1016/j.compositesb.2018.06.029.

[61] C. W. Visser, D. N. Amato, J. Mueller, and J. A. Lewis, “Architected Polymer Foams via Direct Bubble Writing,” *Advanced Materials*, vol. 31, no. 46, 2019, doi: 10.1002/adma.201904668.

[62] N. Domingues, A. Gaspar-Cunha, and J. A. Covas, “Estimation of the morphology development of immiscible liquid-liquid systems during single screw extrusion,” *Polym Eng Sci*, vol. 50, no. 11, pp. 2194–2204, Nov. 2010, doi: 10.1002/pen.21756.

[63] C. J. Howick, *Handbook Polymer of foams*. 2004.

[64] H. Patel, M. Bonde, and G. Srinivasan, “Biodegradable polymer scaffolds for tissue engineering,” *Trends Biomater. Artif. Organs*, vol. 25, no. 1, pp. 20–29, 2011, doi: 10.1038/nbt0794-689.

[65] A. G. Mikos *et al.*, “Preparation and characterization of poly(l-lactic acid) foams,” *Polymer (Guildf)*, vol. 35, no. 5, pp. 1068–1077, 1994, doi: 10.1016/0032-3861(94)90953-9.

[66] P. Pötschke and D. R. Paul, “Formation of co-continuous structures in melt-mixed immiscible polymer blends,” *Journal of Macromolecular Science - Polymer Reviews*, vol. 43, no. 1, pp. 87–141, 2003, doi: 10.1081/MC-120018022.

[67] H. A. Barnes, “A review of the slip (wall depletion) of polymer solutions, emulsions and particle suspensions in viscometers: its cause, character, and cure,” *J Nonnewton Fluid Mech*, vol. 56, no. 3, pp. 221–251, 1995, doi: 10.1016/0377-0257(94)01282-M.

[68] C. Macosko, *Rheology: Principles, Measurements and Applications*. 1994.

[69] M. Doi and A. Onuki, “Dynamic coupling between stress and composition in polymer solutions and blends,” *Journal de Physique II*, vol. 2, no. 8, pp. 1631–1656, Aug. 1992, doi: 10.1051/jp2:1992225.

[70] T. Nishimura, “Capillary flow behavior of bicomponent polymer blends,” *Rheol Acta*, vol. 23, no. 6, pp. 617–626, Nov. 1984, doi: 10.1007/BF01438802.

[71] C. Chartier, L. Benyahia, J. F. Tassin, H. Dang Ngoc, and J. F. Bardeau, “Selective migration in polyethylene/rubbery particles blends during capillary flow,” *Polym Eng Sci*, vol. 50, no. 4, pp. 773–779, 2010, doi: 10.1002/pen.21584.

[72] B. M. Marín-Santibáñez, J. Pérez-González, G. Gómez-Herrera, and F. Rodríguez-González, “Capillary extrusion of polypropylene/high-density polyethylene immiscible blends as studied by rheo-particle image velocimetry,” *Polym Test*, vol. 84, p. 106390, Apr. 2020, doi: 10.1016/j.polymertesting.2020.106390.

[73] W. Chen, J. Chu, G. Wu, Y. Zhang, and M. Yang, “Rheology control of HDPE/PP binary system forming a multilayer structure: Effects of MWD and shear rate,” *Polym Test*, vol. 73, pp. 60–71, Feb. 2019, doi: 10.1016/j.polymertesting.2018.11.009.

[74] Q. Hamid *et al.*, “Fabrication of three-dimensional scaffolds using precision extrusion deposition with an assisted cooling device,” *Biofabrication*, vol. 3, no. 3, 2011, doi: Artn 034109 10.1088/1758-5082/3/3/034109.

[75] W. A. Kernick and N. J. Wagner, “The role of liquid-crystalline polymer rheology on the evolving morphology of immiscible blends containing liquid-crystalline polymers,” *J Rheol (N Y N Y)*, vol. 43, no. 3, pp. 521–549, May 1999, doi: 10.1122/1.551038.

[76] R. A. de Bruijn, “Deformation and breakup of drops in simple shear flows,” 1989. doi: 10.6100/IR318702.

[77] F. Gauthier, H. L. Goldsmith, and S. G. Mason, “Particle motions in non-Newtonian media I: Couette flow*),” 1971. Accessed: Feb. 10, 2021. [Online]. Available: https://link.springer.com/content/pdf/10.1007/BF01993709.pdf

[78] M. D. Elkovitch and D. L. Tomasko, “Effect of supercritical carbon dioxide on morphology development during polymer blending,” *Polym Eng Sci*, vol. 40, no. 8, pp. 1850–1861, Aug. 2000, doi: 10.1002/pen.11317.

[79] P. Tomlins, P. Grant, S. Mikhalovsky, L. Mikhalovska, S. James, and P. Vadgama, “Characterisation of Polymeric Tissue Scaffolds,” *a National Measurement Good Practice Guide*, no. 89, 2006.

[80] Bruker, “Introduction to porosity analysis,” no. June. pp. 1–17, 2014.

[81] R. N. Wenzel, “Resistance of solid surfaces to wetting by water,” *Ind Eng Chem*, 1936, doi: 10.1021/ie50320a024.

[82] C. Ribeiro, V. Sencadas, A. C. Areias, F. M. Gama, and S. Lanceros-Méndez, “Surface roughness dependent osteoblast and fibroblast response on poly(L-lactide) films and electrospun membranes,” *J Biomed Mater Res A*, vol. 103, no. 7, pp. 2260–2268, Jul. 2015, doi: 10.1002/jbm.a.35367.

[83] M. Jafari *et al.*, “Polymeric scaffolds in tissue engineering: a literature review,” *J Biomed Mater Res B Appl Biomater*, vol. 105, no. 2, pp. 431–459, Feb. 2017, doi: 10.1002/jbm.b.33547.

[84] S. A. Park, S. J. Lee, J. M. Seok, J. H. Lee, W. D. Kim, and I. K. Kwon, “Fabrication of 3D Printed PCL / PEG Polyblend Scaffold Using Rapid Prototyping System for Bone Tissue Engineering Application,” *J Bionic Eng*, vol. 15, pp. 435–442, 2018.

[85] Y. Tamada and Y. Ikada, “Effect of preadsorbed proteins on cell adhesion to polymer surfaces,” *J Colloid Interface Sci*, vol. 155, no. 2, pp. 334–339, Feb. 1993, doi: 10.1006/jcis.1993.1044.

[86] J. B. Hoying and S. K. Williams, *Essentials of 3D Biofabrication and Translation*. Winston-Salem, NC, USA: Elsevier, 2015. doi: 10.1016/C2013-0-18665-5.

[87] Q. L. Loh and C. Choong, “Three-Dimensional Scaffolds for Tissue Engineering Applications: Role of Porosity and Pore Size,” *Tissue Eng Part B Rev*, vol. 19, no. 6, pp. 485–502, Dec. 2013, doi: 10.1089/ten.teb.2012.0437.

[88] J. T. Muth, P. G. Dixon, L. Woish, L. J. Gibson, and J. A. Lewis, “Architected cellular ceramics with tailored stiffness via direct foam writing,” *Proceedings of the National Academy of Sciences*, vol. 114, no. 8, pp. 1832–1837, Feb. 2017, doi: 10.1073/pnas.1616769114.

[89] A. M. Leferink, W. J. Hendrikson, J. Rouwkema, M. Karperien, C. A. Van Blitterswijk, and L. Moroni, “Increased cell seeding efficiency in bioplotted three-dimensional PEOT/PBT scaffolds,” *J Tissue Eng Regen Med*, 2013, doi: 10.1002/term.1842.

[90] S. Martino, F. D’Angelo, I. Armentano, J. M. Kenny, and A. Orlacchio, “Stem cell-biomaterial interactions for regenerative medicine,” *Biotechnology Advances*, vol. 30, no. 1. Elsevier, pp. 338–351, Jan. 01, 2012. doi: 10.1016/j.biotechadv.2011.06.015.

[91] Y. W. Wang, Q. Wu, and G. Q. Chen, “Attachment, proliferation and differentiation of osteoblasts on random biopolyester poly(3-hydroxybutyrate-co-3-hydroxyhexanoate) scaffolds,” *Biomaterials*, vol. 25, no. 4, pp. 669–675, Feb. 2004, doi: 10.1016/S0142-9612(03)00561-1.

[92] T. Guo *et al.*, “3D printing PLGA: a quantitative examination of the effects of polymer composition and printing parameters on print resolution,” *Biofabrication*, vol. 9, no. 2, p. 024101, Apr. 2017, doi: 10.1088/1758-5090/aa6370.

[93] C. J. Wilson, R. E. Clegg, D. I. Leavesley, and M. J. Pearcy, “Mediation of biomaterial-cell interactions by adsorbed proteins: A review,” *Tissue Eng*, vol. 11, no. 1–2, pp. 1–18, 2005, doi: 10.1089/ten.2005.11.1.

[94] G. B. Schneider, R. Zaharias, D. Seabold, J. Keller, and C. Stanford, “Differentiation of preosteoblasts is affected by implant surface microtopographies,” *J Biomed Mater Res A*, vol. 69, no. 3, pp. 462–468, Jun. 2004, doi: 10.1002/jbm.a.30016.

[95] A. Di Luca *et al.*, “Surface energy and stiffness discrete gradients in additive manufactured scaffolds for osteochondral regeneration,” *Biofabrication*, vol. 8, no. 1, p. 015014, Feb. 2016, doi: 10.1088/1758-5090/8/1/015014.

[96] Y. Wu, J. P. Zitelli, K. S. TenHuisen, X. Yu, and M. R. Libera, “Differential response of Staphylococci and osteoblasts to varying titanium surface roughness,” *Biomaterials*, 2011, doi: 10.1016/j.biomaterials.2010.10.001.

[97] M. J. Kim, M. U. Choi, and C. W. Kim, “Activation of phospholipase D1 by surface roughness of titanium in MG63 osteoblast-like cell,” *Biomaterials*, 2006, doi: 10.1016/j.biomaterials.2006.06.023.

[98] G. C. Gazquez *et al.*, “Flexible Yttrium-Stabilized Zirconia Nanofibers Offer Bioactive Cues for Osteogenic Differentiation of Human Mesenchymal Stromal Cells,” *ACS Nano*, 2016, doi: 10.1021/acsnano.5b08005.

[99] J. E. Aubin, “Advances in the osteoblast lineage,” *Biochemistry and Cell Biology*, vol. 76, no. 6. National Research Council of Canada, pp. 899–910, Dec. 01, 1998. doi: 10.1139/o99-005.

[100] F. Guilak, D. M. Cohen, B. T. Estes, J. M. Gimble, W. Liedtke, and C. S. Chen, “Control of Stem Cell Fate by Physical Interactions with the Extracellular Matrix,” *Cell Stem Cell*, vol. 5, no. 1, pp. 17–26, Jul. 2009, doi: 10.1016/j.stem.2009.06.016.

[101] G. Kumar *et al.*, “The determination of stem cell fate by 3D scaffold structures through the control of cell shape,” *Biomaterials*, vol. 32, no. 35, pp. 9188–9196, 2011, doi: 10.1016/j.biomaterials.2011.08.054.

[102] S. H. Barbanti, C. A. Carvalho Zavaglia, and E. A. de Rezende Duek, “Effect of salt leaching on PCL and PLGA (50/50) resorbable scaffolds,” *Materials Research*, vol. 11, no. 1, pp. 75–80, Jan. 2008, doi: 10.1590/S1516-14392008000100014.

[103] C. A. Van Blitterswijk and J. De Boer, *Tissue Engineering: Second Edition*. Elsevier, 2014. doi: 10.1016/C2013-0-00564-6.

[104] S. L. Ferrari *et al.*, “Role for N-cadherin in the development of the differentiated osteoblastic phenotype,” *Journal of Bone and Mineral Research*, 2000, doi: 10.1359/jbmr.2000.15.2.198.

[105] P. C. Schiller, G. D’Ippolito, W. Balkan, B. A. Roos, and G. A. Howard, “Gap-junctional communication is required for the maturation process of osteoblastic cells in culture,” *Bone*, 2001, doi: 10.1016/S8756-3282(00)00458-0.

[106] Z. Li, Z. Zhou, C. E. Yellowley, and H. J. Donahue, “Inhibiting gap junctional intercellular communication alters expression of differentiation markers in osteoblastic cells,” *Bone*, 1999, doi: 10.1016/S8756-3282(99)00227-6.

[107] T. Mygind *et al.*, “Mesenchymal stem cell ingrowth and differentiation on coralline hydroxyapatite scaffolds,” *Biomaterials*, vol. 28, no. 6, pp. 1036–1047, Feb. 2007, doi: 10.1016/j.biomaterials.2006.10.003.

[108] A. K. Gaharwar *et al.*, “Nanoclay-Enriched Poly(ε-caprolactone) Electrospun Scaffolds for Osteogenic Differentiation of Human Mesenchymal Stem Cells,” *Tissue Eng Part A*, vol. 20, no. 15–16, pp. 2088–2101, Aug. 2014, doi: 10.1089/ten.tea.2013.0281.

[109] C. Bao, W. Chen, M. D. Weir, W. Thein-Han, and H. H. K. Xu, “Effects of electrospun submicron fibers in calcium phosphate cement scaffold on mechanical properties and osteogenic differentiation of umbilical cord stem cells,” *Acta Biomater*, 2011, doi: 10.1016/j.actbio.2011.06.046.

Chapter 5

SHAPING AND PROPERTIES OF THERMOPLASTIC SCAFFOLDS IN TISSUE REGENERATION: THE EFFECT OF THERMAL HISTORY ON POLYMER CRYSTALLIZATION, SURFACE CHARACTERISTICS AND CELL FATE

Andrea Roberto Calore[1,2], Varun Srinivas[2], Shivesh Anand[1], Ane Albillos-Sanchez[1], Stan F.S.P. Looijmans[3], Lambert C. A. van Breemen[3], Carlos Mota[1], Katrien Bernaerts[2], Jules Harings[2], Lorenzo Moroni[1]

[1] Complex Tissue Regeneration department, MERLN Institute for Technology-Inspired Regenerative Medicine, Faculty of Health, Medicine and Life Sciences, Maastricht University, Maastricht, The Netherlands

[2] Aachen-Maastricht Institute for Biobased Materials (AMIBM), Faculty of Science and Engineering, Maastricht University, Urmonderbaan 22, 6167 RD Geleen, The Netherlands

[3] Polymer Technology, Eindhoven University of Technology, Eindhoven, The Netherlands

Chapter published in Journal of Materials Research, 36, 3914-3935.

ABSTRACT

Thermoplastic semi-crystalline polymers are excellent candidates for tissue engineering scaffolds thanks to facile processing and tunable properties, employed in melt-based additive manufacturing. Control of crystallization and ultimate crystallinity during processing affect properties like surface stiffness and roughness. These in turn influence cell attachment, proliferation and differentiation. Surface stiffness and roughness are intertwined via crystallinity, but never studied independently. The targeted stiffness range is besides difficult to realize for a single thermoplastic. Via correlation of thermal history, crystallization and ultimate crystallinity of vitamin E plasticized poly(lactide), surface stiffness and roughness are decoupled, disclosing a range of surface mechanics of biological interest. In osteogenic environment, human mesenchymal stromal cells were more responsive to surface roughness than to surface stiffness. Cells were particularly influenced by overall crystal size distribution, not by average roughness. Absence of mold-imposed boundary constrains makes additive manufacturing ideal to spatially control crystallization and henceforward surface roughness of semi-crystalline thermoplastics.

5.1 INTRODUCTION

Additive manufacturing (AM) has emerged as a successful set of techniques in tissue engineering and regenerative medicine (TERM) for scaffold production as it gives full control over scaffold morphology. This feature is extremely important when manufacturing scaffolds for load bearing tissues, such as bone and cartilage, where the architecture plays an essential role in determining their mechanical performances [1], [2].

Melt-extrusion based techniques are a subset of AM methods that have become one of the most investigated strategies to produce scaffolds with thermoplastic polymers. This success is due to the relatively simple equipment needed and the lack of many requirements for the materials to be used, which only need to be thermoplastic in nature. The material, in the shape of a filament or pellets, is melted and extruded, by the application of pressure, through a nozzle. The AM unit moves in the x-y plane to deposit a layer according to the desired pattern. By then shifting along the vertical axis, the following layers are deposited in the typical layer-by-layer manner, realizing scaffolds with tailored geometries [3].

In the framework of TERM, the flexibility in scaffold design and fabrication offered by AM is often coupled to the multipotency of human mesenchymal stromal cells (hMSCs). hMSCs have in fact gained a lot of interest in TERM thanks to their ability to differentiate, among others, towards the osteogenic and chondrogenic lineages. They can be cultured on scaffolds and their differentiation can be driven by several differentiation cues, to produce the tissue of interest. Cues can be nutrients and oxygen, soluble factors or substrate physico-chemical properties [4]. The choice of physical cues (e.g. material stiffness, surface roughness and topography) to instruct cellular behavior presents major benefits when compared to the use of biochemical stimuli alone, such as manufacturing costs, stability and a lower regulatory load when translated to the clinic [5] .

For hard tissues, synthetic polymers represent a widespread choice when selecting the material for scaffold production. They can be designed and synthesized so that they can cause minimal or mild foreign body reaction, and they can be easily modified in terms of their physico-chemical properties when compared to natural-based counterparts. Additionally, many properties such as biodegradation rate, wettability and mechanical performances can be tailored by varying their chemical structure, architecture and molecular weight. In case of copolymers, swelling and protein adsorption can be influenced as well, by changing the copolymer ratio [6], [7].

Semi-crystalline polymers are often the materials of choice, because crystallization is known to enhance the mechanical performance of the final product. The crystalline phase tends to increase the stiffness and the strength of the material thanks to the strong interactions between adjacent chain segments. The amorphous regions are instead more effective in absorbing impact energy [8]–[11]. This is most evident at temperatures above the glass transition (T_g), where chain segments of the amorphous regions possesses conformational and translational motion, are more mobile and the modulus is affected mainly by the crystalline fraction [12].

However, the interest of tissue engineers for stiffness is not limited only to scaffold mechanical performances at the macro scale, i.e. product level. In fact, it has been shown that cell fate is influenced by the mechanics of the surrounding environment, beyond only soft hydrogels [13]–[16]. The link between substrate stiffness and cell fate has been revealed to be cell shape [17]: cells adhering on stiffer (i.e. with a Young's Modulus E larger than 100 kPa) substrates tend to adopt a more spread conformation compared to those growing on softer (i.e. with $E < 100$ kPa) surfaces. In the case of stem cells, their shape affects their phenotype [18], [19]. In particular, Chatterjee et al. [20] showed that hMSCs tend to secrete osteogenic markers when cultured on stiff substrates, while softer materials seem to induce a chondrogenic response [21]. Di Luca et al. [22] investigated the possibility of driving hMSCs fate with material properties in 3D scaffold fabricated by melt-based AM with no further post-processing. Scaffolds with a discrete gradient in surface stiffness were manufactured by using three different materials in the attempt to mimic the osteochondral region, where the tissue stiffness ranges from 100 MPa to beyond 1 GPa for the bone compartment [23]–[25]. Besides being a promising approach from a TERM perspective, this strategy presents some limitations. From an engineering perspective, multi-material gradients require the use of multiple printheads or several loading and unloading cycles of different materials when a single printhead is used, making the process complicated and laborious. Additionally, variations in materials inherently imply variations in the chemistry of the materials used, which might further affect cell response but also hinder interdiffusion at the material interfaces that is based on miscibility and thus type of chemistry. Weak interfaces could result in poor mechanical properties once the whole scaffold is stressed macroscopically, in particular under shear, leading to implant premature failure.

The role of crystallinity in defining the final scaffold properties is not limited to affecting macroscopic stiffness. In the case of AM, the circumferential wall of the nozzle may template surface roughness, but volumetric constrains imposed by the surface roughness of molds do not exist. The crystals forming in proximity and at the surface will generate roughness, which is influenced by crystal size and density [26], [27]. In the past, it has been reported that hMSCs fate could be driven by culturing the cells on substrates with different levels of roughness [28]. In particular, Faia-Torres et al. [29] found the existence of an optimal range of roughness for hMSCs osteogenic differentiation when cultured on poly(ε-caprolactone) (PCL) membranes in dexamethasone-deprived osteogenic induction medium. Chen et al. [30] demonstrated that electrospun fibers with induced surface roughness supported osteogenic differentiation at high values (roughness average (Ra) = 71 ± 11 nm) while promoted chondrogenesis at lower ones (Ra = 14 ± 2 nm). The mechanism by which cell fate is influenced seems to be deputed to the organization of the actin cytoskeleton associated with the microtopography of the substrate: surface features, as well as surface stiffness, affect cell adhesion and the resultant cell morphology, which is known to impact gene expression [29], [31]–[33]. Nevertheless, it is important to highlight how surface stiffness, chemistry and roughness are strongly intertwined and affected by crystallization. To our knowledge, the effects of surface stiffness and roughness on hMSCs fate have never been decoupled in previous studies and the potential influence of one while varying the other was not considered.

In melt-based AM, the crystallization process is governed mainly by thermal stresses and it is highly sensitive to the overall thermal history, especially when considering slowly crystallizing polymers like poly(L-lactide) (PLLA). Besides, thermal history in AM strategies deviates not only from conventional thermoplastic processing/shaping technologies, but also per additively assembled layer or voxel in three dimensional space. To understand the final material and object properties, it is paramount to note that the deposited material is constantly undergoing thermal stresses along the whole manufacturing process, even after solidification. Following the deposition, the material is often kept above its T_g to promote interfacial diffusion, bonding and crystallization to achieve enhanced mechanical properties. Additionally, because of the raster deposition pattern, the nozzle periodically returns in the proximity of previously deposited material, whether within or on top of a specific layer, and reheats the polymer. Srinivas et al. [34] showed that a spatial variations in crystallinity could be found along the building direction (2D) and may exist even in 3D, resulting in inhomogeneous mechanical properties over the object through controlled in gradients, for example, if the thermal management of the printing process is understood.

Considering the effect of crystallization on key material properties such as stiffness and roughness, thermal management appears to be a critical variable when manufacturing scaffolds with thermoplastic polymers. By accurately tuning it, researchers could influence cell behavior by just applying the proper thermal history to the polymer, without having to embed additives in the polymer matrix [35], [36], post-process the scaffold [37], [38] or use multiple materials [22].

When thermoplastics are kept above their T_g, for a given material chemistry, their elastic modulus typically ranges from 0.5 to 1000 MPa dependent on their crystallinity [12]. As previously mentioned, PLLA is a slowly crystallizing material that allows for fine-tuning of its crystallinity, with a T_g of around 55 - 60 °C. In this work, we propose the plasticization of PLLA to achieve stiffness variations in the order of magnitude of the osteochondral region at body temperature, ranging from 100 – 1000 MPa [23], [28], [39], [40], without relying on multiple materials securing interfacial binding and macroscopic mechanical integrity. In order to control surfaces stiffness within the osteochondral range, we then investigate the effect of typical thermal treatments in melt-based AM on surface stiffness or roughness of thin films, separating the two properties. An illustration of the followed workflow can be found in Figure 1. We show how these surface properties are affected just by varying the thermal history of the material, as in melt-based AM. Stiffness and roughness were then quantified by surface indentation and profilometry. Eventually, the potential influence of these parameters on hMSCs osteogenic differentiation was explored.

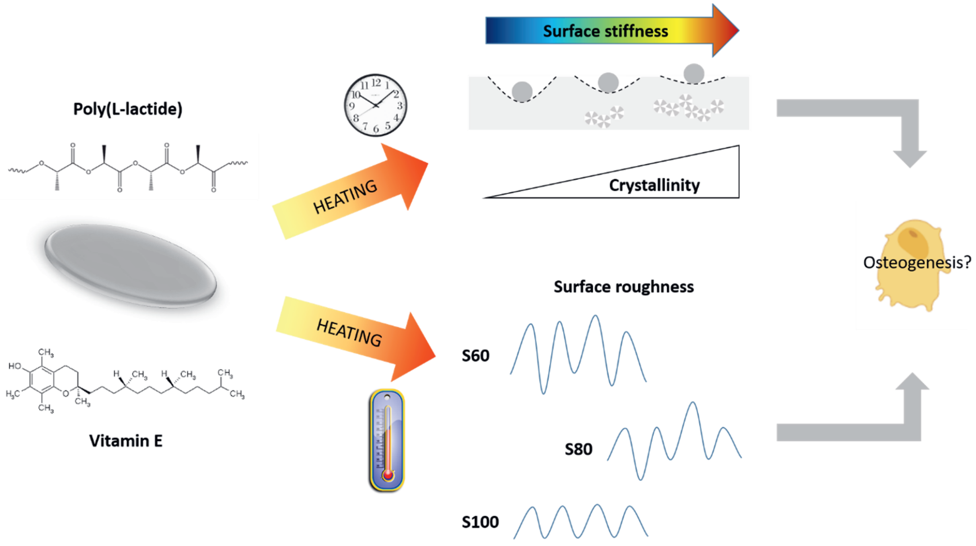

Figure 1. Schematic of the workflow followed to develop the current study.

5.2 MATERIALS AND METHODS

5.2.1 Materials

Poly(L-Lactide), PLLA, with an inherent viscosity midpoint of 1.8 dl/g (PL18), was kindly provided by Corbion (The Netherlands). Poly(3-HydroxyButurate-co-3-hydroxyValerate), PHBV (Enmat Y1000) was supplied by Helian Polymers. Poly(Di-Oxanone), PDO, (Resomer® X 206 S) and Poly(ε-CaproLactone), PCL (M_n 80000 g/mol) were purchased from Sigma-Aldrich. Vitamin E (VE) ((+/-)-alpha-Tocopherol, 95%, synthetic) was supplied by Thermo Fisher Scientific. To prevent hydrolytic degradation under processing conditions, all polymers were dried according to the manufacturer's protocol before any thermal treatment, typically above the glass transition temperature. Silicon wafers were purchased from Si-Mat (Germany).

5.2.2 Material selection

5.2.2.1 PLLA plasticization

Due to the absence of conformational and segmental translational motion the stiffness of polymers below the glass transition temperature (T_g) typically is typically 2-3 GPa. Mobilization of the amorphous phase by increasing the temperature above T_g provides a stiffness range from 0.5 – 1000 MPa. Within this range the stiffness depends among other parameters on crystallinity. In analogy, a reduction of the T_g of PLLA close to or below 37 °C provides access to the targeted stiffness range. Upon screening potentially biocompatible plasticizers, Vitamin E (VE) was found in our laboratory to plasticize PLA. The polymer was blended with VE using different weight fractions by solution-mixing to detect the minimum weight fraction that lowered T_g below body temperature (from now on, referred to as PLLA/VE). Briefly, PLLA and VE were dissolved in chloroform at room temperature and stirred for 1 h. The solution was then cast on a glass petri dish and the solvent was evaporated overnight until a film was formed. All the steps were performed away from direct light to prevent degradation of VE. To remove solvent residue, the samples were dried overnight under vacuum at 35 °C.

5.2.2.2 Thermal analysis

The thermal properties of PDO, PHBV and PLLA/VE were evaluated with a DSC (Q2000, TA instruments). All samples, 5 ± 0.5 mg, were loaded and sealed in hermetic aluminum pans, and the thermal history was erased by heating above the melting temperature (T_m) and quenching in dry ice - acetone mixture (-80 °C). The pans were stored at -30 °C until analyzed. The tests were run using dry nitrogen as purge gas.

The glass transition temperature (T_g) of PLLA/VE blends was determined upon heating from 0 to 200 °C at a rate of 10 °C/min. The concentration was increased stepwise starting from 5 wt%, to reduce the T_g to 37 °C while keeping the amount of plasticizer limited. High concentrations of VE could induce excessive hydrophobicity of the material surface but also accelerate crystallization [41], limiting the control over the process. The PLLA/VE blend with 18 wt% VE (from now on, PLLA/VE18) exhibited a T_g close to 37 °C at a still relatively limited VE concentration. For this reason, PLLA/VE18 was selected among the PLLA/VE blends for further studies.

To evaluate the absence of cold crystallization at body temperature, which would induce undesired changes in crystallinity and thus surface stiffness, isothermal DSC was run on PHBV, PDO and PLLA/VE blends with suppressed crystallization upon fabrication/cooling. Isothermal DSC was run by loading the pans in the DSC machine, heating them at 30 °C/min to 37 °C and leaving them isothermally for 90 min. Samples were further heated up to 200 °C at 10 °C/min and then cooled down to 25 °C at the same rate. The thermal transitions of PCL were screened via fast-scanning chip calorimetry (using a Flash DSC2 from Mettler Toledo as crystallization upon cooling cannot be suppressed at the cooling rates accessible in conventional DSC technology. The sample, previously loaded on a ceramic multistar UFH1 chip, and exposed to multiple heating and cooling ramps ranging from -90 to 100 °C with 3 s of isothermal periods in between. Whereas the heating rate was kept constant, namely 100 °C/s, the cooling rates were varied in a range from 1 to 500 °C/s. The cold crystallization temperature (T_c) was evaluated form the heating cycles.

5.2.2.3 *Thermal stability*

The rheological behavior of the materials over time was measured with a TA DHR rheometer with a parallel plates configuration (25 mm diameter and gap in the range 0.5 – 0.7 mm). The samples were loaded at 190 °C and the time between the loading and the start of the test was kept constant between samples. The materials were sheared for 60 min at 1 rad/s and 1 % strain. As none of the pure polymers showed sufficiently low T_g and stability of the suppressed crystallinity at body temperature, only the PLLA/VE18 sample was considered suitable for further studies.

5.2.3 Surface stiffness

5.2.3.1 *Isothermal crystallization of PLLA/VE18*

The isothermal crystallization behavior was evaluated via DSC. Beforehand, an amorphous sample was prepared by melting the solution-cast film between two silicon wafers at 180 °C for 1 min and then rapidly quenched under running tap water. This was confirmed by 2D WAXD (data included in supporting information, Figure S1). The sample was sealed in a hermetic aluminum pan, heated to 60 °C at 30 °C/min in a TA instruments Q2000 DSC and kept isothermally for 1 h. Relative crystallinities of 0, 50 and 100 % (with respect to the maximum attainable crystallinity for this specific material) were selected for the following studies. From now on, these will be referred to as X_t0, X_t50 and X_t100 respectively.

5.2.3.2 *Annealing*

Solution-cast films were made amorphous as previously described. These were then crystallized at 60 °C in between two silicon wafers, in air, for 45 and 240 s to achieve X_t50 and X_t100, respectively. The films were then rapidly quenched under running tap water.

5.2.3.3 *Mechanical Characterization*

PLLA/VE18 films were mechanically tested to evaluate the shear modulus G' and the surface stiffness.

An Anton Parr MCR 302 was used to record the shear modulus by dynamic mechanical testing in torsion. Samples were subjected to a strain of 0.01 % at a frequency of 1 Hz. Surface stiffness was evaluated by indentation with a Nanoindenter XP (MTS Systems, U.S.A.). Samples were tested with a 2 mm cylindrical flat-ended indenter in controlled displacement mode, with a 3 µm displacement. Five measurements per sample were performed, at different locations. Force as a function of displacement was recorded during the loading and unloading cycles.

5.2.3.4 *Scaffold printing*

A 3Devo single screw extruder was used to prepare a PLLA/VE18 filament by melt extrusion at 190 °C, with a mean diameter of 2.85 mm. Thereafter, an Ultimaker 2+ filament printer was used to fabricate the scaffolds at a nozzle temperature of 190 °C, a build plate temperature of 60 °C and a deposition speed of 50 mm/s. The samples consisted of 18 layers with a layer height of 0.4 mm, an infill of 50% and a deposition patter of 0°/90°, for total dimensions of 20x20x7.2 mm^3. In order to obtain a crystallinity gradient along the vertical axis, where the highest value could be found in the bottom layer, the printing speed was adjusted such that maximum crystallinity could be attained within the part building time. The time to achieve 100% relative crystallinity in the bottom layer was estimated from the isothermal crystallization measurements of PLLA/VE18 at 60 °C.

Additionally, temperature profiling of the bottom layer was performed to ensure that proper heat dissipation along the building height would take place. This would allow the formation of a complete gradient in crystallinity. To this end, the temperature history of the first deposited layer was recorded with varying time intervals between the depositions of consecutive layers. A 0.15 mm K-type thermocouple was placed in the middle of the bottom layer and data were recorded with a DataQ DI718 data acquisition read-out system with 1 kHz sampling frequency.

5.2.4 Surface roughness

5.2.4.1 Annealing

Solution-cast films were made amorphous (0% crystallinity) as previously described. These were all around 25 mm in radius and 0.4 mm in thickness. The films were then fixed on a silicon wafer and annealed at 60, 80 or 100 °C (referred to as S60, S80 and S100) for 240 s to achieve maximum crystallinity. The top surface was allowed to crystallize unconfined. The films were then rapidly quenched.

5.2.4.2 Surface roughness measurement

A Keyence VK-X250 3D Laser Scanning Microscope was used to analyze the surface roughness of the films. Measurements were performed at a 20X magnification in surface profile mode. Data was analyzed using the VK Analyzer software (version 2.5.0.1, Keyence, Japan) and the arithmetic average roughness (Ra) was obtained.

5.2.5 Contact angle measurement

For static contact angle measurements, films were preliminarily incubated overnight at 37 °C in a solution of 1 mg/ml collagen type I from rat tail (Corning) in 0.02 N acetic acid. Collagen was used to further improve cell adhesion in cell culture studies. The next day, they were washed with sterile demineralized H_2O and allowed to dry in air. Contact angle measurements with dH_2O were performed by the sessile drop technique using an optical contact angle device DSA25 (KRÜSS GmbH) equipped with an electronic syringe unit (OCA15, Dataphysics, Germany). The drop analysis and contact angle measurements were evaluated with the software DSA4, by applying the Young-Laplace method.

5.2.6 Cell seeding and culture

5.2.6.1 Cell expansion

hMSCs isolated from bone marrow were purchased from Lonza (Donor 19TL029340, male, age 24). hMSCs and the osteosarcoma cell line MG-63 (ATCC) were plated at 1000 cells/cm^2 in tissue culture flasks and cultured at 37 °C / 5% CO_2 in basic medium (BM), consisting of α-MEM with Glutamax and no nucleosides (Gibco) supplemented with 10 vol% FBS (Sigma-Aldrich), until 80% confluence.

5.2.6.2 Cell seeding and culture

Discs of 13 mm in diameter were punched from X_t0 films. These were then sterilized with exposure to UV light (365 nm) in a CL-1000 Ultraviolet Crosslinker, 20 minutes per side.

MG-63 cells were used to preliminarily assess any potential toxic effect of VE. Trypsinized cells were centrifuged at 500 rcf for 5 min and then resuspended in BM at a density of 50000 cells/ml. 25000 cells/cm^2 were seeded in the wells of a 24-well plate and allowed to attach overnight. The next day (day 0), the medium was replaced with proliferation medium (PM, BM supplemented with penicillin (100 U/ml), streptomycin (100 µg/ml) (Fisher-Scientific) and 200 µM L-ascorbic acid 2-phosphate (Sigma-Aldrich). Transwells (8 µm polycarbonate pore size, Corning) containing the amorphous PLLA/VE18 films were placed inside the wells. The metabolic activity and DNA content of the cultured cells was analyzed at day 1 and 3, with no medium refresh.

To evaluate the seeding efficiency, amorphous films were either plasma treated followed by overnight incubation in BM supplemented with penicillin (100 U/ml) and streptomycin (100 µg/ml) (Fisher-Scientific) or coated with collagen. To plasma treat the films, these were first sealed in plasma sterilization pouches. The pouches were then placed in the chamber of a plasma cleaner (Femto PCCE) and exposed for 2 min to oxygen plasma, at a pressure of 0.53 mbar and 100 W of power [42]. The collagen coating was applied by incubating the films overnight at 37 °C in a solution of 1 mg/ml collagen type I from rat tail (Corning) in 0.02 N acetic acid. Before seeding, all films were dried on top of a sterile filter paper and then placed in the wells of non-threated 24 well plate. Trypsinized MG-63 cells were centrifuged at 500 rcf for 5 min and then resuspended in PM at a density of 50000 cells/ml. The cell suspensions (1 ml) was pipetted on top of each film and the plate was incubated at 37 °C / 5% CO_2. The culture was observed after 24 h.

To investigate any osteogenic effect induced by the different stiffnesses, films were collagen-coated as previously described. The next day, hMSCs (passage 4) were trypsinized and centrifuged for 5 min at 500 rcf. The cells were then resuspended at a density of 50000 cells per 1 ml in PM. The cell suspensions (1 ml) were pipetted on top of each film and the plate was incubated at 37 °C / 5% CO_2. The medium was replaced after 24h and every two or three days from then on. After 7 days (day 0), scaffolds were cultured for another 28 days in PM or mineralization media (DM, PM supplemented with 10 nM dexamethasone (Sigma-Aldrich) and 10 mM β-glycerophosphate (Sigma-Aldrich)). The medium was replaced every two or three days. The culture was analyzed for metabolic activity, alkaline phosphatase (ALP) activity, DNA content both at day 7 and 35, while for osteocalcin and osteopontin production and mineralization at day 28.

5.2.7 Biochemical assays

5.2.7.1 Metabolic activity

PrestoBlue assay (Thermo Fisher Scientific) was used to quantify cell metabolic activity. Briefly, cell culture medium in sample plates was replaced with medium containing 10 v/v% PrestoBlue reagent and the sample plates were incubated in the dark at 37 °C for 1 h. A volume of 100 µl was transferred to a black 96 well plate and fluorescence was measured at 590 nm with a plate reader (CLARIOstar®, BMG Labtech).

5.2.7.2 ALP assay

The scaffolds were washed 3x with PBS and freeze-thawed 3 times. Samples were then incubated for 1h at RT in a cell lysis buffer composed of 0.1 M KH_2PO_4, 0.1 M K_2HPO_4 and 0.1 vol% Triton X-100, at pH 7.8. 10 µl of cell lysate were collected and 40 µl of the chemiluminescent substrate for alkaline phosphatase (CDP-star, Roche) were added. Luminescence (emission = 470 nm) was measured after 15 min incubation, using a spectrophotometer (CLARIOstar®, BMG Labtech). Remaining cell lysates were used for DNA quantification. ALP values were normalized to the DNA content.

5.2.7.3 DNA assay

CyQUANT Cell Proliferation Assay Kit (Thermo Fisher Scientific) was used to quantify the DNA. Samples from ALP assay were first incubated overnight at 56 °C in 1 mg/ml Proteinase K (Sigma-Aldrich) in Tris/EDTA buffer and then freeze-thawed three more times. Subsequently, to degrade the cellular RNA, the lysate was incubated 1 h at RT in a buffer composed of 1:500 RNase A in the cell lysis buffer from the kit diluted 20x in distilled water (dH_2O). The samples were then incubated for 15 min in the fluorescent dye provided by the kit (1:1) for 15 min and fluorescence was measured (emission/excitation = 520/480 nm) with a spectrophotometer. DNA concentrations were calculated from a DNA standard curve.

5.2.7.4 Elisa

The production of osteocalcin (OCN) and osteopontin (OPN) were quantified using ELISA kits (ab270202 and ab192143 respectively, Abcam) according to the manufacturer's instructions. Briefly, at the specified time points, the supernatant from the scaffolds was collected and the protein content was quantified using the ELISA kits. The same samples were used for both assays.

5.2.8 Cell imaging

5.2.8.1 Confocal fluorescence microscopy

Films seeded with hMSCs were fixed in 4 % paraformaldehyde and incubated for 30 min in Triton-X 100 (0.1% v%). A Sudan black solution was added for 60 min to dampen the biomaterial autofluorescence. Then, cell cytoskeleton were stained with 488 Alexa Fluor Phalloidin (Thermo Fisher Scientific, 1:75 dilution in PBS, 1h at RT) and nuclei with DAPI (0.1 µg/mL in PBS, 15 min). Confocal laser scanning microscopy was performed with a tandem confocal system (Leica TCS SP8 STED), equipped with a white light laser (WLL). Samples were excited with the dye specific wavelengths and emission was detected with HyD detectors. For optimal visualization, phalloidin was colored in green and DAPI in blue.

5.2.8.2 Scanning electron microscopy

HMSCs cultured on the polymeric films were fixed in 4 % paraformaldehyde, and subsequently dehydrated using a graded ethanol series (30, 50, 70, 80, 90, 96, 3 x 100 %). The films were washed for 30 min in each solution, after which the ethanol was evaporated in a critical point dryer (Leica EM CPD300) to preserve the surface details of the cultured cells. Finally, a thin layer of gold coating was applied (Quotum Technologies SC7620 Mini Sputter Coater) before imaging them on the scanning electron microscope (Jeol JSM-IT200). The images were captured at magnifications of 130x, 400x and 800x, at an accelerating voltage of 10 kV and working distance of 10 mm.

5.2.9 Statistical analysis

Statistical analyses were performed using GraphPad Prism software. For contact angle, surface stiffness and roughness measurements, a one-way ANOVA test was used. For the transwell study, an unpaired t-test was used to compare between the conditions at the same time point and between the time points of the same condition. For the seeding efficiency study, a one-way ANOVA with Tukey's post-hoc test was used. Statistically significant differences are marked with * ($p<0.05$), ** ($p<0.01$) or *** ($p<0.001$). Experiments were repeated at least 3 times.

For the osteogenic studies, statistical significance was assessed with a one-way ANOVA test with Tukey's post-hoc test for comparison among the conditions in the same medium (surface stiffness or roughness) while with an unpaired t-test when comparing the same condition in the two media. Statistically significant differences are marked with * ($p<0.05$), ** ($p<0.01$) or *** ($p<0.001$) when comparing the effect of different surface stiffness or roughness on cells cultured in the same cell medium and § ($p<0.05$), §§ ($p<0.01$) or §§§ ($p<0.001$) when comparing the effect of different media on cells cultured on films with the same surface stiffness or roughness. Samples in all experiments were in triplicates (n=3).

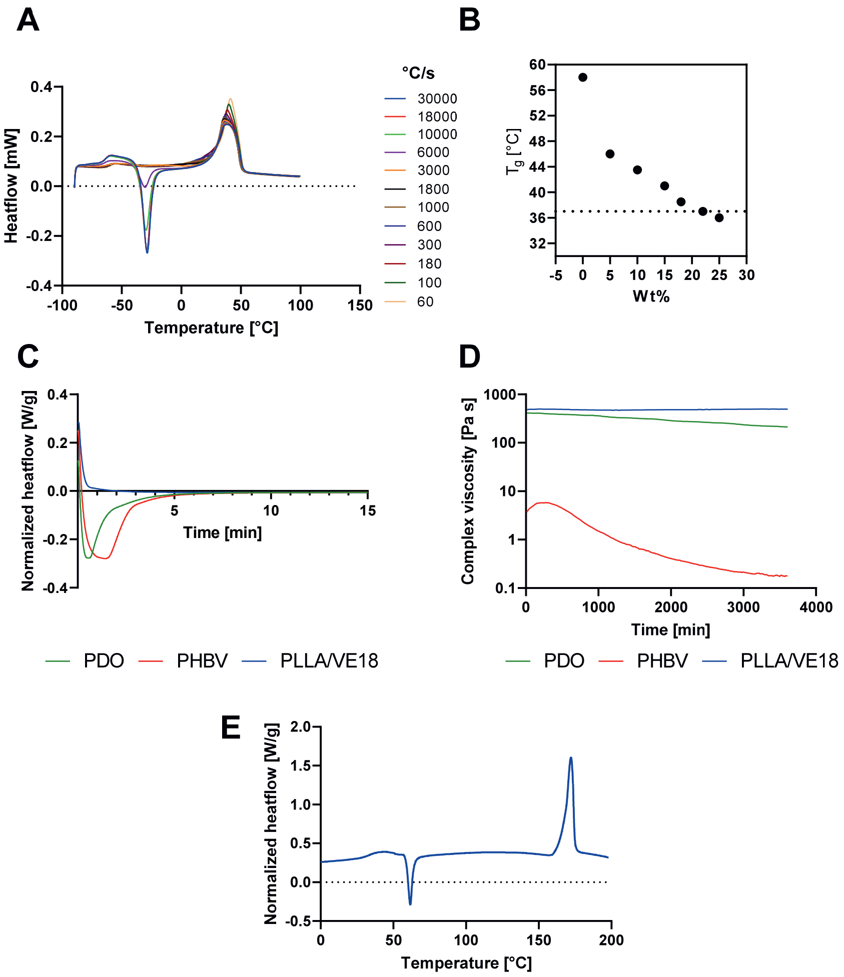

Figure 2. (A) Fast-scanning chip calorimetry thermograms upon heating of PCL with fixed heating rate but made by varying cooling rate ranging from 6.0 E1 to 3.0 E4 °C/min (legend), showing a cold crystallization well below room temperature for samples with incomplete crystallization, i.e. cooled faster than 1.0 E4 °C/min. (B) The effect of increasing weight percentage VE on the glass transition temperature (Tg) of the PLLA/VE blends. (C) Isothermal behavior of PDO, PHBV and PLLA/VE18 at 37 °C. Only the PLLA/VE18 blend did not show any crystallization at body temperature for the time of the test. (D) Melt stability of PDO, PHBV and PLLA/VE18 at 190 °C expressed at complex viscosity over time. (D) (E) DSC thermogram of PLLA/VE18. Measurements were repeated at least 3 times.

5.3 RESULTS

5.3.1 Material selection

A suitable candidate material was required to have T_c and T_g respectively above and below body temperature. Polymer materials with a T_g below body temperature enable the control of (surface) stiffness by means of crystallinity. However, materials with reduced crystallinity, i.e. made via incomplete crystallization, are thermodynamically instable and tend to crystallize if sufficient conformational and translational motion is administered by for example heat. This process is known as cold crystallization and may not occur at body temperature (body conditions) to secure the suppressed crystallinity and associated stiffness. The thermoplastic candidates that comply to the above physiochemical criteria and evaluated in this study are poly(ε-caprolactone) (PCL), poly(dioxanone) (PDO), poly(hydroxybutyrate-co-hydroxyvalerate) (PHBV), and a vitamin E plasticized poly(L-lactide) (PLLA). Due to its known fast crystallization kinetics and low glass transition temperature (~ -60 °C) [43], the thermal behavior of PCL was studied in a fast-scanning chip calorimeter (flash DSC). The PCL sample was melted at 90°C, quenched by cooling with varying cooling ratesand heated again to detect potential cold crystallization as a signature of suppressed crystallinity and its thermal stability. The thermograms in Figure 2A show cold crystallization peak for cooling rates higher than 1.0 E4 °C/min at around -30 °C, with the onset at around -44 °C. This makes this material effectively unusable for the purpose of the study, as it would crystallize even before reaching body temperature.

As PLLA exhibits those slow crystallization kinetics needed to have full control over the process, it was considered as a promising candidate. Nevertheless, the T_g higher than body temperature would make it a glassy material at 37 °C, where changes in crystallinity would result only in slight variations in stiffness. To reduce the T_g, the material was plasticized with vitamin E. The choice was based in the fact that vitamin E is biocompatible and relatively hydrophobic [44], reducing the risk of leaching out that would cause uncontrolled properties over time. A series of blends were prepared and their T_g was measured via DSC. As can be observed in Figure 2B, the glass transition temperature decreased with increasing concentration of VE concentration and, in particular, the blend with 18% showed a T_g close to 37 °C, making it a good candidate for the study. This particular blend was then tested for cold crystallization at body temperature and melt stability, as for the other material candidates. In the isothermal crystallization study at 37 °C using the conventional DSC, PDO and PHBV fully crystallized in less than 10 minutes (Figure 2C). Additionally, PDO and PHBV showed a gradual decrease in complex viscosity over time in the melt rheology analysis (Figure 2D). Only the PLLA/VE18 blend exhibited a stable behavior. In particular, Figure 2C and Figure 2D (blue lines) show that no cold crystallization or viscosity drop happened at the test temperatures during the measurement time.

Figure 2E shows the DSC heating trace of PLLA/VE18 from an amorphous state, recorded at a heating rate of 10 °C/min. It can be seen that the cold crystallization peak starts at 60 °C and finishes at around 105 °C. The annealing temperature of 60 °C was chosen for the surface stiffness study, being the lowest temperature at which crystallization could take place. This would allow high control over the crystallization process with respect to higher temperatures. Temperatures of 60, 80 and 100 °C were selected for the annealing of the films for the surface roughness study.

5.3.2 Surface stiffness

It is well known that polymers upon melt processing cannot be purely crystalline in nature and are in fact semi-crystalline. In this work we define X_t100 as the maximum attainable crystallinity in crystallization from the melt. Amorphous films (X_t0) were prepared and the crystallization kinetics were evaluated by means of isothermal DSC at 60 °C. As it can be seen from Figure 3A, 50% relative crystallinity (X_t50) was achieved in less than 2 minutes while roughly 8 min are necessary for a fully crystallized (X_t100) sample. From these results, 50 % (X_t50) and 100 % (X_t100) crystalline samples were produced by annealing at 60 °C for the indicated time and then rapidly quenched to prevent further crystallization. DSC measurements showed that X_t50 films exhibited an absolute crystallinity of 21% while X_t100 of 52% (data in Supporting Information, Figure S1). Their mechanical properties were evaluated under torsion by DMTA to measure their shear modulus G'. Already at room temperature, the modulus followed the expected increasing trend with crystallinity, with the amorphous, 50 and 100% crystalline samples showing G' values of 396, 653 and 891 MPa respectively. Compared to X_t0, these correspond to an increase in stiffness of 65 and 125% for X_t50 and X_t100. This difference became even more marked at body temperature, where the 50% crystalline sample exhibited a surface stiffness of 465 MPa while full crystallization gave a G’ value of 788 MPa, respectively 104 and 246% higher than the amorphous sample (228 MPa).

As the bulk material properties measured via DMTA are not always representative of the surface stiffness, indentation measurements were performed. The force was recorded as a function of displacement during the loading and unloading cycles on samples kept at 23 and 37 °C. The contact stiffness S was calculated using the method of Pharr et al. [45], according to which S is given by the initial slope of the unloading curve. As in the case of torsional DMTA, Figure 3D and Figure 3E show, respectively, how both S and the maximum force (F_{max}) increased with crystallinity, at both tested temperatures. The 50 and 100% samples showed contact stiffness respectively 17 and 30% higher than the amorphous samples, at room temperature. Instead, at 37 °C, these differences raised to 143 and 207%. The maximum force followed the same trend: at 23 °C, X_t50 and X_t100 showed values 17 and 24% higher than the amorphous film, which increased to 192 and 261% at body temperature.

Table 1. Parameters describing the roughness of the analyzed surfaces: arithmetic mean height of the surface (R_a), root mean square height of the surface (R_q), maximum height of the surface (R_z) and texture aspect ratio (Str). There is no significant difference between the samples.

Sample	R_a [µm]	R_q [µm]	R_z [µm]	Str
S60	0.63 ± 0.47	1280 ± 626.9	6.96 ± 2.09	0.45 ± 0.31
S80	0.64 ± 0.73	1058 ± 853.5	7.05 ± 5.8	0.43 ± 0.27
S100	0.31 ± 0.01	651.1 ± 106	3.72 ± 0.86	0.8 ± 0.07

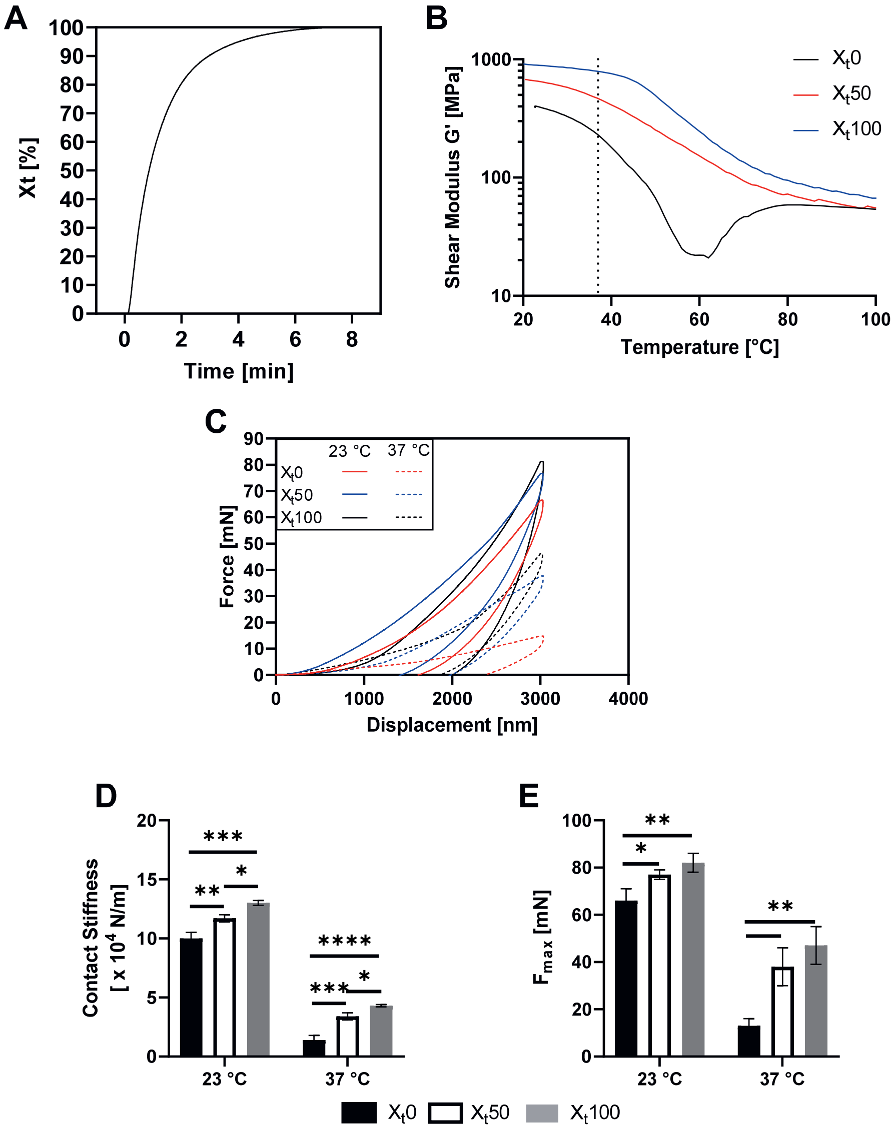

Figure 3. (A) Relative crystallinity plotted as function of time for isothermal crystallization of PLLA/VE18 at 60°C. After less than 8 minutes, full crystallinity is achieved. (B) Dynamic shear modulus of PLLA/VE18 at different crystallinity fractions as a function of temperature. The dashed line indicates 37 °C, where a clear difference in bulk shear modulus can be seen. (C) Force-displacement diagram from indentation tests on films with different crystallinities, at room and body temperature. It can be seen how the trend from bulk mechanical testing is followed by surface mechanics as well. (D) Contact stiffness (S) and (E) maximum force (Fmax) for amorphous, Xt50 and Xt100 crystalline samples measured by indentation at 23°C and 37°C. Data in (D-E) is presented as mean ± standard deviation; n = 3. Statistically significant differences are marked with * ($p<0.05$), ** ($p<0.01$) or *** ($p<0.001$) when comparing the effect of different conditions.

5.3.3 Surface roughness

Surface topography was characterized by laser scanning microscopy (see figure in Supporting Information) and arithmetic mean height of the surface (Ra), the root mean square height of the surface (Rq), the maximum height of the surface (Rz) and texture aspect ratio (Str) were measured. Data in Table 1 show general lower averages for films annealed at 100 °C. Interestingly, S60 and S80 films show a broad distribution for all the parameters evaluated while annealing at 100 °C gave surface features of limited variability. This is reflected in particular in the higher values of texture aspect ratio for S100, which is a measure of the uniformity of the surface texture. Nonetheless, no statistically significant difference was observed across conditions.

5.3.4 Contact angle

To confirm that the annealing did not alter the surface composition, measurements of contact angle by means of the sessile drop technique were performed. As can be seen in Figure 4A, left, there is no statistically relevant difference among films with different crystallinity fraction. The same result was found for films annealed at different temperatures, as shown in Figure 4A, right.

5.3.5 Cell studies

To evaluate the cytotoxicity of the VE, films were placed in transwell on top of well containing a monolayer of MG-63 cells. Cells cultured with VE films were able to grow as shown by the increasing DNA amount over time (Figure 4B). The number of cells was higher for conditions cultured with VE films compared to controls and they also exhibited higher proliferation. However, cells showed a constant metabolic activity over 3 days, which was lower than the controls' at the last day of culture.

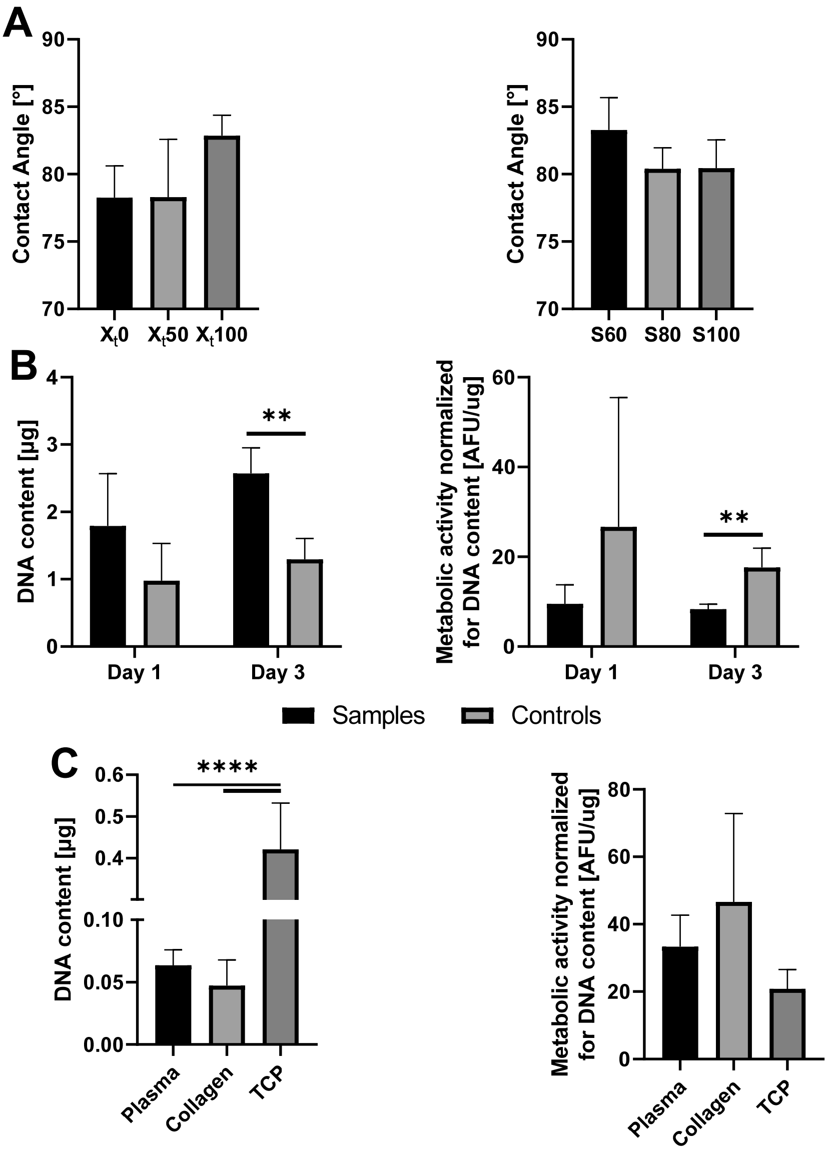

Figure 4. (A) Left: water contact angle of films with different crystallinities. Despite higher mean angle for maximum crystalline films, no significant differences could be seen. Right: water contact angle of films annealed at different temperatures. Despite higher mean angle for maximum crystalline films, no significant differences could be observed. (B) DNA quantification and metabolic activity of MG-63 cells cultured on tissue culture well plates (TCWP) in which transwells with (samples) or without (controls) PLLA/VE18 films were placed. At day 3, cells cultured with films were significantly more than on control plates, but they showed lower metabolic activity per cell. (C) DNA quantification and metabolic activity of MG-63 cells seeded on TCWP and collagen or plasma treated films, after 24 h. Films showed a significantly lower seeding efficiency but a comparable metabolic activity per cell. Statistically significant differences are marked with * ($p<0.05$), ** ($p<0.01$) or *** ($p<0.001$) when comparing the effect of different conditions. Data is presented as mean ± standard deviation; n = 3.

In an attempt to overcome VE hydrophobicity, plasma treatment and collagen coating were tested as methods to maximize the seeding efficiency (Figure 4C). The two strategies did not gave significant differences in the number of cells per film but the amount of attached cells was significantly lower than tissue culture plates for both treatments. However, the metabolic activity per cell seemed higher for cells cultured on film even though not statistically different. Considering that plasma treatment could etch polymeric surfaces [42], [46] and that collagen coating should not mask the surface stiffness nor the surface roughness to cells [14], [16], the latter was chosen as surface treatment method for further studies.

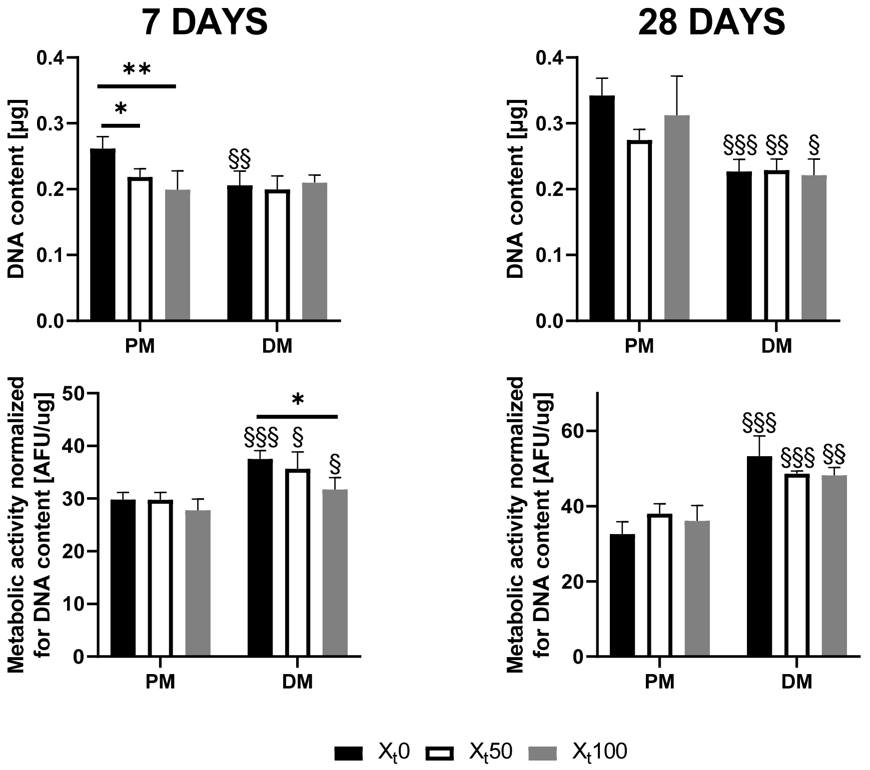

Figure 5. Proliferation and metabolic activity of the human mesenchymal stromal cells (hMSCs) at day 7 (left column) and day 28 (right column), in either proliferation medium (PM) or differentiation medium (DM) conditions (after 7 days in PM), on films with varying crystallinity and surface stiffness. Statistically significant differences are marked with * ($p<0.05$), ** ($p<0.01$) or *** ($p<0.001$) when comparing the effect of different surface stiffness on cells cultured in the same cell medium and § ($p<0.05$), §§ ($p<0.01$) or §§§ ($p<0.001$) when comparing the effect of different media on cells cultured on films with the same surface stiffness. Data is presented as mean ± standard deviation; n = 3.

5.3.5.1 Surface stiffness

The range of achievable surface stiffness during the deposition process was tested for osteogenic effects on hMSCs. Cells were cultured on amorphous, 50% and 100% crystalline films for 28 days, in basic or osteogenic conditions, after 7 days of proliferation. At day 7, cells seemed to have proliferated homogenously on all films (Figure 5, left), besides on the amorphous substrates in PM where the DNA content was higher than the other films in the same medium, but also than the corresponding sample in DM. They also showed to be metabolically active, with those cultured on amorphous and (X_t50) films in osteogenic conditions displaying higher activity than their counterparts in PM. Additionally, the amorphous and X_t50 samples in DM gave a higher reading than the maximum crystalline one. At day 28, the DNA increase was relatively low when compared to values obtained for day 7. The amorphous and X_t50 films in PM showing higher DNA content than their counterparts in DM (Figure 5, right). Furthermore, amorphous films gave higher cell amount than X_t50 sample. Similarly to what observed for day 7, cells on day 21 were significantly more metabolically active in DM than those in basic conditions. Cells also maintained a more rounded morphology in PM and a more spread morphology in DM at both time points (Figure S3, Figure S5).

ALP expression at both time points (Figure 6, left) for all conditions was higher for DM than in PM, which did not show any increase in ALP values over the culture. In PM, X_t50 showed the lowest ALP secretion, but the opposite trend was visible at day 28. In osteogenic conditions, the amorphous films seems to have induced a higher ALP secretion after 7 days, while at day 28 the two different crystallinity conditions supported higher ALP activity.

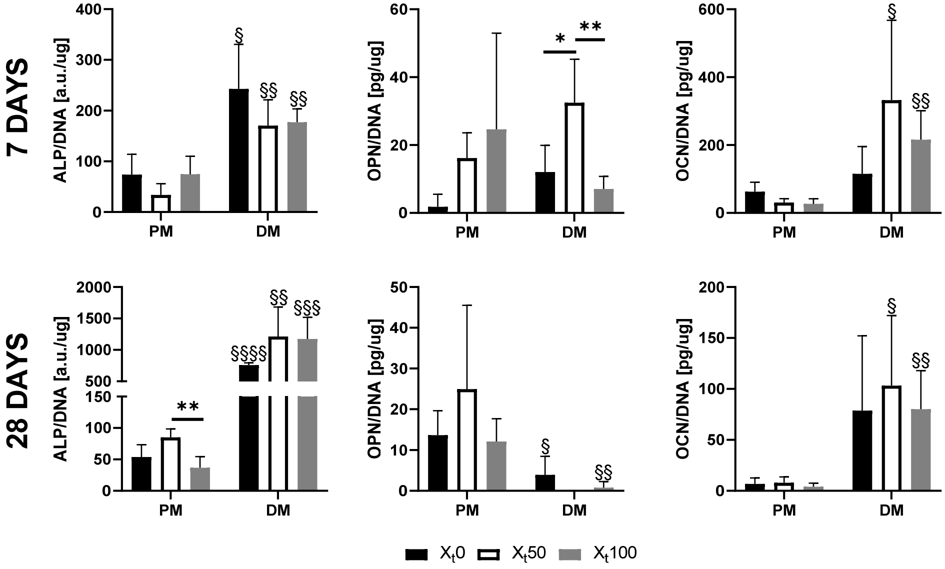

Figure 6. Expression of osteogenic markers from the human mesenchymal stromal cells (hMSCs) at day 7 (top row) and day 28 (bottom row), in either proliferation medium (PM) or differentiation medium (DM) conditions (after 7 days in proliferation medium), on films with varying crystallinity and surface stiffness. Statistically significant differences are marked with * ($p<0.05$), ** ($p<0.01$) or *** ($p<0.001$) when comparing the effect of different surface stiffness on cells cultured in the same cell medium and § ($p<0.05$), §§ ($p<0.01$) or §§§ ($p<0.001$) when comparing the effect of different media on cells cultured on films with the same surface stiffness. Data is presented as mean ± standard deviation; n = 3.

Figure 6 (middle) shows also that osteopontin (OPN) production at day 7 in basic medium followed an increasing trend with stiffness, albeit not statistically significant, while in DM X_t50 resulted in significantly greater secretion. Nevertheless, no significant differences could be seen between the two culture environments. Instead, at day 28 the OPN secretion was higher in PM, with X_t50 showing the highest value. OCN levels in Figure 6 (right) seemed to be decreasing over the culture, resulting in the highest values in DM, at both time points. In particular, cells cultured on the half-crystallized film secreted the most OCN.

5.3.5.2 Surface roughness

Potential osteogenic effects on hMSCs were evaluated also by culturing cells on fully crystalized films in non-confined conditions, so to allow crystals on the surface to freely develop and generate roughness. DNA data showed that cells proliferated in all conditions and both media, with films in basic conditions giving higher cell amount at both time points (Figure 7, top). Interestingly, the fold change over the culture period was roughly the same for both culture environments. Cells were also metabolically active (Figure 7, bottom), with DM cultures supporting enhanced activity at both 7 and 28 days. The expression of all three osteogenic markers was generally higher in osteogenic environment (Figure 8). ALP secretion increased over time, while osteopontin and osteocalcin production decreased. ALP values at day 28 in DM seemed to increase with increasing annealing temperature. Interestingly, the difference between S100 and each of the two other conditions was more significant than the difference between S60 and S80. The secretion of OPN at day 28 in the osteogenic environment showed a very marked peak for S60, while S80 and S100 were comparable to PM culture conditions. Films annealed at 80C supported enhanced osteogenic activity for all the three markers in DM at day 7, but for OCN only at day 28. Cells had a generally spread morphology in both PM and DM culture conditions and at both time points (Figure 9; Figure S4).

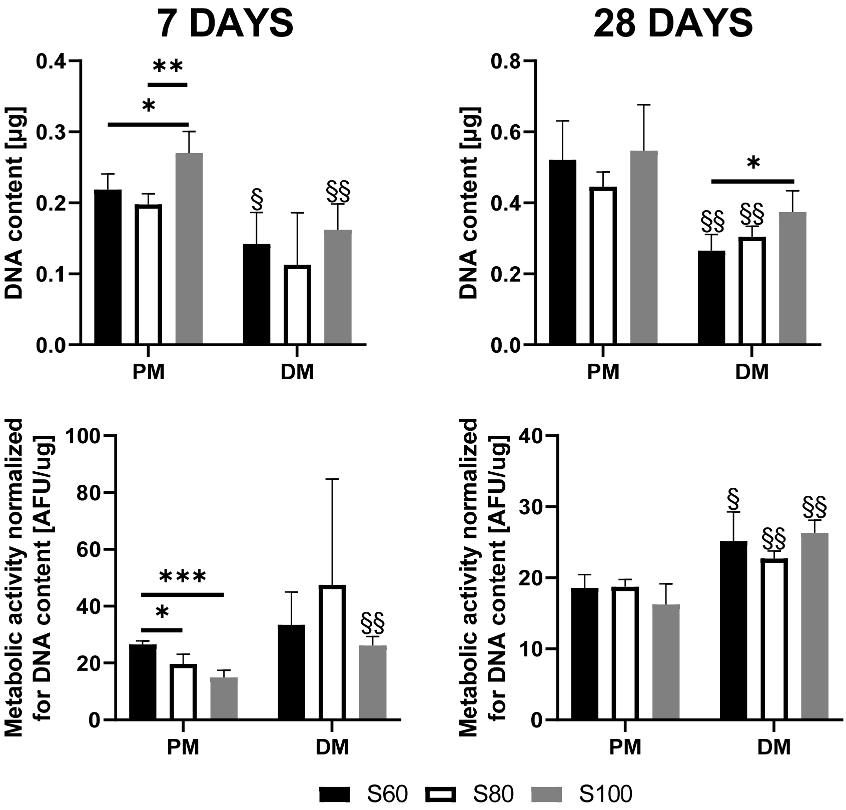

Figure 7. Proliferation and metabolic activity of the human mesenchymal stromal cells (hMSCs) at day 7 (left column) and day 28 (right column), in either proliferation medium (PM) or mineralization medium (DM) conditions (after 7 days in proliferation medium), on films annealed at different temperatures. Statistically significant differences are marked with * (p<0.05), ** (p<0.01) or *** (p<0.001) when comparing the effect of different surface roughness on cells cultured in the same cell medium

and § (p<0.05), §§ (p<0.01) or §§§ (p<0.001) when comparing the effect of different media on cells cultured on films with the same surface roughness. Data is presented as mean ± standard deviation; n = 3.

5.4 DISCUSSION

The main aim of the current study was to investigate the polymer crystallization directed evolution of polymer surface stiffness and surface roughness during additive manufacturing and their potential osteogenic effects on mesenchymal stromal cells. The effect of these two features has been extensively explored, although most studies that focused on the influence of material stiffness on cell differentiation employed hydrogels [13], [16], [47], [48]. Some pioneering work with semi-crystalline polymers was done by Hendrikson et al. [14]. They showed that hMSCs were able to sense the difference in stiffness between scaffolds made of different M_w PCL: cells cultured on softer PCL resulted in a higher hypertrophic chondrogenic differentiation. Di Luca et al. [22] fabricated scaffolds with a gradient in stiffness by sequentially using a poly(ethylene oxide terephthalate)/poly(butylene terephthalate) (PEOT/PBT) copolymer, PCL and PLA and noted that the softer PEOT/PBT showed the highest ALP activity of seeded hMSCs after seven days under osteogenic conditions. On the other hand, the influence of crystallinity-induced surface roughness on cell differentiation has not been much investigated to our knowledge. Most studies either generated surface roughness by other means [29]–[31] or evaluated other effects (e.g. cell proliferation) than differentiation [27], [49]. Nevertheless, despite we cannot exclude also the effect of material chemistry, surface stiffness and roughness are deeply intertwined as both are influenced by the development of crystallinity. To our knowledge, these two properties have never been really decoupled. The same properties were herein investigated separately for the induction of osteogenesis on hMSCs.

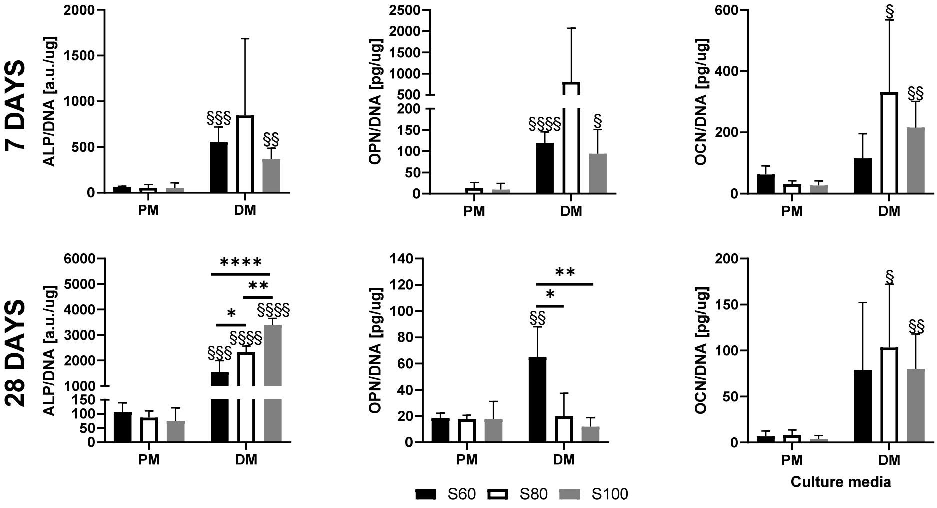

Figure 8. Expression of osteogenic markers from the human mesenchymal stromal cells (hMSCs) at day 7 (top row) and day 28 (bottom row), in either proliferation medium (PM) or differentiation medium (DM) conditions (after 7 days in PM), on films annealed at different temperatures. Statistically significant differences are marked with * (p<0.05), ** (p<0.01) or *** (p<0.001) when comparing the effect of different surface roughness on cells cultured in the same cell medium and § (p<0.05), §§ (p<0.01) or §§§ (p<0.001) when comparing the effect of different media on cells cultured on films with the same surface roughness. Data is presented as mean ± standard deviation; n = 3.

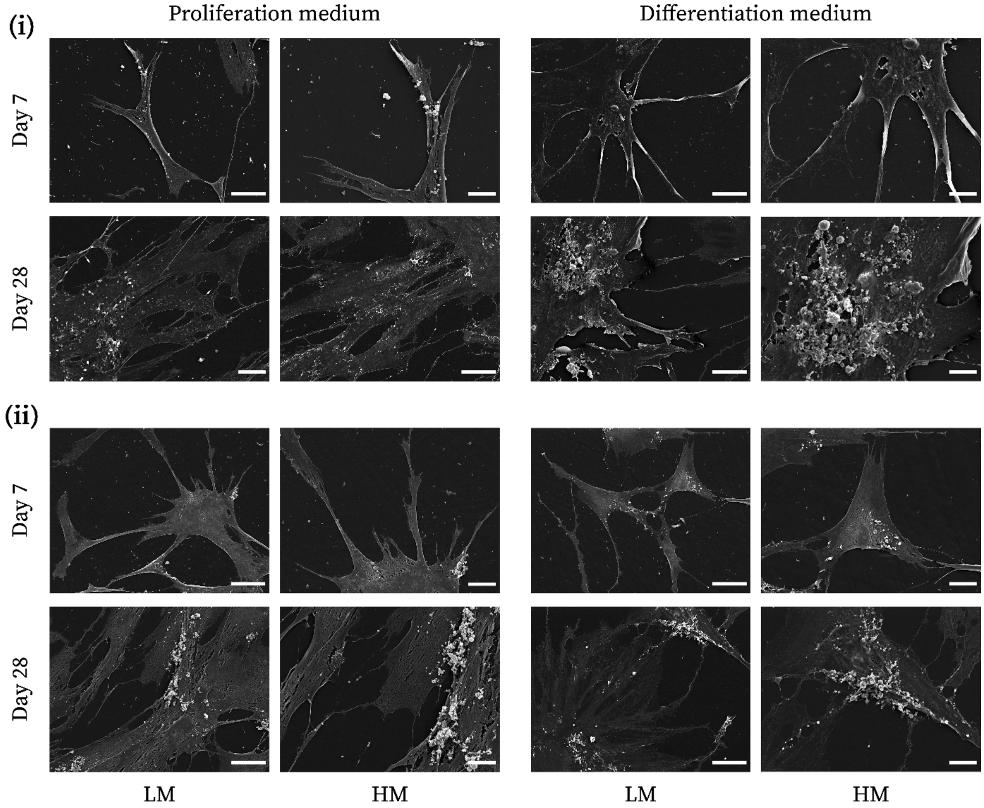

Figure 9. Cell morphology as observed under scanning electron microscopy at day 7 and day 28 for the hMSCs cultured on (i) S80 and (ii) S100 films. The micrographs revealed no visual differences between the cells cultured on different films. Scale bars: low magnification (LM) 50 µm; high magnification (HM) 20 µm.

The first part of the study focused on finding a proper semi-crystalline polymer whose crystallization could be finely controlled to tune its properties at the temperature of interest. The material was expected to have a T_g below 37 °C so that the polymer could exhibit a rubbery behavior at body temperature and a sufficiently low crystallization rate to control its stiffness by means of crystallinity fraction. Additionally, the absence of cold crystallization at 37 °C was necessary to provide constant properties over time, and stable melt processability was needed to allow the preservation of material properties during processing. Several polymers were taken into consideration because of their T_g below body temperature. These were poly(ε-caprolactone) (PCL), poly(dioxanone) (PDO) and poly(hydroxybutyrate-co-hydroxyvalerate) (PHBV). PCL is a well-known thermoplastic polymer widely used in tissue engineering and in AM for scaffold production thanks to its easy processing and stable thermal properties [43]. PDO has been used in sutures and offers a shorter biodegradation time than PCL [50]. PHBV is a copolymer whose degradation rate and crystallinity can be tailored by varying the copolymerization ratio [51]. Fast-scanning chip calorimetry showed that PCL exhibited the cold crystallization peak at around -30 °C, making the material crystallize to its maximum extent at room and body temperature. Since this would give no margin to control the material's crystallinity and therefore its stiffness, PCL was discarded. In isothermal studies, PDO and PHBV both showed cold-crystallization at 37 °C over time. This characteristic hinders their use as scaffold materials as the product properties would not be constant over time under body conditions. Additionally, PHBV displayed very poor thermal stability in rheological tests, affecting the material properties during melt-processing. Due to its slow crystallization kinetics and control in crystallinity via cooling rate, PLLA was considered as potential alternative. As its T_g is around 58 °C, we decided to plasticize it with vitamin E (α-tocopherol). This selection was based on the fact that vitamin E is biocompatible and relatively hydrophobic, reducing the risk of leaching out in aqueous body conditions and causing changes in material properties. As seen Figure 2B, the addition of VE successfully increases the mobility of the conformational and local translational polymer chains with a resulting decrease in the glass transition temperature proportional to the VE content. As an excessively low T_g could result in cold crystallization over time and consequent unstable mechanical properties [52], the blend with 18 wt% was chosen for further studies.

Apart from decoupling the development of the two surface properties for the first time, we intended to explore the possibility of providing a material system that allows for production of scaffolds with predictable and controllable surface stiffness or surface roughness, given the appropriate thermal history, without recurring to multi-material systems [22]. The clear advantages are several: i) easy processing as only one material would be used; ii) enhanced mechanical performance due to better interlayer adhesion; iii) possibility of tuning surface stiffness and/or roughness without changes in surface chemistry or energy. Given the known influence of surface stiffness and roughness on cell activity, and in particular on hMSCs differentiation, we wanted to explore whether the achievable ranges of properties with this material system would affect cell response. Subjecting this material system to annealing conditions typical of melt-based AM, we controlled the crystallization process in an attempt to produce films with a wide range of surface stiffness but also to explore the effects of crystallinity development on surface roughness. By changing crystallization time in confined conditions, films with different crystallinity fractions and therefore surface stiffness were obtained, while maintaining a constant roughness. On the other hand, fully crystallizing films in non-confined condition, allowed us to affect the surface roughness of the films while reaching maximum stiffness. When annealed for different times, the material crystallinity fraction could be controlled and a wide range of bulk stiffness at body temperature could be obtained, as confirmed by DMTA data. In torsional experiments, the steeper drop in moduli for the amorphous sample is due to the fact the in semi-crystalline polymers the crystals are responsible for network formation and load-bearing at temperatures above the T_g [53]. Upon heating towards higher temperatures, the initial decrease in moduli for the amorphous sample is followed by an increase. This can be explained by the process of cold crystallization above the glass transition temperature, which does not happen for the sample with maximum crystallinity. This confirms that maximum crystallinity was achieved. As the bulk properties as measured by DMTA are not always representative for what happens at the surface, the local surface stiffness was investigated by indentation, which confirmed the results obtained in tensile and torsional testing. The described results confirm that the plasticization process allowed us to reduce PLLA T_g so that to have a material in the rubbery plateau at body temperature. This allowed us to obtain a substantial variation in surface stiffness at body temperature by changing the crystallinity fraction. In particular, the achieved range is within the observed values in the osteochondral interface, making this material system a valid choice as thermoplastic polymer for AM of gradient scaffolds.

Bearing in mind that crystallization does not have an influence on surface stiffness only but affects its roughness as well, films were annealed until achievement of full crystallinity, at 60, 80 and 100 °C. This approach was meant to induce the same surface stiffness to all the samples while investigating the effect of possible printing bed or chamber temperatures on the roughness of the fibers. Data showed that the samples all exhibited comparable mean roughness values but with different size distribution. In terms of average, the result is in line with the findings of Tsuji et al. [54], who studied the effect of annealing after quenching on crystal properties of PLLA films. They reported that the spherulite nucleation density or radius seemed to be unchanged with the annealing temperature, in their studied range (100 – 160 °C). In this study, the evaluated range was 60 – 100 °C. However, in our opinion, the wide size distribution of S60 and S80 films may still be explained by the competition between heating, and nucleation and growth kinetics. As described by Li [55], the heating process can be modelled with the lumped-capacity approach whereas the Biot number is lower than 0.1. Given a film with radius of 25 mm and thickness of 0.4 mm, a convection coefficient h = 50 ~ 100 $W/(m^2\ °C)$ and thermal conductivity k = 0.2 $W/(m\ °C)$ [56], we can estimate a Biot number in the range 0.049 ~ 0.098. This allows us to assume uniform temperature distribution throughout the horizontal section and thus to simplify the film heating process into a one-dimensional transient heat transfer model with a convection cooling term:

$$\frac{\partial T}{\partial t} = \frac{k}{\rho C}\frac{\partial^2 T}{\partial z^2} - \frac{hP}{\rho CA}(T - T_{amb})$$

Where z is the coordinate along the film thickness, t is time, $T(z,t)$ is the temperature, T_{amb} is the environmental temperature, ρ is the density, C is the heat capacity. The solution of the equation with the appropriate boundary and initial conditions shows that the time to reach the annealing temperature is inversely proportional to the temperature itself. Samples annealed at 100 °C reached the annealing temperature from RT sooner than the two others did. We hypothesize that heating of the sample happened faster than the start of nucleation. In fact, there exists a time to reach the steady state population of crystal embryos or nuclei, called the induction time [57]. This is a function of temperature and follows a concave parabolic trend [58]. It is possible that the time to heat to 100 °C was shorter than the induction time. Therefore nuclei would form all the same time and thus spherulites would grow homogeneously within the same time window. This is called athermal nucleation. For S60 and S80, the time taken to reach the annealing temperature was probably longer than the induction time, allowing stable nuclei to form at different temperatures along the process. In the meanwhile, these nuclei would grow into crystals over time. Crystals formed at earlier stages had more time to grow while crystals formed later grew to a lesser extent (thermal nucleation).

Different crystallinities did not result in different water contact angles. This is in line with the study of (A. Park and Cima 1996), where it was found that the water advancing contact angle for amorphous and maximum crystalline PLLA films were identical. No differences in contact angle suggest that the changes in bulk properties due to crystallization did not affect the surface wettability of the films. Different surface wettability would affect how water molecules and proteins would adsorb on the surface, thus influencing cell adhesion and consequently morphology and activity (Wei et al. 2009). Films for the roughness study did not show different contact angles as well. According to Wolanksy and Marmur [59], the contact angle measured experimentally on the macroscopic scale (apparent contact angle) describes an average for the entire contact line, which might differ from the actual local contact angle on rough surfaces. The high standard deviations of S60 and S80 state that there is a wide absolute variation in crystal size, which averages out to the same value for all three sample types. Assuming a random distribution of these crystals on the surface, we hypothesize that on the macroscopic scale their contributions counterbalance, giving a similar apparent contact angle for all the three sample types. Finally, it is important to note that, in both studies, the water contact angle of around 80° was at the border of the ideal region identified by Tamada et al. [60] for optimal cell attachment.

Vitamin E is known to be bioactive and it has already been used for TE purposes in past studies [61], [62]. Nevertheless, here PLLA was plasticized with a relatively high concentration that might have induced toxic effects to cells. For this purpose, a transwell study was run. Cells cultured where films were placed, showed as much proliferation as the controls, meaning that the presence of VE did not induce any cytotoxic effect. However, PrestoBlue^{TM} results indicated lower metabolism, in particular at day 3. This could be a sign of the potential excessive plasticizer on the surface slowly diffusing in the cell medium, which could have affected cell activity over time. VE is in fact relatively hydrophobic and its dissolution even in small amounts takes time. The results were considered positive nonetheless, as possible excessive plasticizer diffusion from the surface is counterbalanced in longer cultures with regular medium refresh while here the same medium was used for the whole experiment. Hence, the decrease in metabolic activity could be likely due to the exhaustion of cell nutrients over the first 3 days of culture, thus excluding any potential toxicity associated to VE.

Vitamin E hydrophobicity was expected to influence cell attachment as well. A cell seeding efficiency study was run, comparing the performance of two of the most common used surface treatments to increase cell adhesion, plasma modification and collagen coating. The two strategies led to comparable amounts of cells on the films, which were significantly lower than TCP controls. This was most likely due to excessive vitamin molecules on the surface, which might have hindered the effectiveness of the surface treatments when compared to plain TCP. In selecting the appropriate treatment method, it was considered that the action of plasma might etch the polymer surface, affecting the crystallization-induced surface roughness. On the other hand, collagen is a semi-flexible polymer with a persistence length of 15 nm [63], [64], which forms fibrils of 200 – 2500 nm in diameter [65]. Given these elements and the hydration induced softening in aqueous conditions, we postulated that the collagen molecules would not excessively mask the surface roughness of the films annealed at different temperatures and we chose this as a surface treatment method.

We successfully produced polymer films where we decoupled the effects of crystallinity on surface roughness and surface stiffness. We first achieved a wide range of surface stiffness and quantified the effect of annealing on surface roughness, and then assessed their impact on the osteogenic differentiation of hMSCs. Cells cultured on films with varying stiffness showed limited proliferation over time, which could be the result of poor affinity with the substrates. This could be due to the relatively high water contact angle or due the smoothness of the surface given by the silicon wafers [66], [67]. Nevertheless, they were metabolically active, although differences could be seen between the two media used. Cells in basic environment proliferated more. but showed lower metabolic activity per cell than their counterparts in DM. PrestoBlue^{TM} assay is based on the reduction of resazurin to resorufin by mitochondrial activity; [68] and [69] noted that differentiation often leads to an increase in mitochondrial oxidation. This suggests that cells in DM might already be differentiating at the early time point.

From the ALP profile in PM at day 28, it can be hypothesized that X_t50% might trigger osteogenic differentiation more than the other conditions in PM, as it is the only conditions showing an increase over time. Considering that ALP is an early osteogenic marker, we can postulate either that the peak had already occurred before day 28 or that we are in the presence of the onset of a relatively late one. Nevertheless, values are extremely far from those in osteogenic environment, indicating that the extent of the possible differentiation might be very limited. This hypothesis seems to be supported by the quantification of osteocalcin secretion, where it can be seen that in basic culture no condition appears to support osteogenic differentiation more than the others and values were far from the positive controls in DM. Here, it is worth to notice that cells cultured on X_t50 films seemed to have secreted more OCN than those on amorphous and maximum crystalline films, although not significantly. The OPN profile is somewhat counterintuitive, as at day 7 cells in basic conditions performed comparably to the osteogenic environment but they outperformed at day 28, with X_t50 standing out. Aubin et al. [70] noted that ALP production first increases then decreases when mineralization is in an advanced stage, and that osteopontin should appear prior to osteocalcin, which becomes detectable with mineralization. The results obtained here suggest that the cells cultured in osteogenic conditions are in an advanced stage of the differentiation process, with OCN already present. Instead, considering the lower ALP and osteocalcin levels, cells in PM might be in an earlier osteogenesis phase, when OPN has just started appearing. In general, there is no specific condition outperforming the others although X_t50 films seem to induce a higher secretion of osteogenesis-related proteins in several conditions but never significantly. Most of the studies that investigated the influence of material stiffness on cell differentiation were based on hydrogels and reported a stiffness range of 1 – 100 kPa to instruct cell fate [13], [16], [47], [48]. In this research, the surface stiffness of the polymer is far greater than the stiffness of hydrogels and it is plausible that the relative difference between the conditions in PM is too limited to induce different responses between each other. This seems to be confirmed by the culture in osteogenic environment, where the soluble factors pushed the osteogenic differentiation, probably overcoming the variations between the conditions. In fact, Engler et al. [16] showed that hMSCs grown on a osteogenic matrix can be induced by soluble cues to express factors from another lineage, yielding to a “mixed hMSC phenotype”.

As crystal formation and growth influences the topography of thermoplastic polymers, the effect of typical annealing conditions in melt-based AM on the surface roughness of PLLA/VE18 films was investigated. In fact, the topography of biomedical materials has been known to influence stem cell differentiation both in 2D [29], [33] and 3D [5], [30], [31] constructs. As previously described, there were no significant differences in terms of R_a between the conditions, although a wide distribution was found for S60 and S80 films. To assess whether these surface features could influence hMSCs fate, cells were cultured for 28 days on films annealed at 60, 80 and 100 °C in unconfined conditions. DNA data indicate that cells adhered and proliferated homogeneously on all films, and appeared to be metabolic active. However, cells cultured in osteogenic conditions showed a slightly higher metabolic activity, probably sign of progressing differentiation as previously mentioned. This seemed to be confirmed by the values for osteogenic markers, which were generally higher in DM than in basic conditions, at both time points. Probably, the relative differences in surface roughness among the conditions was not enough to induce a significant response by one of them, but also the effect of surface cues seemed to be weaker than that by the soluble factors. Nevertheless, considering the surface roughness profiles from the films, the interesting ALP results at day 28 in osteogenic conditions are complicated to be placed in context with previous studies. [5] found that the roughest etched scaffolds ($R_a \approx 1.06$ μm) induced osteogenic differentiation on hMSCs while [31] showed higher osteogenic markers in scaffolds with surface roughness lower than 0.227 μm. Because of the high variability in roughness values for S60 and S80, it does not seem possible to categorize the data into “low” or “high” relative roughness in our study. What we seem to observe is that ALP production is influenced by the overall crystal size distribution rather than the average roughness. In fact, samples annealed at 100 °C showed a relatively low variability and ALP production more significantly higher than the two other conditions, which did not differ from each other as much. Whether smaller or bigger crystals are favoring osteogenic differentiation, ALP values are affected also by those cells growing on surface portions not inducing osteogenesis, thus fading the effect of those crystals domains influencing cell fate. Results from OPN at day 28 showed comparable values for S80 and S100 over the two media, probably indicating that cells in DM are in the osteoprogenitor phase, when there is ALP expression but uncertain osteopontin secretion [4]. Instead, cells cultured on S60 gave a very marked peak for OPN, suggesting that they might be in a later phase of differentiation when the level of ALP starts to decline and OPN to be observed [71], [72]. It might be that S60 induced more ALP expression than S100 in a time point earlier than 28 days, which was not considered here. Considering OPN and ALP values together, we hypothesize that S60 in DM accelerated osteogenic differentiation compared to S100 while cells cultured on this film appeared to be still in an earlier phase. It is important to note that S60 and S80 films showed roughly the same surface roughness values but different OPN expression. This should not be ascribed to differences in stiffness, as the samples are maximum crystalline and thus they should show the same modulus [54]. Instead, the surface roughness results showed a wider size distribution for S80, indicating the presence of both smaller and bigger crystals compared to S60. Reminding that S100 showed the narrowest crystal size distribution and the highest ALP values at day 28, it appears that extreme roughness values in the obtained range did not particularly favor osteogenesis. In the study of Faia-Torres et al. [29], hMSCs were cultured on PCL substrates where a gradient in surface roughness was induced. It was found that a specific roughness range induced faster osteogenic commitment compared to tissue culture polystyrene. In this work as well, there seems to be an effective size distribution that promotes faster differentiation in osteogenic conditions, corresponding to S60. Wider crystal size distribution means that cells adhered both on very small and very big crystals. Whereas crystals had dimensions outside the effective range, the cells adhering on them did not contribute to the osteogenic signals, reducing the overall expression, as shown by S80 films.

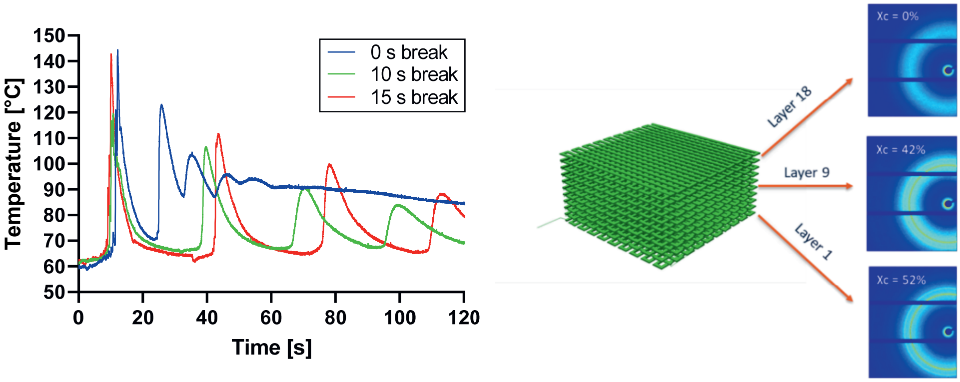

Figure 10. (Left) Temperature profiles of printing scaffolds recorded at the center of the bottom layer at 50 mm/s printing speed with breaks of 0, 10 and 15 seconds after each layer deposition. (Right) Scaffold printed employing a break of 10 seconds after the deposition of each layer. 2D WAXD patterns of layer1, 9 and 18 reveal the crystallinity gradient achieved.

The preliminary assessment of the impact of typical AM annealing conditions on the surface properties of polymer films indicates that stiffness can be controlled in a finer way than roughness. Nevertheless, the latter seemed to affect cell fate more strongly than surface stiffness in the range evaluated in this study. Furthermore, the whole crystal size distribution appeared to play an important role, rather than the average roughness. Our study supports that the thermal history in AM must be carefully considered when extruding polymers with controllable crystallization kinetics, as it can influence surface properties known to impact cell behavior and potentially induce "priming" [73]. In this respect, future studies should also aim at evaluating the effect of long-term cell culture on the surface properties of the substrates. PLLA is a hydrolytically degradable polymer and the degradation process preferentially takes place in the amorphous regions, resulting in an increase in crystallinity [74]. It seems reasonable to assume that some conformational modification might occur at the surface, thus influencing cell response to the evolving substrate. In addition, the effect of annealing in 3D should be investigated as well, as more complicated thermal phenomena such as conductive dissipation within the filament and radial trends might appear. In a preliminary test (experimental procedure not described), the incorporation of breaks between subsequent layers deposition showed lower temperature peaks, resulting from greater heat dissipation (Figure 10, left). Reduced heat accumulation is likely to improve the control over spatial variations in cold crystallization. Figure 10, right, shows the crystallinity over height in a scaffold printed employing a 10 s break between layers. The 2D WAXD confirmed the achievement of a crystallinity gradient, which suggests that material and scaffold properties can be tuned by carefully controlling the temperature profile during printing. This method could provide a potential simpler approach to induce stem cell differentiation towards the osteogenic lineage compared to the more conventional approaches of creating polymer composite scaffolds [75], despite the use of specific inorganic fillers could still be combined with the control in surface roughness and crystallinity here proposed to further provide the fabricated scaffolds with other biofunctional properties. Examples of further instructive AM scaffolds include bioglasses to stimulate angiogenesis in combination with osteogenesis [76], and antibiotics to prevent possible risks of infections [77], among others.

5.5 CONCLUSIONS

This study presents the development of a material system to achieve a surface stiffness range in the order of magnitude of the adult osteochondral region, at body temperature. Furthermore, we report that surface stiffness and surface roughness can be separately influenced by finely control crystallinity formation via thermal annealing typical of melt-based AM. Indentation tests revealed that the polymeric films presented surface stiffness that varied as function of the crystalline fraction, over a range typical of the osteochondral region. Surface roughness showed no variations in average with annealing temperature, but substantial differences in crystal size distribution. The impact of these two surface properties on hMSCs osteogenic commitment was investigated, showing that cells seemed to respond more sensibly to the crystal size distribution, although only in osteogenic culture conditions, than the achieved stiffness range. This suggests that the impact of thermal history on the properties of thermoplastic polymers should be carefully considered to control cell “priming”, in particular when driving cell fate towards other lineages.

ACKNOWLEDGMENTS

Some of the materials were kindly provided by Corbion (The Netherlands). This work was financed by Brightlands Material Center and by the Dutch Province of Limburg.

REFERENCES

[1] C. Mota, D. Puppi, F. Chiellini, and E. Chiellini, 'Additive manufacturing techniques for the production of tissue engineering constructs', *J Tissue Eng Regen Med*, vol. 9, no. 3, pp. 174–190, 2015, doi: 10.1002/term.1635.

[2] S. Camarero-Espinosa, C. Tomasina, A. R. Calore, and L. Moroni, 'Additive manufactured, highly resilient, elastic, and biodegradable poly(ester)urethane scaffolds with chondroinductive properties for cartilage tissue engineering', *Mater Today Bio*, vol. 6, p. 100051, Mar. 2020, doi: 10.1016/j.mtbio.2020.100051.

[3] A. R. Calore, R. Sinha, J. Harings, K. V Bernaerts, C. Mota, and L. Moroni, 'Chapter 7 Thermoplastics for Tissue Engineering', in *Computer-Aided Tissue Engineering*, A. Rainer and L. Moroni, Eds., 2021, pp. 75–99.

[4] C. A. Van Blitterswijk and J. De Boer, *Tissue Engineering: Second Edition*. Elsevier, 2014. doi: 10.1016/C2013-0-00564-6.

[5] G. Kumar, M. S. Waters, T. M. Farooque, M. F. Young, and C. G. Simon, 'Freeform fabricated scaffolds with roughened struts that enhance both stem cell proliferation and differentiation by controlling cell shape', *Biomaterials*, vol. 33, no. 16, pp. 4022–4030, Jun. 2012, doi: 10.1016/j.biomaterials.2012.02.048.

[6] J. C. Middleton and A. J. Tipton, 'Synthetic biodegradable polymers as orthopedic devices', *Biomaterials*, vol. 21, no. 23, pp. 2335–2346, 2000, doi: Doi 10.1016/S0142-9612(00)00101-0.

[7] D. W. Hutmacher, 'Scaffold design and fabrication technologies for engineering tissues - State of the art and future perspectives', *J Biomater Sci Polym Ed*, vol. 12, no. 1, pp. 107–124, 2001, doi: 10.1163/156856201744489.

[8] T. Miyata and T. Masuko, 'Crystallization behaviour of poly(L-lactide)', *Polymer (Guildf)*, vol. 39, no. 22, pp. 5515–5521, Oct. 1998, doi: 10.1016/S0032-3861(97)10203-8.

[9] G. Perego, G. D. Cella, and C. Bastioli, 'Effect of molecular weight and crystallinity on poly(lactic acid) mechanical properties', *J Appl Polym Sci*, vol. 59, no. 1, pp. 37–43, Jan. 1996, doi: 10.1002/(sici)1097-4628(19960103)59:1<37::aid-app6>3.0.co;2-n.

[10] F. W. Billmeyer, *Textbook of Polymer Science*, vol. 12, no. 3. 1963. doi: 10.1295/kobunshi.12.240.

[11] M. Cocca, M. L. Di Lorenzo, M. Malinconico, and V. Frezza, 'Influence of crystal polymorphism on mechanical and barrier properties of poly(l-lactic acid)', *Eur Polym J*, vol. 47, no. 5, pp. 1073–1080, May 2011, doi: 10.1016/j.eurpolymj.2011.02.009.

[12] H. F. Brinson and L. C. Brinson, *Polymer Engineering Science and Viscoelasticity*. Boston, MA: Springer US, 2015. doi: 10.1007/978-1-4899-7485-3.

[13] N. Huebsch *et al.*, 'Harnessing traction-mediated manipulation of the cell/matrix interface to control stem-cell fate', *Nat Mater*, vol. 9, no. 6, pp. 518–526, Apr. 2010, doi: 10.1038/nmat2732.

[14] W. J. Hendrikson, J. Rouwkema, C. A. Van Blitterswijk, and L. Moroni, 'Influence of PCL molecular weight on mesenchymal stromal cell differentiation', *RSC Adv*, vol. 5, no. 67, pp. 54510–54516, 2015, doi: 10.1039/c5ra08048g.

[15] J. H. Wen *et al.*, 'Interplay of matrix stiffness and protein tethering in stem cell differentiation', *Nat Mater*, vol. 13, no. 10, pp. 979–987, Oct. 2014, doi: 10.1038/nmat4051.

[16] A. J. Engler, S. Sen, H. L. Sweeney, and D. E. Discher, 'Matrix Elasticity Directs Stem Cell Lineage Specification', *Cell*, vol. 126, no. 4, pp. 677–689, Aug. 2006, doi: 10.1016/j.cell.2006.06.044.

[17] T. Yeung *et al.*, 'Effects of substrate stiffness on cell morphology, cytoskeletal structure, and adhesion', *Cell Motil Cytoskeleton*, vol. 60, no. 1, pp. 24–34, Jan. 2005, doi: 10.1002/cm.20041.

[18] A. Zemel, F. Rehfeldt, A. E. X. Brown, D. E. Discher, and S. A. Safran, 'Cell shape, spreading symmetry, and the polarization of stress-fibers in cells', *Journal of Physics Condensed Matter*, vol. 22, no. 19, p. 194110, Apr. 2010, doi: 10.1088/0953-8984/22/19/194110.

[19] L. MacQueen, Y. Sun, and C. A. Simmons, 'Mesenchymal stem cell mechanobiology and emerging experimental platforms', *J R Soc Interface*, vol. 10, no. 84, p. 20130179, Jul. 2013, doi: 10.1098/rsif.2013.0179.

[20] K. Chatterjee *et al.*, 'The effect of 3D hydrogel scaffold modulus on osteoblast differentiation and mineralization revealed by combinatorial screening', *Biomaterials*, vol. 31, no. 19, pp. 5051–5062, Jul. 2010, doi: 10.1016/J.BIOMATERIALS.2010.03.024.

[21] J. S. Park *et al.*, 'The effect of matrix stiffness on the differentiation of mesenchymal stem cells in response to TGF-β', *Biomaterials*, vol. 32, no. 16, pp. 3921–3930, Jun. 2011, doi: 10.1016/J.BIOMATERIALS.2011.02.019.

[22] A. Di Luca *et al.*, 'Surface energy and stiffness discrete gradients in additive manufactured scaffolds for osteochondral regeneration', *Biofabrication*, vol. 8, no. 1, p. 015014, Feb. 2016, doi: 10.1088/1758-5090/8/1/015014.

[23] K. A. Athanasiou, C.-F. Zhu, D. R. Lanctot, C. M. Agrawal, and X. Wang, 'Fundamentals of Biomechanics in Tissue Engineering of Bone', Mary Ann Liebert, Inc, 2000.

[24] A. Di Luca, C. Van Blitterswijk, and L. Moroni, 'The osteochondral interface as a gradient tissue: From development to the fabrication of gradient scaffolds for regenerative medicine', *Birth Defects Res C Embryo Today*, vol. 105, no. 1, pp. 34–52, Mar. 2015, doi: 10.1002/bdrc.21092.

[25] S. Camarero-Espinosa, A. R. Calore, A. Wilbers, J. Harings, and L. Moroni, 'Additive manufacturing of an elastic poly(ester)urethane for cartilage tissue engineering', *Acta Biomater*, vol. 102, pp. 192–204, Jan. 2020, doi: 10.1016/j.actbio.2019.11.041.

[26] A. Larena and G. Pinto, ‘The effect of surface roughness and crystallinity on the light scattering of polyethylene tubular blown films’, *Polym Eng Sci*, vol. 33, no. 12, pp. 742–747, Jun. 1993, doi: 10.1002/pen.760331204.

[27] N. R. Washburn, K. M. Yamada, C. G. Simon, S. B. Kennedy, and E. J. Amis, ‘High-throughput investigation of osteoblast response to polymer crystallinity: influence of nanometer-scale roughness on proliferation’, *Biomaterials*, vol. 25, no. 7–8, pp. 1215–1224, Mar. 2004, doi: 10.1016/j.biomaterials.2003.08.043.

[28] F. Guilak, D. M. Cohen, B. T. Estes, J. M. Gimble, W. Liedtke, and C. S. Chen, ‘Control of Stem Cell Fate by Physical Interactions with the Extracellular Matrix’, *Cell Stem Cell*, vol. 5, no. 1, pp. 17–26, Jul. 2009, doi: 10.1016/j.stem.2009.06.016.

[29] A. B. Faia-Torres *et al.*, ‘Osteogenic differentiation of human mesenchymal stem cells in the absence of osteogenic supplements: A surface-roughness gradient study’, *Acta Biomater*, vol. 28, pp. 64–75, 2015, doi: 10.1016/j.actbio.2015.09.028.

[30] H. Chen *et al.*, ‘Tailoring surface nanoroughness of electrospun scaffolds for skeletal tissue engineering’, *Acta Biomater*, vol. 59, pp. 82–93, Sep. 2017, doi: 10.1016/j.actbio.2017.07.003.

[31] S. C. Neves, C. Mota, A. Longoni, C. C. Barrias, P. L. Granja, and L. Moroni, ‘Additive manufactured polymeric 3D scaffolds with tailored surface topography influence mesenchymal stromal cells activity’, *Biofabrication*, vol. 8, no. 2, p. 025012, May 2016, doi: 10.1088/1758-5090/8/2/025012.

[32] C. J. Wilson, R. E. Clegg, D. I. Leavesley, and M. J. Pearcy, ‘Mediation of biomaterial-cell interactions by adsorbed proteins: A review’, *Tissue Eng*, vol. 11, no. 1–2, pp. 1–18, 2005, doi: 10.1089/ten.2005.11.1.

[33] G. B. Schneider, R. Zaharias, D. Seabold, J. Keller, and C. Stanford, ‘Differentiation of preosteoblasts is affected by implant surface microtopographies’, *J Biomed Mater Res A*, vol. 69, no. 3, pp. 462–468, Jun. 2004, doi: 10.1002/jbm.a.30016.

[34] V. Srinivas, C. S. J. van Hooy-Corstjens, and J. A. W. Harings, ‘Correlating molecular and crystallization dynamics to macroscopic fusion and thermodynamic stability in fused deposition modeling; a model study on polylactides’, *Polymer (Guildf)*, vol. 142, pp. 348–355, Apr. 2018, doi: 10.1016/j.polymer.2018.03.063.

[35] P. F. Costa, A. M. Puga, L. Díaz-Gomez, A. Concheiro, D. H. Busch, and C. Alvarez-Lorenzo, ‘Additive manufacturing of scaffolds with dexamethasone controlled release for enhanced bone regeneration’, *Int J Pharm*, vol. 496, no. 2, pp. 541–550, 2015, doi: 10.1016/j.ijpharm.2015.10.055.

[36] B. P. Hung *et al.*, ‘Three-Dimensional Printing of Bone Extracellular Matrix for Craniofacial Regeneration’, *ACS Biomater Sci Eng*, vol. 2, no. 10, pp. 1806–1816, Oct. 2016, doi: 10.1021/acsbiomaterials.6b00101.

[37] L. R. Jaidev and K. Chatterjee, ‘Surface functionalization of 3D printed polymer scaffolds to augment stem cell response’, *Mater Des*, vol. 161, pp. 44–54, Jan. 2019, doi: 10.1016/j.matdes.2018.11.018.

[38] S. Li, Y. Xu, J. Yu, and M. L. Becker, ‘Enhanced osteogenic activity of poly(ester urea) scaffolds using facile post-3D printing peptide functionalization strategies’, *Biomaterials*, vol. 141, pp. 176–187, Oct. 2017, doi: 10.1016/j.biomaterials.2017.06.038.

[39] A. Di Luca, A. Longoni, G. Criscenti, C. Mota, C. van Blitterswijk, and L. Moroni, ‘Toward mimicking the bone structure: design of novel hierarchical scaffolds with a tailored radial porosity gradient’, *Biofabrication*, vol. 8, no. 4, p. 045007, 2016, doi: 10.1088/1758-5090/8/4/045007.

[40] R. Langer and J. P. Vacanti, ‘Tissue engineering’, *Science (1979)*, 1993, doi: 10.1126/science.8493529.

[41] J.-F. Agassant, P. Avenas, P. J. Carreau, B. Vergnes, and M. Vincent, *Polymer Processing*, vol. 33, no. 22. München: Carl Hanser Verlag GmbH & Co. KG, 2017. doi: 10.3139/9781569906064.

[42] J. Yang, J. Bei, and S. Wang, ‘Enhanced cell affinity of poly (D,L-lactide) by combining plasma treatment with collagen anchorage’, *Biomaterials*, vol. 23, no. 12, pp. 2607–2614, Jun. 2002, doi: 10.1016/S0142-9612(01)00400-8.

[43] M. A. Woodruff and D. W. Hutmacher, ‘The return of a forgotten polymer—Polycaprolactone in the 21st century’, *Prog Polym Sci*, vol. 35, no. 10, pp. 1217–1256, Oct. 2010, doi: 10.1016/j.progpolymsci.2010.04.002.

[44] E. Reboul, ‘Vitamin e bioavailability: Mechanisms of intestinal absorption in the spotlight’, *Antioxidants*, vol. 6, no. 4, 2017, doi: 10.3390/antiox6040095.

[45] G. M. Pharr and W. C. Oliver, ‘Measurement of Thin Film Mechanical Properties Using Nanoindentation’, *MRS Bull*, 1992, doi: 10.1557/S0883769400041634.

[46] K. Tsougeni, A. Tserepi, G. Boulousis, V. Constantoudis, and E. Gogolides, ‘Control of Nanotexture and Wetting Properties of Polydimethylsiloxane from Very Hydrophobic to Super-Hydrophobic by Plasma Processing’, *Plasma Processes and Polymers*, vol. 4, no. 4, pp. 398–405, May 2007, doi: 10.1002/ppap.200600185.

[47] O. Chaudhuri *et al.*, ‘Substrate stress relaxation regulates cell spreading’, *Nat Commun*, vol. 6, no. 1, pp. 1–7, Feb. 2015, doi: 10.1038/ncomms7365.

[48] N. S. Hwang, S. Varghese, H. Li, and J. Elisseeff, ‘Regulation of osteogenic and chondrogenic differentiation of mesenchymal stem cells in PEG-ECM hydrogels’, *Cell Tissue Res*, vol. 344, no. 3, pp. 499–509, Jun. 2011, doi: 10.1007/s00441-011-1153-2.

[49] V. Bernardo, G. M. Luz, N. M. Alves, and J. F. Mano, ‘Cell behaviour in new poly(l-lactic acid) films with crystallinity gradients’, *Mater Lett*, vol. 87, pp. 105–108, Nov. 2012, doi: 10.1016/j.matlet.2012.07.088.

[50] M. Niaounakis, *Biopolymers: Processing and Products*. 2014. doi: 10.1016/C2013-0-09982-3.

[51] J. E. Mark, *Physical properties of polymers handbook*, vol. 1076. Springer, 2007.

[52] S. Varun, ‘Timing of interfacial diffusion and (stereo)crystallization to tailor mechanical properties of additively manufactured poly(lactides)’, maastricht university, 2020. doi: 10.26481/dis.20201013vs.

[53] A. Gleadall, ‘Mechanical properties of biodegradable polymers for medical applications’, in *Modelling Degradation of Bioresorbable Polymeric Medical Devices*, Elsevier Ltd, 2015, pp. 163–199. doi: 10.1533/9781782420255.2.163.

[54] H. Tsuji and Y. Ikada, ‘Properties and morphologies of poly(L-lactide): 1. Annealing condition ts on properties and morphologies of poly(L-lactide)’, *Polymer (Guildf)*, vol. 36, no. 14, pp. 2709–2716, 1995.

[55] L. Li, ‘Analysis and Fabrication of FDM Prototypes with Locally Controlled Properties’, 2002.

[56] E. Zhmayev, H. Zhou, and Y. L. Joo, ‘Modeling of non-isothermal polymer jets in melt electrospinning’, *J Nonnewton Fluid Mech*, vol. 153, no. 2–3, pp. 95–108, 2008, doi: 10.1016/j.jnnfm.2007.11.011.

[57] B. Wunderlich, *Macromolecular Physics, Volume 2: Crystal Nucleation, Growth, Annealing*, vol. 2. Academic Press Inc., 1976.

[58] R. D. Sudduth, P. Kyarala, and Q. Sheng, ‘A comparison of induction time and crystallization rate for syndiotactic polystyrene’, *Polym Eng Sci*, vol. 42, no. 4, pp. 694–706, Apr. 2002, doi: 10.1002/pen.10982.

[59] G. Wolansky and A. Marmur, ‘The actual contact angle on a heterogeneous rough surface in three dimensions’, *Langmuir*, vol. 14, no. 18, pp. 5292–5297, 1998, doi: 10.1021/la960723p.

[60] Y. Tamada and Y. Ikada, ‘Effect of preadsorbed proteins on cell adhesion to polymer surfaces’, *J Colloid Interface Sci*, vol. 155, no. 2, pp. 334–339, Feb. 1993, doi: 10.1006/jcis.1993.1044.

[61] S. K. Misra *et al.*, ‘Incorporation of vitamin E in poly(3hydroxybutyrate)/Bioglass composite films: effect on surface properties and cell attachment’, *J R Soc Interface*, vol. 6, no. 33, pp. 401–409, Apr. 2009, doi: 10.1098/rsif.2008.0278.

[62] F. Renò, V. Aina, S. Gatti, and M. Cannas, ‘Effect of vitamin E addition to poly(d,l)-lactic acid on surface properties and osteoblast behaviour’, *Biomaterials*, vol. 26, no. 28, pp. 5594–5599, Oct. 2005, doi: 10.1016/J.BIOMATERIALS.2005.02.015.

[63] B. Trappmann *et al.*, ‘Extracellular-matrix tethering regulates stem-cell fate’, *Nat Mater*, vol. 11, no. 7, pp. 642–649, May 2012, doi: 10.1038/nmat3339.

[64] C. Storm, J. J. Pastore, F. C. MacKintosh, T. C. Lubensky, and P. A. Janmey, ‘Nonlinear elasticity in biological gels’, *Nature*, vol. 435, no. 7039, pp. 191–194, May 2005, doi: 10.1038/nature03521.

[65] K. J. Langenbach, J. T. Elliott, A. Tona, D. McDaniel, and A. L. Plant, ‘Thin films of Type 1 collagen for cell by cell analysis of morphology and tenascin-C promoter activity’, *BMC Biotechnol*, vol. 6, no. 1, p. 14, Mar. 2006, doi: 10.1186/1472-6750-6-14.

[66] J. Qu, B. Chehroudi, and D. M. Brunette, ‘The use of micromachined surfaces to investigate the cell behavioural factors essential to osseointegration’, *Oral Dis*, vol. 2, no. 1, pp. 102–115, 1996, doi: 10.1111/j.1601-0825.1996.tb00210.x.

[67] Y. Wan *et al.*, ‘Adhesion and proliferation of OCT-1 osteoblast-like cells on micro- and nano-scale topography structured poly(L-lactide)’, *Biomaterials*, vol. 26, no. 21, pp. 4453–4459, Jul. 2005, doi: 10.1016/j.biomaterials.2004.11.016.

[68] K. Helm *et al.*, ‘In Vitro Cell Death Discrimination and Screening Method by Simple and Cost-Effective Viability Analysis’, *Cellular Physiology and Biochemistry*, vol. 41, no. 3, pp. 1011–1019, May 2017, doi: 10.1159/000460910.

[69] N. Shyh-Chang and H. H. Ng, ‘The metabolic programming of stem cells’, *Genes and Development*, vol. 31, no. 4. Cold Spring Harbor Laboratory Press, pp. 336–346, Feb. 15, 2017. doi: 10.1101/gad.293167.116.

[70] J. E. Aubin, ‘Advances in the osteoblast lineage’, *Biochemistry and Cell Biology*, vol. 76, no. 6. National Research Council of Canada, pp. 899–910, Dec. 01, 1998. doi: 10.1139/o99-005.

[71] G. S. Stein, J. B. Lian, and T. A. Owen, ‘Relationship of cell growth to the regulation of tissue-specific gene expression during osteoblast differentiation’, *The FASEB Journal*, vol. 4, no. 13, pp. 3111–3123, 1990, doi: 10.1096/fasebj.4.13.2210157.

[72] J. E. Aubin, ‘Regulation of Osteoblast Formation and Function’, *Rev Endocr Metab Disord*, vol. 2, no. 1, pp. 81–94, 2001, doi: 10.1023/A:1010011209064.

[73] C. Yang, M. W. Tibbitt, L. Basta, and K. S. Anseth, ‘Mechanical memory and dosing influence stem cell fate’, *Nat Mater*, vol. 13, no. 6, pp. 645–652, Mar. 2014, doi: 10.1038/nmat3889.

[74] S. Li, H. Garreau, and M. Vert, ‘Structure-property relationships in the case of the degradation of massive poly(α-hydroxy acids) in aqueous media - Part 3 Influence of the morphology of poly(l-lactic acid)’, *J Mater Sci Mater Med*, vol. 1, no. 4, pp. 198–206, Nov. 1990, doi: 10.1007/BF00701077.

[75] O. Bas *et al.*, ‘Tuning mechanical reinforcement and bioactivity of 3D printed ternary nanocomposites by interfacial peptide-polymer conjugates’, *Biofabrication*, vol. 11, no. 3, p. 035028, Jun. 2019, doi: 10.1088/1758-5090/aafec8.

[76] T. Distler *et al.*, ‘Polymer-Bioactive Glass Composite Filaments for 3D Scaffold Manufacturing by Fused Deposition Modeling: Fabrication and Characterization’, *Front Bioeng Biotechnol*, vol. 8, Jun. 2020, doi: 10.3389/fbioe.2020.00552.

[77] M. Cámara-Torres *et al.*, ‘3D additive manufactured composite scaffolds with antibiotic-loaded lamellar fillers for bone infection prevention and tissue regeneration’, *Bioact Mater*, vol. 6, no. 4, pp. 1073–1082, Apr. 2021, doi: 10.1016/j.bioactmat.2020.09.031.

Supporting Information

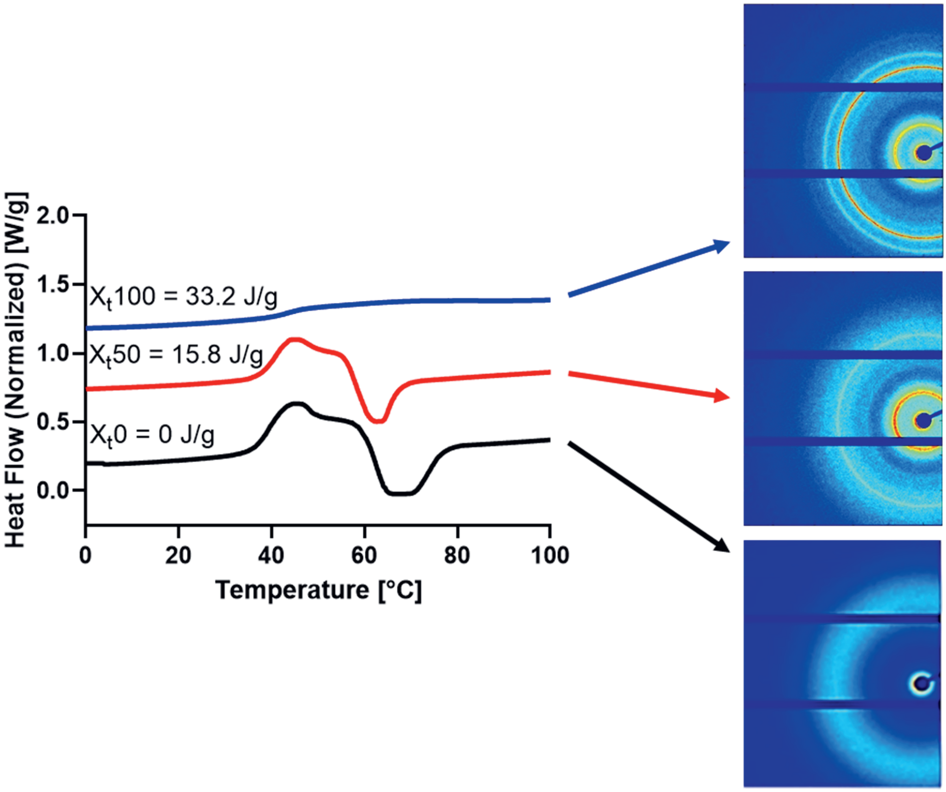

Figure S1. On the left: DSC thermogram of amorphous (X_t0), 50% (X_t50) and 100% (X_t100) relative-crystalline PLLA/VE18 films. The relative value correspond to 0, 15.8 and 33.2 J/g respectively. On the right: 2D WAXD pattern from PLLA/VE18 films: it can be seen that the broad amorphous halo leaves place to a crystal-induced sharp circumferential diffraction signal that is more pronounced with increasing crystallinity.

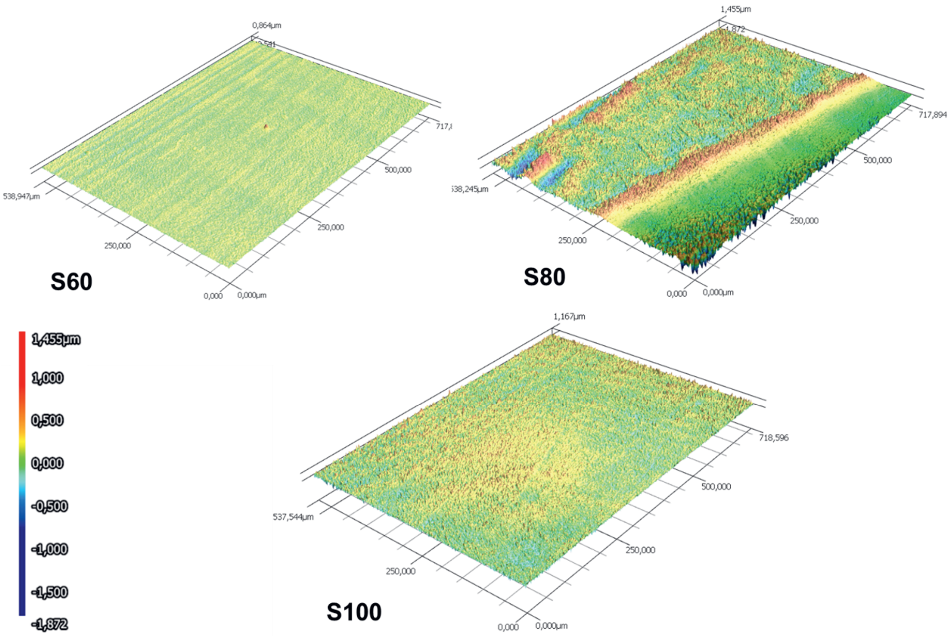

Figure S2. Surface map of S60, S80 and S100 PLLA/VE18 films as provided by profilometry.

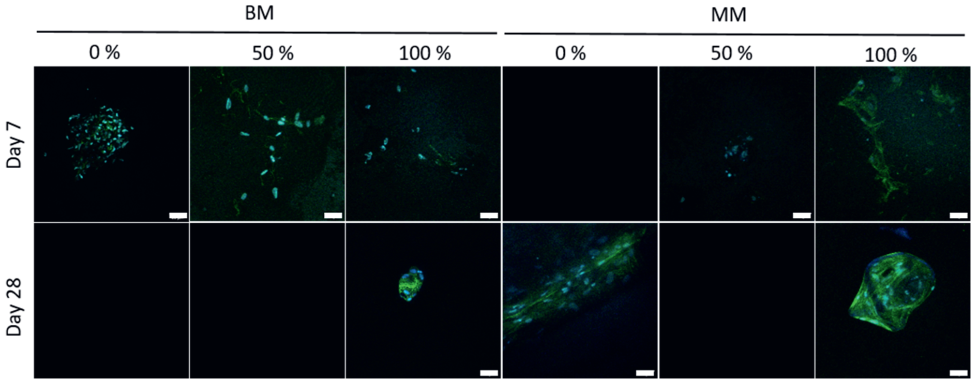

Figure S3. Cell morphology of hMSCs at day 7 and day 28 in PM and DM culture conditions on substrates with of amorphous (X_t0), 50% (X_t50) and 100% (X_t100) relative-crystalline. Scale bars: 50 µm.

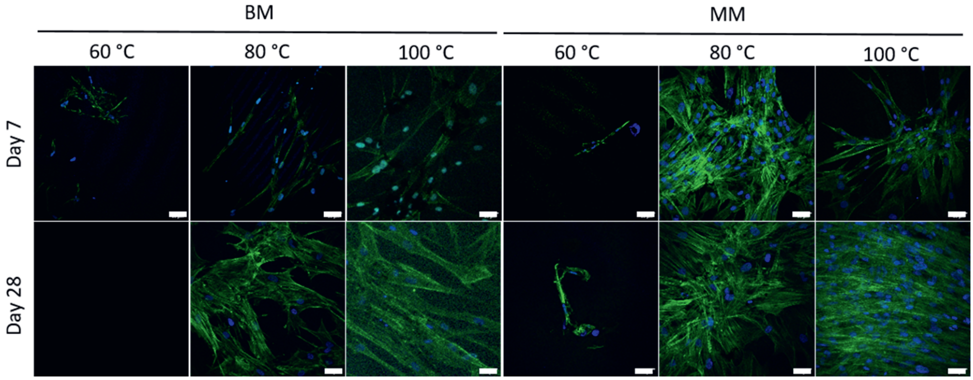

Figure S4. Cell morphology of hMSCs at day 7 and day 28 in PM and DM culture conditions on substrates with of S60, S80 and S100 relative roughness. Scale bars: 50 µm.

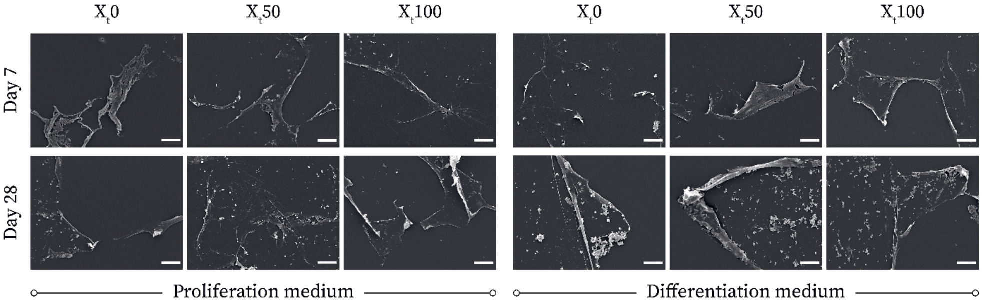

Figure S5. Scanning electron micrographs demonstrating the morphology of hMSCs cultured on X_t0, X_t50 and X_t100 films in proliferation and differentiation medium, respectively. Scale bars: 20 µm.

Chapter 6

GENERAL DISCUSSION

In this Chapter, the most important findings of the thesis will be discussed and put into perspective of the main goal of this work, which is the optimization of melt extrusion additive manufacturing (ME-AM) of scaffolds for bone regeneration via the acquisition of a deep understanding of material and processing properties. We highlight the reasons for (i) material and manufacturing technique of choice, (ii) the importance of a deep knowledge of the manufacturing process and (iii) how to apply it for better performing scaffolds in biological environments.

6.1 WHY MELT EXTRUSION ADDITIVE MANUFACTURING?

Additive Manufacturing (AM) is a set of fabrication techniques that perfectly encompasses the level of production freedom required by tissue engineering and regenerative medicine (TERM). The layer-by-layer building strategy allows to have full control over the overall object morphology, which is paramount in the framework of personalized medicine. In fact, in the medical field, the awareness that every patient is unique has been growing over the years [1]. Therefore, a typical workflow for personalized medical implants starts with imaging the geometry of the patient’s defect via 3D scanning methods [2]. Then, a 3D model of the defect is obtained, and this can be utilized to produce patient-specific implants. AM allows to easily and flexibly fabricate shapes that correspond to the specific defect in object, without the need for the corresponding mold as in injection molding and avoiding material waste as in subtractive manufacturing [3]. Additionally, the imposed deposition pattern within a single layer, coupled to multiple layer stacking, results into the formation of a 3D interconnected pore network that is a prerequisite for scaffold manufacturing to improve cell nutrition availability. Unlike the so-called “conventional methods” for scaffold production, such as gas foaming/particulate leaching [4], [5], freeze-drying [6], [7] or phase separation [8], [9], AM offers the user the possibility to control how the pores are distributed, resulting in the potential creation of constructs with porosity gradients in terms of shape, size or density [10]–[12]. In addition, there is no need for the fabrication of molds as in the case of Subtractive Manufacturing, lowering the economic and time demands for scaffold production.

Among the plethora of AM techniques, melt-extrusion based AM currently represents the golden standard for the fabrication of scaffolds for hard-tissue engineering, such as bone and cartilage [13]. For the filling of a defect in such tissues, adequate mechanical properties are required, which cannot be provided by hydrogels, either natural or synthetic, or a combination thereof. Synthetic polymers represent, therefore, the preferred materials of choice to produce such scaffolds thanks to their superior mechanics and chemical tunability. This class of materials can be processed by selective laser sintering (SLS), stereolithography (SLA), three-dimensional printing (3DP) and extrusion techniques (solution- and melt-based) [14]. However, SLS, SLA and 3DP require complex equipment based on, respectively, laser beams, UV light apparatus or actuator cartridges. In addition, manufacturing via SLA requires photosensitive polymers, while SLS and 3DP necessitates of very fine powders. Lastly, 3DP involves the use of binders and solution extrusion is often based on organic solvents, both of which might be potentially toxic to the biological environment. On the other hand, the only requirement for materials to be processable by ME-AM is to be thermoplastic grades, which greatly widens the palette of suitable candidates. Therefore, no harmful compounds are needed, and the equipment simply consists of a heated cartridge or printhead and an extrusion mechanism. For research purposes, but also in view of potential future upscaling, a production line as straightforward as possible can only reduce manufacturing time and costs [15].

In view of all the aforementioned reasons, a ME-AM technique was chosen for this thesis, to study the material/equipment relationship during scaffold manufacturing and make use of this knowledge to improve the production quality and the biological performances of scaffolds for hard-tissue engineering.

6.2 WHY PLA?

Nowadays, poly(ε-caprolactone) (PCL) is the most widespread thermoplastic polymer for the fabrication of scaffolds for bone tissue engineering applications via ME-AM [13]. The success of this material is due to its high compression strength, relatively long degradation time and a low processing temperature that allows for less performant equipment. However, its fast crystallization kinetics limits its versatility. In fact, properties such as water absorption, *in vitro* degradation time, and mechanics are the result of the interplay between amorphous and crystalline domains, where crystalline fraction and crystal size can hardly be controlled and tuned during the typical ME-AM cooling process of PCL.

From this perspective, poly(lactide) (PLA) represents a more flexible and customizable alternative. By adjusting the enantiomeric L/D ratio, the polymer can be either fully amorphous or semicrystalline. The extent of the crystallization fraction can be controlled not only via the enantiomeric ratio, but also via the molecular weight (M_w), offering greater flexibility in terms of material and, consequently, scaffold properties. PLA has already been successfully used in several medical applications, including regenerative medicine. Examples are protein delivery [16], surgical sutures [17], nerve guides [18] breast [19], [20] and bone scaffolds [21]–[27]. However, its high sensitivity to thermal treatments could potentially lead to thermal degradation [28], [29]. Therefore, it can be considered an interesting thermoplastic polymer as a model material to study ME-AM more in depth. The purpose of this thesis is to gain a deeper knowledge of the physics behind the ME-AM process, and to apply it to optimize scaffold biological performances. Such understanding is meant to first achieve full control over material behavior, making the choice of such a versatile material as PLA a good benchmark.

6.3 THE NEED FOR KNOWLEDGE

A challenge encountered when processing new thermoplastic polymers by ME-AM was the uncertainty on how to set the machine. The most straightforward strategy was to choose random values for the three main deposition parameters of bioextrusion, namely applied pressure, screw revolutions per minute and printhead translational speed, and evaluate the morphology of the first deposited layers. Depending on the outcome, one or more parameters would have been to be changed but, without an *a priori* understanding about the interplay thereof, the desired result could be obtained, whereas possible, only after several experimental loops [30]–[32]. In addition, little attention could be given to the resulting scaffold mechanical properties, which could only be assessed by further experimentation only after reaching of an acceptable overall morphology. This is the so-called printability issue, a persistent concern associated with the limited knowledge of material science and polymer processing, which up to now has been managed by suboptimal use of expensive medical polymers and time in a tedious loopy workflow.

Chapter 3 of this thesis has addressed this issue by analyzing the fluid-dynamics of the bioextrusion process, using a ME-AM technique based on an auger screw providing the driving force for material flow. A model of fluid flow during and upon extrusion was proposed, which offers a prediction of the final scaffold morphology and mechanical performances. The solution of the presented set of equations requires from the user only the characteristics of the used device and a few thermo-rheological parameters of the polymer to process. The model, then, provides values for the parameters describing the scaffold manufacturing process, i.e. the flow rate at the printer nozzle and the related printhead translational speed, the power requirement for polymer extrusion, the filament width and actual layer height upon deposition and cooling, the amount of sagging in between filaments from the layer underneath and the mechanical strength of the interlayer bonding. This approach differs from previous works in terms of: 1) the modelling based on the actual physics of the process and not on statistical or regression approaches, which are bound to a specific polymer or a specific piece of equipment; 2) the description of the melt flow according to the Cross approach, which describes the polymer behavior over the entire range of shear rates unlike the usual Newtonian or power-law formulations; 3) the evaluation of the extrudability of the polymer of choice with the equipment in use; 4) the description of the bridging phenomenon at an earlier stage, before reaching the second supporting point (supported beam approach).

6.4 TOWARDS BIOMIMICRY

Following the investigation on the printability issue, we proceeded on the road of scaffold manufacturing optimization for bone-tissue regeneration by focusing on one of the major drawbacks of synthetic polymers: bioinertness. In fact, synthetic polymers generally lack the bioactivity typical of biologically-derived materials because of the native absence of cell-recognizable biological signals [32], [33]. In addition, the high shear rates involved in melt-extrusion render the surface of the material rather smooth [34]. This further impacts the biomimicry of the constructs by depriving the cells of the morphological cues typical of the surrounding hosting tissue. In **Chapter 4** and in **Chapter 5**, we developed strategies to overcome the limited biological performances of synthetic thermoplastic polymers. This was done by specifically applying concepts derived in **Chapter 3** based on material science, so that to tackle also processing-related issues at the same time.

6.4.1 Chemical cues

In the framework of TERM, scaffolds are usually coupled to chemical signals to promote tissue formation and guide it along the desired path. These are usually employed in the form of soluble factors added to the culture media or by immobilization on the scaffold surface via post -manufacturing modifications [35]–[38]. However, these scaffold treatments may involve toxic solvents, may be temporary or may just lengthen the production process because of time-demanding chemical steps, thus potentially hindering upscaling [39]. Alternative approaches are based on loading the polymer matrix with the active compound itself, which is then released in the incubation media over time as a function of the matrix degradation rate [40]–[42].

In **Chapter 4**, we tested the effects of scaffolds manufactured with a blend of PLA and cholecalciferol or Vitamin D3 (VD3) on the osteogenic differentiation of human mesenchymal stromal cells (hMSCs). Vitamin D is a group of vitamins involved in the calcium and phosphate metabolism of the bone homeostasis and the active form calcitriol is known to play a role in the differentiation of osteoblasts and in the commitment of hMSCs to the osteogenic lineage [43]–[45]. However, calcitriol is a rather expensive compound that is unsuitable for large scale research [46], [47]. Cholecalciferol, the inactive form, is more accessible and it was recently suggested that some cell types possess the ability to activate it into calcitriol [48]. Therefore, we manufactured PLA scaffolds with various percentages of VD3 and evaluated the release kinetics in physiological-alike and accelerated conditions to then investigate any potential osteogenic effect on hMSCs. Ultraliquid chromatography (ULC)/mass spectrometry (MS) (ULC-MS) showed no release over time of VD3 in physiological-alike conditions. This was ascribed to the insolubility of cholecalciferol in water, which could potentially result in the aggregation of vitamin molecules on the surface of the scaffold rather than diffusion into the medium. Despite the limited availability of VD3 in the culture medium, hMSCs cultured on PLA/VD3 scaffolds for 35 days showed supported osteogenic differentiation and mineralization as much as those cultured on PLA constructs in mineralization culture conditions. This finding indeed suggested the presence of VD3 on the scaffold surface, in a form suitable for cellular uptake. Furthermore, the results confirmed that hMSCs do possess the enzymatic toolbox to metabolize the inactive cholecalciferol into the active form calcitriol.

As previously mentioned, the strategy of loading of PLA with VD3 was designed not only to increase the biomimicry of scaffolds manufactured via ME-AM, but also to tackle a printability issue. Specifically, thermosensitive polymers such as PLA, might undergo degradation upon the application of high temperatures, resulting in drop in molar mass, viscosity and mechanical properties [28], [32] For this reason, processing at lower temperatures would be recommended but the driving forces provided by small-scale lab equipment is often insufficient. Chain extenders (CE) are chemical compounds meant to reconnect broken chains caused by degradation [49]. Despite being there plenty of works on CEs for industrial applications, biomedical literature is rather scarce due to the fact that these compounds are often toxic. In addition to thermosensitive polymers, the limited extrusion force is an issue that concerns high M_w polymers as well. These are generally preferred for their superior mechanical properties in the solid state but, because of their high molar mass and consequent viscosity, high extrusion torques are needed [50]. Among the possible choices, the method described in **Chapter 4** to increase the biomimicry of scaffolds was specifically chosen so that that exact compound could act as a plasticizer. Plasticizers are low M_w molecules that favor the relative motion between bigger molecules, thus easing their processability [51], [52]. This was confirmed by the rheological tests, where the important drop in viscosity upon the addition of VD3 confirmed that the molecule's molar mass was sufficiently low to diffuse in between PLA chains. From a processing point of view, the reduction in viscosity was accompanied by a reduction (analytically estimated) in torque requirement, which would allow processing at lower temperatures with consequent slowing down of the degradation process.

These findings suggest that by smartly improving the scaffold manufacturing process, limitations can be overcome while still keeping the overall workflow slim, in favor of upscaling.

6.4.2 Surface features and mechanical response

As previously mentioned, the lack of morphological signals on extruded polymers is a factor that might hinder the successful population of a scaffold. In fact, featureless surfaces are known to affect cell attachment and spreading, which are the prerequisites for cell proliferation and tissue formation [53]–[57]. Over the years, several strategies have been tested to promote bioactivity, including coating, chemical treatment and functionalization. However, these methods require further post-processing steps and often involve toxic agents, as in the case of chemical etching.

In **Chapter 5**, we addressed the lack of biomimicry while aiming at preserving the straightforwardness of the manufacturing process. To this end, we focused on surface morphology, by developing a method to induce roughness in a limited amount of extra-printing steps. PLA, water-soluble poly (vinyl alcohol) (PVA) and a foaming agent (sodium citrate (SOCIT)) were pre-blended and processed via bioextrusion. Upon material deposition and subsequent scaffold incubation in water, roughness was introduced on the construct surface by leaching of PVA. In addition, high temperatures intentionally caused SOCIT decomposition, which resulted in the formation of porosity within the scaffold fibers. Removal of the PVA phase had the further effect of connecting the internal pores with each other and to the outer environment, thus creating an open and interconnected internal pore network as demonstrated by microCT imaging and porosity measurements by buoyancy. The introduction of an additional level of porosity resulted in constructs more similar to trabecular bone, not only from a morphological point of view but also in terms of mechanics. In fact, these microporous scaffolds exhibited a more ductile behavior than their pure PLA counterparts, which is a typical behavior of cellular solids, such as trabecular bone, that prevents them from failing at once. *In vitro* biological tests showed greater cell adhesion at 24 h on microporous scaffolds, which was ascribed to either enhanced wettability (and subsequent protein adsorption) of the rougher surface or higher density of anchoring sites for filopodia. Furthermore, cells exhibited higher metabolic activity on microporous scaffolds at day 7, as a potential result of increased anchoring and stretching activity on the micro-sized rough topography [58]. Eventually, increased secretion of some osteogenic proteins both at day 7 and at day 35 was detected, in line with previous studies where surface topography was shown to influence cell fate via cytoskeletal reorganization following adhesion [59]–[61]. Overall, this study showed the possibility of increasing the morphological biomimicry of ME-AM scaffolds for bone regeneration in a limited number of steps. In particular, the materials and the extra-printing phases were carefully chosen so that to potentially reduce the entire workflow to printing and cell culture: blending of the material can be carried out directly in a bioextrusion printer, being it provided with an auger screw, and PVA leaching can be achieved during the first stages of cell culture. The results of this study demonstrated the suitability of our method for upscaling.

6.5 POWER IS NOTHING WITHOUT CONTROL

The processing-related take-home message of **Chapter 4** is that the palette of usable materials in ME-AM can be wider than expected. In fact, even the most viscous ones can be processed, with the proper expedient. However, power is nothing without control and the level of control of a very important intrinsic property of some thermoplasts, i.e. crystallinity, appeared quite limited in ME-AM for TERM. In fact, crystallinity has an effect not only the mechanical performance of the bulk material [62]–[65] but also surface stiffness, which is known to influence cell fate [66]–[70]. In addition, surface roughness can be influenced as well, via those crystals forming in the proximity of and at the surface of the polymer [71]. As shown in past works [54], [56], [72]–[74] as well as in **Chapter 5**, cell fate is susceptible to surface morphology as well. Nevertheless, unlike AM for technical purposes, TERM reports in literature rarely evaluated the effect of processing conditions on polymer crystallinity, and of this on both surface stiffness and surface roughness [54], [71]. The intertwine between surface stiffness and roughness via crystallinity is an element that must not be ignored when developing methods to influence cell fate. This is because systematically varying either material property might unwillingly result in affecting the other, with potential counteracting effects. The lack of awareness of the effects of crystallization is clearly shown by the manufacturing setup, including that used in **Chapter 4** and **Chapter 5**, which rarely is meant to optimize, or even simply control, polymer crystallization via proper thermal management. This applies in particular to those slowly crystallizing polymers, such as PLA, whose properties might vary notably depending on the thermal history they undergo.

For these reasons, in **Chapter 6** we studied the effect of crystallization on, separately, surface stiffness and roughness, in typical (but controlled) ME-AM conditions. Eventually, we explored the influence of these properties on hMSCs fate. The osteochondral region was chosen as sample tissue, showing variations in stiffness magnitude between 10 and 1000 MPa [69]. To achieve such a range, poly(L-lactide) (PLLA) was plasticized with Vitamin E (VE), instead of relying on a multiple-material system with potential issues related to incompatible chemistry at the interface and overall mechanical integrity. VE was selected as plasticizer because of its biocompatibility and hydrophobicity, being the latter essential to avoid leaching out in aqueous environment and potential properties change. The proper concentration was determined by the need of having a glass transition temperature (T_g) below body values. Such low T_g resulted in a sufficiently low crystallization rate as confirmed by differential scanning calorimetry (DSC), which allowed to control material stiffness via its crystallinity fraction. In addition, the absence of cold crystallization was paramount to have stable properties over time [75]. Films made of VE-plasticized PLLA (PLLA/VE) were subjected to annealing conditions typical of ME-AM, either in confined or free conditions. The former was needed to obtain samples with either varying crystalline fraction (and theoretically surface stiffness), but identical roughness. Instead, annealing at different temperatures until reaching full crystallinity in a non-confined environment was meant to allow the spontaneous formation of surface roughness. Indentation tests at body temperature confirmed the variation in surface stiffness as a function of crystalline fraction, over a range typical of the osteochondral region. On the other hand, profilometry data showed comparable mean roughness values for the fully crystalline films, but with different size distribution. This was ascribed to a competition between sample heating time and induction time, which is the time to reach a steady-state population of crystal embryos or nuclei [76], [77]. For annealing at higher temperatures, the heating of the samples might have been faster than the start of nucleation, leading to crystal spherulites all forming at the same time and thus growing homogenously within the same time window. In this case, the surface roughness would have a narrow distribution, unlike samples annealed at lower temperatures. These might have taken longer to reach the annealing temperature, having therefore nuclei forming all along the heating phase and with different extents of growth. hMSCs were cultured on the two groups of films to evaluate whether the stiffness and roughness values reachable upon ME-AM might have had any potential osteogenic effect. Although stiffness could be controlled in a finer way than roughness, cells appeared to be more sensitive to the latter than to variations in stiffness in osteogenic culture conditions. This was not surprising as studies about the influence of stiffness on cell fate have usually considered hydrogel materials and have reported ranges of 1 – 100 kPa to instruct cells [78]–[81]. The interesting finding was the fact that cells responded more to the crystal size distribution than to the average crystal size. In fact, ALP and OPN secretions at day 28 (in osteogenic conditions) suggested that cells differentiated earlier when cultured on films with a halfway size distribution among the samples considered. In the work of Faia-Torres et al. [74], hMSCs were cultured on PCL substrates with a gradient in roughness. It was found that faster osteogenic commitment was achieved by cells grown on a specific roughness range. Our findings seemed to be in line with this research, with the existence of an effective crystal size distribution.

The results of **Chapter 6** suggest that thermal history has an undeniable impact not only on scaffold properties from a mechanical perspective, but also on its performances in biological environments. Therefore, proper knowledge of the material of choice and careful planning of the thermal management are both prerequisites for optimal biological results.

6.6 IN THE FUTURE

6.6.1 Automatic process optimization

The model developed in **Chapter 3** describes the interaction between a thermoplastic polymer and the device used to process it into a scaffold, predicting the result of the interaction thereof. In particular, the thermo-rheological properties of the material, the device features and the manufacturing parameters chosen by the user are used as input and the final scaffold characteristics in terms of morphology and mechanics are predicted. However, a user's intervention is still needed to adjust the processing parameters whereas the results outputted by the model are not satisfying. In view of upscaling and scaffold in-series manufacturing, future studies should aim at turning the developed model into a minimization algorithm so that the solution of the model itself would suggest how to manufacture. As noted in **Chapter 3**, scaffold features are all interdependent via thermal management: whereas higher temperatures favor mechanics development and extrusion of high M_w grades, they reduce morphological quality. Therefore, it appears clear how manufacturing scaffolds with features fully respecting the design criteria is impossible, and how the production goal should be nothing but the minimization of the discrepancy from the targeted requirements. With this in mind, future works should focus on inverting the structure of the equations describing the final scaffold features, which are currently a function of the chosen processing parameters. Suggested values for these latter should be, in fact, the output of the model, such that the estimated scaffold properties are as close as possible to the initial design. Considering the impossibility of perfectly matching it because of the counterplay between different scaffold features, the user would have to provide a priority rank so that the algorithm could solve the equations depending on the feature of the highest importance. Ideally, such an optimization algorithm would be embedded in the printer controlling software, which would suggest a set of processing parameters based on material properties, device characteristics, scaffold features and their order or importance.

6.6.2 Multifunctional scaffolds

Projecting this research into the future, the aforementioned strategies to enhance scaffold bioactivity should be combined into a single product, so that to offer clinicians a direct solution for the treatment on bone defects. By combining VD3 and the PLA:PVA:SOCIT blend, tissue engineers could obtain scaffolds able to favor cell attachment (given by PLA:PVA:SOCIT) and to subsequently trigger osteogenic differentiation via both the release of VD3 and the presence of morphological cues (given by PLA:PVA:SOCIT). In addition, both approaches would contribute to compensate for the main limitation in PLA mechanics, i.e. its brittleness, by increasing scaffold toughness and, consequently, its biomimicry. The release of chemical factors from scaffolds as well as the induction of surface features have both been already tested in previous studies [40], [59], [82], [83]. However, to our knowledge, the production of scaffolds able to provide morphological and chemical cues at the same time has never been explored. Mentioned literature together with the findings from our studies of **Chapter 4** and **Chapter 5** suggest to combine the loading of VD3 and the PLA:PVA:SOCIT blend into one multifunctional scaffold for more biological-alike mechanics and enhanced osteogenic properties. As suggested by the extensive literature on blending [84]–[88], these composite constructs could be prepared in one step by in-situ mixing of the components during the extrusion process, with a screw-based printer. This would ease upscaling by reducing the amount of manufacturing steps, in particular those where the user contribution is needed, in favor of quicker translation to clinical application.

6.6.3 Mono-material gradient scaffolds

Future studies should exploit the knowledge originated by the investigation of **Chapter 6** and dedicate to translate it to 3D. Accurate control of the polymer thermal history could allow to finely tune crystallinity so that to induce either the desired surface stiffness or roughness, in a separate manner. By creating gradients in properties, tissue-transition areas such as the osteochondral region [89] could be treated by implants exhibiting properties varying along the desired direction with a continuous trend. In fact, this would be achieved by employing a single-material scaffold instead of a multicomponent construct, going beyond the current limitations in discrete gradients. These are mainly based on the use of multiple materials, which usually have different chemistries, as shown in the work of Di Luca et. al. [69]. Potential consequences are a localized biological response depending on the specific scaffold section but also hindered diffusion at the weld between two different materials, affecting the overall scaffold mechanics. In **Chapter 6**, we presented a scaffold with a vertical gradient in crystallinity (and thus stiffness), produced by combining a heated printbed, reheating from the printhead and brakes between layers to dissipate the accumulated heat. However, the manufacturing protocol was the result of extremely fine tuning based on experience and empirical observation, and applicable only to the specific material, device and scaffold morphology in object. Different production setups would require different processing parameters, and therefore new optimization phases. For this reason, future studies should aim at getting a more thorough understanding of the thermal history experienced by the polymer not only upon extrusion and cooling, but also during the reheating caused by the deposition of subsequent layers [90]. Specific attention should also be given to the role of porosity in dissipating the heat accumulated during processing, which might affect the final morphology (cross-section and bridges, as described in **Chapter 3**) as well. The establishment of models able to grasp this phenomenon would assist in avoiding uncontrolled properties development over the scaffold in favor of willingly induced gradients. In addition, the evolution of surface roughness was not evaluated upon the production of the gradient scaffold, and further investigation is advisable to avoid the intertwined development of surface stiffness and roughness. Learning from the methodology developed in **Chapter 6**, fully crystalline scaffolds might be manufactured by means of a heated chamber and adequate breaks between the deposition of consecutive layers. Adopting this strategy, all the layers might be annealed to reach full crystallinity, leaving roughness as only experimental variable.

6.7 CONCLUSION

Within this thesis, we have proposed significant scientific and technological solutions to optimize the fabrications of scaffolds via ME-AM for bone-tissue engineering. We have increased the knowledge in the process and applied it to obtain more biologically-relevant implants for the treatment of bone defects. Along with the advantages of each developed strategy, we have highlighted their limitations as well, and suggested paths for future research to further optimize the proposed methods.

REFERENCES

[1] M. Salmi, “Additive manufacturing processes in medical applications,” *Materials*, vol. 14, no. 1, pp. 1–16, 2021, doi: 10.3390/ma14010191.

[2] R. Bibb, *Medical modelling*. Cambridge: Woodhead Publishing Limited, 2006. doi: 10.1533/9781845692001.

[3] A. Zadpoor, “Design for Additive Bio-Manufacturing: From Patient-Specific Medical Devices to Rationally Designed Meta-Biomaterials,” *Int J Mol Sci*, vol. 18, no. 8, p. 1607, Jul. 2017, doi: 10.3390/ijms18081607.

[4] Y. S. Nam, J. J. Yoon, and T. G. Park, “A novel fabrication method of macroporous biodegradable polymer scaffolds using gas foaming salt as a porogen additive,” *J Biomed Mater Res*, vol. 53, no. 1, pp. 1–7, Jan. 2000, doi: 10.1002/(SICI)1097-4636(2000)53:1<1::AID-JBM1>3.0.CO;2-R.

[5] S. S. Kim, M. Sun Park, O. Jeon, C. Yong Choi, and B. S. Kim, “Poly(lactide-co-glycolide)/hydroxyapatite composite scaffolds for bone tissue engineering,” *Biomaterials*, vol. 27, no. 8, pp. 1399–1409, Mar. 2006, doi: 10.1016/j.biomaterials.2005.08.016.

[6] C. M. Murphy, M. G. Haugh, and F. J. O’Brien, “The effect of mean pore size on cell attachment, proliferation and migration in collagen-glycosaminoglycan scaffolds for bone tissue engineering,” *Biomaterials*, vol. 31, no. 3, pp. 461–466, Jan. 2010, doi: 10.1016/j.biomaterials.2009.09.063.

[7] N. Sultana and M. Wang, “PHBV/PLLA-based composite scaffolds fabricated using an emulsion freezing/freeze-drying technique for bone tissue engineering: Surface modification and in vitro biological evaluation,” *Biofabrication*, vol. 4, no. 1, p. 015003, Mar. 2012, doi: 10.1088/1758-5082/4/1/015003.

[8] G. Wei and P. X. Ma, “Structure and properties of nano-hydroxyapatite/polymer composite scaffolds for bone tissue engineering,” *Biomaterials*, vol. 25, no. 19, pp. 4749–4757, Aug. 2004, doi: 10.1016/j.biomaterials.2003.12.005.

[9] R. Akbarzadeh and A.-M. Yousefi, “Effects of processing parameters in thermally induced phase separation technique on porous architecture of scaffolds for bone tissue engineering,” *J Biomed Mater Res B Appl Biomater*, vol. 102, no. 6, pp. 1304–1315, Aug. 2014, doi: 10.1002/jbm.b.33101.

[10] A. Di Luca, A. Longoni, G. Criscenti, C. Mota, C. van Blitterswijk, and L. Moroni, “Toward mimicking the bone structure: design of novel hierarchical scaffolds with a tailored radial porosity gradient,” *Biofabrication*, vol. 8, no. 4, p. 045007, 2016, doi: 10.1088/1758-5090/8/4/045007.

[11] A. Di Luca *et al.*, “Tuning Cell Differentiation into a 3D Scaffold Presenting a Pore Shape Gradient for Osteochondral Regeneration,” *Adv Healthc Mater*, vol. 5, no. 14, pp. 1753–1763, Jul. 2016, doi: 10.1002/adhm.201600083.

[12] A. Di Luca *et al.*, “Gradients in pore size enhance the osteogenic differentiation of human mesenchymal stromal cells in three-dimensional scaffolds,” *Sci Rep*, vol. 6, no. 1, p. 22898, Sep. 2016, doi: 10.1038/srep22898.

[13] M. Cámara Torres, “Tracing fast roads towards bone regeneration,” maastricht university, 2021. doi: 10.26481/dis.20210913mt.

[14] C. Mota, D. Puppi, F. Chiellini, and E. Chiellini, “Additive manufacturing techniques for the production of tissue engineering constructs,” *J Tissue Eng Regen Med*, vol. 9, no. 3, pp. 174–190, 2015, doi: 10.1002/term.1635.

[15] A. R. Calore, R. Sinha, J. Harings, K. V Bernaerts, C. Mota, and L. Moroni, “Chapter 7 Thermoplastics for Tissue Engineering,” in *Computer-Aided Tissue Engineering*, A. Rainer and L. Moroni, Eds., 2021, pp. 75–99.

[16] E. N. Antonov *et al.*, “Three-dimensional bioactive and biodegradable scaffolds fabricated by surface-selective laser sintering,” *Advanced Materials*, vol. 17, no. 3, pp. 327–330, 2005, doi: 10.1002/adma.200400838.

[17] Y. Baimark, R. Molloy, N. Molloy, J. Siripitayananon, W. Punyodom, and M. Sriyai, “Synthesis, characterization and melt spinning of a block copolymer of L-lactide and ε-caprolactone for potential use as an absorbable monofilament surgical suture,” *J Mater Sci Mater Med*, vol. 16, no. 8, pp. 699–707, 2005, doi: 10.1007/s10856-005-2605-6.

[18] B. Thapsukhon, N. Thadavirul, P. Supaphol, P. Meepowpan, R. Molloy, and W. Punyodom, “Effects of copolymer microstructure on the properties of electrospun poly(l -lactide-co-ε-caprolactone) absorbable nerve guide tubes,” *J Appl Polym Sci*, vol. 130, no. 6, pp. 4357–4366, 2013, doi: 10.1002/app.39675.

[19] M. P. Chhaya, F. P. W. Melchels, B. M. Holzapfel, J. G. Baldwin, and D. W. Hutmacher, “Sustained regeneration of high-volume adipose tissue for breast reconstruction using computer aided design and biomanufacturing,” *Biomaterials*, vol. 52, no. 1, pp. 551–560, 2015, doi: 10.1016/j.biomaterials.2015.01.025.

[20] P. S. P. Poh *et al.*, “Evaluation of polycaprolactone − poly-D,L-lactide copolymer as biomaterial for breast tissue engineering,” *Polym Int*, vol. 66, no. 1, pp. 77–84, 2017, doi: 10.1002/pi.5181.

[21] Z. Xiong, Y. Yan, S. Wang, R. Zhang, and C. Zhang, “Fabrication of porous scaffolds for bone tissue engineering via low-temperature deposition,” *Scr Mater*, vol. 46, no. 11, pp. 771–776, 2002, doi: 10.1016/S1359-6462(02)00071-4.

[22] J. M. Kanczler *et al.*, “Biocompatibility and osteogenic potential of human fetal femur-derived cells on surface selective laser sintered scaffolds,” *Acta Biomater*, vol. 5, no. 6, pp. 2063–2071, 2009, doi: 10.1016/j.actbio.2009.03.010.

[23] R. L. Simpson *et al.*, “Development of a 95/5 poly(L-lactide-co-glycolide)/hydroxylapatite and β-tricalcium phosphate scaffold as bone replacement material via selective laser sintering,” *J Biomed Mater Res B Appl Biomater*, vol. 84B, no. 1, pp. 17–25, Jan. 2008, doi: 10.1002/jbm.b.30839.

[24] B. Duan, M. Wang, W. Y. Zhou, W. L. Cheung, Z. Y. Li, and W. W. Lu, "Three-dimensional nanocomposite scaffolds fabricated via selective laser sintering for bone tissue engineering," *Acta Biomater*, vol. 6, no. 12, pp. 4495–4505, 2010, doi: 10.1016/j.actbio.2010.06.024.

[25] W. Y. Zhou, S. H. Lee, M. Wang, W. L. Cheung, and W. Y. Ip, "Selective laser sintering of porous tissue engineering scaffolds from poly(L-lactide)/carbonated hydroxyapatite nanocomposite microspheres," *J Mater Sci Mater Med*, vol. 19, no. 7, pp. 2535–2540, 2008, doi: 10.1007/s10856-007-3089-3.

[26] S. Tanodekaew, S. Channasanon, P. Kaewkong, and P. Uppanan, "PLA-HA scaffolds: Preparation and bioactivity," *Procedia Eng*, vol. 59, pp. 144–149, 2013, doi: 10.1016/j.proeng.2013.05.104.

[27] M. Xu *et al.*, "Fabricating a pearl/PLGA composite scaffold by the low-temperature deposition manufacturing technique for bone tissue engineering," *Biofabrication*, vol. 2, no. 2, p. 025002, Jun. 2010, doi: 10.1088/1758-5082/2/2/025002.

[28] K. Ragaert, A. Dekeyser, L. Cardon, and J. Degrieck, "Quantification of Thermal Material Degradation During the Processing of Biomedical Thermoplastics," *J Appl Polym Sci*, vol. 120, no. 5, pp. 2872–2880, 2011, doi: 10.1002/app.33323.

[29] K. Ragaert, L. Cardon, A. Dekeyser, and J. Degrieck, "Machine design and processing considerations for the 3D plotting of thermoplastic scaffolds," *Biofabrication*, vol. 2, no. 1, p. 14107, 2010, doi: 10.1088/1758-5082/2/1/014107.

[30] S. Jain, T. Fuoco, M. A. Yassin, K. Mustafa, and A. Finne-Wistrand, "Printability and Critical Insight into Polymer Properties during Direct-Extrusion Based 3D Printing of Medical Grade Polylactide and Copolyesters," *Biomacromolecules*, vol. 21, no. 2, pp. 388–396, Feb. 2020, doi: 10.1021/acs.biomac.9b01112.

[31] S. Kyle, Z. M. Jessop, A. Al-Sabah, and I. S. Whitaker, "'Printability'' of Candidate Biomaterials for Extrusion Based 3D Printing: State-of-the-Art,'" *Adv Healthc Mater*, vol. 6, no. 16, pp. 1–16, 2017, doi: 10.1002/adhm.201700264.

[32] P. S. P. Poh *et al.*, "Polylactides in additive biomanufacturing," *Adv Drug Deliv Rev*, vol. 107, pp. 228–246, 2016, doi: 10.1016/j.addr.2016.07.006.

[33] L. R. Jaidev and K. Chatterjee, "Surface functionalization of 3D printed polymer scaffolds to augment stem cell response," *Mater Des*, vol. 161, pp. 44–54, Jan. 2019, doi: 10.1016/j.matdes.2018.11.018.

[34] C. Wang *et al.*, "3D printing of bone tissue engineering scaffolds," *Bioact Mater*, vol. 5, no. 1, pp. 82–91, Mar. 2020, doi: 10.1016/j.bioactmat.2020.01.004.

[35] Z. Ma, Z. Mao, and C. Gao, "Surface modification and property analysis of biomedical polymers used for tissue engineering," *Colloids and Surfaces B: Biointerfaces*, vol. 60, no. 2. Elsevier, pp. 137–157, Nov. 15, 2007. doi: 10.1016/j.colsurfb.2007.06.019.

[36] M. Cámara-Torres *et al.*, "Tuning Cell Behavior on 3D Scaffolds Fabricated by Atmospheric Plasma-Assisted Additive Manufacturing," *ACS Appl Mater Interfaces*, vol. 13, no. 3, 2021, doi: 10.1021/acsami.0c19687.

[37] Y. Zhu, M. F. Leong, W. F. Ong, M. B. Chan-Park, and K. S. Chian, "Esophageal epithelium regeneration on fibronectin grafted poly(l-lactide-co-caprolactone) (PLLC) nanofiber scaffold," *Biomaterials*, vol. 28, no. 5, pp. 861–868, Feb. 2007, doi: 10.1016/j.biomaterials.2006.09.051.

[38] G. Marchioli *et al.*, "Hybrid Polycaprolactone/Alginate Scaffolds Functionalized with VEGF to Promote de Novo Vessel Formation for the Transplantation of Islets of Langerhans," *Adv Healthc Mater*, vol. 5, no. 13, pp. 1606–1616, 2016, doi: 10.1002/adhm.201600058.

[39] E. S. Place, J. H. George, C. K. Williams, and M. M. Stevens, "Synthetic polymer scaffolds for tissue engineering," *Chem Soc Rev*, vol. 38, no. 4, pp. 1139–1151, Mar. 2009, doi: 10.1039/b811392k.

[40] J. J. Yoon, J. H. Kim, and G. Park, "Dexamethasone-releasing biodegradable polymer scaffolds fabricated by a gas-foaming/salt-leaching method," *Biomaterials*, vol. 24, pp. 2323–2329, 2003, doi: 10.1016/S0142-9612(03)00024-3.

[41] M. A. Bhutto, T. Wu, B. Sun, H. EI-Hamshary, S. S. Al-Deyab, and X. Mo, "Fabrication and characterization of vitamin B5 loaded poly (l-lactide-co-caprolactone)/silk fiber aligned electrospun nanofibers for schwann cell proliferation," *Colloids Surf B Biointerfaces*, vol. 144, pp. 108–117, Aug. 2016, doi: 10.1016/J.COLSURFB.2016.04.013.

[42] F. F. R. Damanik, C. van Blitterswijk, J. Rotmans, and L. Moroni, "Enhancement of synthesis of extracellular matrix proteins on retinoic acid loaded electrospun scaffolds," *J Mater Chem B*, vol. 6, no. 40, pp. 6468–6480, Oct. 2018, doi: 10.1039/C8TB01244J.

[43] P. H. Anderson and G. J. Atkins, "The skeleton as an intracrine organ for vitamin D metabolism," *Molecular Aspects of Medicine*, vol. 29, no. 6. Pergamon, pp. 397–406, Dec. 01, 2008. doi: 10.1016/j.mam.2008.05.003.

[44] S. Zhou, M. S. LeBoff, and J. Glowacki, "Vitamin D Metabolism and Action in Human Bone Marrow Stromal Cells," *Endocrinology*, vol. 151, no. 1, pp. 14–22, Jan. 2010, doi: 10.1210/en.2009-0969.

[45] S. Geng, S. Zhou, Z. Bi, and J. Glowacki, "Vitamin D metabolism in human bone marrow stromal (mesenchymal stem) cells," *Metabolism: Clinical and Experimental*, vol. 62, no. 6. W.B. Saunders, pp. 768–777, Jun. 01, 2013. doi: 10.1016/j.metabol.2013.01.003.

[46] D. J. Kang, H. S. Lee, J. T. Park, J. S. Bang, S. K. Hong, and T. Y. Kim, "Optimization of culture conditions for the bioconversion of vitamin D3 to 1α,25-dihydroxyvitamin D3 using Pseudonocardia autotrophica ID9302," *Biotechnology and Bioprocess Engineering*, vol. 11, no. 5, pp. 408–413, Oct. 2006, doi: 10.1007/BF02932307.

[47] D. Feldman, J. W. Pike, and J. S. Adams, *Vitamin D*. Elsevier, 2011. doi: 10.1016/C2009-1-63406-7.

[48] F. Meng *et al.*, "Fibroblast growth factor 23 counters vitamin D metabolism and action in human mesenchymal stem cells," *J Steroid Biochem Mol Biol*, vol. 199, p. 105587, May 2020, doi: 10.1016/j.jsbmb.2020.105587.

[49] G. Y. H. Choong and D. S. A. De Focatiis, "A method for the determination and correction of the effect of thermal degradation on the viscoelastic properties of degradable polymers," *Polym Degrad Stab*, vol. 130, pp. 182–188, 2016, doi: 10.1016/j.polymdegradstab.2016.06.018.

[50] T. Osswald and N. Rudolph, *Polymer Rheology*. München: Carl Hanser Verlag GmbH & Co. KG, 2014. doi: 10.3139/9781569905234.

[51] T. D. Ngo, A. Kashani, G. Imbalzano, K. T. Q. Nguyen, and D. Hui, "Additive manufacturing (3D printing): A review of materials, methods, applications and challenges," *Composites Part B: Engineering*, vol. 143. Elsevier Ltd, pp. 172–196, Jun. 15, 2018. doi: 10.1016/j.compositesb.2018.02.012.

[52] Norman E. Dowling, *Mehcanical Behavior of Materials*. Prentice hall, 2013.

[53] S. Neuss *et al.*, "Assessment of stem cell/biomaterial combinations for stem cell-based tissue engineering," *Biomaterials*, vol. 29, pp. 302–313, 2008, doi: 10.1016/j.biomaterials.2007.09.022.

[54] N. R. Washburn, K. M. Yamada, C. G. Simon, S. B. Kennedy, and E. J. Amis, "High-throughput investigation of osteoblast response to polymer crystallinity: influence of nanometer-scale roughness on proliferation," *Biomaterials*, vol. 25, no. 7–8, pp. 1215–1224, Mar. 2004, doi: 10.1016/j.biomaterials.2003.08.043.

[55] T. P. Kunzler, T. Drobek, M. Schuler, and N. D. Spencer, "Systematic study of osteoblast and fibroblast response to roughness by means of surface-morphology gradients," *Biomaterials*, vol. 28, pp. 2175–2182, 2007, doi: 10.1016/j.biomaterials.2007.01.019.

[56] S. C. Neves, C. Mota, A. Longoni, C. C. Barrias, P. L. Granja, and L. Moroni, "Additive manufactured polymeric 3D scaffolds with tailored surface topography influence mesenchymal stromal cells activity," *Biofabrication*, vol. 8, no. 2, p. 025012, May 2016, doi: 10.1088/1758-5090/8/2/025012.

[57] J. Y. Kim, J. J. Yoon, E. K. Park, D. S. Kim, S. Y. Kim, and D. W. Cho, "Cell adhesion and proliferation evaluation of SFF-based biodegradable scaffolds fabricated using a multi-head deposition system," *Biofabrication*, vol. 1, no. 1, 2009, doi: Artn 015002 10.1088/1758-5082/1/1/015002.

[58] A. K. Gaharwar *et al.*, "Nanoclay-Enriched Poly(ε-caprolactone) Electrospun Scaffolds for Osteogenic Differentiation of Human Mesenchymal Stem Cells," *Tissue Eng Part A*, vol. 20, no. 15–16, pp. 2088–2101, Aug. 2014, doi: 10.1089/ten.tea.2013.0281.

[59] G. Kumar, M. S. Waters, T. M. Farooque, M. F. Young, and C. G. Simon, "Freeform fabricated scaffolds with roughened struts that enhance both stem cell proliferation and differentiation by controlling cell shape," *Biomaterials*, vol. 33, no. 16, pp. 4022–4030, Jun. 2012, doi: 10.1016/j.biomaterials.2012.02.048.

[60] Y. W. Wang, Q. Wu, and G. Q. Chen, "Attachment, proliferation and differentiation of osteoblasts on random biopolyester poly(3-hydroxybutyrate-co-3-hydroxyhexanoate) scaffolds," *Biomaterials*, vol. 25, no. 4, pp. 669–675, Feb. 2004, doi: 10.1016/S0142-9612(03)00561-1.

[61] C. Bao, W. Chen, M. D. Weir, W. Thein-Han, and H. H. K. Xu, "Effects of electrospun submicron fibers in calcium phosphate cement scaffold on mechanical properties and osteogenic differentiation of umbilical cord stem cells," *Acta Biomater*, 2011, doi: 10.1016/j.actbio.2011.06.046.

[62] T. Miyata and T. Masuko, "Crystallization behaviour of poly(L-lactide)," *Polymer (Guildf)*, vol. 39, no. 22, pp. 5515–5521, Oct. 1998, doi: 10.1016/S0032-3861(97)10203-8.

[63] G. Perego, G. D. Cella, and C. Bastioli, "Effect of molecular weight and crystallinity on poly(lactic acid) mechanical properties," *J Appl Polym Sci*, vol. 59, no. 1, pp. 37–43, Jan. 1996, doi: 10.1002/(sici)1097-4628(19960103)59:1<37::aid-app6>3.0.co;2-n.

[64] F. W. Billmeyer, *Textbook of Polymer Science*, vol. 12, no. 3. 1963. doi: 10.1295/kobunshi.12.240.

[65] M. Cocca, M. L. Di Lorenzo, M. Malinconico, and V. Frezza, "Influence of crystal polymorphism on mechanical and barrier properties of poly(l-lactic acid)," *Eur Polym J*, vol. 47, no. 5, pp. 1073–1080, May 2011, doi: 10.1016/j.eurpolymj.2011.02.009.

[66] T. Yeung *et al.*, "Effects of substrate stiffness on cell morphology, cytoskeletal structure, and adhesion," *Cell Motil Cytoskeleton*, vol. 60, no. 1, pp. 24–34, Jan. 2005, doi: 10.1002/cm.20041.

[67] L. MacQueen, Y. Sun, and C. A. Simmons, "Mesenchymal stem cell mechanobiology and emerging experimental platforms," *J R Soc Interface*, vol. 10, no. 84, p. 20130179, Jul. 2013, doi: 10.1098/rsif.2013.0179.

[68] J. S. Park *et al.*, "The effect of matrix stiffness on the differentiation of mesenchymal stem cells in response to TGF-β," *Biomaterials*, vol. 32, no. 16, pp. 3921–3930, Jun. 2011, doi: 10.1016/J.BIOMATERIALS.2011.02.019.

[69] A. Di Luca *et al.*, "Surface energy and stiffness discrete gradients in additive manufactured scaffolds for osteochondral regeneration," *Biofabrication*, vol. 8, no. 1, p. 015014, Feb. 2016, doi: 10.1088/1758-5090/8/1/015014.

[70] W. Zhong, Y. Li, L. Li, W. Zhang, S. Wang, and X. Zheng, "YAP-mediated regulation of the chondrogenic phenotype in response to matrix elasticity," *J Mol Histol*, vol. 44, no. 5, pp. 587–595, Oct. 2013, doi: 10.1007/s10735-013-9502-y.

[71] A. Larena and G. Pinto, "The effect of surface roughness and crystallinity on the light scattering of polyethylene tubular blown films," *Polym Eng Sci*, vol. 33, no. 12, pp. 742–747, Jun. 1993, doi: 10.1002/pen.760331204.

[72] F. Guilak, D. M. Cohen, B. T. Estes, J. M. Gimble, W. Liedtke, and C. S. Chen, “Control of Stem Cell Fate by Physical Interactions with the Extracellular Matrix,” *Cell Stem Cell*, vol. 5, no. 1, pp. 17–26, Jul. 2009, doi: 10.1016/j.stem.2009.06.016.

[73] H. Chen *et al.*, “Tailoring surface nanoroughness of electrospun scaffolds for skeletal tissue engineering,” *Acta Biomater*, vol. 59, pp. 82–93, Sep. 2017, doi: 10.1016/j.actbio.2017.07.003.

[74] A. B. Faia-Torres *et al.*, “Osteogenic differentiation of human mesenchymal stem cells in the absence of osteogenic supplements: A surface-roughness gradient study,” *Acta Biomater*, vol. 28, pp. 64–75, 2015, doi: 10.1016/j.actbio.2015.09.028.

[75] S. Varun, “Timing of interfacial diffusion and (stereo)crystallization to tailor mechanical properties of additively manufactured poly(lactides),” maastricht university, 2020. doi: 10.26481/dis.20201013vs.

[76] B. Wunderlich, *Macromolecular Physics, Volume 2: Crystal Nucleation, Growth, Annealing*, vol. 2. Academic Press Inc., 1976.

[77] R. D. Sudduth, P. Kyarala, and Q. Sheng, “A comparison of induction time and crystallization rate for syndiotactic polystyrene,” *Polym Eng Sci*, vol. 42, no. 4, pp. 694–706, Apr. 2002, doi: 10.1002/pen.10982.

[78] N. Huebsch *et al.*, “Harnessing traction-mediated manipulation of the cell/matrix interface to control stem-cell fate,” *Nat Mater*, vol. 9, no. 6, pp. 518–526, Apr. 2010, doi: 10.1038/nmat2732.

[79] A. J. Engler, S. Sen, H. L. Sweeney, and D. E. Discher, “Matrix Elasticity Directs Stem Cell Lineage Specification,” *Cell*, vol. 126, no. 4, pp. 677–689, Aug. 2006, doi: 10.1016/j.cell.2006.06.044.

[80] O. Chaudhuri *et al.*, “Substrate stress relaxation regulates cell spreading,” *Nat Commun*, vol. 6, no. 1, pp. 1–7, Feb. 2015, doi: 10.1038/ncomms7365.

[81] N. S. Hwang, S. Varghese, H. Li, and J. Elisseeff, “Regulation of osteogenic and chondrogenic differentiation of mesenchymal stem cells in PEG-ECM hydrogels,” *Cell Tissue Res*, vol. 344, no. 3, pp. 499–509, Jun. 2011, doi: 10.1007/s00441-011-1153-2.

[82] P. F. Costa, A. M. Puga, L. Díaz-Gomez, A. Concheiro, D. H. Busch, and C. Alvarez-Lorenzo, “Additive manufacturing of scaffolds with dexamethasone controlled release for enhanced bone regeneration,” *Int J Pharm*, vol. 496, no. 2, pp. 541–550, 2015, doi: 10.1016/j.ijpharm.2015.10.055.

[83] G. Kumar *et al.*, “The determination of stem cell fate by 3D scaffold structures through the control of cell shape,” *Biomaterials*, vol. 32, no. 35, pp. 9188–9196, 2011, doi: 10.1016/j.biomaterials.2011.08.054.

[84] W. D. Mohr, R. L. Saxton, and C. H. Jepson, “Theory of Mixing in the Single-Screw Extruder,” *Engineering aspects of polymer processes*, vol. 49, no. 11, 1957, Accessed: Feb. 12, 2019. [Online]. Available: https://pubs.acs.org/sharingguidelines

[85] N. Domingues, A. Gaspar-Cunha, and J. A. Covas, “Estimation of the morphology development of immiscible liquid-liquid systems during single screw extrusion,” *Polym Eng Sci*, vol. 50, no. 11, pp. 2194–2204, Nov. 2010, doi: 10.1002/pen.21756.

[86] O. Celik and C. Bonten, “A novel experimental setup for characterization of polymer blends in single-screw extruders,” 2019, p. 020008. doi: 10.1063/1.5084809.

[87] K. Wilczyński, A. Tyszkiewicz, and Z. Szymaniak, “Modeling for morphology development during single-screw extrusion of LDPE/PS blend,” *J Mater Process Technol*, vol. 109, no. 3, pp. 320–323, Feb. 2001, doi: 10.1016/S0924-0136(00)00820-7.

[88] M. Esseghir, C. G. Gogos, D.-W. Yu, D. B. Todd, and B. David, “A comparative study on the performance of three single-screw elements in melt?melt mixing of immiscible blends,” *Advances in Polymer Technology*, vol. 17, no. 1, pp. 1–17, 1998, doi: 10.1002/(SICI)1098-2329(199821)17:1<1::AID-ADV1>3.0.CO;2-Y.

[89] A. Di Luca, C. Van Blitterswijk, and L. Moroni, “The osteochondral interface as a gradient tissue: From development to the fabrication of gradient scaffolds for regenerative medicine,” *Birth Defects Res C Embryo Today*, vol. 105, no. 1, pp. 34–52, Mar. 2015, doi: 10.1002/bdrc.21092.

[90] V. Srinivas, C. S. J. van Hooy-Corstjens, and J. A. W. Harings, “Correlating molecular and crystallization dynamics to macroscopic fusion and thermodynamic stability in fused deposition modeling; a model study on polylactides,” *Polymer (Guildf)*, vol. 142, pp. 348–355, Apr. 2018, doi: 10.1016/j.polymer.2018.03.063.

Chapter 7

IMPACT

7.1 SCIENTIFIC IMPACT

Due to the constant subjection to loading and the related injury risk, bone was one of the first tissues to be studied in the context of Tissue Engineering (TE). However, despite the large amount of available research and the undeniable scientific progress along the years, tissue engineers are still searching for a highly reproducible and upscalable solution to promote and speed up bone regeneration *in vivo*. The current lack of a golden standard is due to the complex interplay among bone properties such as composition, structure, and mechanics. In the classical paradigm of TE, scaffolds have been used to mimic these features to provide a temporary tissue replacement in terms of mechanical support, porosity and surface properties, able as much as possible to carry out the same biological functions while the surrounding native bone regenerates. Additive Manufacturing (AM) is a class of techniques that allow the production of constructs with personalized size and shape, and that give a certain control on the construct's mechanical properties by adjusting the disposition pattern and the thermal management. Being first born for industrial and technical applications, AM has been employed for TE purposes because it offers that degree of control over the fabricated object required in the context of personalized medicine. More than in other tissues, the mechanical properties of bone are highly linked to its structure, as in the case of cancellous regions where the tissue is organized to dissipate stresses and propagate the residuals towards the stiffer cortical tissue. Therefore, it is not surprising how widely AM techniques have been adopted for the regeneration of such mechanically-complex tissues. However, despite the large technological advancements since the adoption of AM in TE, production is still far from being optimal and standardized, a fact that is highly hindering the employment of such class of technique on a larger scale.

Within this thesis, innovative scientific knowledge was generated and novel strategies based on it were proposed, with the goal of providing solutions to current issues in melt-extrusion AM (ME-AM) for bone tissue engineering. We believe that the information presented, consisting of a numerical model of the scaffold fabrication process, new methods to induce material bioactivity or to introduce roughness and microporosity with no chemical processing, and on an insight of thermal history effects, contributes to a better understanding of the scaffold manufacturing process and to the optimization thereof, providing a steppingstone for future studies on the upscaling of ME-AM for bone tissue engineering. We also trust that this research will have a scientific impact beyond tissue engineering for bone regeneration and can be the foundation of future research in the biomedical, biomaterial and overall regenerative medicine fields.

Within the first chapters, we found necessary to provide a deep physical description of the scaffold manufacturing process via ME. On one side, in **Chapter 3** we proposed a simple numerical model based on fluid-dynamics that could be easily used by other researchers to estimate the final morphology of the manufactured scaffolds, for different applications. We believe in the great scientific impact of this model, since it helps minimizing costly material and time waste for material processing screening and optimization, and allows to maximize throughput and scaffold manufacturing rate, which currently are still at research level. By having a support tool to tackle the initial optimal fabrication issue, researchers not only are free to explore with higher flexibility different scaffold designs or materials, but can also dedicate greater efforts to evaluate the final biological response. In **Chapter 3**, we went one step further and, while modelling the impact of processing conditions on scaffold morphology, we also implemented tools to predict the compatibility of a specific couple material/printer and to estimate in advance the scaffold mechanical response. The completeness of our model lays the foundation for future additions by describing further phenomena involved in the scaffold manufacturing process, such as crystallinity and molecular dynamics. Furthermore, since established and optimized protocols are a prerequisite for upscaling of the scaffold fabrication process, we envision the implementation of our model into a software embedded in ME-AM printers in the scaffold production pipeline, allowing the manufacturing of standardized constructs and thus a faster translation to the clinic.

In subsequent chapters, the scaffold manufacturing process via ME-AM was optimized to enhance scaffold performance in biological environments, but also further studied to investigate its intrinsic impact on material properties and consequently on cell response. Complex methodologies from several scientific fields were employed, from material science and rheology to processing engineering and biology, to design, develop and optimize strategies to overcome the current biological limitations of ME-AM for TE applications, such as the lack of bioactivity and biomimicry, and gain further insights on the impact of processing on cell activity. In particular, **Chapter 4** showed that plasticizers, a typically industrial solution to improve the processability of a material, can be applied in ME-AM for TE applications to widen the palette of selectable materials, thus allowing to turn the attention to those high molar mass thermoplastic polymers with favorable mechanical properties that cannot be usually processed with research-scale equipment. In addition to being (necessarily) biocompatible, they can be accurately chosen to carry out a double function by additionally having a bioactive effect, such as inducing osteogenic differentiation in human mesenchymal stromal cells (hMSCs). This allowed to overcome the inherent bioinertness of thermoplastic polymers for ME-AM for TE. However, non-physiological workarounds to achieve cell attachment were necessary, thus raising questions related to manufacturing scaffolds with more biomimicking surfaces. For this reason, we believe that our work in **Chapter 5** on inducing roughness on the otherwise not-biologically-alike smooth surfaces of melt-extruded scaffolds constitutes a solid contribution to the field of scaffold fabrication for TE. In fact, the presented scaffold manufacturing strategy allowed to achieve a higher cell seeding efficiency without any media modification or scaffold handling during cell attachment, by creating a more physiological surface morphology. Moreover, it had the further effect of introducing microporosity within the filaments structuring the scaffolds, providing them with a more physiological ductile behavior under loading, thus further improving scaffolds biomimicry. Finally, we believe that the study presented in **Chapter 6** provided, for the first time, meaningful knowledge on the inherent effects of typical ME-AM thermal stresses on those properties of semicrystalline thermoplastics that are known to influence cell activity, namely surface stiffness and surface roughness. In a field where researchers use chemical, morphological and mechanical cues to drive cell fate, we trust that the results of our investigation can generate great awareness about the importance of proper thermal history management, so that to avoid any undesired properties modification and consequent cell response. In addition, we are confident that the provided knowledge serves as a basis for future research to manufacture scaffolds with controlled gradients in surface properties, so that to fabricate suitable implants for those interface regions such as the osteochondral tissue, which currently are not properly mimicked.

7.2 SOCIAL IMPACT

Bone is one of the most exposed tissues to injuries because of its constant engagement and loading during daily life, being it involved in the support and motion functions of the body. Bone can undergo further stresses in the case of sport activities or because of the onset of osteoporosis, a disease mostly related to ageing that causes weakening of the tissue. Whereas loads exceed the bone bearing capabilities, fractures may occur. Although these are usually properly treated, prolonged healing or non-unions may take place in the case of patients suffering from diabetes, obesity, genetic conditions or osteoporosis too. In addition, removal of bone tumors can leave large defects in bone tissue, which may be beyond the bone's own self-healing ability. It is estimated that the risk of developing a non-union reaches up to 5% worldwide, with higher peaks in country with less advanced medical care [1]. The highest location incidence is given by the tibial bone with up to 15% of the occurring fractures, followed by the femur with 11%. These percentages further increase when focusing on elderlies, which are becoming a more important segment of the population in developed countries, due to higher life standards and better medical care. Besides involving a long medical recovery path, non-unions are often accompanied by pain and can cause functional and psychosocial disability [2], [3]. The costs associated with non-unions can reach up to 100k € depending on the case, most of which often derive from collateral issues, such as inability to start working soon.

A current widespread clinical practice for bone repair is based on natural grafts, which are tissue portions harvested from a donor and implanted into the defect to be treated. Donors can be either the patient himself, another person entirely or a cadaver. In the first two cases, grafts come from specific healthy areas where the harvesting procedure will not affect the functionality of the area itself. Instead, synthetic grafts make use of ceramic materials, collagen-ceramic composites and polymers as source materials to create bone substitutes. As these materials are indeed synthetic, the use of such grafts does not require a donor, which is the reason why this approach has been recently gaining great interest, resulting in predictions of strong market growth over the coming years. However, the manufacturing of synthetic implants with adequate mechanical properties, in particular for long bones repair, still represents an issue and an open quest.

Implants fabricated by AM could be of great benefit for the treatment of bone defects, with particular focus on non-unions in long bones. The inherent adavnatge of this technology is the morphological freedom, which allows to manufacture scaffolds that perfectly fit a specific defect simply by using from CT or MRI images of the site anatomy as models. In addition, mechanical properties can be tailored by optimizing the manufacting pattern and, thus, pore size and distribution. Porosity, together with the specific chemistry of the material of choice, allows to tune another key property for defect treatment such as resorption rate. Whereas scaffolds are degraded by the body at a pace matching the formation of new bone, implant stability is maintained all along defect recovery and revision surgeries can be avoided. Despite the high degree of freedom and tunability offered by AM, it seems that the application of additively-manufactured scaffold in the clinics is still quite limited and that most of the work is still being done at research level. Mainly emerging small companies have started exploring the sector by commercializing products fabricated via AM. For example, *Xilloc* has been manufacturing custom-made craniomaxilofacial implants in titanium or polyetheretherketone (PEEK) for over 10 years within Maastricht University Medical Centre (MUMC) and has recently started providing their solutions to surgeons and patients outside MUMC. However, their two main materials of choice are non-resorbable, which means that a perfect match of timed mechanical properties cannot be achieved. *Osteopore International* is the only company to our knowledge that has managed to enter the market with polymeric scaffolds fabricated via ME-AM for bone defects. Recently, a poly(caprolactone) (PCL) scaffold from *Osteopore* was successfully implanted to restore a tibial non-union at MUMC, in a surgery that drew the media's attention [4]. The uncountable explorative and optimization studies available in literature on ME-AM of 3D polymeric scaffolds for bone regeneration provide a large pool of data to draw from to start evaluating the most feasible solution in the clinical activity. We believe that the research presented in this thesis will have an impact in guiding the future research on such products, as we propose strategies to optimize their manufacturing and enhancing their biofunctionality, with the goals of improving the surgical outcome, of shortening healing times and reducing the burden for patients and society. The combination of the knowledge presented in the single chapters of this thesis into a single product can be seen as a reasonable next step to research and translate into clinic. Such scaffold would: i) be manufactured following an optimal procedure, which would take care of the morphological accuracy as well as of the mechanical properties, ii) induce greater cell attachment and have more ductile behavior under compression, iii) have osteogenic effect, iv) present a gradient in stiffness to properly mimic the osteochondral region. Of course, as previously mentioned, further optimization would be required for each of the strategies and solutions presented along this thesis, before obtaining a “ready-to-use” scaffold. Yet, we believe we traced the road towards more morphologically and mechanically optimal, cheaper, more biomimicking and bioactive products for bone non-union treatment compared to the current state-of-the-art.

REFERENCES

[1] B. Wildemann *et al.*, "Non-union bone fractures," *Nat Rev Dis Primers*, vol. 7, no. 1, p. 57, Aug. 2021, doi: 10.1038/s41572-021-00289-8.

[2] M. R. Brinker, B. D. Hanus, M. Sen, and D. P. O'Connor, "The Devastating Effects of Tibial Nonunion on Health-Related Quality of Life," *J Bone Joint Surg*, vol. 95, no. 24, pp. 2170–2176, Dec. 2013, doi: 10.2106/JBJS.L.00803.

[3] M. R. Brinker, A. Trivedi, and D. P. O'Connor, "Debilitating Effects of Femoral Nonunion on Health-Related Quality of Life," *J Orthop Trauma*, vol. 31, no. 2, pp. e37–e42, Feb. 2017, doi: 10.1097/BOT.0000000000000736.

[4] "Osteopore and Maastricht UMC+ develop bioresorbable bone implant." https://www.nsmedicaldevices.com/news/osteopore-maastricht-umc/# (accessed Jun. 12, 2023).

APPENDIX

SUMMARY

Currently, clinical treatments for the repair of critical-size bone defects are mainly based on autografts. These strategies are generally inefficient due to restricted availability, lack of structural properties, and even donor site morbidity. Recently, the field of tissue engineering has been investigating for innovative solutions to be applied in orthopedics to regenerate bone tissue. Among various research areas, the pursuit of a manufacturing method able to provide patient-personalized implants resulted in the rise of Melt-extrusion additive manufacturing (ME-AM). This class of implant fabrication techniques allows to produce scaffolds with custom morphologies, biodegradable, highly porous and with tailorable mechanics, able to provide the necessary environment and support to cells in the process of new bone formation. However, despite the promising characteristics, implant fabrication is still far from being an optimal process. In fact, the manufacturing procedure itself is usually carried out in a somewhat random manner, being the result of trial-and-error loops where the interaction between material properties and processing equipment is not considered from a fluid-dynamics-perspective. Furthermore, these scaffolds are fabricated with synthetic polymers, which lack those chemical and topographical cues typical of biological materials that promote and support tissue regeneration. At last, improper planning of the manufacturing process may result in uncontrolled development of scaffolds properties, such as surface stiffness and roughness, which are known to influence cell behavior and tissue regeneration. **Chapter 1** of this thesis presents a deep analysis of the current limitations in ME-AM for bone regeneration and reviews the several strategies elaborated over the last years to obtain more optimal implants, highlighting the directions for further research. Strategies such as the development of fluid-dynamics models to optimize manufacturing and post-fabrication physical and chemical treatments to augment biomimicry and bioactivity are reviewed. In the search for optimal manufacturing of scaffolds able to boost bone regeneration, the aim of this thesis is to further contribute to the field by developing a deeper knowledge of the ME-AM process to then integrate it into material- and fabrication-driven approaches to optimize the manufacturing and the performances of scaffolds for bone tissue regeneration.

To start with, **Chapter 2** provides a solution to the recurrent issue of the choice of proper scaffold manufacturing parameters. In **Chapter 2**, a mathematical model was developed to estimate in advance the morphological and mechanical properties of scaffolds manufactured via ME-AM, to assist in screening new materials, shifting to new equipment or optimizing the current production in terms of performance in a biological environment. This model was derived by considering the interaction between the thermal and rheological properties of the material with the manufacturing device and the surrounding environment. First, the possibility of extruding the material in object, depending on the features of a specific device, was evaluated, allowing to assess in advance the compatibility of the couple material/device. Subsequently, the model quantified the flow rate out of the printer, which, together with the cooling kinetics, influences the possibility of crossing the gap over a pore (bridging). The modelling of the thermal behavior also allowed to describe the shape retention of the filament cross-section upon deposition and over cooling, which determines the actual scaffold layer height and the final morphological accuracy. Eventually, the mechanical behavior of the welding points between layers was estimated as a function of the extrusion temperature and environmental conditions, highlining the interdependence among the difference phenomena. The goal of the model was to allow a user to evaluate in advance the morphological and mechanical properties of scaffold manufactured

with a specific set of processing parameters, so that to possibly adjust the fabrication phase towards more accurate implants.

Once a model to support the manufacturing of scaffolds with the intended requirements had been established, in **Chapter 3** the bioactivity issue was tackled together with the widening of the suitable materials for ME-AM. In fact, high molecular weight (M_w) polymers, although favorable materials because of their enhanced mechanical properties, are often not processable because of their associated high melt viscosity. In **Chapter 3**, scaffolds were fabricated upon the blending of a common biocompatible thermoplastic polymer of high M_w, poly(D,L-lactic acid) (PDLLA), with an additive with known bioactive effects, vitamin D3 (VD3). The inclusion of VD3 led to a decrease in melt viscosity and, consequently, in the power requirement for fabrication. This enabled the processing of such polymer grade without risking molecular degradation, a potential consequence of the usual approach based on the increase of the manufacturing temperature. As demonstrated by differentiation studies with mesenchymal stromal cells (hMSCs), the blending with VD3 allowed also to overcome the inherent bioinertness of synthetic polymers, thus avoiding post-processing treatments. In particular, results indicated that VD3 supported osteogenic differentiation more than the osteogenic culture medium, suggesting that the blending of such additive with synthetic polymers is an elegant strategy to increase the versatility of ME-AM and promote bone tissue regeneration.

After widening the palette of processable materials while overcoming their inherent bioinertness at the same time, in **Chapter 4** another limitation of scaffold manufacturing by ME was tackled. Despite bone being a rather complex tissue from the morphological point of view, with rough surfaces and pores of a size spanning hundredths of microns, ME-AM scaffolds usually present relatively smooth surfaces and bulky filaments. In fact, porosity is present only in the voids originating from the deposition pattern, resulting in a limited biomimicry. In **Chapter 4**, scaffolds presenting surface topography and intra-filament microporosity accessible from the outside were fabricated. Sodium citrate (SOCIT) and poly(vinyl alcohol) (PVA) were chosen as additives to the main poly(L-lactide) (PLLA) matrix to originate different scales of porosity, with a rather straightforward workflow. Upon the application of heat during manufacturing, SOCIT decomposes originating voids within the polymer filaments. PVA, thoroughly mixed with PLLA by extrusion with a screw-based printer, phase-separated into water-soluble domains. Subsequent incubation in water resulted into surface roughness and interconnection of the pores from SOCIT decomposition, which were additionally opened to the outside. These microporous scaffolds did not show any decrease in elastic modulus but instead higher strain at maximum load, resulting in a more biological-alike ductile behavior. Biological tests showed greater hMSCs adhesion after 24 h of culture, with a more spread and random cellular morphology, and enhanced metabolic and osteogenic activity after 7 days.

In **Chapter 5**, we explored how proper planning of the manufacturing process allows to control the development of scaffold features such surface stiffness and surface roughness. Semi-crystalline polymers are grades with superior mechanics but are particularly sensitive to thermal stresses. Currently, limited investigation and planning are carried out on the outcomes of the chosen printing strategy and, as a result, different crystal sizes and densities can be achieved. This influences surface stiffness and roughness, intertwined properties that, in turn, can affect cell activity. In **Chapter 5**, we designed a strategy to innovatively study the effect of crystallinity on, separately, the stiffness and roughness of the surface of polymer films, by applying thermal stresses typical of ME-AM. *In vitro* tests were carried out in order to evaluate how different thermal histories, usually unaccounted for, might affect cell fate. In osteogenic environment, hMSCs showed to be more responsive to surface roughness than to surface stiffness. Overall crystal size distribution resulted to influence cellular behavior more than the average roughness. These findings suggest that awareness and proper planning of the thermal history applied to semi-crystalline polymers during ME-AM are necessary in order to avoid potential unwanted effects on cell fate.

All the aforementioned results are discussed and placed into the state of the art context, in **Chapter 6,** while providing future perspectives. To finalize, a reflection on the scientific and societal impact of the research carried out in this thesis is presented in **Chapter 7.**

SAMENVATTING

Momenteel zijn klinische behandelingen voor het herstel van botdefecten van kritische grootte voornamelijk gebaseerd op autotransplantaten. Deze strategieën zijn over het algemeen inefficiënt vanwege de beperkte beschikbaarheid, het gebrek aan structurele eigenschappen en zelfs de morbiditeit op de donorlocatie. Onlangs heeft het gebied van weefselmanipulatie onderzoek gedaan naar innovatieve oplossingen die in de orthopedie kunnen worden toegepast om botweefsel te regenereren. Op verschillende onderzoeksgebieden resulteerde het streven naar een productiemethode die patiënt-gepersonaliseerde implantaten kon leveren in de opkomst van Melt-extrusie additive manufacturing (ME-AM). Deze klasse van implantaatfabricagetechnieken maakt het mogelijk om steigers te produceren met op maat gemaakte morfologieën, biologisch afbreekbaar, zeer poreus en met op maat gemaakte mechanica, die in staat zijn om de noodzakelijke omgeving en ondersteuning te bieden aan cellen in het proces van nieuwe botvorming. Ondanks de veelbelovende eigenschappen is de vervaardiging van implantaten echter nog steeds verre van een optimaal proces. In feite wordt het fabricageproces zelf meestal op een enigszins willekeurige manier uitgevoerd, omdat het het resultaat is van vallen en opstaan, waarbij de interactie tussen materiaaleigenschappen en verwerkingsapparatuur niet vanuit een vloeistofdynamica-perspectief wordt bekeken. Bovendien zijn deze steigers vervaardigd met synthetische polymeren, die de chemische en topografische kenmerken missen die typisch zijn voor biologische materialen en die weefselregeneratie bevorderen en ondersteunen. Uiteindelijk kan een onjuiste planning van het productieproces resulteren in een ongecontroleerde ontwikkeling van eigenschappen van steigers, zoals oppervlaktestijfheid en ruwheid, waarvan bekend is dat ze het celgedrag en de weefselregeneratie beïnvloeden. **Hoofdstuk 1** van dit proefschrift presenteert een diepgaande analyse van de huidige beperkingen van ME-AM voor botregeneratie en bespreekt de verschillende strategieën die de afgelopen jaren zijn ontwikkeld om optimalere implantaten te verkrijgen, waarmee de richting voor verder onderzoek wordt benadrukt. Strategieën zoals de ontwikkeling van vloeistofdynamicamodellen om de productie te optimaliseren en fysische en chemische behandelingen na de fabricage om biomimicry en bioactiviteit te vergroten, worden besproken. In de zoektocht naar een optimale productie van steigers die botregeneratie kunnen stimuleren, is het doel van dit proefschrift om verder bij te dragen aan het veld door een diepere kennis van het ME-AM-proces te ontwikkelen om het vervolgens te integreren in materiaal- en fabricagegedreven benaderingen van botregeneratie. het optimaliseren van de productie en de prestaties van steigers voor de regeneratie van botweefsel.

Om te beginnen biedt **Hoofdstuk 2** een oplossing voor het terugkerende probleem van de keuze van de juiste parameters voor de productie van steigers. In **Hoofdstuk 2** werd een wiskundig model ontwikkeld om vooraf de morfologische en mechanische eigenschappen te schatten van steigers vervaardigd via ME-AM, om te helpen bij het screenen van nieuwe materialen, het overstappen op nieuwe apparatuur of het optimaliseren van de huidige productie in termen van prestaties in een biologische omgeving. . Dit model is afgeleid door rekening te houden met de interactie tussen de thermische en reologische eigenschappen van het materiaal met het productieapparaat en de omgeving. Eerst werd de mogelijkheid om het materiaal in het object te extruderen, afhankelijk van de kenmerken van een specifiek apparaat, geëvalueerd, waardoor vooraf de compatibiliteit van het koppelmateriaal/apparaat kon worden beoordeeld. Vervolgens kwantificeerde het model de stroomsnelheid uit de printer, die, samen met de koelkinetiek, de mogelijkheid beïnvloedt om de opening over een porie te overschrijden (brugvorming). De modellering van het thermische gedrag maakte het ook mogelijk om het vormbehoud van de filamentdwarsdoorsnede bij afzetting en overkoeling te beschrijven, wat de werkelijke hoogte van de steigerlaag en de uiteindelijke morfologische nauwkeurigheid bepaalt. Uiteindelijk werd het mechanische gedrag van de laspunten tussen de lagen geschat als een functie van de extrusietemperatuur en de omgevingsomstandigheden, wat de onderlinge afhankelijkheid tussen de verschillende verschijnselen benadrukte. Het doel van het model was om een gebruiker in staat te stellen vooraf de morfologische en mechanische eigenschappen te evalueren van een steiger die met een specifieke reeks verwerkingsparameters is vervaardigd, zodat de fabricagefase mogelijk kan worden aangepast in de richting van nauwkeurigere implantaten.

Nadat een model ter ondersteuning van de productie van steigers met de beoogde eisen was opgesteld, werd in **hoofdstuk 3** het probleem van de bioactiviteit aangepakt, samen met de verruiming van de geschikte materialen voor ME-AM. In feite zijn polymeren met hoog molecuulgewicht (Mw), hoewel gunstige materialen vanwege hun verbeterde mechanische eigenschappen, vaak niet verwerkbaar vanwege de daarmee gepaard gaande hoge smeltviscositeit. In **Hoofdstuk 3** werden scaffolds vervaardigd door het mengen van een gangbaar biocompatibel thermoplastisch polymeer met een hoog Mw , poly (D,L-melkzuur) (PDLLA), met een additief met bekende bioactieve effecten, vitamine D3 (VD3). De opname van VD3 leidde tot een afname van de smeltviscositeit en bijgevolg van het benodigde vermogen voor de fabricage. Dit maakte de verwerking van een dergelijke polymeerkwaliteit mogelijk zonder het risico van moleculaire degradatie, een mogelijk gevolg van de gebruikelijke aanpak gebaseerd op de verhoging van de productietemperatuur. Zoals aangetoond door differentiatiestudies met mesenchymale stromale cellen (hMSC's), maakte het mengen met VD3 het ook mogelijk om de inherente bio-inertheid van synthetische polymeren te overwinnen, waardoor nabewerkingsbehandelingen werden vermeden. De resultaten gaven in het bijzonder aan dat VD3 osteogene differentiatie meer ondersteunde dan het osteogene kweekmedium , wat suggereert dat het mengen van een dergelijk additief met synthetische polymeren een elegante strategie is om de veelzijdigheid van ME-AM te vergroten en de regeneratie van botweefsel te bevorderen.

tegelijkertijd hun inherente bio-inertie te overwinnen , werd in **Hoofdstuk 4** een andere beperking van de productie van steigers door ME aangepakt. Ondanks dat bot vanuit morfologisch oogpunt een nogal complex weefsel is, met ruwe oppervlakken en poriën met een grootte van honderdsten van microns, vertonen ME-AM-scaffolds doorgaans relatief gladde oppervlakken en omvangrijke filamenten. In feite is porositeit alleen aanwezig in de holtes die voortkomen uit het afzettingspatroon, wat resulteert in een beperkte biomimicry. In **Hoofdstuk 4** werden steigers vervaardigd die oppervlaktetopografie en intra-filament microporositeit vertonen die van buitenaf toegankelijk zijn. Natriumcitraat (SOCIT) en poly(vinylalcohol) (PVA) werden gekozen als additieven aan de belangrijkste poly(L-lactide) (PLLA)-matrix om verschillende porositeitsschalen te creëren, met een vrij eenvoudige workflow. Bij toepassing van warmte tijdens de productie ontleedt SOCIT de oorspronkelijke holtes in de polymeerfilamenten. PVA, grondig gemengd met PLLA door extrusie met een op schroeven gebaseerde printer, fasegescheiden in wateroplosbare domeinen. Daaropvolgende incubatie in water resulteerde in oppervlakteruwheid en onderlinge verbinding van de poriën door SOCIT-afbraak, die bovendien naar buiten werden geopend. Deze microporeuze steigers vertoonden geen enkele afname van de elastische modulus, maar in plaats daarvan een hogere spanning bij maximale belasting, resulterend in een meer biologisch-achtig ductiel gedrag. Biologische tests toonden een grotere adhesie van hMSC's aan na 24 uur kweken, met een meer gespreide en willekeurige cellulaire morfologie, en verbeterde metabolische en osteogene activiteit na 7 dagen.

In **Hoofdstuk 5** hebben we onderzocht hoe een goede planning van het productieproces het mogelijk maakt om de ontwikkeling van steigerkenmerken, zoals oppervlaktestijfheid en oppervlakteruwheid, te beheersen. Semikristallijne polymeren zijn kwaliteiten met superieure mechanica, maar zijn bijzonder gevoelig voor thermische spanningen. Momenteel wordt er beperkt onderzoek en planning uitgevoerd naar de resultaten van de gekozen printstrategie en als gevolg daarvan kunnen verschillende kristalgroottes en -dichtheden worden bereikt. Dit beïnvloedt de stijfheid en ruwheid van het oppervlak, verweven eigenschappen die op hun beurt de celactiviteit kunnen beïnvloeden. In **Hoofdstuk 5** hebben we een strategie ontworpen om op innovatieve wijze het effect van kristalliniteit op, afzonderlijk, de stijfheid en ruwheid van het oppervlak van polymeerfilms te bestuderen, door thermische spanningen toe te passen die typisch zijn voor ME-AM. Er werden *in vitro* tests uitgevoerd om te evalueren hoe verschillende thermische geschiedenissen, die gewoonlijk niet worden vermeld, het lot van de cellen zouden kunnen beïnvloeden. In een osteogene omgeving bleken hMSC's beter te reageren op oppervlakteruwheid dan op oppervlaktestijfheid. De algehele kristalgrootteverdeling had tot gevolg dat het cellulaire gedrag meer werd beïnvloed dan de gemiddelde ruwheid. Deze bevindingen suggereren dat bewustzijn en een goede planning van de thermische geschiedenis toegepast op semi-kristallijne polymeren tijdens ME-AM noodzakelijk zijn om mogelijke ongewenste effecten op het lot van de cellen te voorkomen.

Alle bovengenoemde resultaten worden in **hoofdstuk 6 besproken en in de** state-of-the-art context geplaatst, terwijl ze toekomstperspectieven bieden. Ter afsluiting wordt in **Hoofdstuk 7** een reflectie gepresenteerd op de wetenschappelijke en maatschappelijke impact van het onderzoek dat in dit proefschrift wordt uitgevoerd.

LIST OF PUBLICATIONS

PUBLICATIONS RELATED TO THIS THESIS

A. R. Calore, V. Srinivas, S. Anand, A. Albillos-Sanchez, S. Looijmans, L. van Breemen, C. Mota, K. Bernaerts, J. Harings, L. Moroni. Shaping and properties of thermoplastic scaffolds in tissue regeneration: The effect of thermal history on polymer crystallization, surface characteristics and cell fate. Journal of Materials Research, 2021, 36, 3914-3935.

A. R. Calore, D. Hadavi, M. Honing, A. Albillos-Sanchez, C. Mota, K. Bernaerts, J. Harings, L. Moroni. Cholecalciferol as Bioactive Plasticizer of High Molecular Weight Poly (D, L-Lactic Acid) Scaffolds for Bone Regeneration. Tissue Engineering Part C: Methods, 2022, 28, 335-350.

A. R. Calore, V. Srinivas, L. Groenendijk, A. Serafim, I. C. Stancu, A. Wilbers, N. Leoné, A. Albillos Sanchez, D. Auhl, C. Mota, K. Bernaerts, J. Harings, L. Moroni. Manufacturing of scaffolds with interconnected internal open porosity and surface roughness. Acta Biomaterialia, 2023, 156, 158-176.

A. R. Calore, C. Mota, K. Bernaerts, J. Harings, L. Moroni. Melt-Extrusion Additive Manufacturing for Tissue Engineering: applications and limitations. (Accepted in 3D Printing and Additive Manufacturing, 2023).

A. R. Calore, C. Mota, K. Bernaerts, J. Harings, L. Moroni. How will it print? A rheology-based numerical model to predict the properties of melt-extruded scaffolds for bone tissue engineering. (In preparation)

OTHER PUBLICATIONS

H. W. Ooi, C. Mota, A. T. Ten Cate, A. R. Calore, L. Moroni, M. Baker. Thiol–ene alginate hydrogels as versatile bioinks for bioprinting. Biomacromolecules, 2018, 19 (8), 3390-3400.

S. Camarero-Espinosa, A. R. Calore, A. Wilbers, J. Harings, L. Moroni. Additive manufacturing of an elastic poly (ester) urethane for cartilage tissue engineering. Acta biomaterialia, 2020, 102, 192-204.

S. Camarero-Espinosa, C. Tomasina, A. R. Calore, L. Moroni. Additive manufactured, highly resilient, elastic, and biodegradable poly (ester) urethane scaffolds with chondroinductive properties for cartilage tissue engineering. Materials Today Bio, 2020, 6, 100051.

A. R. Calore, R. Sinha, J. Harings, K. Bernaerts, C. Mota, L. Moroni. Additive manufacturing using melt extruded thermoplastics for tissue engineering. Computer-Aided Tissue Engineering: Methods and Protocols, 2021, 75-99.

R. Sinha, A. Sanchez, M. Camara-Torres, I. C. Uriszar-Aldaca, A. R. Calore, et al. Additive manufactured scaffolds for bone tissue engineering: physical characterization of thermoplastic composites with functional fillers. ACS Applied Polymer Materials, 2021, 3 (8), 3788-3799.

V. Ansari, A. R. Calore, J. Zonderland, J. Harings, L. Moroni, K. Bernaerts. Additive manufacturing of α-amino acid based poly (ester amide) s for biomedical applications. Biomacromolecules, 2022, 23 (3), 1083-1100.

G. Montalbano, A. R. Calore, C Vitale-Brovarone. Extrusion 3D printing of a multiphase collagen-based material: An optimized strategy to obtain biomimetic scaffolds with high shape fidelity. Journal of Applied Polymer Science, 2023, 140 (10), e53593.

SCIENTIFIC COMUNICATIONS

Oral presentations

Enhanced surface roughness of additive manufactured scaffolds via foaming agents, TERMIS World Congress, Kyoto (Japan), 2018.

Printability window for thermoplastic polymers in bioextrusion, 29th Annual Conference of the European Society of Biomaterials, Maastricht (The Netherlands), 2018.

Poster presentations

Processing routes for 3D scaffolds in Tissue Engineering, 3D Printing Materials Conference, Geleen (The Netherlands), 2017.

Processing routes for 3D scaffolds in Tissue Engineering, Dutch Polymer Days, Lunteren (The Netherlands), 2017.

Induced microporosity and surface roughness on 3D printed scaffolds, European Polymer Congress, Hersonissos Heraklion Crete (Greece), 2019.

AWARDS

Poster Prize Awarding, European Polymer Federation, European Polymer Congress, 2019.

Gordon E. Pike Prize for the JMR Paper of the Year, Journal of Material Research, 2021.

ACKNOWLEDGMENTS

Unbelievably, this experience that cannot be defined as a journey but rather as an adventure, has come to an end. Many thought this was not going to happen. Honestly, I was one of them. I was definitely one of them. If instead I managed, it is because of the support of many people, many precious people who believed in me and my work.

First of all, I want to thank my family, Orietta, Giancarlo and Luna, who constantly believed in me, pushing me forward with their kind (and often resolute) words and love. They have always supported me in all the decisions I have made and in all the adventures I have embarked, including this very one. Especially this very one, despite the Italian-parents style tears on their faces the moment I communicated them my decision. It is mainly thanks to them and their support during my more-than-I'd-like-to-admit crises if I reached this result. Without their teachings on being persistent with my goals, I would have never made it.
(Prima di tutto, voglio ringraziare la mia famiglia, Orietta, Giancarlo e Luna, che hanno costantemente creduto in me, spingendomi avanti con le loro gentili (e spesso risolute) parole e con il loro amore. Mi hanno sempre supportato in tutte le decisioni che ho preso ed in tutte le avventure in cui mi sono imbarcato, inclusa questa. Specialmente in questa, nonostante le lacrime sui loro volti in pieno stile genitore italiano nel momento in cui ho comunicato loro la mia decisione. È principalmente grazie a loro e al loro supporto durante le mie crisi (in numero maggiore di quanto vorrei ammettere) se ho raggiunto questo risultato. Senza i loro insegnamenti sull'essere deciso con i miei obiettivi, non ce l'avrei mai fatta.)

It is impossible not to thank Lorenzo, who decided to believe in me from the very beginning, offering me this great opportunity. Despite your (sometimes uncontrollable) enthusiasms leading to further countless experiments, I could have not expected or demanded a better supervisor. In my days as a doc-less postdoc, I often celebrated you as an example, able to transmit your passion for the field, to create even a daily connection with your students, being constantly available in case of doubts but also open to learn from your team's work. Together with you, I have to thank Jules as well. The incredible team formed by the two of you constantly (apparently) trusted me in achieving my goals and was always ready to see in my results a side brighter and more encouraging than I did. You were always extremely supportive especially when I was too harsh and critical with myself. Your enthusiasm for my work was always contagious and managed to give me enough confidence to complete my work.

Thank you also Katrien and Carlos, who always provided very targeted and accurate suggestions. Thank you, Carlos, for helping me with very practical and technical issues, often providing me with smart solutions to everyday problems. The daily supervisor I needed at the beginning of my journey. Thank you Katrien for all your feedbacks during our 3D printing meetings, where you were always ready to notice details and unravel weak points often invisible to others. And you kept this approach also when revising my drafts, which allowed to me to add more value to my work.

Many thanks to my unofficial supervisors, Dr. Laurence Malaka and Dr. Ravi Chloroform. Laurence, thank you for all the support during the development of my model. I was tackling a topic completely new for the whole team, which absorbed 75% of my PhD and of my energies, and you selflessly helped me providing guidance and hints to tackle it. Always available and with demands in return, you taught me a lot and supported me with equations and codes. Ravi, you brought positivity to my tough presence in the Biofabrication lab, helping me in taking philosophically all the uncountable issues with the Bioscaffolder and brightening my printing days with the soundtrack played by the FAST printer. With your versatile skills and knowledge, with your wisdom and wet socks, you made my life easier by

providing brilliant hints, always accompanied by your contagious laughter. Your experience spanning from cells to modelling and material science makes you the most complete scientist I have ever met. I have learned a lot from you, and I cannot thank you enough for this.

Big thanks to my all friends and colleagues in MERLN, starting with the Latin gang David, Victor, Daniel and Danielle, who helped me to feel at home during my very first months. Thanks to our cultural similarities, the initial impact with the Dutch society, so different from my standards, was less harsh and dramatic. I thank you for the time spent together also outside the office, especially at both Portuguese headquarters, so cozy and relaxing. You really played an important role in the most unstable phase of my experience in The Netherlands.

I must thank Maria and Kenny as well, with whom I shared so many moments in the Biofabrication lab. Maria, with your toughness even in front of the most horrible printing sessions, and Kenny, with your positivity and your support to mocking Ravi, you both helped me easing the pain of manufacturing uncountable scaffolds of doubtful quality. I want to thank you, together with Clarissa and Jip, also for your precious biological consultation, which allowed me to carry out my (hateful) cell studies and thus conclude my PhD journey. The importance of the contribution the 4 of you gave to my work in undeniable.

Big thanks to Jiaping, David K (“The Butcher”), Gabriele; Francis, and all the other colleagues of the Biofabrication group for the productive meetings and discussions, which often allowed me to easily solve problems which otherwise would have taken way more tears to be overcome. Special thanks to Gabriele and Francis in particular: Gabriele, you helped me feeling a bit of Italy around me, despite your bauscia births; Francis, we shared the passion for rheology and swimming, having great discussions about the former and training sessions of the latter (and unfortunately, I did not stand a chance in either).

Many thanks also to the AMIBM people, with whom I shared the passion for material science and most of my days as a PhD student. I would like to thank Dario and Nils in particular. Dario, you showed me the proper way of living, the classy-Napolitan style, a balanced mix between professional behavior and cazzimma/slaps when other people were not looking. We even met in Naples where you granted me the honor of being insulted (with love) at Trattoria da Nennella. You taught me the art of coffee sweetened with honey, which I have been putting into practice ever since. You often realized my doubts and delusion about my work and provided wise advices despite not being part of my research group. How to thank you adequately if not by saying “Juve M****”? Nils, you were always there to help me with last minute or, better, last second measurements, even remotely when I was already back to Italy during the very last phases of the thesis writing. You showed incredible patients when it was time to instruct me on instruments that I had never heard before and later on topics I had no background on. You were the lab technician I did need.

And last, but definitely not least, some more people to thank from AMIBM. Last because I wanted to give proper credit and enough room to the most important people during my experience in The Netherlands. However, the moment I started writing this, I realize that whatever I could say, it would never be enough. As stated in one of my propositions, colleagues can become collaborators, collaborators can become friends, friends can become family. Because you guys, Geert, Gijs, Manta, Sarah and Varun, really were my family in The Netherlands. For this, for all the support (work-related and emotional) you gave me, for always being there when I needed, but also for all the fun, all the shenanigans, all the despair and all the stress together, I will never be able to thank you sufficiently. Geert, you were my reference for serious topics and discussions about life. I always valued very much your opinion and I often acted upon your suggestions in this matter. You were not only this, but also a very unpredictable source of fun (the priest costume and the to-the-left sneeze to name a few), which makes you a very complete person. Gijs, you were there silently but always present and available, ready to comfort me and help in situations of need. I knew I could always count on you. Even now, that our paths have parted, you are still available towards me, and you are always keen to hosting me. Manta, I really loved making you laugh, because your laughter was the manifestation of the lightheartedness of your heart. And your heart was really big and full of love for all of us. You were our big sister or our mom depending on the times, but I always knew I could rely on your affection. You constantly took care of us with your loving soul and your spicy food. Sarah, you joined our gang much later and, initially, only occasionally. But, from the very beginning, you were already one of us. Good-hearted and caring, you immediately showed us how much you cared for the whole group. And you still do. And while I am writing this, I hate knowing that you are not going to be at my defense, but we will celebrate all together for sure because you too are part of the family. Varun, I cannot give you any other definition than brother, my preposterous and inaccurate brother. I loved and hated you, like in all great bromances. And it still goes on. You were there for me more than anybody else, even when I just wanted to practice my best skill, complaining. You very often tolerated me, never getting angry when you actually had all the right to do so. Because, after all, you are not only a rich Indian guy from a rich family from a poor country, but you are rich in your heart.

Despite all the differences, all the arguments and all the periods when we drifted slightly apart, the six of us kept loving each other, like a real family.

BIOGRAPHY

Andrea Roberto was born on the 17th December 1988 in Padua, Italy. Pursuing his interest in engineering and medicine, he completed his BSc. in Biomedical Engineering at the University of Padua, Italy, in 2010, after performing his bachelor thesis at the National Research Council of Italy (CNR). He then started his MSc. in Bioengineering at the University of Padua but, eager to gain international experienced, he enrolled in the Erasmus Program and spent the second year at the Chalmers University of Technology of Gothenburg, Sweden. There, he performed his master thesis as well, at the Biosynthetic Blood Vessels lab, where he evaluated bacterial nanocellulose as scaffold material for the production of model tumors *in vitro*. After a 4-year long experience in the medical industry as a clinical engineer first, and as a support engineer and specialist then, he decided to follow his passion for research and tissue engineering and, in 2016, he joined MERLN Institute for Technology-Inspired Regenerative Medicine and Aachen-Maastricht Institute for Biobased Materials (AMIBM), as a PhD candidate. There, he worked on an interdisciplinary and collaborative project entitled “Brightlands Materials Center Program on Additive Manufacturing: 3D Printing Biomedical Applications”, which aimed at developing innovative methods to optimize the fabrication of scaffolds for bone tissue regeneration via melt-extrusion additive manufacturing and improve their performance in a biological environment. In his research, he focused on the optimization of the fabrication via melt-extrusion additive manufacturing of scaffolds for bone tissue regeneration, and on the improvement of their performances in a biological environment. With the vital goal of contributing to the progress of healthcare, in the future he aims at developing innovative solutions to improve patients’ life quality.

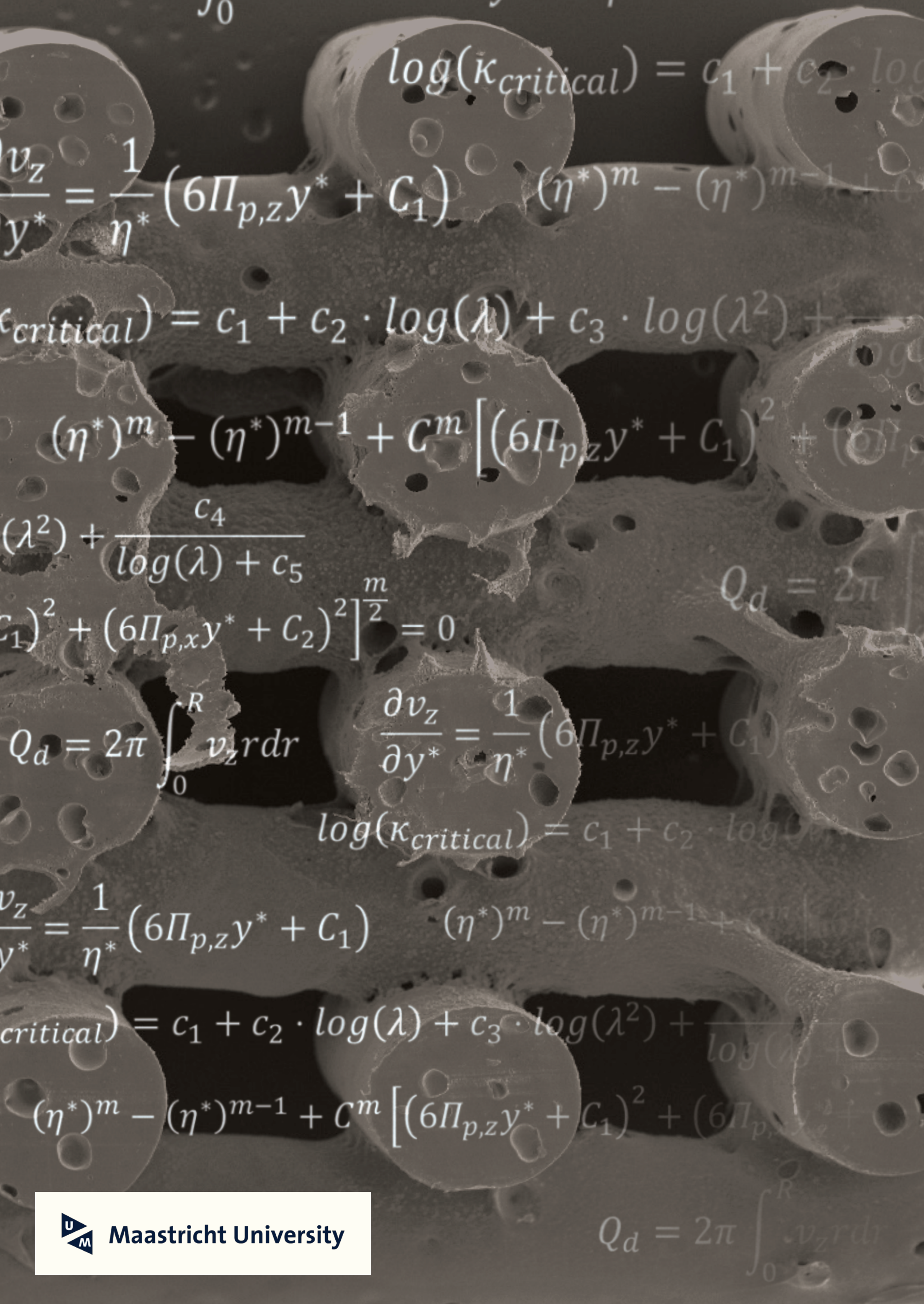

Maastricht University